Department of Physics and Astronomy

University of Heidelberg

Master thesis

in Physics

submitted by

Ram-Janik Petzold

born in Tübingen

2020

Few ultracold fermions in a two-dimensional trap

This Master thesis has been carried out by Ram-Janik Petzold

at the

Physikalisches Institut Heidelberg

under the supervision of

Prof. Dr. Selim Jochim

Few ultracold fermions in a two-dimensional trap:

This master thesis concerns the development, design, installation, alignment and characterization of a novel experimental setup, which was designed to explore the emergence of many-body quantum effects of ultracold fermion gases in two dimensions starting from the few-particle level. It mainly consists of a quasi-two-dimensional optical dipole trap for a system of countable few fermionic ^{6}Li atoms. The trap is created by two red-detuned laser beams interfering in their crossing region and providing a strong vertical confinement by an optical standing wave pattern. An additional single focused beam trap perpendicular to this light-sheet structure allows an independent control over the radial restriction of the harmonic trapping potential. Furthermore, the setup enables accurate control over the absolute number of particles in the trap as well as the inter-particle interaction strength and spin-resolved single-atom detection, which has already been demonstrated in a quasi-one-dimensional configuration. It is expected that this experimental simulator will allow to study the onset of quantum many-body physics in two dimensions by mapping out correlations in position and momentum space.

Wenige ultrakalte Fermionen in einer zwei-dimensionalen Falle:

Diese Masterarbeit beschäftigt sich mit der Entwicklung, dem Design, der Installation, der Justage und der Charakterisierung eines neuen experimentellen Aufbaus, der konstruiert wurde, um die Entstehung von Vielteilchen-Quanteneffekten mit ultrakalten fermionischen Gasen in zwei Dimensionen zu entdecken, beginnend von der Wenigteilchen-Ebene. Er besteht hauptsächlich aus einer quasi-zweidimensionalen optischen Dipolfalle für ein System aus abzählbar wenigen fermionischen ^{6}Li-Atomen. Die Falle wird durch zwei rot-verstimmte Laserstrahlen erzeugt, die in ihrem Kreuzungsbereich interferieren und einen starken vertikalen Einschluss in Form einer optischen stehenden Welle bereitstellen. Eine zusätzliche Falle aus einem einzelnen fokussierten Strahl rechtwinklig zu dieser Lichtscheibenstruktur erlaubt die unabhängige Kontrolle über die radiale Begrenzung des harmonischen Fallenpotenzials. Des Weiteren ermöglicht der Aufbau die genaue Kontrolle über die absolute Teilchenzahl in der Falle, genauso wie über die Wechselwirkungsstärke zwischen den Teilchen und Spin-aufgelöste Einzelatom-Erkennung, welche bereits für die quasi-eindimensionale Konfiguration demonstriert worden ist. Es wird erwartet, dass dieser experimentelle Simulator es erlaubt, das Einsetzen von Quanten-Vielteilchen-Physik zu studieren, indem Korrelationen im Positions- und Impulsraum ausgemessen werden.

Contents

1 Introduction

1.1 Quantum simulation

One of the key problems in physics is how to deal with the challenge of many-body complexity on different length scales. If one considers objects of the size of an atom, one can describe them in terms of matter-waves in the context of quantum mechanics. Here the state of an object, like the position, can be characterized by a probability amplitude function reflecting the probability to find the particle at a certain position. The time evolution of such a quantum mechanical state follows the Schrödinger equation. If one considers the regime, where the wave-functions of interacting particles can overlap so strongly, that they become indistinguishable, one can separate two types of particles: particles belonging to systems described by a wave-function, which is symmetric under particle exchange, are called bosons and particles belonging to a system described by a wave-function, which is antisymmetric with respect to the exchange of two particles, are called fermions. The ground state of bosons can be described by a single macroscopic wave-function and a Bose-Einstein condensation occurs. In the case of fermions the essential consequence is that each quantum state can be occupied by not more than a single fermion, known as Pauli's exclusion principle. Here the ground state is different, because each available energy level can be occupied by a single fermion of the same type. So starting with the lowest energy levels the spectrum is successively filled with fermions until a maximum energy level, called the Fermi energy. However with increasing number of interacting particles it becomes impossible to solve the Schrödinger equation explicitly even for a small number of particles. Although in the context of statistical physics many fruitful methods to deal with these challenges were developed by starting from the many-body limit, the bridge between few-particle interactions and many-body phenomena is still under construction from both sides. As even numerical efforts for the solution of such many-particle systems are nearly hopeless, because the Hilbert space of available states scales exponentially with particle number, various physical systems have been investigated, which are able to mimic the relevant quantum mechanical problems in an experimental system. Apart from photonic systems ([15]) or trapped ions ([40]), one of the most prominent examples of such an artificial quantum simulator are systems of ultracold atoms localized in arbitrarily shaped traps, as for example optical lattices ([12]). The crucial advantages of this system, is that one can investigate both categories of particles, bosons or fermions, and even mixtures of them. Furthermore, one is able to tune the interaction between the particles by an external magnetic field, via the so-called Feshbach resonances. On top of that, one also can design the precise form of the localizing potentials by shaping the light intensity of optical dipole potentials, which are proportional to the intensity, meaning the particles are pulled to or repelled from the intensity maxima. These shallow traps allow to cool particle ensembles to the nano-Kelvin regime, where the quantum nature of the particles dominates. In this way various trap shapes were realized and one is even able to select the number of spatial dimensions in which the particles effectively can move. So apart from three-dimensional traps, also quasi-one- and two-dimensional traps were constructed to investigate new phenomena arising under extreme conditions ([42], [41], [17], [31], [21]). In this row one can add the work of this thesis with a quasi-two-dimensional trap for few ultracold fermions. In contrast to many other setups, this experimental simulator should provide full single-particle resolution in position and momentum space. Some exemplary reasons to investigate a quasi-two-dimensional system are that it leads to an energy shell structure like that observed in atomic systems ([30]) and the layer structure is expected to be a key property of high-T_C superconductors ([14]).

1.2 Content of this thesis

This thesis contributes the construction, alignment, and characterization of a quasi-two-dimensional trapping potential, after the development and the design were mainly finished during a Bachelor thesis. In the second chapter some basic information about ultracold fermionic atoms is mentioned together with some exemplary phenomena occurring in systems confined to two dimensions. The third chapter tries to summarize the main experimental steps to create, control, and observe an ultracold sample of few fermions. After this more general information, the thesis focusses on the creation of a tunable two-dimensional trap from a theoretical perspective. In this context, the main ideas for the conceptional development are formulated. For this purpose, the fourth chapter introduces the basic knowledge which is necessary to understand the working principle of optical dipole traps. On this basis, the tunable 2D Trap consisting of three Gaussian beams is described theoretically in chapter 5. In this chapter the essential trap parameters are presented and target values are selected to reach the desired trap properties. The final part of the thesis concentrates on the realization of the target trap. Chapter 6 starts with an overview to the opto-mechanical design of the full setup. Subsequently, the essential steps for the installation and alignment of the opto-mechanical system are presented in chapter 7. Chapter 8 analyses the characteristics of the realized quasi-two-dimensional optical dipole trap, which enables the comparison of the real trap properties with the target values. Against this background, in chapter 9 a final conclusion is drawn.

Part I

Few ultracold fermions in two dimensions

2 Few ultracold fermions confined to two dimensions

This chapter summarizes some basic knowledge about the quantum statistical behaviour of bosons and fermions, introduces the basic system of interest consisting of a cluster of particles with tunable interaction strength, and tries to collect some of the essential phenomena, which can be observed in a Fermi gas confined to two-dimensions.

2.1 Quantum statistics

One possible approach to the many-particle problem is statistical physics, which describes for example a classical gas of particles not by the position and velocity of all constitutes, but for example by the so-called Maxwell-Boltzmann velocity distribution: ([7]).

$$f_{MB}(v) = 4\pi\left(\frac{m}{2\pi k_B T}\right)^{\frac{3}{2}} v^2 \exp\left(-\frac{mv^2}{2k_B T}\right) \tag{2.1}$$

with the particle velocity v, the particle mass m, the temperature of the gas T, and the Boltzmann-constant k_B. In a classical description, particles appear usually as hard balls. Here one can attach names to each particle even if they might collide with each other in the case of a real gas. However, if one considers an atomic gas of the same species the particles become indistinguishable when they are too close to each other, and it was discovered that particles as small as atoms have to be described similar to photons as matter waves with a characteristic de Broglie wavelength ([6], p. 92):

$$\lambda_{dB} = \frac{h}{p} = \frac{h}{\sqrt{2mE}} = \frac{h}{\sqrt{3mk_B T}} \tag{2.2}$$

with the Plank-constant h, the particle momentum p, the particle mass m, and the classical particle energy E. First of all, one can realize that the wavelength increases with decreasing particle mass. If one inserts the thermal energy of a classical gas one can reach a temperature dependence of the de Broglie wavelength. So also for decreasing temperature, the de Broglie wavelength is increasing. This behaviour is important, because the wave-nature of the particles only matters if the wavelength is large compared to the interparticle spacing and the particles might overlap with each other. In this regime, so for small particle mass and for low temperatures, the particles really have to be described as waves, which follow the rules of the theory of quantum mechanics. The central equation in this context is of course the Schrödinger equation ([33]):

$$i\hbar\partial_t|\psi(\vec{x},t)\rangle = \hat{H}|\psi(\vec{x},t)\rangle \tag{2.3}$$

in which the energy operator $\hat{H}$ governs the temporal evolution of the state vector $|\psi(\vec{x},t)\rangle$ and the state vector can be related to a probability amplitude of the matter wave. Unfortunately this equation becomes very complex to solve for many of such quantum particles described by a many-body wave-function $\Psi = \Psi(\vec{x}_1, ..., \vec{x}_N, t)$ of N particles. Furthermore the indistinguishability of particles, which overlap strongly, has the consequence that all observables have to be unchanged if one exchanges two of those particles with each other ([38] and [19]). Therefore, also the probability density of the many-body wave-function has to be unchanged ([7]):

$$|P_{ij}\Psi(..., \vec{x}_i, ..., \vec{x}_j, ...)|^2 = |\Psi(..., \vec{x}_j, ..., \vec{x}_i, ...)|^2 = | \pm \Psi(..., \vec{x}_i, ..., \vec{x}_j, ...)|^2 \tag{2.4}$$

$$\Longleftrightarrow P_{ij}\Psi = \pm\Psi \tag{2.5}$$

Here the particle exchange operator is introduced as: P_{ij}. From this relation one can conclude, that one can distinguish two types of many-particle wave-functions, which are either symmetric or anti-symmetric according to the exchange of two indistinguishable particles. If the exchange of two particles leads to a plus sign, the particles described by the many-body wave-function are called bosons, and if the exchange of two particles causes a minus sign, the particles described by Ψ are called fermions. The antisymmetry condition for the fermions leads to the fact, that each quantum state can be occupied by not more than one fermion at a time. This circumstance is known as Pauli's exclusion principle. The energy of the highest lying particle in the ground state configuration corresponds to the Fermi energy $E_F = \frac{\hbar^2 k_F^2}{2m}$, depending on the Fermi wave vector k_F. In contrast many bosons are able to occupy a single quantum state at the same time. This causes a fundamentally different behaviour near the ground state of a quantum system, which is reached at low temperatures, as demonstrated in figure 2.1.

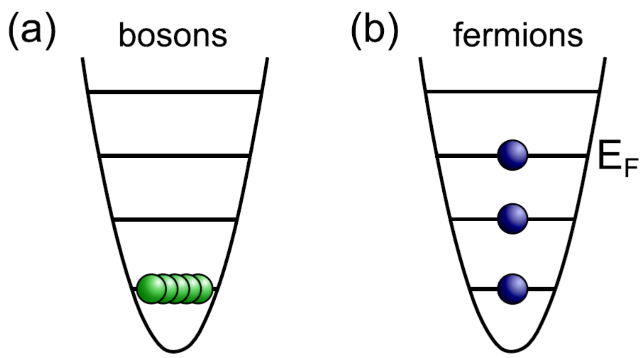

Figure 2.1: On the left the ground state of a bosonic many-body state is shown, and on the right the one of a fermionic many-body state is depicted. The figure is taken from [38].

It is not surprising that for this reason also the mean occupation number distribution functions of fermions and bosons are different. For bosons this has the form of the so-called Bose-Einstein distribution ([7]):

$$n_B = \frac{1}{\exp(\beta(\epsilon - \mu)) - 1} \tag{2.6}$$

with the factor $\beta = \frac{1}{k_B T}$ as the non-relativistic one-particle energy $\epsilon = \frac{p^2}{2m}$ and the chemical potential μ, corresponding to the energy to add or remove one particle. For fermions the mean occupation number can be expressed as([7]):

$$n_F = \frac{1}{\exp(\beta(\epsilon - \mu)) + 1} \tag{2.7}$$

For $T = 0$ the so-called Fermi-Dirac distribution for fermions corresponds to a step-function positioned at μ while the step is smoother for higher temperatures as depicted in figure 2.2.

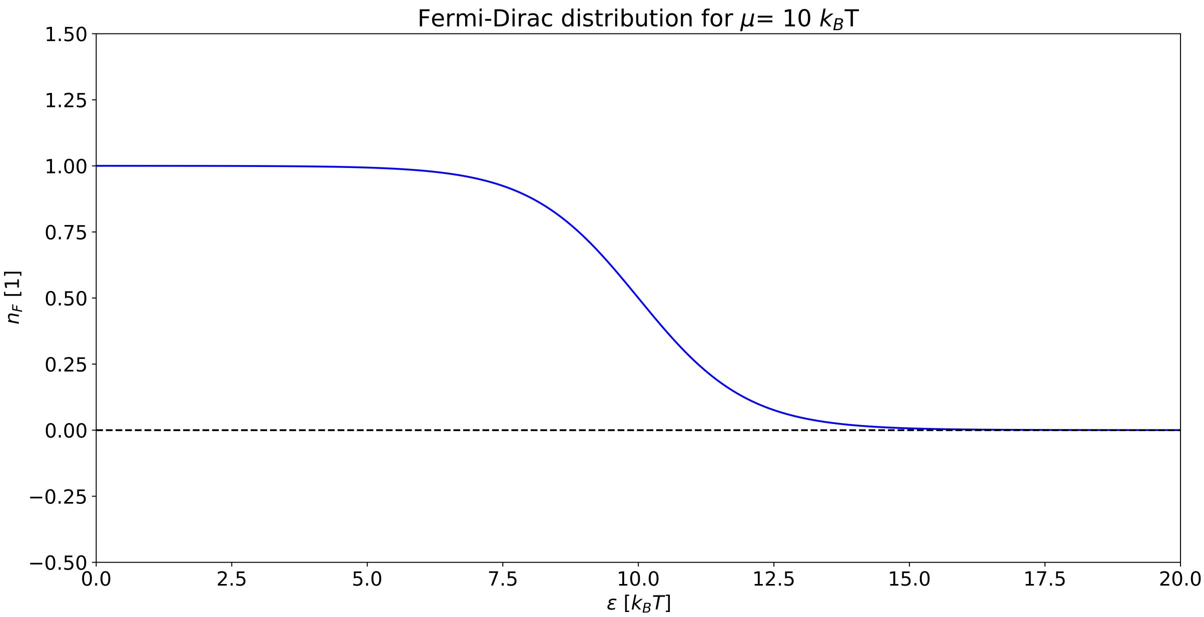

Figure 2.2: The Fermi-Dirac-distribution n_F for a chemical potential of $\mu = 10\ \mathrm{k_B T}$.

2.2 Tuning of interactions

The actual quantum problem is fully described by the Hamiltonian of the system, which has in general for a trapped system of N particles the from of ([38]):

$$\hat{H} = \sum_{i=1}^{N} \hat{T}(\dot{\vec{x}}_i) + \sum_{i=1}^{N} \hat{V}_{trap}(\vec{x}_i) + \sum_{i=1}^{N} \hat{V}_{int}(\vec{x}_i, \vec{x}_j) \tag{2.8}$$

with the kinetic energy term $\hat{T}(\vec{p}_i) = \frac{\hat{p_i}^2}{2m_i}$, the trapping potential term $\hat{V}_{trap}(\vec{x}_i)$, and the interaction term $\hat{V}_{int}(\vec{x}_i, \vec{x}_j)$ between the particle i and j. The trapping potential might be for example a harmonic one: $\hat{V}_{trap}(\vec{x}_i) = \frac{1}{2} m_i \omega^2 \hat{\vec{x}}^2$. The interaction of the particles can be treated in the context of quantum mechanical scattering where one can introduce the scattering length a to characterize the scattering process ([28]). If the energy of the interacting particles is small enough, such that their de Broglie wavelength is much larger than the range of the interaction potential, the interaction potential can be effectively described by a pseudo-potential with a point-like interaction([38]):

$$V(\vec{x}) = g\delta(\vec{x}) \tag{2.9}$$

with the interaction constant:

$$g = \frac{4\pi\hbar^2 a}{2m} \tag{2.10}$$

One strong advantage of ultracold atom experiments is that one can tune the interaction between the particles via Feshbach resonances, described in the next chapter. This opens the door to a phase diagram of interacting fermions. In this context one considers usually a Fermi mixture of two different spin states. The phase diagram for such an interacting Fermi mixture is shown in figure 2.3, where $\frac{1}{k_F a}$ reflects the interaction strength. From high to low temperatures, there appears a phase transition from the normal to the superfluid state.

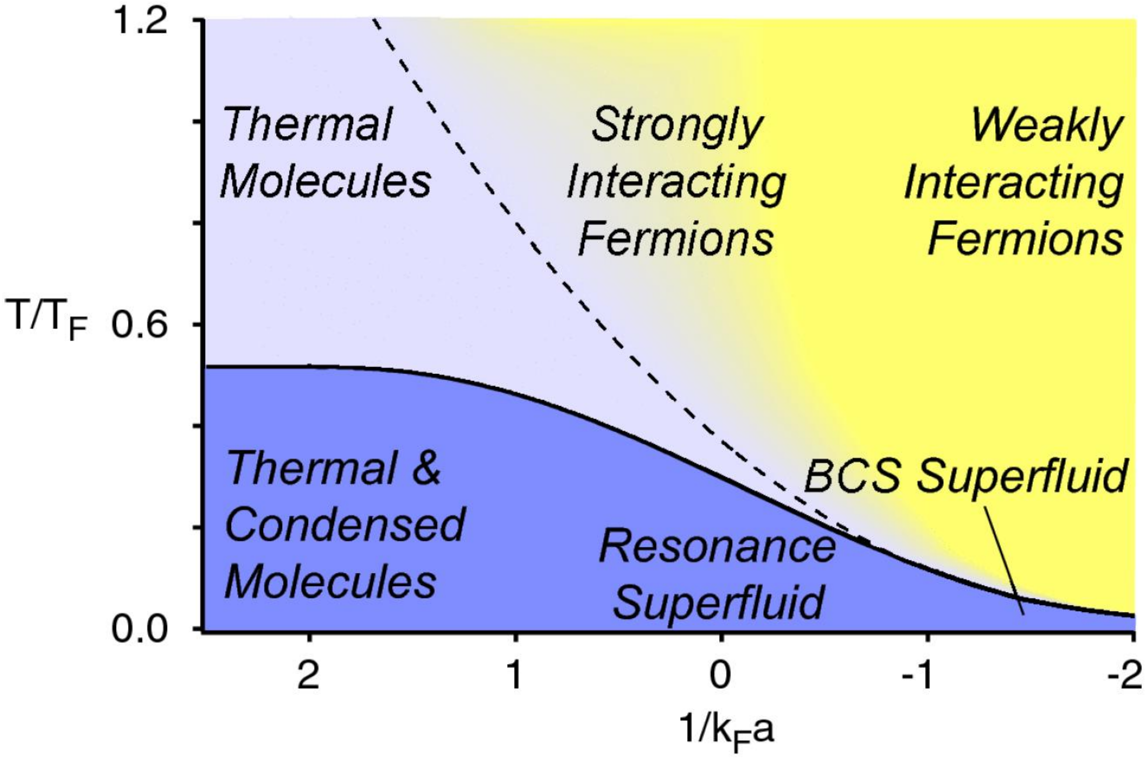

Figure 2.3: Phase diagram of interacting Fermi mixtures in a harmonic trap. The figure is taken from [18].

As depicted in figure 2.4, there exist two limits along the interaction strength. For weak repulsive interaction with $\frac{1}{k_F a} \to +\infty$, the two-component Fermi gas forms molecules of different spin types, which behave effectively as bosons. For weak attractive interaction with $\frac{1}{k_F a} \to -\infty$, the two-component Fermi gas forms very weakly bound long-range Cooper pairs with opposite momenta or pairs in momentum space ([18]).

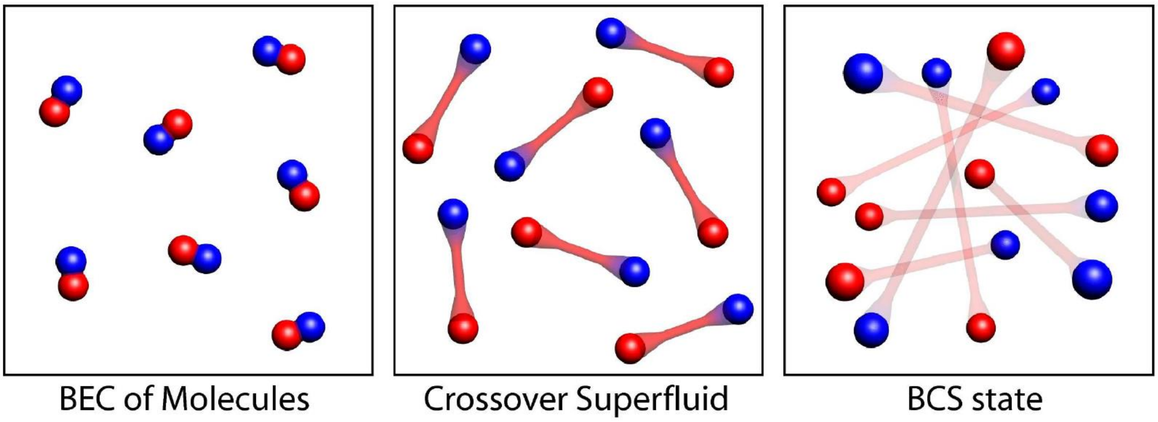

Figure 2.4: Schematic picture of the BEC-BCS-crossover. Left one can see the state of a Bose-Einstein condensate with tightly bound molecules in the form of pairs of opposite spin fermions. On the right the Bardeen–Cooper–Schrieffer state is sketched with loosely bound Cooper pairs, meaning pairs of fermions with opposite spin and momentum. In the centre, the crossover superfluid between the two limits on the left and right is depicted. The figure is taken from [18].

2.3 Phenomena with fermions confined to two dimensions

There appear various differences in the behaviour of fermionic systems if one reduces the dimensionality of the system to two dimensions. For example there exists a two-body dimer at all interaction strengths in two dimensions and not only for positive scattering lengths as in three dimensions ([25]). Besides there exists also no unitary regime in two dimensions as the scattering length does not diverge at the Feshbach resonance ([25]). But most importantly, in two dimensions it is not allowed that a BEC with true long-range order can be created at finite temperatures ([22]). However one can observe a phase transition from the normal to the superfluid phase, which is called the Berenzinskii-Kosterlitz-Thouless (BKT) transition. Qualitatively this phase transition can be understood as described in [25]: In the normal phase vortices as excitations with quantized angular momentum prevent long range order in the phase. The transition to the superfluid state occurs due to pairing of vortices with opposite rotation. In this way their disturbing effect disappears.
The resulting behaviour of the system is characterized by the term of quasi-long range order in the sense of an algebraic decay of the first order correlation function. In contrast to that, in the normal phase one can register an exponential decay. This was observed in our group and published in [23] with the central figure 2.5.

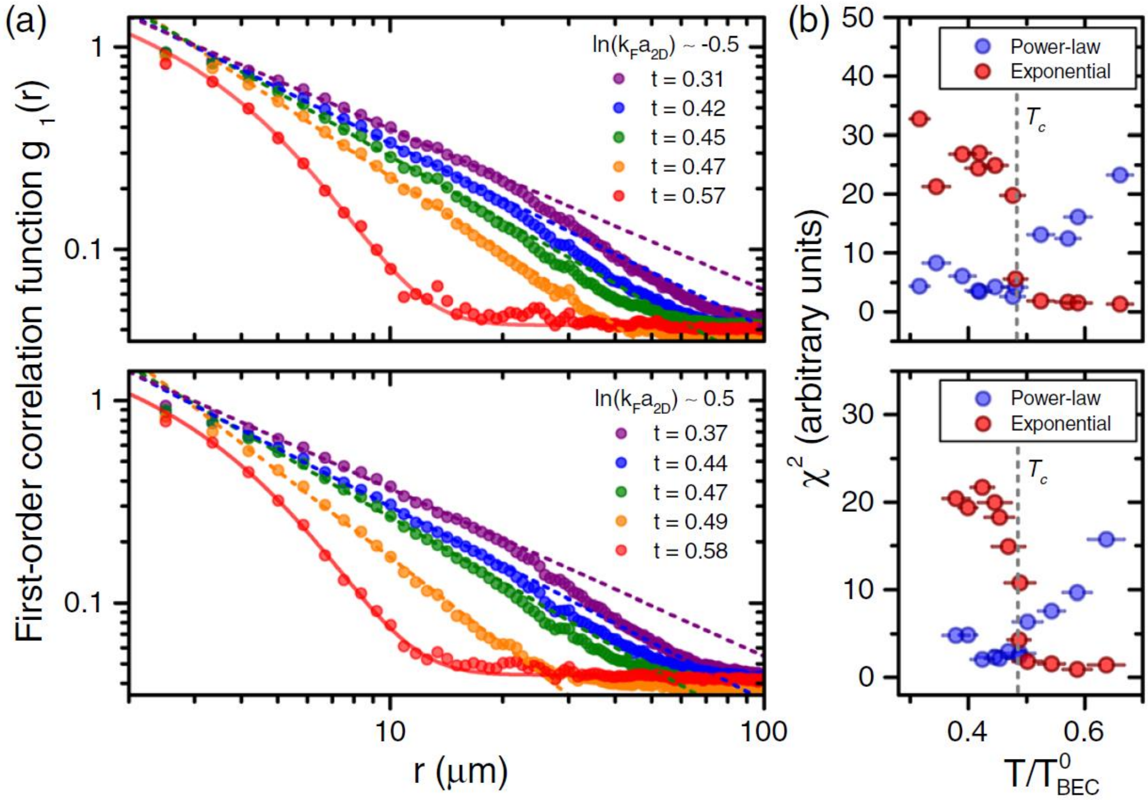

Figure 2.5: Given in (a) is the first-order correlation function for different temperatures. The interaction parameter in the top graph is: $\ln(k_F a_{2D}) \sim -0.5$ and in the bottom graph: $\ln(k_F a_{2D}) \sim 0.5$. In (b) the χ^2 values for the power-law and the exponential fit are shown. The figure is taken from [23].

The phase diagram for a Fermi gas confined to two dimensions was measured in [29] and is shown in figure 2.6. It portrays the non-thermal fraction as function of temperature and interaction strength. One can conclude that there appears a phase transition for all interaction strengths.

A further topic discussed in [3] considers the Higgs mode in a Fermi gas from few to many particles. The model Hamiltonian in this paper considers a fermion system in a balanced mixture of two spin states in a two-dimensional harmonic trap and has the form ([3]):

$$\hat{H} = \sum_{i=1}^{N} \left(-\frac{\hbar^2 \nabla_i^2}{2m} + \frac{1}{2} m\omega^2 \vec{r}_i^{\,2} \right) + g \sum_{k,l} \delta(\vec{r}_k - \vec{r}_l) \quad \text{with :} \quad g < 0 \tag{2.11}$$

including the kinetic energy term with $\nabla_i^2 = \partial_{x_i}^2 + \partial_{y_i}^2$, a harmonic potential term, and a point-contact interaction potential term between particles of different spin where $\vec{r}_i = (x_i, y_i)$ corresponds to the spatial coordinate of particle i. The energy spectrum of a two-dimensional harmonic oscillator forms a shell structure depicted in figure 2.7 ((a),(b),(c)), meaning there are states of equal energy forming an energy shell. This can be easily seen

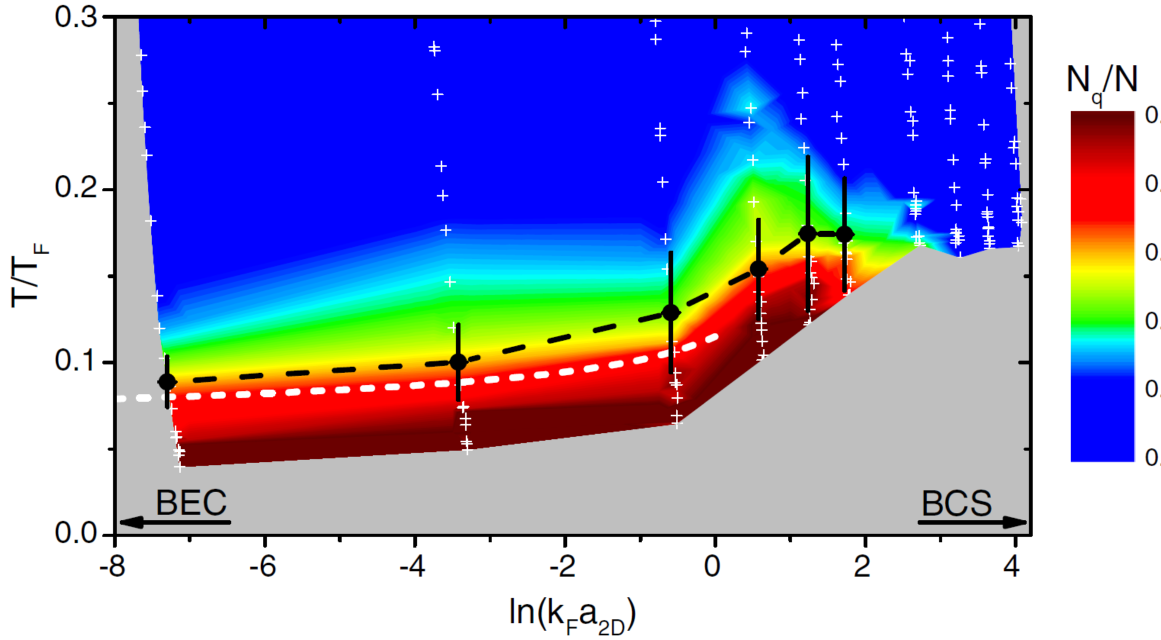

Figure 2.6: Phase diagram of a Fermi gas in two dimensions with the non-thermal fraction as function of interaction parameter $\ln(k_F a)$ and temperature T normalized to the Fermi temperature T_F. The figure is taken from [29].

from the single particle harmonic oscillator energy spectrum in two-dimensions:

$$E(n_x, n_y) = \hbar\omega_x\left(n_x + \frac{1}{2}\right) + \hbar\omega_y\left(n_y + \frac{1}{2}\right) = \hbar\omega(n_x + n_y + 1) \quad \text{for :} \quad \omega_x = \omega_y = \omega \quad (2.12)$$

Here all states with the same value for the sum $n_x + n_y$ have the same energy, although the precise numbers for n_x and n_y might be different.
Alternatively one can formulate the energy spectrum as ([3]):

$$E(n, m) = \hbar\omega(n + |m| + 1) \quad \text{with :} \quad n = 0, 1, 2, 3, ... \quad \text{and} \quad m = 0, \pm 1, \pm 2, \pm 3, ... \quad (2.13)$$

with the main quantum number n and angular momentum quantum number m. For a closed shell configuration of for example 3+3 particles (three spin-up particles and three spin-down particles), there are various different excitations possible in the case of the lowest monopole excitation, with vanishing total angular momentum, as demonstrated in figure 2.7.
In figure 2.7 (part (d)) the lowest monopole excitation is shown in red compared to the second excitation state as function of interaction strength parametrized by the binding energy $\epsilon_b = \frac{\hbar^2}{ma^2}$, which is normalized by the critical binding energy ϵ_c for the occurrence of the Higgs mode in the many-particle limit.
The Higgs mode ‘corresponds to oscillations in the size of the order parameter for a given broken symmetry’ ([3]). One can see a qualitative difference between the first and second excitation. The first excitation energy decreases first with interaction strength and then increases from the critical interaction strength onwards. This can be interpreted as ‘the

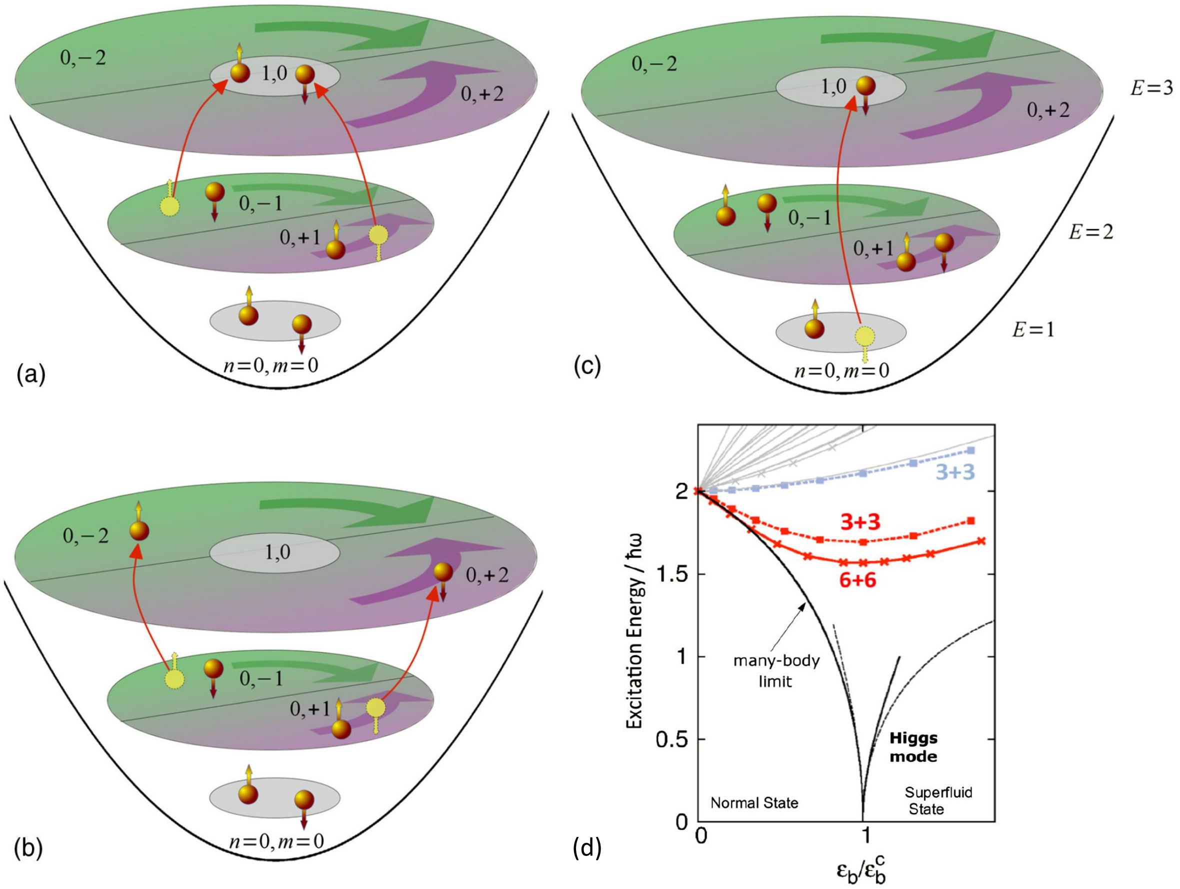

Figure 2.7: In part (a),(b) and (c) the energy level schema for the case of 3+3 fermions in a two-dimensional harmonic oscillator potential is depicted. For the excitation energy of $2\hbar\omega$ there are three different excitation configurations possible, where the total angular momentum vanishes. For (a) and (b) 'time-reversed pairs' are formed with $(n, m, \uparrow)_1$ for one particle and $(n, -m, \downarrow)_2$ for the other. In part (d) the excitation energy spectrum as function of the binding energy ϵ_b is shown, which depends on the interaction strength. The lowest monopole excitation for 3+3 fermions of both spin states is shown as dashed red line and for 6+6 fermions as solid red line. The second excited state for 3+3 fermions is depicted as light blue dashed line together with grey solid lines representing higher excited states for 3+3 fermions. The black line marks the 'numerical (analytical) many-body Higgs mode energy' as mentioned in [3]. The figures are taken from [3].

precursor of the Higgs mode in a Fermi gas' ([3]). In contrast to that, the second excited state energy increases monotonously with interaction strength.

The minimum in the excitation energy spectrum can be explained according to [3] with the fact that the two excited states in figure 2.7 (a) and (b) can exploit different configurations in the empty shell to increase their overlap. The excited particle pair in figure 2.7 (a) and

(b) is called a ‘time-reversed pair’ with the two sets of quantum numbers: $(n, m, \uparrow)$ and $(n, -m, \downarrow)$. The paper suggests the experimental observation of this phenomenon.

Part II

Creating a system of few ultracold fermions

3 Creating and observing a system of few ultracold fermions

This chapter describes the basic steps to create a well-controlled ultracold sample of few fermions and how to detect its behaviour.

3.1 Basic elements: ^{6}Li-atoms

As basic elements to be trapped, ^{6}Li-atoms were chosen. The following characteristics were mainly extracted from [8] where one can also find more detailed information. Lithium as an alkali atom provides many transitions which can be addressed by normal lasers. Most importantly, ^{6}Li behaves as a fermion because, as an alkali atom, it has a single valance electron leading to a spin quantum number of $S = 1/2$. Besides the nuclear spin of ^{6}Li is $I = 1$ ([18]). The mass of the neutral atom ^{6}Li is about: $m(^6Li) = 6.01512280$ u [16]. The crucial line used for cooling and trapping is the D_2-line with a wavelength of $\lambda(D_2) = 670.977338$ nm and a natural line width of $\Gamma = 5.8724$ MHz as published in [8] and shown in the left part of figure 3.1. In the experiment only the three lowermost hyperfine states are used whose energy spectrum as function of external magnetic field is portrayed in the right part of figure 3.1.

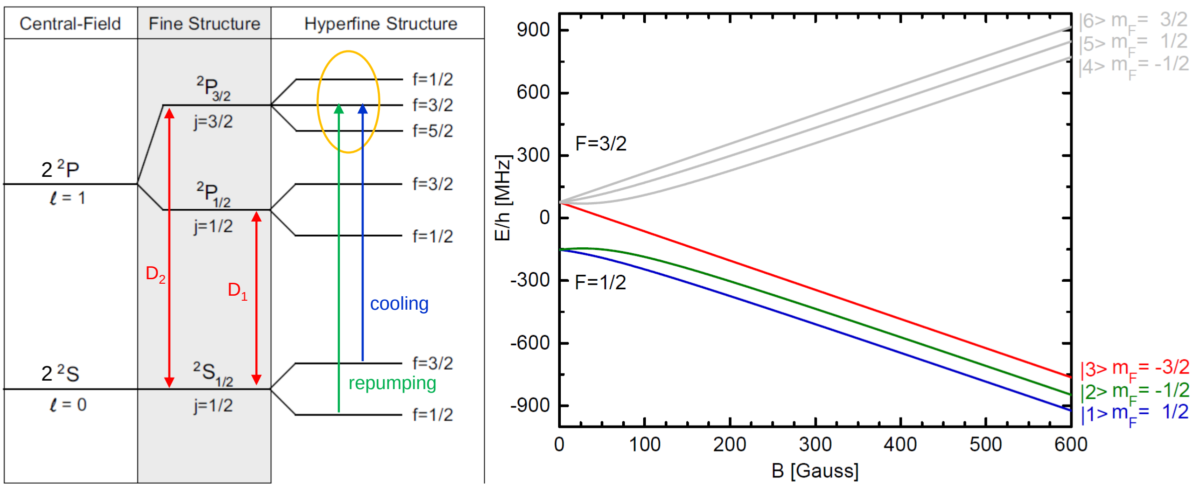

Figure 3.1: On the left: The energy level spectrum of ^{6}Li. The figure was taken from [27] and is based on a graph in [8]. On the right: Lowest hyperfine state energy spectrum of ^{6}Li as function of external magnetic field. The figure was taken from [28].

3.2 Tuning interactions with Feshbach resonances

The concept of tuning the interaction strength via a Feshbach resonance can be understood in the following way using figure 3.2. The phenomenon of the Feshbach resonance, as described in [5], appears during a scattering process of two particles with a small collision energy E. In this context one has to consider two molecular potentials: At large inter-particle distances, the background molecular potential describes the case of two free atoms and therefore connects the free atoms case with the case of two bound atoms. This potential represents the so-called open channel or entrance channel and describes the actual scattering state. The second potential corresponds to the closed channel in the scattering process and is able to evoke molecular bound states near the scattering state of the open channel. Exactly if the molecular bound state of the closed channel in energy space reaches the scattering continuum of the open channel a Feshbach resonance can be observed and the scattering length increases. By tuning the energy difference ΔE

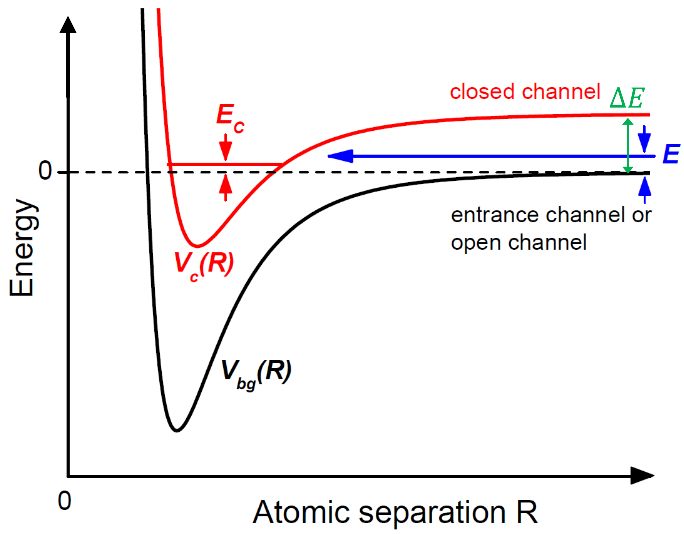

Figure 3.2: The principle of a Feshbach resonance: A molecular level of a closed channel molecular potential V_c approaches the energy level of the scattering continuum of the open channel molecular potential V_{bg}. The closed channel potential and the open channel potential are separated by an energy ΔE, which can be changed by an external magnetic field. The figure is taken from [5] and was slightly modified.

between the two molecular potentials, one can tune the small energy difference between the scattering state of the open channel and the molecular bound state of the closed channel. In this way one is able to scan through the Feshbach resonance. The scattering length is positive if the closed channel is energetically lower than the open channel and negative if the closed channel has a larger energy than the open channel ([28]). Fortunately, the energy difference ΔE can be controlled by an external magnetic field, exploiting the magnetic moment difference $\Delta\mu$ between the two channels ([28]):

$$\Delta E = \Delta\mu B \tag{3.1}$$

The s-wave scattering length can be written as ([5]):

$$a(B) = a_{bg}\left(1 - \frac{\Delta}{B - B_0}\right) \tag{3.2}$$

including the background scattering length a_{bg} from the open channel potential, the Feshbach resonance position in magnetic field space B_0 and the resonance width Δ.

As published in [41], the Feshbach resonances for the three lowest hyperfine states were measured to have the form shown in figure 3.3.

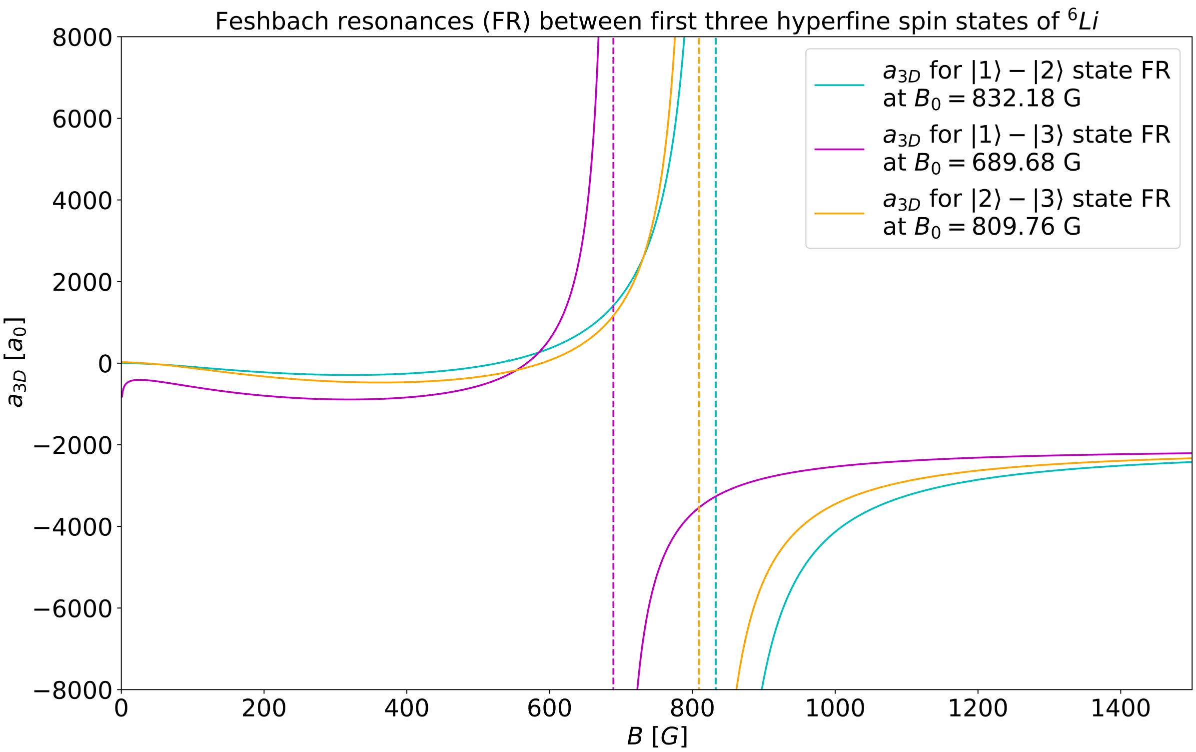

Figure 3.3: Measured Feshbach resonance spectra of the three possible hyperfine state mixtures ($|1\rangle - |2\rangle$, $|1\rangle - |3\rangle$, and $|2\rangle - |3\rangle$) for the three lowest hyperfine states of ^{6}Li.

In this way, one can scan the magnetic field through the BEC-BCS-crossover as demonstrated in figure 3.4.

3.3 Basic steps of cooling and trapping

The following chapter will summarize the essential steps to reach well controlled, isolated and localized samples of trapped fermionic atoms.

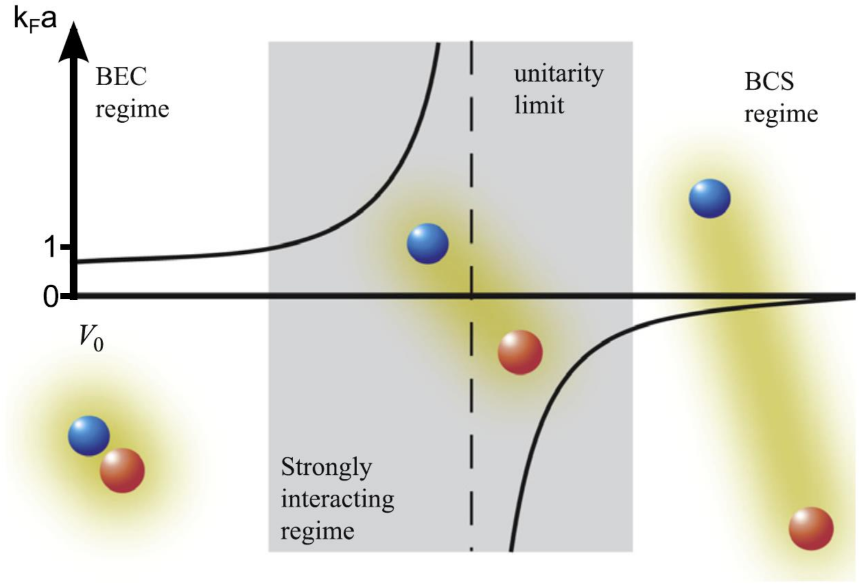

Figure 3.4: Sketch of the interaction parameter as function of magnetic field over the Feshbach resonance. The figure is exploited to demonstrate the three relevant regions in the diagram: On the left the molecular BEC, one the right the BEC regime of Cooper pairs and in the centre the regime of strong interactions including the unitary limit. This figure is taken from [38] and based on [13].

First of all, one has to mention that the experiment takes place in robust vacuum system as shown in figure 3.5 providing a good isolation by an internal pressure of $p_{oven} \approx 10^{-10}$ mbar in the oven section and even $p_{exp} \approx 10^{-12}$ mbar in the experimental chamber ([35]).

In a first step, solid ^{6}Li is heated to about 400 °C to produce hot and fast free atoms. The free atoms can escape through a small aperture out of the oven and in this way form an atomic beam towards the experimental chamber, consisting of a spherical octagon with 6 CF40 view ports and two CF100 flanges.
Figure 3.6 provides an overview to the basic elements, which will be introduced in the following. The velocity of the atoms in the atomic beam is decreased by a Zeeman slower. The Zeeman slower between the atomic oven and the experimental chamber consists of a tube enfolded by a magnetic coil with decreasing diameter and number of windings to produce a decreasing magnetic field along the propagation direction of the atoms. The second essential element of the Zeeman slower is a red-detuned laser beam pointing against the atomic beam. By a laser cooling mechanism in which the moving atoms absorb photons of the laser beam taking its directional photon momentum and loosing unidirectional momentum during a spontaneous emission process, the atoms are slowed down towards the experimental chamber. The magnetic field gradient compensates the Doppler shift of the moving atoms and guarantees that the moving atoms are always in resonance with the counter-propagating laser beam. The Zeeman slower is designed such that the atoms get out of resonance with respect to the laser frequency if they reach the

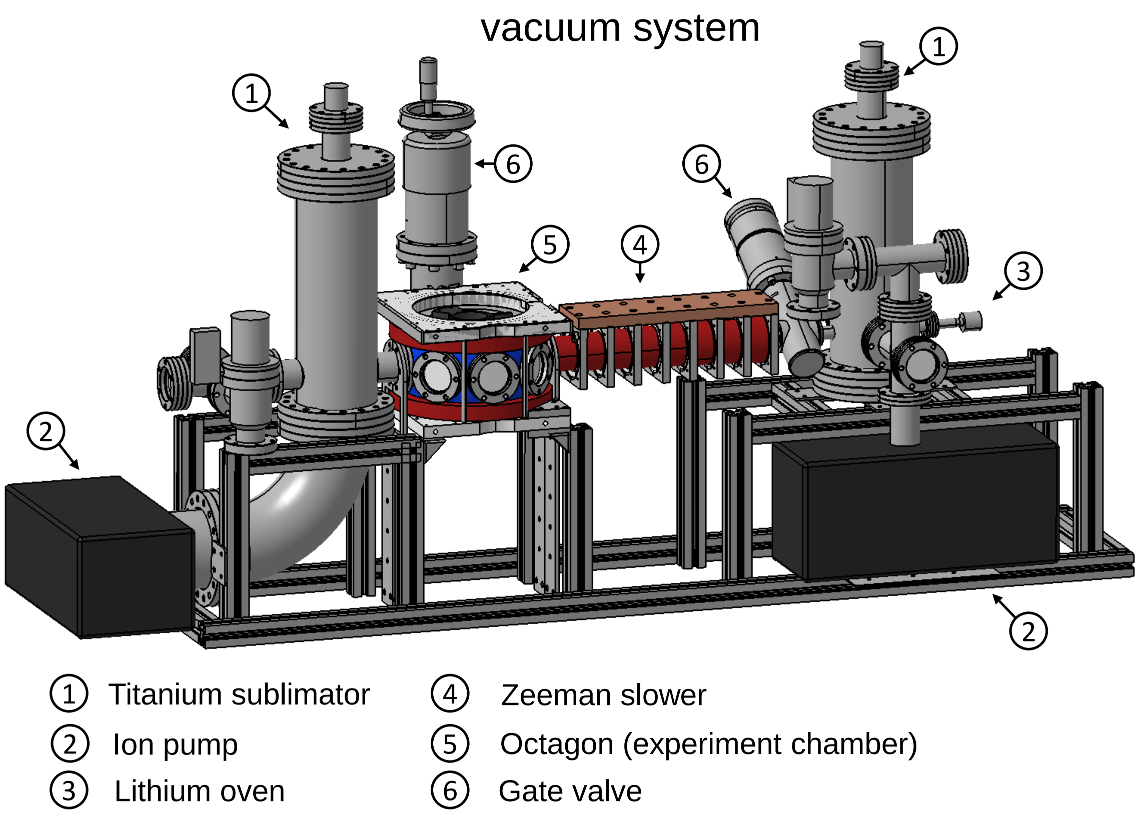

Figure 3.5: View on the experimental apparatus including the parts of the vacuum infrastructure (1,2,6), the Lithium oven (3), the Zeeman slower (4) which decreases the velocity of the atomic beam from the Lithium oven, and the experimental chamber (5) where the atoms are localized in different kinds of traps. The picture was taken from a Solid-works file of [35].

centre of the experimental chamber where the magnetic field is zero. In this way the atoms are slowed down from about 700 m/s to a few m/s ([35]).

As sketched in figure 3.7, after the atoms are slow enough, they can be trapped via a magneto-optical trap consisting of three pairs of opposite circular polarized laser light beams in all three spatial dimensions together with a magnetic field produced by two magnetic coils in anti-Helmholtz configuration. The magnetic field corresponds to a linear magnetic field gradient around the centre while in the centre the field vanishes. In this way, the magnetic field causes a Zeeman splitting of the atomic levels, such that the atoms always absorb photons of the right laser beam if they are on the right side and absorb mainly photons from the left laser beam when they are displaced to the left side because the two opposite laser beams have also opposite circular polarization and through the Zeeman splitting the detuning to the two laser beams is therefore different. This mechanism holds for all three spatial dimensions and leads to a localizing potential in which a cloud of few million atoms can be trapped. A more detailed description can be

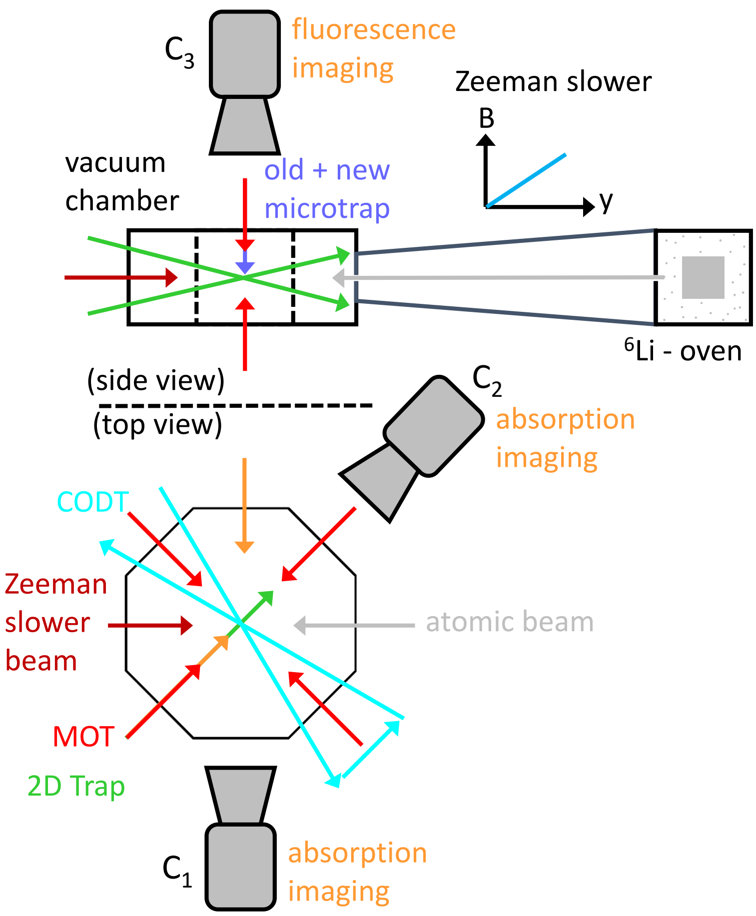

Figure 3.6: Schematic view on the experimental chamber including the different laser beams for cooling and trapping the atoms. The top part of the figure provides a side view on the experimental chamber, the lithium oven, and the Zeeman slower connecting both with each other. From the Lithium oven, an atomic beam, depicted in grey, points to the experimental chamber and is slowed down by the Zeeman slower beam portrayed in dark red. The bottom part of the figure shows the top view on the setup. After slowing down the atoms, six MOT-beams in red localize the atoms in the centre of the octagon. The atoms can be transferred into the crossed optical dipole trap depicted in light blue. Afterwards, a second transfer into the 2D trap, drawn in green, is possible. Besides, there are three cameras detecting absorption and fluorescence signals from the experimental chamber.

found for example in [37].

An exemplarily achieved loading result are up to $\sim 10^8$ trapped atoms after two seconds loading time with a temperature of about 400 μK ([1], p. 34). However the temperature of the atoms trapped in the MOT lies at least above the so-called Doppler-limit of about

140 μK caused by monotonously appearing absorption and spontaneous emission events of resonant photons ([28], p. 35). To further cool the atomic sample, one can transfer the atoms into a shallow optical dipole trap which consists for example as depicted in figure 3.7 of two crossed laser beams which produce a large attractive intensity maximum in the overlapping region where the two single Gaussian beam foci with a minimal waist of about $W_0 \approx 40$ μm meet each other under a crossing angle of about 15°([36]). The so-called optical dipole trap (ODT) provides, with a beam power of up to $P_{dip} = 200$ W, a relatively deep optical trapping potential. According to [1] (p. 34) the transfer efficiency is about 1%. Furthermore, one can create a balanced mixture of the two lowest hyperfine states by a long radio frequency laser pulse between the two lowest hyperfine levels. In a next step, the temperature of the gas can be further cooled by evaporation, meaning one waits until the hotter particles escape from the trap. For example the temperature of the atomic gas is after 6 seconds of evaporation about $T \sim 250$ nK and only a number of about $6 \cdot 10^4$ atoms are remaining ([1]). In this way, a reservoir of cold atoms is created. These atoms can be transferred into differently shaped optical dipole traps. For example a quasi-one-dimensional cigar-shaped trap or quasi-two-dimensional pancake-like-shaped trap can be used for the experimental investigation. In the context of this thesis the creation of a tunable 2D Trap for this purpose will be discussed. Here one can populate only one single layer of the 2D Trap by applying a magnetic field gradient and empty the side layers. By overlapping a single focused beam trap, called a Microtrap, the radial confinement can be adjusted separately from the vertical confinement given by the light green sheet in figure 3.7. This system results into a tunable 2D Trap.

3.4 Few-particle preparation

Especially for the experiments planned for the tunable 2D Trap, the preparation of a few-particle system of about one to ten or maybe 100 trapped particles is relevant. After the previously described production of a reservoir of cold atoms, one can create a deterministic system of few particles in the way depicted in figure 3.8. On the left side of figure 3.8, the fermionic occupation distribution is plotted. By overlapping a deep optical dipole trap, like the Microtrap, one can locally increase the occupation probability inside that Microtrap dramatically to about one. So after turning off the reservoir, all available energy levels of the Microtrap are occupied. In a second step, one can apply a magnetic field gradient and empty the Microtrap partially by this so-called spilling process until only the desired number of particles stays inside the trap. Finally, the magnetic field gradient can be removed and only a few particles remain, occupying the lowest energy levels of the trap with a ground state preparation fidelity of about $\sim 90\%$ ([1], p. 37). This schema was first described in [34].

3.5 Imaging

Finally, the question arises how one can observe the trapped atomic sample. Here one can refer to figure 3.6, where the three available cameras are depicted. Camera C_1 and C_2 are mainly used for absorption imaging, in which the shadow of the atoms is detected.

3.5.1 'Spin-resolved single-atom imaging'

The third camera C_3 can be used for fluorescence imaging, where the camera detects the light emitted from the atoms after they have absorbed it from a resonant laser beam. As described in detail in [2], the experimental setup allows spin-resolved single-atom imaging in the following way: the atoms trapped for example in the Microtrap are excited to emit fluorescent light by shining resonant laser light in horizontal direction on them as sketched in figure 3.9.

The laser light consists of two counter-propagating laser beams which are pulsed and shifted against each other, such that only one of the two beams is reaching the atoms at a time. In this way one can prevent the build-up of an optical trapping potential by a laser cooling mechanism. The fluorescent light is collected by a high-numerical aperture objective guiding the light to an EMCCD camera which is able to detect single photons. As described in [2], for an exposer time of 20 μs, one detects about 20 photons per atom. After an appropriate data analysis including a binarization and a low-pass filter, one can identify single atoms with a fidelity of about $(99.4 \pm 0.3)\%$. One advantage of this imaging technique is that it allows the detection of atoms without a trapping potential, so also free space imaging is possible. In this way one can also detect atoms after time-of-flight experiments. It is mentioned in [2] that the setup allows also the detection of the momentum distribution by imaging the atomic cloud after it was expanding in a shallow trap for exactly a quarter of the trap period time $T/4$. The shallow trap holds the atoms in the focal plane of the objective and after the expansion time $T/4$ the momentum distribution is completely reproduced in the density distribution in position space. Because of the diffusive motion of the atoms during the imaging process the position error is about 4 μm. On top of that, one can detect different spin states separately one after the other by selecting different optical transitions during the imaging process one after the other, displaced by 50μs in time. This is possible, because the three lowest hyperfine states, which serve as pseudo-spin states, are separated at the relevant magnetic field of about 80 MHz corresponding to about 12 times of the natural line width of the transitions ([2]).

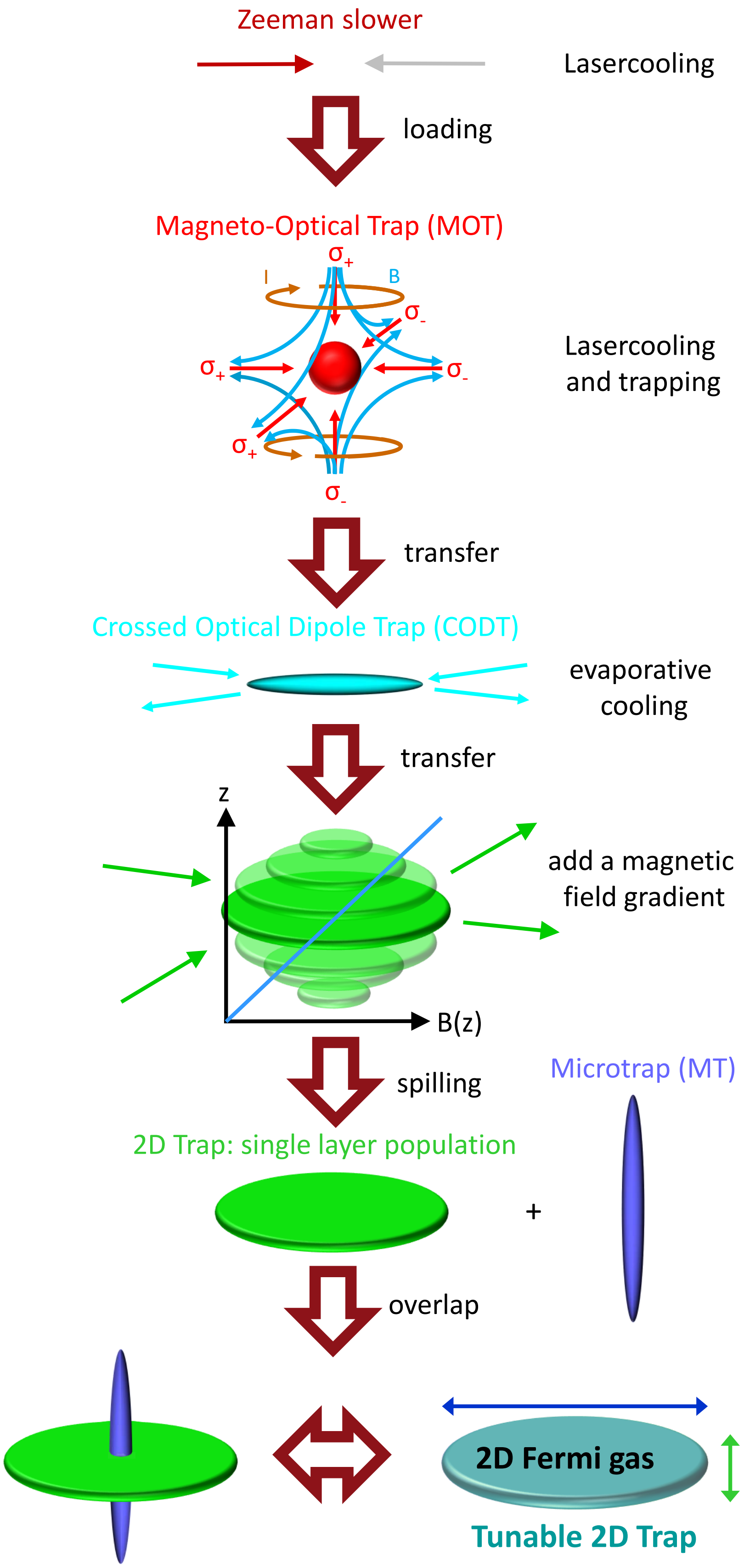

Figure 3.7: Demonstration of the basic steps for the cooling and trapping of atoms and the trap shaping.

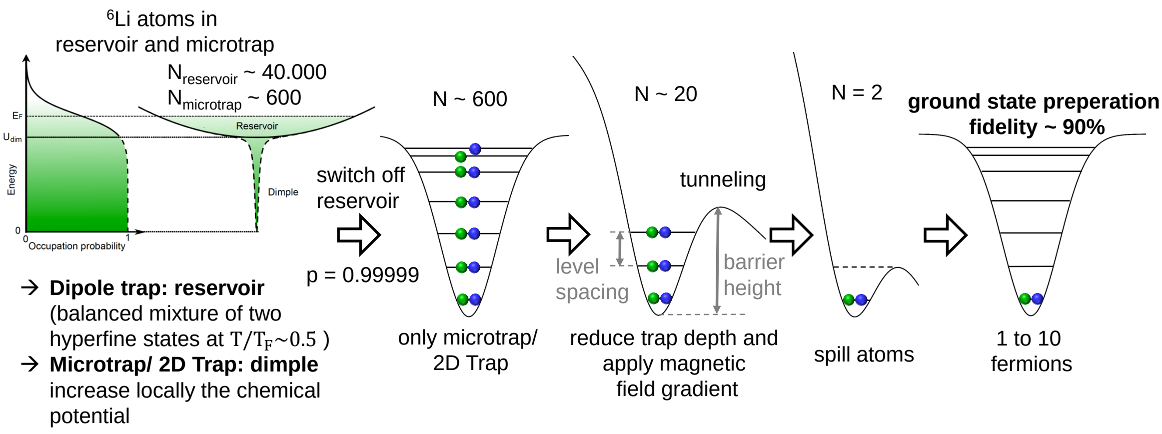

Figure 3.8: Schema to deterministically prepare a few-particle system: Starting with the overlap of a tight Microtrap with the atomic reservoir in the dipole trap, one can locally increase the Fermi energy and guarantee that all states in the Microtrap are occupied. After turning off the dipole trap, leaving a fully occupied Microtrap, the atoms in the upper energy levels can tunnel out if one adds a magnetic field gradient to the potential. Finally, the magnetic field gradient can be removed and only few particles in the ground state of the trap are remaining. The figure is based on figures in [36] and [1].

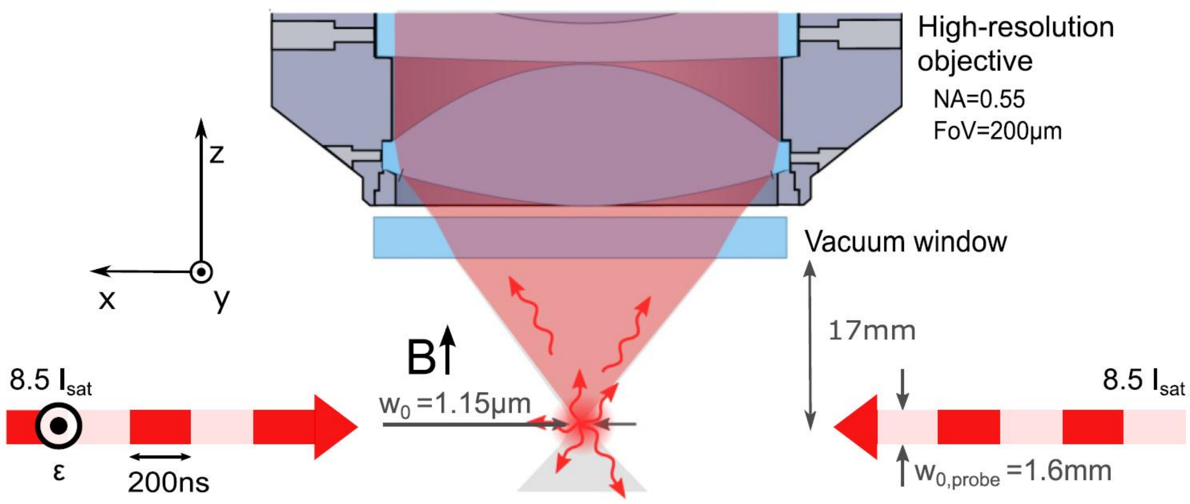

Figure 3.9: Two pulsed laser beams from the left and from the right excite one after the other the atoms in the centre to emit spontaneously photons in all directions. Some of the photons are collected by a high-NA objective from the top. The figure is taken from [2].

Part III

Creating a tunable quasi-two-dimensional optical dipole trap

4 optical dipole traps

This chapter focusses on the conceptional working principle of optical dipole traps, which represent a basic toolbox to form nearly arbitrarily shaped trapping potentials. The chapter is adapted from [27].

4.1 Theoretical concept

In contrast to a magneto-optical trap with radiation pressure forces from resonant laser beams, optical dipole traps provide much weaker trapping potentials due to an interaction of far off-resonant laser light with the dipole moment of the atoms and therefore lead to much lower temperatures of the trapped atomic systems. As discussed in [10], the working principle of optical dipole traps can be explained in the context of a simple classical oscillator model. The external laser field drives the oscillation of the atomic dipole moment. If the laser frequency ω_L is smaller than the resonance frequency ω_0 of the atom, the dipole moment oscillates in phase with the external field and the interaction is attractive. But if the laser frequency ω_L is larger than the resonance frequency ω_0 of the atom, the dipole moment oscillates out of phase with the external field and the interaction is repulsive ([28]). In the experiment the wavelength of the lasers which are used for optical dipole traps is with $\lambda_{ODT} \approx 1064$ nm nearly about twice as large the resonance wavelength $\lambda_0 \approx 671$ nm and therefore strongly red-detuned. The off-resonance condition to the laser light guarantees that the dipole force dominates over resonant radiation pressure. To mention the classical oscillator model in a more formal way the laser light can be introduced as a classical electric field in complex notation ([10]):

$$E(\vec{x}, \omega_L, t) = \vec{\epsilon} \cdot E_0(\vec{x}) \exp(-i\omega_L t) + \vec{\epsilon} \cdot E_0^\star(\vec{x}) \exp(+i\omega_L t) \tag{4.1}$$

which oscillates with the driving frequency ω_L and amplitude $E_0(\vec{x})$ in direction of the polarization vector $\vec{\epsilon}$. The external electric field $\vec{E}$ induces a dipole moment $\vec{d}$ in the atomic charge distribution which is overall neutral but can have local charges. In a classical picture, one can imagine that the single valance electron of the ^{6}Li atoms oscillates forced by the external electric field. This leads to an induced dipole moment of the form:

$$d(\vec{x}, \omega_L, t) = \alpha(\omega_L) E(\vec{x}, \omega_L, t) \tag{4.2}$$

Here α corresponds to the complex polarizability of the atoms and quantifies the interaction strength of the atomic dipole with the electric field. By time averaging over the fast oscillating terms, one can describe the interaction potential of the atomic dipole moment $\vec{d}$ in the external electric field $\vec{E}$ by the following expression:

$$U_{dip}(\vec{x}) = -\frac{1}{2}\langle \vec{d}\vec{E} \rangle_t = -\frac{1}{2} Re(\alpha) \langle |\vec{\epsilon}|^2 (E_0^2 e^{-2i\omega_L t} + |E_0|^2 + |E_0|^2 + (E_0^\star)^2 e^{+2i\omega_L t}) \rangle_t \tag{4.3}$$

The time average is reasonable because the atomic motion is slow compared to the oscillation frequency of the laser light, such that one can simplify the potential with $I(\vec{x}) = 2\epsilon_0 c|E_0(\vec{x})|^2$ to:

$$U_{dip}(\vec{x}) = -Re(\alpha)|E_0(\vec{x})|^2 = -\frac{1}{2\epsilon_0 c}Re(\alpha)I(\vec{x}) \sim I(\vec{x}) \tag{4.4}$$

The spatial dependency of this dipole potential is fully given by the intensity distribution of the external laser light field. The actual form of the polarization has to be derived explicitly, but here only the result should be given on which the following quantitative results are based.

Under the boundary conditions of large detuning $\delta = \omega_0 - \omega_L$ and very small saturation the optical dipole potential can be written as [10]:

$$\boxed{U_{dip} = -\frac{3\pi c^3}{2\omega_0^3}\left(\frac{\Gamma}{\omega_0 - \omega_L} + \frac{\Gamma}{\omega_0 + \omega_L}\right)I(\vec{x}) = -a \cdot I(\vec{x})} \tag{4.5}$$

with the proportionality factor $a \equiv \frac{3\pi c^3}{2\omega_0^3}\left(\frac{\Gamma}{\omega_0-\omega_L} + \frac{\Gamma}{\omega_0+\omega_L}\right)$, depending on the speed of light c and Γ as the natural line width of the resonance transition.

4.2 Trap configurations

Based on this concept of optical dipole traps, one can distinguish two types of trap configurations: For red-detuned traps, the laser frequency is smaller then the atomic resonance frequency and the atoms are pulled to the intensity maximum. This case of negative detuning leads to an attractive potential. In contrast to that, for blue-detuned traps, the laser frequency is larger then the atomic resonance frequency and the atoms are pushed away from the intensity maxima and pulled to its minimum. So the latter case of positive detuning creates a repulsive potential which can trap atoms only between potential wells around the preferred atom position. This behaviour is schematically portrayed in figure 4.1.

4.3 Usual trap geometries for ultracold atom experiments

One of the most common trap geometries realized with simple red-detuned and focused Gaussian laser beams is shown in figure 4.2. The Gaussian profile of the single beams is portrayed in figure 4.2 (a). An elongated, like a cigar, shaped trap geometry can be produced by a single focused Gaussian laser beam as shown in 4.2 (c) and leads to a quasi-one-dimensional trap configuration. In this case, the trap shape is given by the nature of the single Gaussian beam focus.

In contrast, two counter-propagating round Gaussian laser beams with parallel polarizations form a stack of circular light sheets through their interference and in this way a

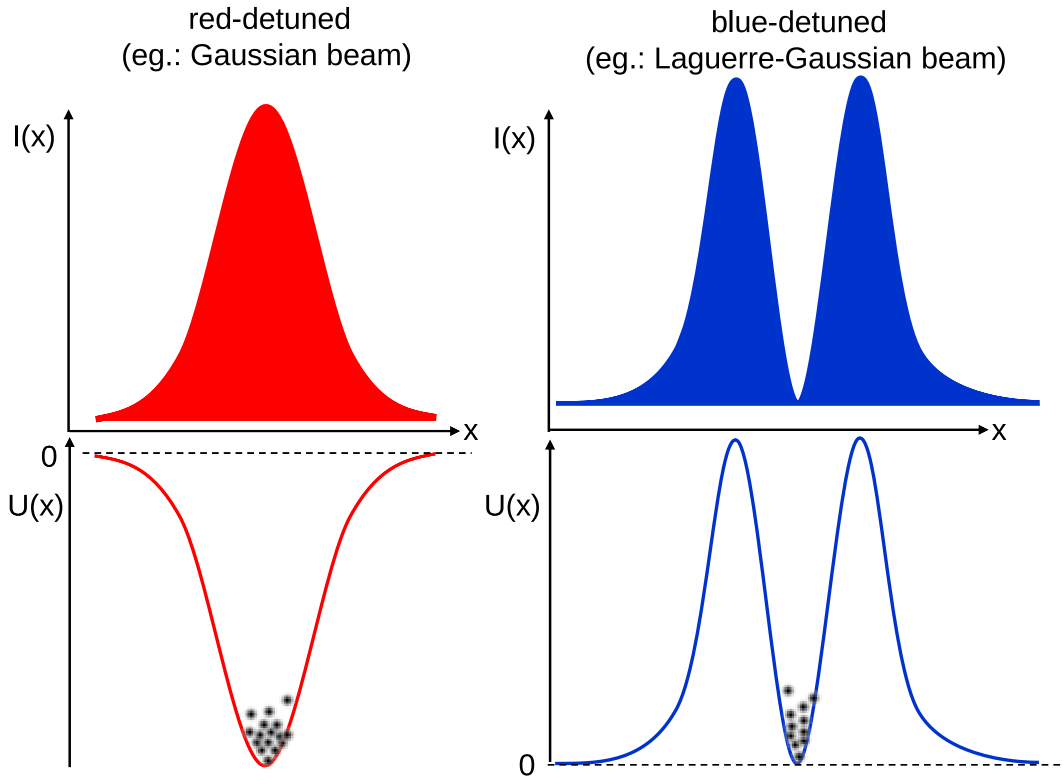

Figure 4.1: Two categories of optical dipole traps: First, red-detuned intensity distribution and optical dipole potential on the left side which traps atoms in regions of intensity maxima. Second, blue-detuned intensity distribution and optical dipole potential on the right side which traps atoms in regions of intensity minima. The figure was taken from [27] and inspired by [10].

quasi-two-dimensional trap geometry in each light sheet (figure 4.2, (b)). Here, the radial restriction by a Gaussian profile is given by the beam focusing while the axial confinement part is fully dominated by the interference pattern. The spacing between the light sheets is $d = \lambda/2$.
Finally, for the last case discussed in this context, one can cross two Gaussian beams under an angle $\chi = 2\theta$, as depicted in figure 4.2 (d). If the polarizations are orthogonal, one can create for orthogonal and equally round beams a deep spherical trap where the two foci overlap. On the other hand, if the polarizations are parallel, the interference pattern determines again the vertical confinement and the radial restriction is given by the beam focusing. However now, both confinement shapes are depending on the crossing angle and the light sheets are elliptical for circular Gaussian beams. Nevertheless, one can produce circular light sheets if one chooses the ellipticity of the incoming Gaussian beams in the right way. The spacing of the light sheets is now larger compared to case (b) with $d = \frac{\lambda}{2\sin(\theta)}$. This last possibility will be exploited in this thesis in order to create

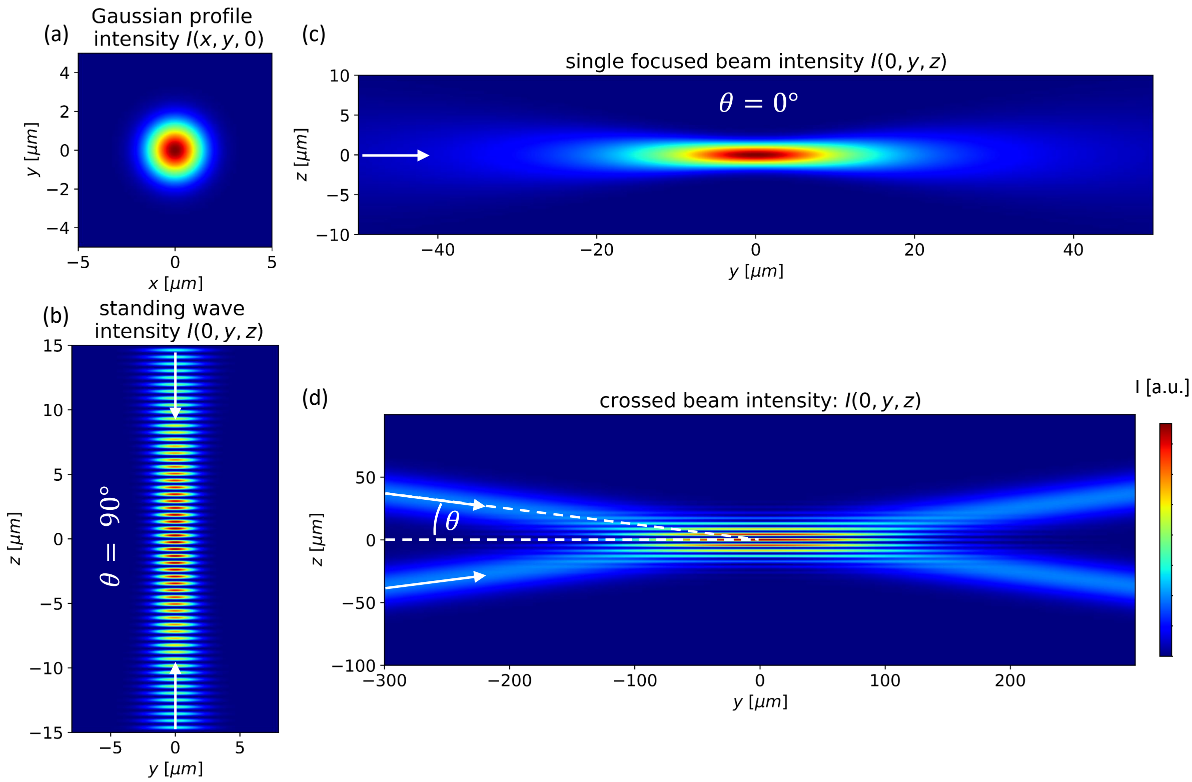

Figure 4.2: Three possible trap geometries created by red-detuned and focused Gaussian laser beams. (a) shows the Gaussian profile of a single beam. (b) shows a configuration of two counter-propagating laser beams creating a standing wave interference pattern, which can be seen as a stack of light-sheets with a quasi-two-dimensional geometry. (c) depicts a quasi-one-dimensional trap configuration produced by a single focused laser beam. (d) portrays a crossover configuration between the two former ones by two beams crossing each other under an angle in their foci. For parallel polarization, (d) leads again to a standing wave pattern along the vertical axis, as the vertical components of the two beam correspond still to two counter-propagating beams. In contrast, orthogonal polarizations result in an ellipsoidal trap. The sketch is based on [4] and [10].

a quasi-two-dimensional trap.

5 A tunable 2D Trap

In this chapter, the theoretical steps for the description of the target trap, a tunable 2D Trap, are shown. The target trap consists of a 2D Trap formed by two Gaussian laser beams interfering in their crossing point and leading to a stack of light sheets, together with an additional single focused beam from the top which overlaps with the light sheet structure and dominates the radial confinement. This chapter is based on [27].

5.1 The 2D Trap

5.1.1 Two crossed Gaussian beams

As mentioned in the previews chapter, two focused Gaussian laser beams with parallel polarizations crossing each other under a half-crossing angle of θ can produce a quasi-two-dimensional potential through a stack of light sheets as depicted in figure 4.2 (d).
In order to describe the potential distribution precisely, one has to consider the intensity distribution of two crossing Gaussian beams. As described in [27] and based on [32], a single Gaussian beam intensity distribution propagating along the z-axis has the formal shape of:

$$\boxed{I(r,z) = \frac{2P}{\pi \cdot W^2(z)} \cdot \exp\left(-\frac{2r^2}{W^2(z)}\right) \quad \text{with :} \quad r = \sqrt{x^2+y^2}} \tag{5.1}$$

with P as the beam power. The cross-section of the beam corresponds to a two-dimensional Gaussian distribution, whereas along the axial direction one can see a Lorentzian maximum around the focus at $z = 0$. As demonstrated in figure 5.1, the parameter $W(z)$ relates to the beam width along the propagation direction:

$$\boxed{W(z) = W_0 \cdot \sqrt{1 + \left(\frac{z}{L_R}\right)^2}} \tag{5.2}$$

where $W_0 = W(z = 0)$ is the minimal beam width and $L_R = \frac{\pi \cdot W_0^2}{\lambda}$ is called the Rayleigh length. The beam radius $W(z)$ is defined as the distance from the central axis at which the intensity of the Gaussian beam is decreased to $\frac{1}{e^2}$ of its maximum value in the centre: $I(r = W(z), z) = \frac{1}{e^2} \cdot I_{max}(r = 0, z)$. Besides, the beam width matches twice the usual Gaussian standard deviation: $W(z) = 2\sigma(z)$.
As already mentioned above, one needs Gaussian beams with an elliptically shaped cross-section depending on the half-crossing angle for the creation of circular light sheets in the interference pattern. Each elliptical-beam axis is parametrized by a corresponding beam

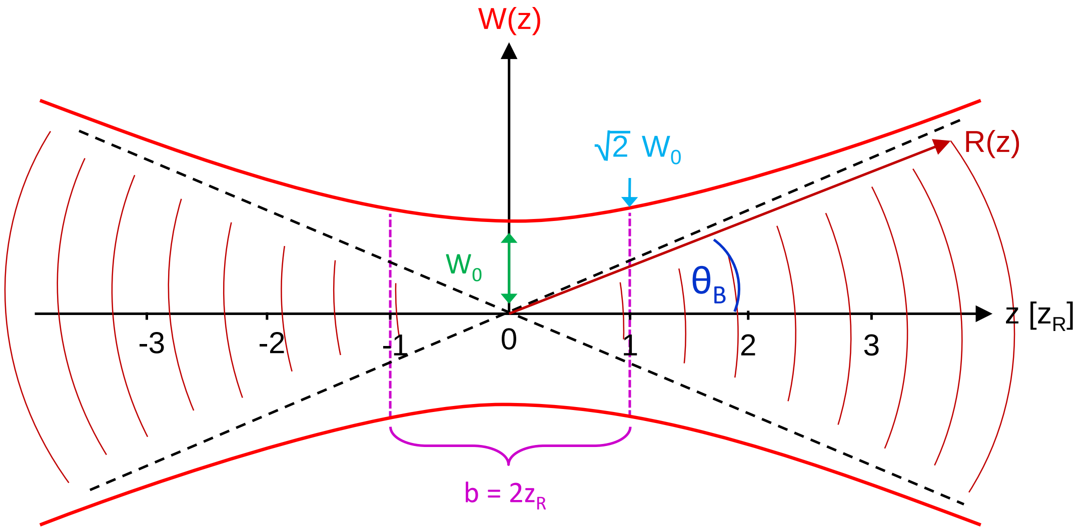

Figure 5.1: Axial profile of a general Gaussian beam, parametrized by the beam width $W(z)$ and the radius curvature $R(z)$. On top of that, the focal depth $b = 2z_R = 2L_R$ and the beam divergence θ_B can be used for further characterization. The figure was taken from [27].

width: W_x and W_y and the full intensity distribution of the elliptical Gaussian beam can be expressed as ([27]):

$$I_{elliptical}(x, y, z) = \frac{2P}{\pi \cdot W_x(z)W_y(z)} \cdot \exp\left(-\frac{2x^2}{W_x^2(z)} - \frac{2y^2}{W_y^2(z)}\right) \tag{5.3}$$

Subsequently, two such elliptical Gaussian beams have to cross each other under an angle of $\chi = 2 \cdot \theta$ in the zy-plane (figure 5.2). So for each beam, one starts with a beam propagating in y-direction:

$$I(x, y, z) = \frac{2P}{\pi \cdot W_x(y)W_z(y)} \cdot \exp\left(-\frac{2x^2}{W_x^2(y)} - \frac{2z^2}{W_z^2(y)}\right) \tag{5.4}$$

Then, one can rotate the beam around the x-axis about θ and $-\theta$, respectively for each beam. This can be executed by the application of the according rotation matrix:

$$R_x(\theta) = \begin{pmatrix} 1 & 0 & 0 \\ 0 & \cos(\theta) & -\sin(\theta) \\ 0 & \sin(\theta) & \cos(\theta) \end{pmatrix} \tag{5.5}$$

The coordinate transformation has for the first beam the form:

$y \quad \Longrightarrow \quad \cos(\theta)y - \sin(\theta)z,$

$z \quad \Longrightarrow \quad \sin(\theta)y + \cos(\theta)z.$

and for the second beam:
$y \implies \cos(-\theta)y - \sin(-\theta)z = \cos(\theta)y + \sin(\theta)z,$
$z \implies \sin(-\theta)y + \cos(-\theta)z = -\sin(\theta)y + \cos(\theta)z.$
The two individual intensity distributions can be written as ([27]):

$$I_1(x,y,z) = \frac{2P_1}{\pi \cdot W_x(l_2)W_z(l_2)} \cdot \exp\left(-\frac{2x^2}{W_x^2(l_2)} - \frac{2}{W_z^2(l_2)} \cdot (\sin(\theta)y + \cos(\theta)z)^2 \right) \quad (5.6)$$

$$I_2(x,y,z) = \frac{2P_2}{\pi \cdot W_x(l_1)W_z(l_1)} \cdot \exp\left(-\frac{2x^2}{W_x^2(l_1)} - \frac{2}{W_z^2(l_1)} \cdot (-\sin(\theta)y + \cos(\theta)z)^2 \right) \quad (5.7)$$

where $l_1 = \cos(\theta)y - \sin(\theta)z$ for the first beam and $l_2 = \cos(\theta)y + \sin(\theta)z$ for the second beam are the distances to the focal points which lie on the crossing point of both beams. However, the central characteristic interference can only be added to the description by introducing the electric fields connected with the two Gaussian beams:

$$\vec{E}_{(1,2)}(\vec{x},t) = \vec{\epsilon}_{(1,2)} \cdot E_{0(1,2)}(x,y,z) \cdot \cos\left(\vec{k}_{(1,2)} \cdot \vec{x} - \omega_{(1,2)}t + \phi_{(1,2)}\right) \quad (5.8)$$

with the space-dependent amplitude $E_{0(1,2)}(x,y,z)$ reflecting the Gaussian beam shape similar to the intensity distribution. The wave-vectors indicating the propagation direction of both beams are:

$$\vec{k}_1 = k \cdot (0, \cos(\theta), -\sin(\theta)) \quad \text{and} \quad \vec{k}_2 = k \cdot (0, \cos(\theta), \sin(\theta)) \quad (5.9)$$

where the wave-number $k = \frac{2\pi}{\lambda}$ can be expressed by the wavelength λ, which in the experiment is red-detuned to $\lambda = 1064$ nm. For perfect interference one has to choose the polarization vectors parallel and linearly polarized, pointing both in x-direction:

$$\vec{\epsilon}_1 = \vec{\epsilon}_2 = (1,0,0) \quad (5.10)$$

The intensity can be calculated from the electric field with ([32], p.41):

$$I(\vec{x}) = 2\langle \vec{E}(\vec{x},t)^2 \rangle_t \quad (5.11)$$

Here the time average can be done over one period of light frequency, which is justified, because the light oscillates much faster than the atoms move. To simplify the calculation, one can use the complex representation of the electric fields ([32], p.42):

$$\tilde{\vec{E}}_{(1,2)}(\vec{x},t) = \vec{\epsilon}_{(1,2)} \cdot E_{0(1,2)}(x,y,z) \cdot \exp\left(i(\vec{k}_{(1,2)} \cdot \vec{x} - \omega t + \phi_{(1,2)})\right) \quad (5.12)$$

with

$$\vec{E}_{(1,2)}(\vec{x},t) = Re(\tilde{\vec{E}}_{(1,2)}(\vec{x},t)) \quad (5.13)$$

This is an advantage because the intensity can just be calculated from ([32], p.42):

$$I(\vec{x}) = |\tilde{\vec{E}}(\vec{x},t)|^2 \quad (5.14)$$

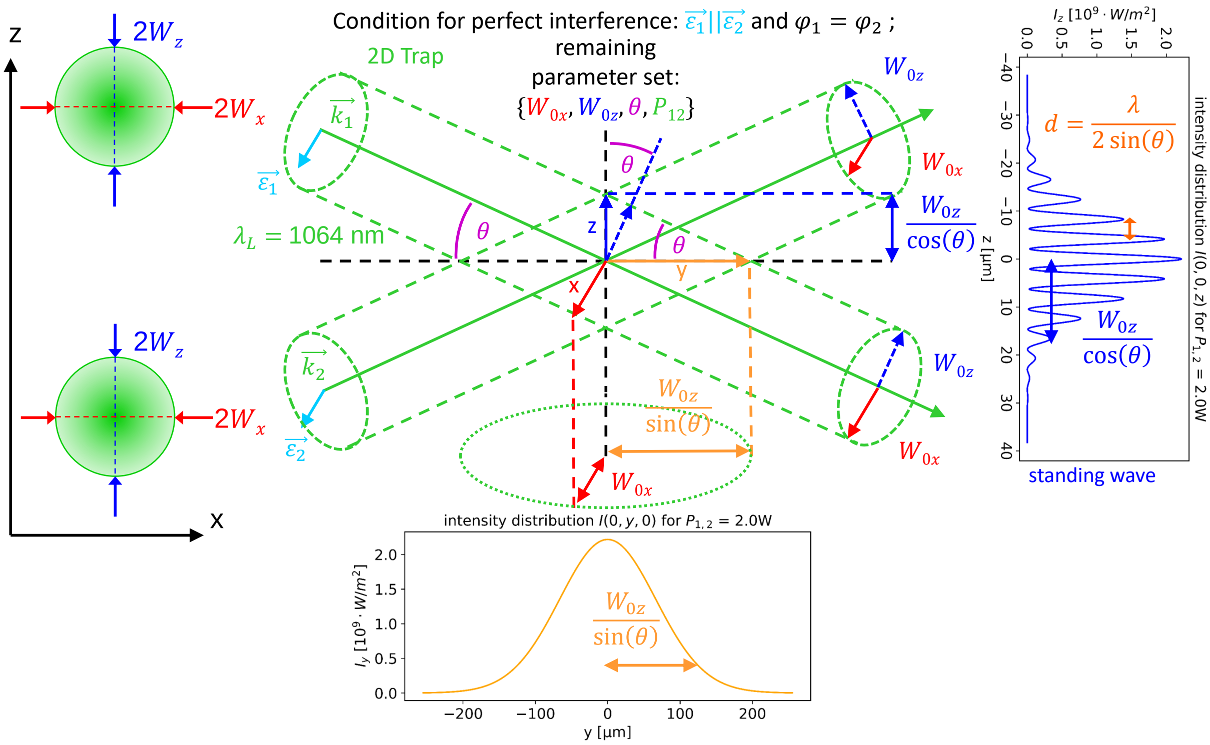

Figure 5.2: Two crossed Gaussian beams with a half-crossing angle θ interfering in the crossing region like two counter-propagating beams, as depicted on the right, but with a larger spacing depending on the half-crossing angle. The shape of the single-beam profile can be characterized by two orthogonal beam widths for the Gaussian beams in z- and x-direction as portrayed on the left. The intensity profile in the intersection region in both horizontal directions corresponds to a Gaussian profile as shown at the bottom for the y-direction. The size of the intersection region characterizes the size of the interference pattern. The horizontal size of the intersection region is in the x-direction just the beam radius W_{0x} and in y-direction $\frac{W_{0z}}{\sin(\theta)}$. In vertical direction the intersection region height is about $\frac{W_{0z}}{\cos(\theta)}$.

The total intensity is then:

$$I_{tot}(x, y, z) = |\tilde{\vec{E}}_1 + \tilde{\vec{E}}_2|^2 = (\tilde{\vec{E}}_1^* + \tilde{\vec{E}}_2^*) \cdot (\tilde{\vec{E}}_1 + \tilde{\vec{E}}_2) \tag{5.15}$$

which leads to:

$$I_{tot}(x, y, z) = |\tilde{\vec{E}}_1|^2 + \tilde{\vec{E}}_1^* \cdot \tilde{\vec{E}}_2 + \tilde{\vec{E}}_1 \cdot \tilde{\vec{E}}_2^* + |\tilde{\vec{E}}_2|^2 \tag{5.16}$$

This expression can be simplified further to the compartments of:

$$|\tilde{\vec{E}}_{1,2}|^2 = |\vec{\epsilon}_{(1,2)}|^2 \cdot |E_{0(1,2)}(x, y, z)|^2 = 1 \cdot |E_{0(1,2)}(x, y, z)|^2 = I_{1,2}(x, y, z) \tag{5.17}$$

and

$$\tilde{\vec{E}}_1^* \cdot \tilde{\vec{E}}_2 = 1 \cdot E_{0,1}^*(x, y, z) \cdot E_{0,2}(x, y, z) \cdot \exp\left(i(\vec{k}_2 \cdot \vec{x} + \phi_2) - i(\vec{k}_1 \cdot \vec{x} + \phi_1)\right) \tag{5.18}$$

$$\tilde{\vec{E}}_1 \cdot \tilde{\vec{E}}_2^* = 1 \cdot E_{0,1}(x,y,z) \cdot E_{0,2}^*(x,y,z) \cdot \exp\left(i(\vec{k}_1 \cdot \vec{x} + \phi_1) - i(\vec{k}_2 \cdot \vec{x} + \phi_2)\right) \tag{5.19}$$

As the amplitudes are real: $E_{0,(1,2)}^*(x,y,z) = E_{0,(1,2)}(x,y,z)$, the compartments of the total intensity distribution can be rewritten with $K \equiv ((\vec{k}_1 \cdot \vec{x} + \phi_1) - (\vec{k}_2 \cdot \vec{x} + \phi_2))$ as:

$$\tilde{\vec{E}}_1^* \cdot \tilde{\vec{E}}_2 + \tilde{\vec{E}}_1 \cdot \tilde{\vec{E}}_2^* = E_{0,1}(x,y,z) \cdot E_{0,2}(x,y,z) \cdot \big(\exp(-iK) + \exp(+iK)\big) \tag{5.20}$$

, which simplifies to a real part:

$$\tilde{\vec{E}}_1^* \cdot \tilde{\vec{E}}_2 + \tilde{\vec{E}}_1 \cdot \tilde{\vec{E}}_2^* = E_{0,1}(x,y,z) \cdot E_{0,2}(x,y,z) \cdot 2\cos(K) \tag{5.21}$$

By exploiting the relation: $E_{0,(1,2)}(x,y,z) = \sqrt{I_{(1,2)}(x,y,z)}$ the total intensity can be brought to the form of:

$$I_{tot}(\vec{x}) = I_1(\vec{x}) + I_2(\vec{x}) + 2 \cdot \sqrt{I_1(\vec{x})}\sqrt{I_2(\vec{x})} \cdot \cos((\vec{k}_1 - \vec{k}_2) \cdot \vec{x} + \Delta\phi) \tag{5.22}$$

with the phase difference $\Delta\phi = \phi_1 - \phi_2$. Inserting the wave-vectors, one can find:

$$(\vec{k}_1 - \vec{k}_2) \cdot \vec{x} = k(\cos(\theta)y + \sin(\theta)z) - k(\cos(\theta)y - \sin(\theta)z) = 2k \cdot \sin(\theta)z \tag{5.23}$$

Finally the total intensity distribution has the form of:

$$\boxed{I_{tot}(\vec{x}) = I_1(\vec{x}) + I_2(\vec{x}) + 2 \cdot \sqrt{I_1(\vec{x})}\sqrt{I_2(\vec{x})} \cdot \cos\left(\frac{4\pi}{\lambda} \cdot \sin(\theta)z + \Delta\phi\right) = I_{2D}} \tag{5.24}$$

with the layer spacing:

$$\boxed{d = \frac{\lambda}{2\sin(\theta)}} \tag{5.25}$$

5.1.2 Harmonic approximation of the centre potential

Due to the low temperature of the trapped particles, they are localized near the central minimum of the confining potential and it is useful and reasonable to characterize the centre of the optical dipole trap within a harmonic approximation:

$$\boxed{U_{HO}(\vec{x}) = U_0 + \frac{1}{2}m(\omega_x^2 x^2 + \omega_y^2 y^2 + \omega_z^2 z^2) \approx U_{2D} = -aI_{2D}} \tag{5.26}$$

As shown in a detailed calculation in [27], the trap frequencies can be derived from a second-order Taylor expansion of the total intensity distribution in each spatial dimension:

$$I_{2D}(x_i) \approx I_0 - \frac{1}{2}q \cdot x_i^2 \tag{5.27}$$

with the relation:

$$U_{HO} = -aI_{2D} \quad \Longleftrightarrow \quad \frac{1}{2}m\omega_i^2 x_i^2 = a \cdot \frac{1}{2}q \cdot x_i^2 \quad \Longleftrightarrow \quad \omega_i = \sqrt{\frac{aq}{m}} \tag{5.28}$$

leading to the following results:

$$\boxed{\omega_x = \sqrt{\frac{32aP_{1,2}}{\pi m W_{0x}^3 W_{0z}}}} \tag{5.29}$$

$$\boxed{\omega_y = \sqrt{\frac{16aP_{1,2}}{\pi m W_{0x} W_{0z}}\left[\frac{2\sin^2(\theta)}{W_{0z}^2} + \left(\frac{\lambda\cos(\theta)}{\pi}\right)^2 \cdot \left(\frac{1}{W_{0x}^4} + \frac{1}{W_{0z}^4}\right)\right]}} \tag{5.30}$$

$$\boxed{\omega_z = \sqrt{\frac{16aP_{1,2}}{\pi m W_{0x} W_{0z}}\left[\frac{2\cos^2(\theta)}{W_{0z}^2} + \left(\frac{\lambda\sin(\theta)}{\pi}\right)^2 \cdot \left(\frac{1}{W_{0x}^4} + \frac{1}{W_{0z}^4}\right) + \left(\frac{\pi}{d}\right)^2\right]}} \tag{5.31}$$

$$\boxed{U_0 = -\frac{8aP_{1,2}}{\pi W_{0x} W_{0z}}} \tag{5.32}$$

An additional central quantity in this context is the harmonic oscillator length:

$$\boxed{l_i = \sqrt{\frac{\hbar}{m\omega_i}} \quad \text{with :} \quad i = x, y, z} \tag{5.33}$$

reflecting the size of a ground-state wave-function in the harmonic oscillator potential. In z-direction, the harmonic oscillator length should be much smaller than the layer spacing d of the 2D Trap to prevent any tunnelling between the layers ([27]). In order to be able to calculate also the trap parameters from measured trap properties, one can invert the equations as shown in the appendix.

5.1.3 Quasi-two-dimensional

The term quasi-two-dimensional, which has to be fulfilled for the target trap, describes quantum mechanically that the confinement in one of the three trapping dimensions dominates strongly over the other two ones. Figure 5.4 tries to illustrate this circumstance.

Any deep minimum can be approximated by a harmonic potential with equally spaced quantum mechanical energy levels for a single trapped particle. The energy level spacing depends on the curvature, namely the trapping frequency, of the harmonic potential in the specific direction, such that the energy spectrum in each spatial direction has the form [33]:

$$E_{x,y,z}(n_{x,y,z}) = \left(n_{x,y,z} + \frac{1}{2}\right)\hbar\omega_{x,y,z} \quad \text{with :} \quad n_i \in \mathbb{N} \tag{5.34}$$

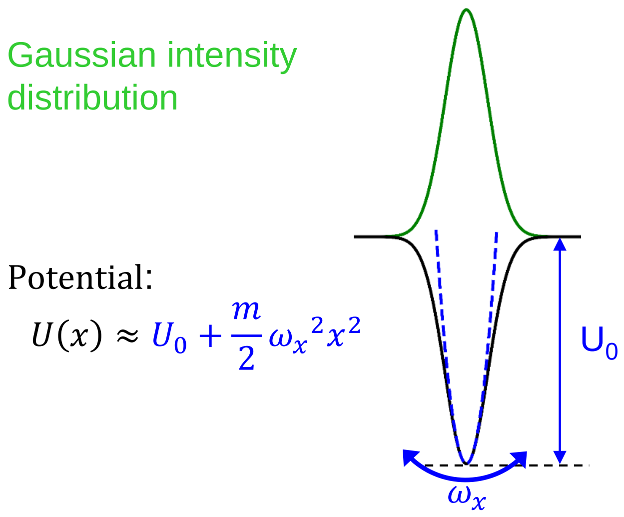

Figure 5.3: Demonstration of the harmonic approximation (in blue) to the attractive potential (black) which is proportional to the Gaussian intensity distribution (green). Around the centre of the trap, this harmonic approximation can be executed in all three spatial dimensions.

And this holds for each spatial dimension independently, leading to a total energy of:

$$E(n_x, n_y, n_z) = E_x(n_x) + E_y(n_y) + E_y(n_y) \tag{5.35}$$

If for example the restriction in the vertical axis is much stronger than in the two horizontal axes: $\omega_z >> \omega_{x,y}$, a cold trapped particle with small excitation energy of the order of $\hbar\omega_{x,y}$ stays always in the ground state of the vertical harmonic oscillator and only populates excited levels in the two horizontal dimensions. In this way, a cold particle has effectively a two-dimensional energy spectrum and behaves as if it moves in a two-dimensional potential. An important quantity in this context is the absolute number of trapped particles for which the trap behaves still quasi-two-dimensional. So the question is, how much particles can be trapped such that the trap acts still as a quasi-two-dimensional trap. The estimation of this number can be found for example in [4]. As the equidistant energy spectrum of the harmonic oscillator is known with the form above, one can calculate the number of possible states in the harmonic trap similar to the volume:

$$N_{tot} = \prod_i n_i = n_x \cdot n_y \cdot n_z \quad \text{with :} \quad i = x, y, z \tag{5.36}$$

Although this number is in principle infinitely large as $n_i \in \mathbb{N}$, the real trap corresponds to a Gaussian potential and it is preferred to occupy only states in the centre of the trap,

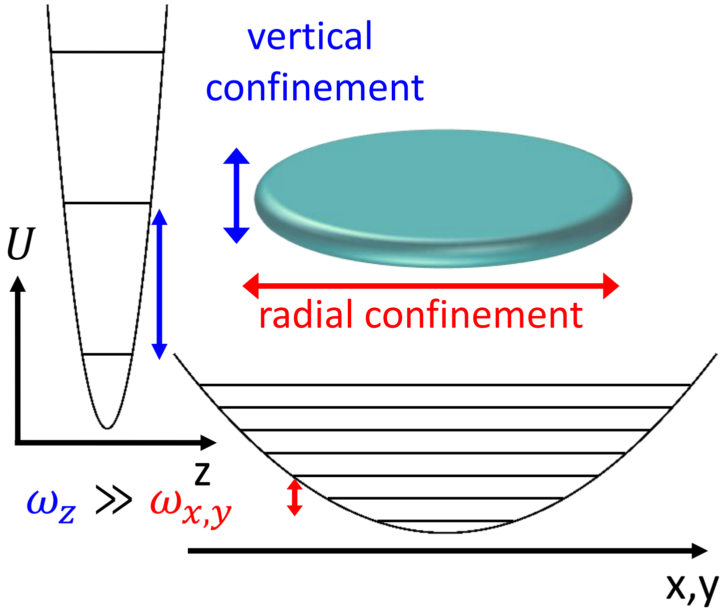

Figure 5.4: Conceptional principle of quasi-two-dimensional traps: The trapping potential can be approximated near the minimum by a harmonic oscillator potential. In one dimension, for example the z-direction, the level spacing is much larger than in the other two dimensions, such that for low energies only the lowest harmonic oscillator level in z-direction is occupied. The dynamics of the system happens for low energies only in excitations in the x- and y-directions. So the system effectively behaves as a two-dimensional system.

where the harmonic oscillator approximation is still valid. So only a finite number of particles will be trapped in the potential. Furthermore the target configuration is the one where the vertical trap frequency is so large compared to the radial trap frequencies that it holds $n_z = 0$ for all trapped particle states. This condition limits the number of particles which can be trapped and is equivalent to:

$$\hbar\omega_x\left(n_x + \frac{1}{2}\right) + \hbar\omega_y\left(n_y + \frac{1}{2}\right) + \frac{1}{2}\hbar\omega_z < \frac{3}{2}\hbar\omega_z \tag{5.37}$$

The quasi-two-dimensional total number of particles is just:

$$N_{tot,2D} = n_x \cdot n_y \tag{5.38}$$

By considering the equality of the inequality above, one can estimate the maximal number of atoms which can be trapped to recover the quasi-two-dimensional configuration. The equality of the above inequality is approximately reached in the case of:

$$n_{x,max} = \frac{\omega_z}{2\omega_x} \quad \text{and} \quad n_{y,max} = \frac{\omega_z}{2\omega_y} \tag{5.39}$$

From this fact one can conclude an approximation of the maximal number of trapped particles which lie still in the quasi-two-dimensional regime:

$$\boxed{N_{max,2D} = n_{x,max} \cdot n_{y,max} = \frac{\omega_z^2}{4\omega_x\omega_y}} \tag{5.40}$$

5.1.4 2D Trap parameters and properties

The characteristic parameters for the two-dimensional trap are now the beam power $P_{1,2}$, the elliptical minimal beam waists W_{0x} and W_{0z}, the half-crossing angle θ, and the phase difference $\Delta\phi$. Besides, the trap properties relevant for the trapped atoms in the centre of the trap are the three spatial trap frequencies $f_{x,y,z}$ and the connected flatness ratio: $R_{2D} = \frac{f_z}{f_r} = \frac{f_z}{f_{x,y}}$ together with the roundness ratio: $R_{xy} = \frac{f_x}{f_y}$, and the potential depth U_0.

5.1.5 Finding the target trap

Because the wavelength is fixed in the experiment to $\lambda = 1064$ nm, the total intensity of the two crossed beams to reach the quasi-two-dimensional optical dipole potential depends still on various parameters, even for identical beams, where $P_1 = P_2 = P_{1,2}$, $W_{0x1} = W_{0x2} = W_{0x}$, $W_{0z1} = W_{0z2} = W_{0z}$, and $\theta_1 = \theta_2 = \theta$:

$$\boxed{I_{tot}(\vec{x}) = I_{2D}(x, y, z, P_{1,2}, W_{0x}, W_{0z}, \theta, \Delta\phi)} \tag{5.41}$$

Under ideal conditions the relative phase should vanish: $\Delta\phi = \phi_1 - \phi_2 = 0$ and the beam power $P_{1,2}$ can be used as a tuning parameter.

Circular light sheet condition

The ellipticity $E \equiv \frac{W_{0x}}{W_{0z}}$ has to be chosen such that the layers are circular. The exact circularity condition from the condition: $f_x = f_y$ is after [27]:

$$\frac{1}{E} = \frac{W_{0z}}{W_{0x}} = \frac{\pi W_{0z}}{\lambda\cos(\theta)}\sqrt{1 - \sqrt{1 - \left[2\left(\frac{\lambda\cos(\theta)\sin(\theta)}{\pi W_{0z}}\right)^2 + \left(\frac{\lambda\cos(\theta)}{\pi W_{0z}}\right)^4\right]}} \tag{5.42}$$

A simplified version which holds for large enough angles is:

$$W_{0x} \approx \frac{W_{0z}}{\sin(\theta)} \quad \Leftrightarrow \quad E \approx \frac{1}{\sin(\theta)} \tag{5.43}$$

and follows just from figure 5.2. Figure 5.5 illustrates the effect of elliptical beams. So, the circular light sheet condition fixes the ellipticity of the single Gaussian beams depending on the chosen half-crossing angle. In this way the parameter W_{0x} can already be fixed because one can express it in terms of the two free parameters W_{0z} and θ.

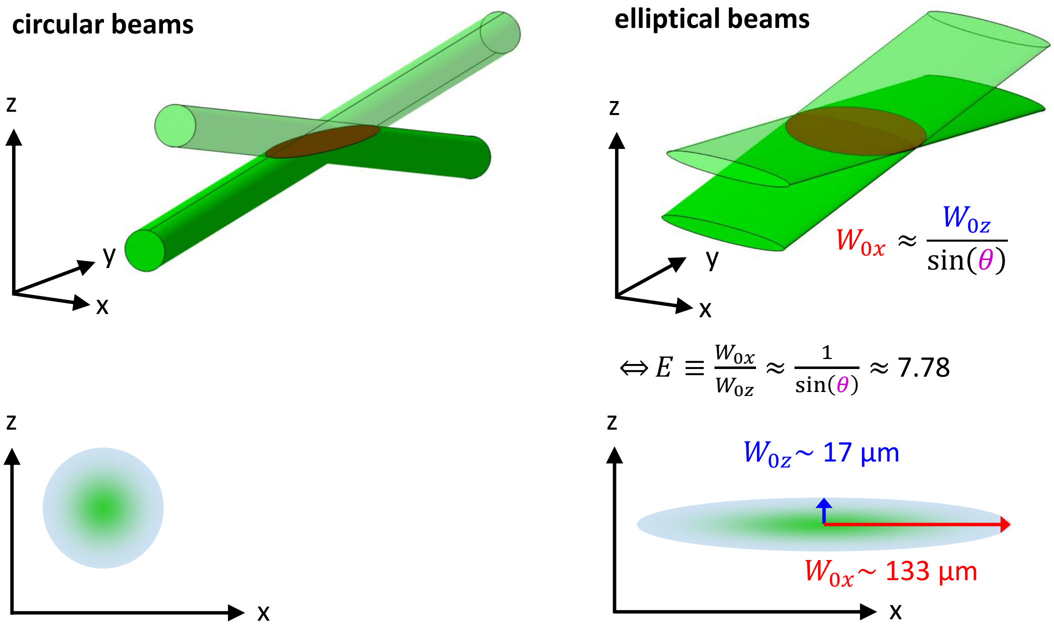

Figure 5.5: Visual demonstration of the effect of elliptical beams for the crossed beam optical dipole trap. On the left top side, two green beams with circular profile meet each other with an elliptical overlap region portrayed in red, which is formed like a surf board. On the left bottom side the circular profile of the Gaussian beams is shown. On the right side, two elliptical Gaussian beams with an ellipticity of $E \approx 7.8$ cross each other with a circular overlap region so the elliptical beams allow the creation of circular shaped interference layers in the overlap region.

Experimental boundary conditions

The other free parameters W_{0z} and θ have to be fixed by the design criteria under the experimental boundary conditions. A detailed discussion of the experimental boundary conditions for these two parameters can be found in [27]. In this context only the most important steps should be summarized. The basic restriction is the size of the view port to the experimental chamber depicted in figure 5.6. To check if the two beams fit through the view-port window, first one has to define how to measure the size, so the radius, of the beam. After [27] a useful choice is:

$$\boxed{W_{mainpower} = 1.7 \cdot W_{x,z}} \tag{5.44}$$

because this part of the beam radius includes 99.83% of the integrated beam power, such that only a very small fraction of the beam power reaches the blind in front of the view-port window. The blind should protect the window from heating damages.

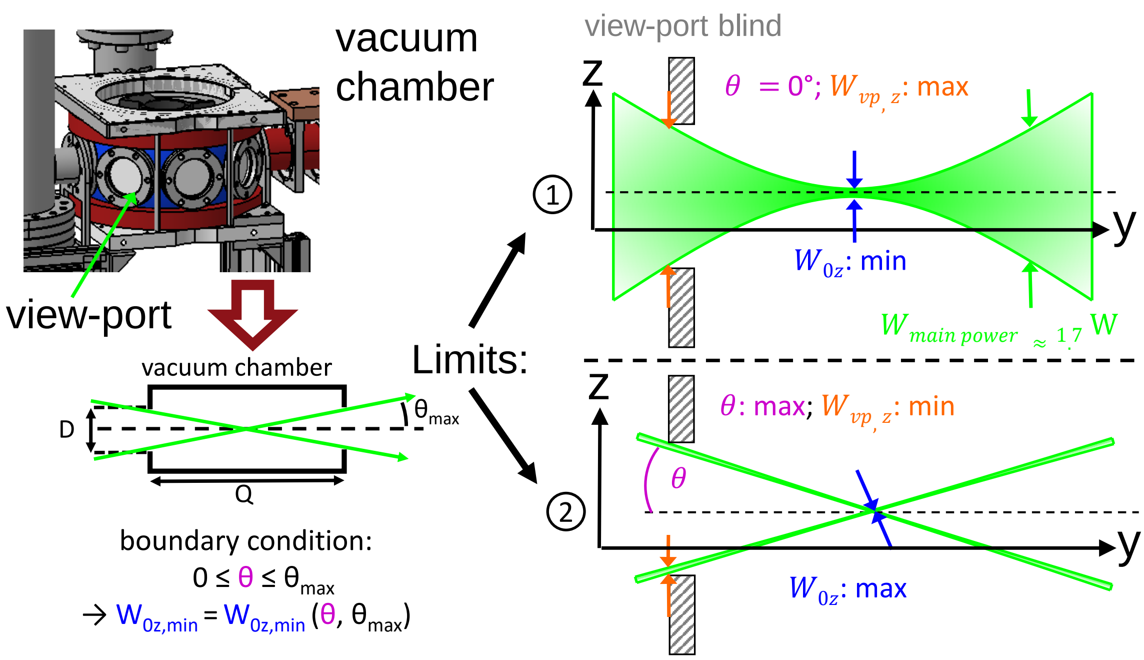

Figure 5.6: Experimental boundary conditions: Top left side shows the vacuum chamber with the view port restricting the half-crossing angle of the 2D Trap. At the same time, this restricts the beam width at the viewport to a maximal value and the minimal beam width to a minimal value depending on the given half-crossing angle. On the top right, there are two limits depicted: first the half-crossing angle vanishes and the beam width at the window is maximal, leading to a minimized minimal beam width in the focus of the Gaussian beam. Second, the half-crossing angle is maximized and the beam width at the view port minimal, such that the minimal beam width of the single beams is maximal.

Now one can realize that there are two possible limits (figure 5.6):
First one can minimize the half-crossing angle to zero and maximize the beam width at the view port in vertical direction. As the minimal waist W_{0z} of the beam decreases in this case, this would maximize the vertical trap frequency $f_z \sim \frac{1}{\sqrt{W_{0z}}}$. However, the ratio $R_{2D} \equiv \frac{f_z}{f_{x,y}}$ decreases linearly for decreasing minimal waist. For the second scenario, the half-crossing angle can be maximized while the beam width at the blind for the view port is minimized. This would maximize the minimal beam waist, leading to smaller vertical trap frequency f_z and larger flatness ratio R_{2D}. To investigate the configuration region between these two limits, one can calculate the maximal possible beam width at the view-port blind for any half-crossing angle between zero and the maximal possible angle θ_{max}. From this curve one can deduce the minimal possible minimal beam waist parameter $W_{0z,min}(\theta)$ as function of half-crossing angle. The precise calculation can be found in [27] and a short

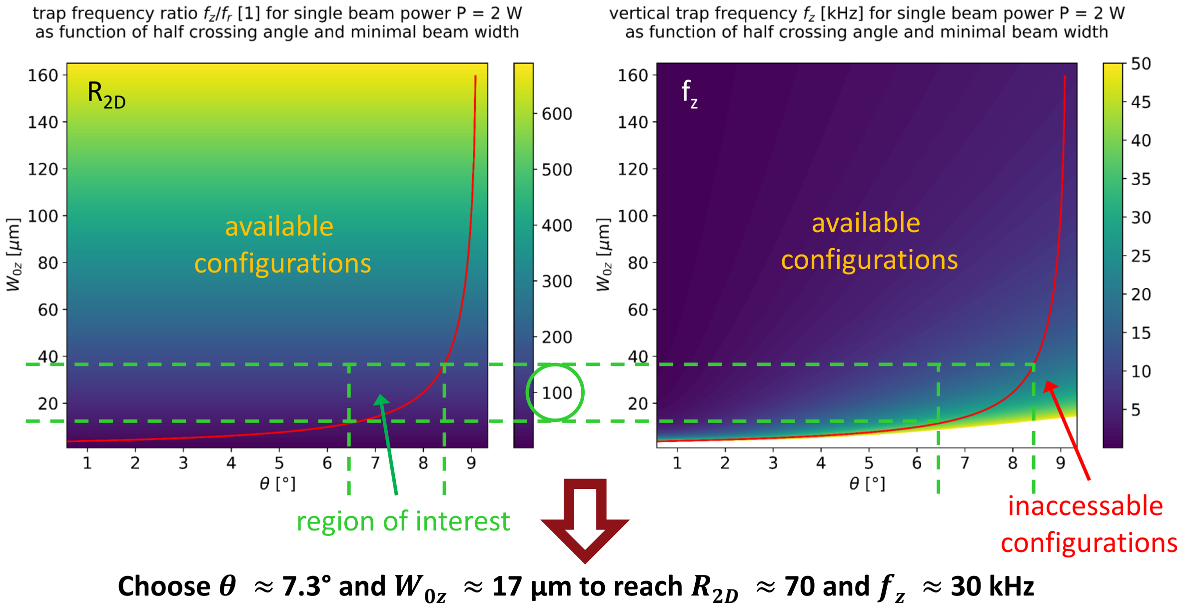

Figure 5.7: Flatness ratio R_{2D} and the vertical trap frequency f_z in the parameter space given by the half-crossing angle θ and the minimal beam width in vertical direction W_{0z}. The red line corresponds to the optimization curve given by the experimental boundary conditions. Above the red line are the available configurations and below are the inaccessible ones. To reach a quasi-two-dimensional system, a region of interest around a flatness ratio of about $R_{2D} \approx 100$ was chosen and finally the precise trap parameters were selected to be: $\theta \approx 7.3°$ and $W_{0z} \approx 17\ \mu$m to reach trap properties with the values: $R_{2D} \approx 70$ and $f_z \approx 30$ kHz.

version is given in the appendix. In figure 5.6 this optimization curve is plotted as red line in the full parameter space for the two relevant trap properties: f_z and R_{2D}. Above this optimization curve lie the available configurations and below the forbidden configurations. To select a reasonable parameter set for a quasi-two-dimensional trap, one can fix the region of interest to an area around $R_{2D} \approx 100$. Finally the parameter set was chosen to be: $\theta \approx 7.3° \implies W_{0z} \geq 16.2\ \mu m \implies W_{0z} \approx 17\ \mu$m. The corresponding trap properties are: $f_z \approx 30$ kHz and $R_{2D} \approx 70$. So, the intensity distribution of the target trap has now the shape portrayed in figure 5.8.

5.2 New Microtrap

In order to be able to tune the radial confinement of the 2D Trap independently from the vertical confinement, it is desired to overlap an additional trap. For this purpose, one just

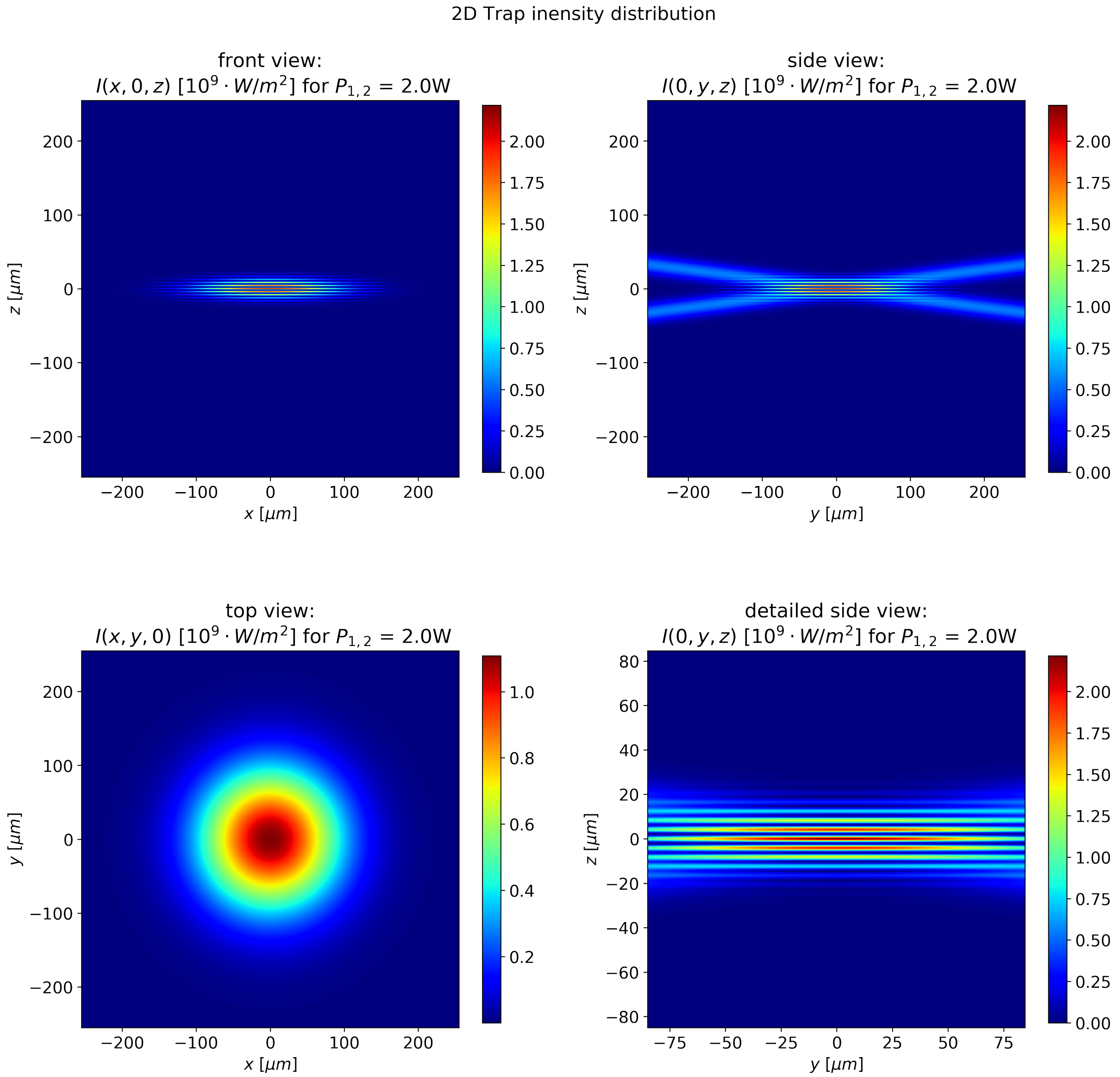

Figure 5.8: Four two-dimensional views on the three-dimensional intensity distribution of the 2D Trap formed by two elliptically shaped Gaussian beams crossing each other under an angle of $\theta = 7.3°$ and interfering in the crossing region. The vertical minimal beam width of the single beams is $W_{0z} = 17$ μm and the horizontal minimal beam width is $W_{0x} \approx 133$ μm. The two-dimensional cuts are placed through the centre of the intensity distribution: the top left provides a front view, the top right a side view and the bottom left a top view on the intensity distribution. The bottom right view allows to register the interference pattern in detail.

has to choose a Gaussian beam from the top:

$$\boxed{I_{NMT}(r,z) = \frac{2P_3}{\pi \cdot W^2(z)} \cdot \exp\left(-\frac{2r^2}{W^2(z)}\right) \quad \text{with :} \quad r = \sqrt{x^2+y^2}} \tag{5.45}$$

with P_3 as the beam power and beam waist:

$$\boxed{W(z) = W_0 \cdot \sqrt{1 + \left(\frac{z}{L_R}\right)^2}} \tag{5.46}$$

The Rayleigh length is just: $L_R = \frac{\pi \cdot W_0^2}{\lambda}$ and the laser wavelength is fixed to $\lambda = 1064$ nm. So, the intensity distribution for the additional trap is just a function of two experimental parameters:

$$\boxed{I_{NMT} = I_{NMT}(r, z, P_3, W_0)} \tag{5.47}$$

Here again, the power can be tuned individually, but the minimal beam width W_0 has to be chosen appropriately.
Although there already exists such a single focused beam trap in the experiment, called a Microtrap, its minimal waist of $W_{0,MT} = 1.0\ \mu$m ([20], p.33) is too small because it would also dominate the vertical confinement. Therefore an additional parallel new Microtrap was planned and built during this thesis. By comparing the resulting trap frequencies, a minimal waist of $W_0 = W_{0,NMT} \approx 10\ \mu$m was chosen.

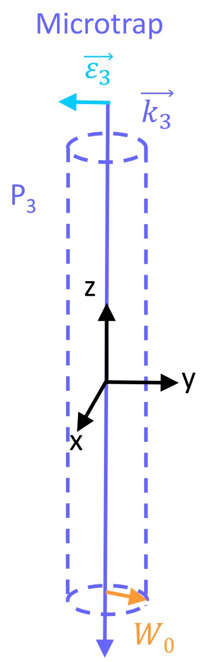

Figure 5.9: Sketch of the new Microtrap consisting of a single Gaussian beam from the top with a chosen minimal beam width of about $W_0 \approx 10\ \mu$m, such that the vertical trap frequency is dominated by the 2D Trap and the radial confinement by the new Microtrap.

The main trap property of the new Microtrap is its radial trap frequency:

$$\boxed{f_r = \frac{1}{2\pi}\sqrt{\frac{8aP_3}{\pi m W_0^4}}} \tag{5.48}$$

derived from a second-order Taylor expansion of the intensity distribution similar to the previously described procedure. Compared to this frequency, the vertical trap frequency is much smaller:

$$\boxed{f_z = \frac{1}{2\pi}\sqrt{\frac{4aP_3}{\pi m W_0^2 L_R^2}} = \frac{1}{2\pi}\sqrt{\frac{4aP_3\lambda^2}{\pi^2 m W_0^6}}} \tag{5.49}$$

The central depth of the potential is:

$$\boxed{U_0 = -\frac{2aP_3}{\pi W_0^2}} \tag{5.50}$$

In order to avoid any interference between the Microtrap and the 2D Trap, both laser frequencies are shifted against each other appropriately. Besides, one can invert the equations above to calculate the trap parameters from the trap properties:

$$\boxed{W_0 = \left(\frac{8aP_3}{\pi m (2\pi f_r)^2}\right)^{\frac{1}{4}}} \tag{5.51}$$

5.3 Combined tunable 2D Trap

Combining the described target 2D Trap with the chosen new Microtrap leads to a quasi-two-dimensional trap with tunable trap properties. This means the vertical confinement characterized by the trap frequency $f_z \approx f_{z,2D}$ can be separately changed from the radial restriction given by the trap frequency $f_r \approx f_{r,NMT}$. This can be achieved by tuning the left free parameters: the laser powers $P_{1,2} = P_1 = P_2$ and P_3.

The reason for this circumstance can be identified by comparing the trap frequencies for reasonable powers $P_{1,2} = 2$ W and $P_3 = 0.2$ W. The most important characteristic quantities for this choice are summarized in table 5.11. Under this condition, in the vertical direction the 2D Trap frequency dominates over the new Microtrap frequency as already can be concluded from figure 5.10: $f_{z,NMT} \ll f_{z,2D} \sim \sqrt{P_{1,2}}$. In contrast to that, in the radial direction the new Microtrap frequency plays the dominant role: $f_{r,2D} \ll f_{r,MT} \sim \sqrt{P_3}$. This observation from figure 5.10 can be supported by the comparison in table 5.11 where one can always see at least a factor of ten between the relevant frequencies.

In order to give a more detailed perspective on the exact shape of the trap, figure 5.12 shows the relevant slides through the three-dimensional intensity distribution.

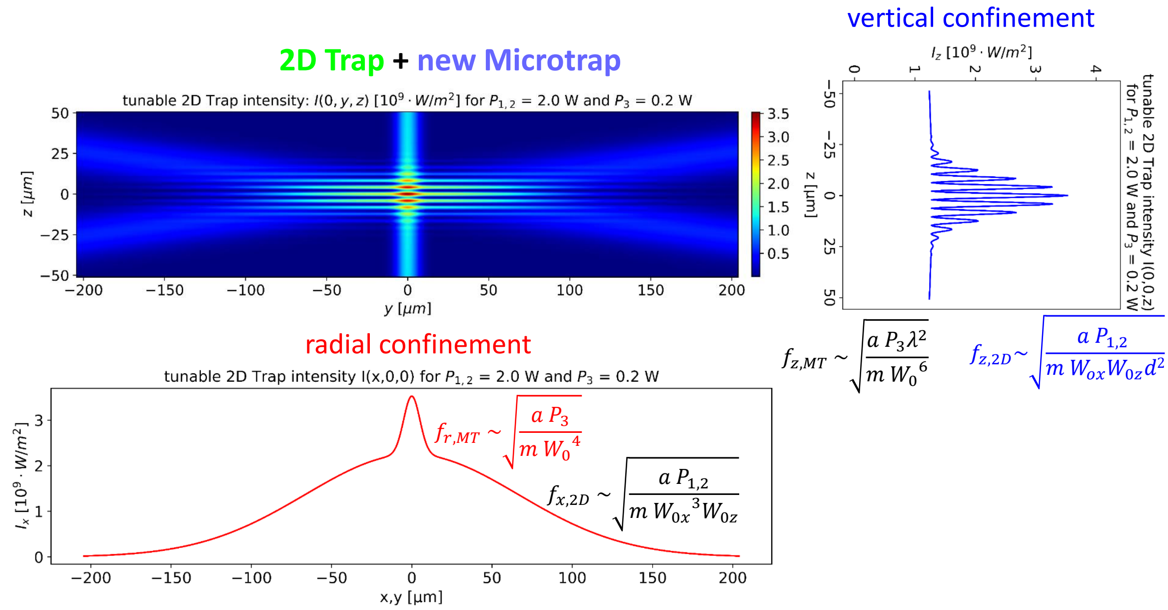

Figure 5.10: Different views on the combined intensity distribution for the tunable 2D Trap, consisting of the two elliptical Gaussian beams for the 2D Trap from the side and the single focused Gaussian beam of the new Microtrap from the top. On the top left one can see a two-dimensional graph of the tunable 2D trap as a side view through the centre of the distribution. On the top right a one-dimensional graph through the centre of the distribution along the vertical direction is depicted, demonstrating that the vertical direction is dominated by the interference structure of the 2D Trap. The graph on the bottom shows a one-dimensional cut through the intensity distribution along the horizontal x-direction. Here one can clearly see that the new Microtrap dominates in the radial confinement. The trap parameters were chosen as follows: $P_{1,2} = 2$ W, $P_3 = 0.2$ W, $W_{0z} = 17$ μm, $W_{0z} \approx 133$ μm, $\theta = 7.3°$, $W_0 = 10$ μm.

Tunable 2D Trap		2D Trap	New Microtrap	Combined trap:
Trap parameters	$P_{single\ beam}$	2 W	0.2 W	tune $P_{1,2}/P_3$
	λ	1064 nm	1064 nm	
	θ	7.3 °	-	
	W_{0z}	17 µm	-	
	W_{0x}	133 µm	10 µm	
	$E \equiv W_{0x}/W_{0z}$	7.8	-	
Trap properties	$d = \dfrac{\lambda}{2\sin(\theta)}$	4.19 µm	-	-
	f_z	**29 kHz**	99 Hz	**29 kHz**
	$f_r \approx f_x \approx f_y$	414 Hz	**4.1 kHz**	**4.2 kHz**
	$R_{2D} \equiv f_z/f_r$	71	0.024	**7,1**
	$R_{xy} \equiv f_x/f_y$	≈ 1	1	**1**
	$U_0 = -a \cdot I_0$	-22 µK·k_B	-12 µK·k_B	**-34 µK·k_B**
	$N_{max,2D} = \dfrac{{f_z}^2}{4 f_x f_y}$	~1200	-	~**12**

Figure 5.11: Table with the central target trap parameters and properties for the 2D Trap, the new Microtrap, and the combined trap.

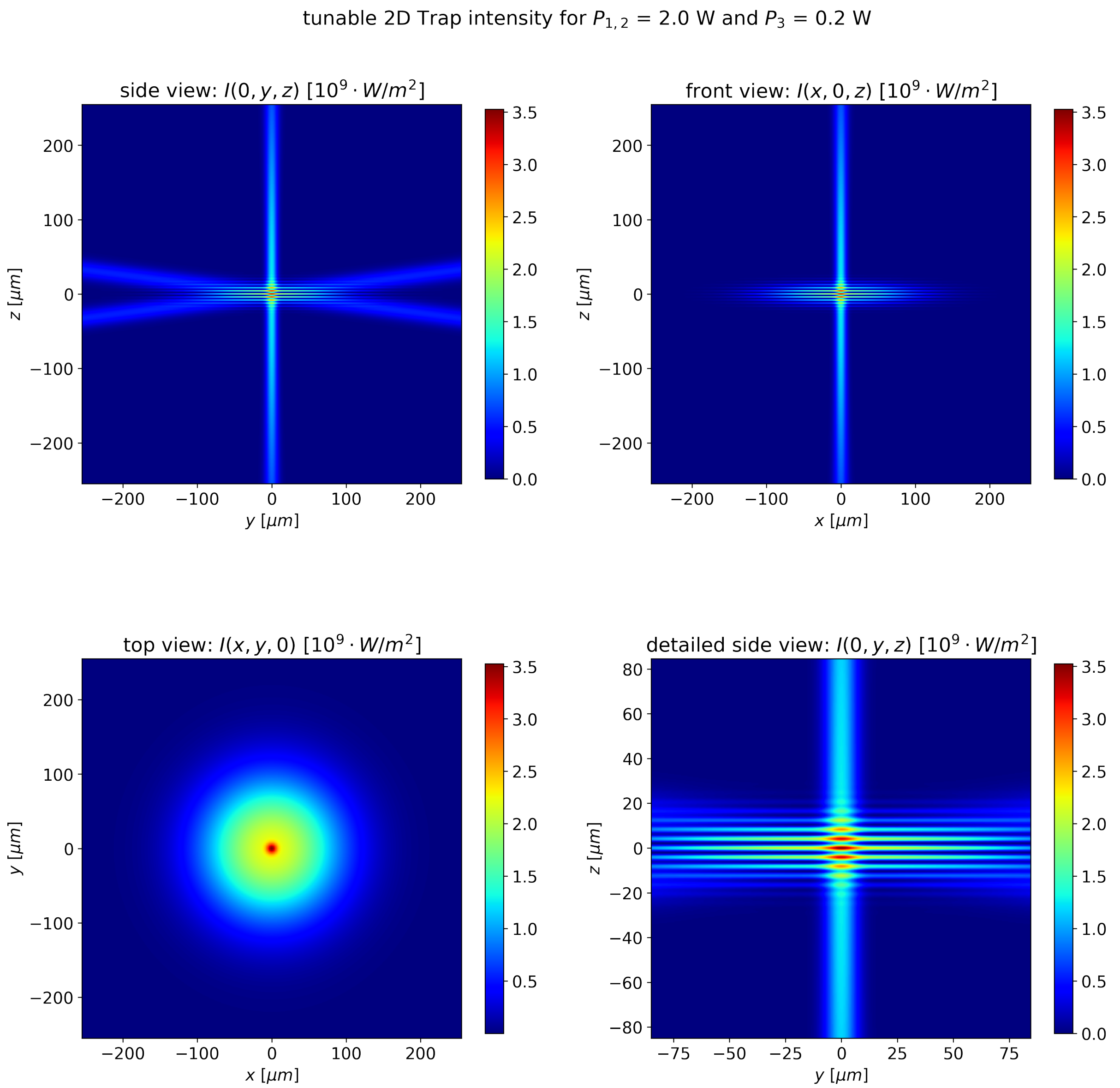

Figure 5.12: Four two-dimensional views on the three-dimensional intensity distribution of the tunable 2D Trap formed by two elliptically shaped Gaussian beams crossing under an angle of $\theta = 7.3°$ and interfering in their crossing region together with an additional new Microtrap beam from the top which does not interfere with the other beams. The vertical minimal beam width for the two 2D trap beams is $W_{0z} = 17$ μm and the horizontal minimal beam width is $W_{0x} \approx 133$ μm. The minimal beam width of the new Microtrap beam is about $W_0 = 10$ μm. The two-dimensional cuts are placed through the centre of the intensity distribution: the top left cut provides a front view, the top right cut a side view and the bottom left cut a top view on the intensity distribution. The bottom right view allows to register the interference pattern in detail. The beam powers were chosen to be: $P_{1,2} = 2$ W and $P_3 = 0.2$ W.

Part IV

Realization of the tunable 2D Trap

6 Opto-mechenical design

As mentioned already in [27], but also during this thesis a compact opto-mechanical system for the creation of the tunable 2D Trap was designed. In this context, the main elements should be described in detail, but first one has the opportunity to gain a rough overview.

6.1 Setup overview

The opto-mechanical setup depicted in figure 6.1 which was built up during this thesis can be separated into three parts. The first part consists of the setup which provides power-controlled and clean polarized infrared laser light for the 2D Trap coupled into a high-power fibre. In the second part, the infrared laser light is shaped elliptical and is split in two identical parts such that it has the right properties to create the desired trap when entering the experimental chamber. At the same time, other laser beams for the magneto-optical trap and atom absorption imaging are integrated on the same optical axis. The last part of the setup consists of an imaging setup which should be able to image the trapped atoms as well as the intensity distribution of the trap itself for diagnostic purposes.
After the infrared trapping beam is split into two identical parts, the beam path is covered by a mechanically rigid box in the sense of a container, called a Trapping-Box, in order to guaranty the phase stability of the created interference structure produced by the two beams. The Imaging-Box in the third part of the setup is equally covered to provide the same stability for the image of the 2D Trap. In this way, one should be able to observe the actual trap stability of the real trap in the image of the trap. The following pictures: 6.2 and 6.3 show the parts of the setup which were designed with the CAD-program CATIA. For clarity the project was integrated into the enclosing vacuum system. In this way, it was also possible to check if all parts fit well into the enclosing apparatus.

6.2 Laser setup

The first part of the full setup is portrayed in figure 6.5, and a legend of the optical components can be found in figure 6.4. The heart of the laser setup is of course an infrared laser with a wavelength of $\lambda = 1064$ nm providing a laser power of up to $P \leq 50$ W. The laser is specified to produce a collimated beam with a minimal width of about $W_0 \approx 750$ μm, but unfortunately the output beam reaches its minimal waist even after about one and a half meter (~ 1.4 m) and it has a different value. Additionally one has to remark that the beam profile corresponds not to a smooth Gaussian over along the first meter. After that distance the shape gets smoother and seems more reliable. Therefore, a short telescope is integrated directly after the laser output which is optimized to provide

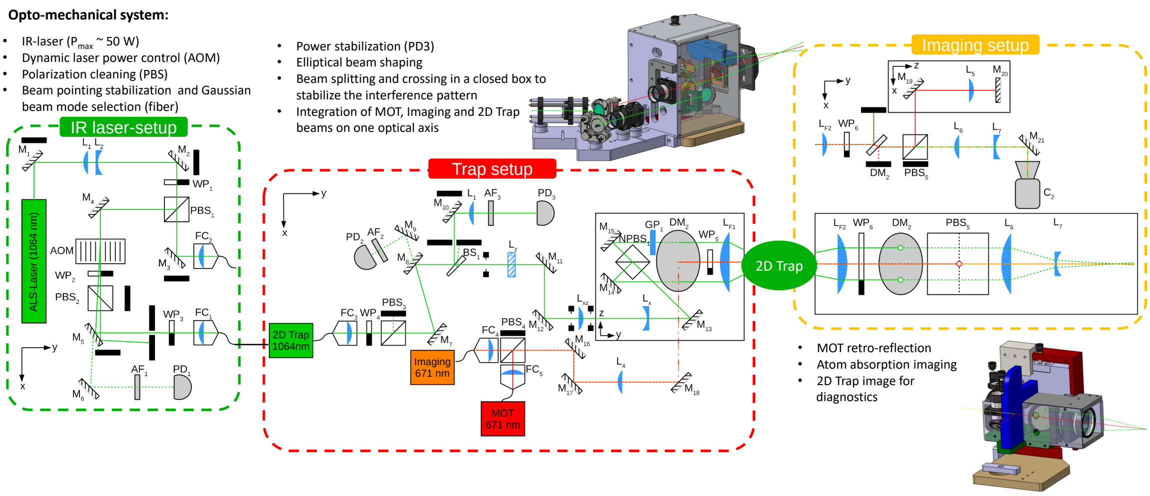

Figure 6.1: Overview to the opto-mechanical system, consisting of a laser setup, a trap setup, and an imaging setup. The laser setup provides a pure polarization-cleaned beam with a single Gaussian mode selected by a high-power fibre. The beam power from the laser can be adjusted to up to $P_{max} \sim 50$ W and can be dynamically controlled with an acousto-optical modulator (AOM). One has to remark that the high-power fibre is only specified for a beam power of $P = 8$ W, but it was observed to be possible to use even higher beam power for a short time. Here the time scale of milliseconds should be realistic to recover a high enough coupling efficiency and prevent strong heating effects. The trap setup produces two identical and elliptical shaped beams and focusses them under a half-crossing angle of about $\theta \approx 7.3°$ to the centre of the experimental chamber. Besides an atom absorption imaging-beam and a beam for the magneto-optical trap is integrated on the same optical axis as the 2D Trap beams. Photodiodes are used for power stabilization and control. Finally the imaging setup reflects the MOT-beam back and creates an image of the atoms and the 2D Trap which can be detected by a camera.

a collimated beam with the preferred beam size of about 1320 μm in diameter at about one meter distance from the laser to couple into a fibre with a coupling lens of $f = 8$ mm. In this way, the coupling efficiency into the high-power fibre at the end of the optical path could be optimized to values of up to about 90%. The short telescope is positioned about 24 cm after the laser output and consists of two spherical lenses with a distance of about 20.6 mm. The first focal length is $f_1 = 75$ mm, and the second one is $f_2 = -50$ mm. Just after the telescope a high-power polarizing beam splitter is used to split the laser beam into two polarized beams. The $\lambda/2$-wave-plate in front of the polarizing beam splitter cube can be used to distribute the beam power over the two arms. The arm with the vertically polarized light is used for the 2D Trap, whereas the arm with the horizontally polarized light can be used for future projects. So, the vertically polarized light enters an acousto-optical modulator which can be used to control the absolute amount of laser power provided for the 2D Trap beam. By tuning the rf-power,

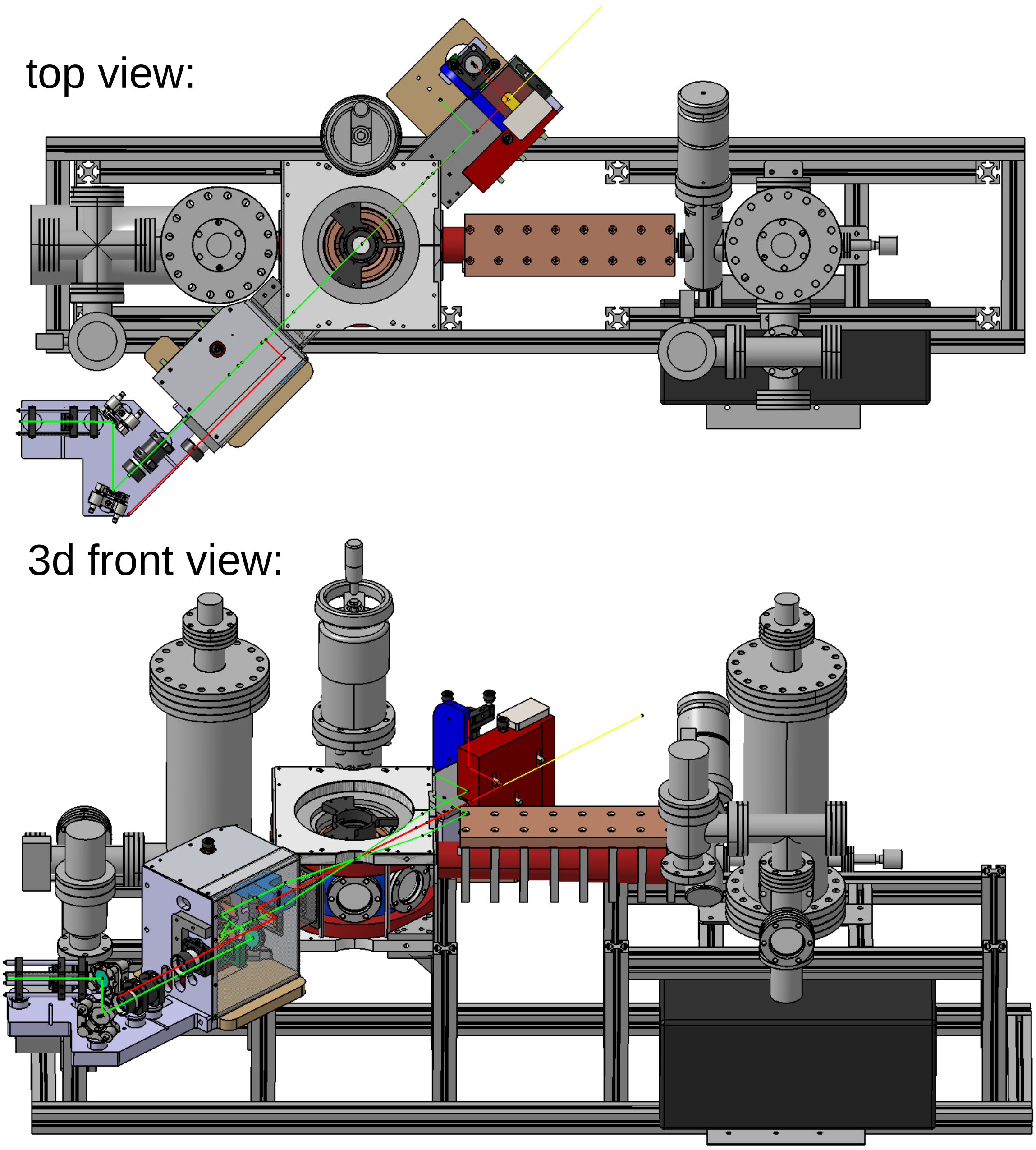

Figure 6.2: Picture from the CAD-model designed in CATIA: Integration of the Trapping-Box and the Imaging-Box into the vacuum system. The path of the 2D Trap beams is depicted as green line. The path of the MOT-beam is drawn as red line and overlaps most of the time with the path of the imaging-beam shown as yellow line.

the amplitude of the created sound wave in the AOM crystal is changed and therefore the power fraction which is deflected by the sound wave changes. For this purpose only

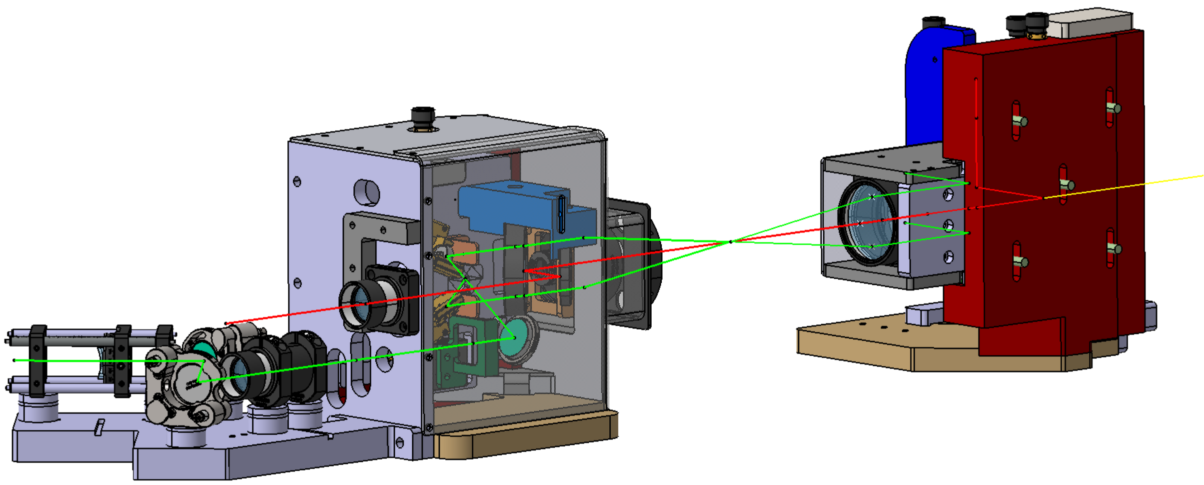

Figure 6.3: Picture from the CAD-model designed in CATIA: the Trapping-Box with the telescope plate together with the Imaging-Box. The path of the 2D Trap beams is depicted as green line. The path of the MOT-beam is drawn as red line and overlaps most of the time with the path of the imaging-beam shown as yellow line.

the output of the first diffraction order is power-optimized by the alignment of the AOM. However, it was realized that the polarization after the AOM is not very clean. For this reason a $\lambda/2$-wave-plate is used to rotate the main polarization to a horizontal one and a second high-power polarizing beam splitter cleans the polarization to pure horizontally linear-polarized output light which can be coupled into a high-power fibre at Port 1 with a lens of focal length $f = 8$ mm. In this way a single Gaussian mode can be selected from the input laser beam which guarantees a pure single mode output beam from the fibre. A beam dump is used to select only the first diffraction order from the AOM. One has to remark that the $\lambda/2$-wave-plate WP_3 is used to align the linear input polarization accordingly to the internal axis of the high-power fibre as this was not fixed during the fabrication process. On top of that, the fibre is specified for a beam power of up to $P = 8$ W. It was observed that one can couple light at even much more power into the fibre, meaning at least twice as much, but the coupling efficiency decreases strongly during this process on the second time scale, probably because of heating effects. So one can conclude, that it should be possible to couple more than 8 W of power into the high-power fibre for a shorter time in the range of milliseconds. In parallel, a small fraction of the beam transmits through mirror M_4 and is guided onto a photodiode to measure the laser power in front of the fibre.

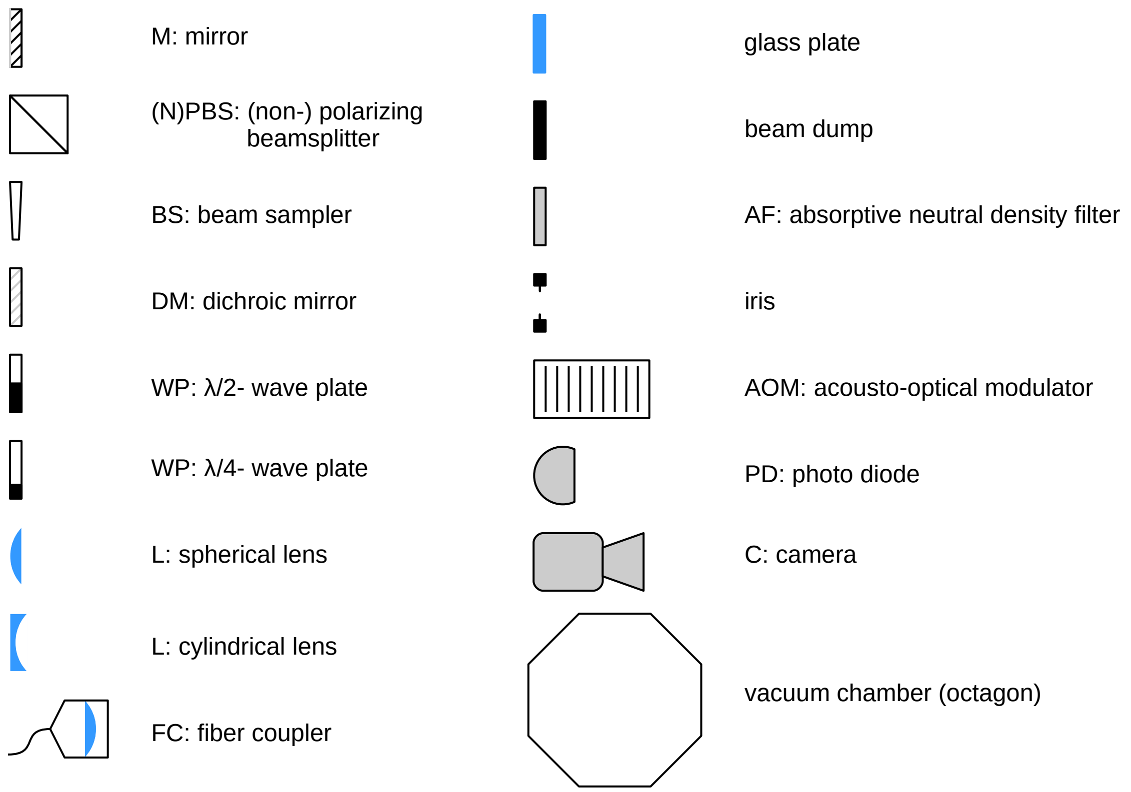

Figure 6.4: Legend of optical elements used in the setup sketches.

6.3 Trapping setup

In figure 6.6 the second part of the setup is depicted. The infrared laser light from the laser setup is coupled out of the fibre with a lens of $f = 6.24$ mm focal length and collimated to a beam diameter of about $2W_0 \approx 1040\ \mu$m. The fibre out-coupler is mounted on a z-axis-adjustable mount (Thorlabs: SM1Z) which itself is fixed on a two-angle-adjustable tube mount (Thorlabs: KM100T) to get three degrees of freedom, if necessary. Again a $\lambda/2$-wave-plate and a high-power polarizing cube are used to clean the polarization to purely horizontally linear-polarized light and the fraction of the beam which transmits through mirror M_8 is collected on a second photodiode measuring the laser power out of the fibre. In this way, the coupling efficiency of the fibre can be measured simultaneously during the experiment to be able to turn the laser power off if the coupling efficiency becomes too small. This procedure helps to prevent damages of the high-power fibre. On top of that, a beam sampler BS_1 is used to distribute a small part of the beam power to another parallel path. At the end of this parallel path follows a third, logarithmic photodiode which is used to stabilize the laser power during the experiment. About 40 cm from the fibre out-coupler away the mechanically combined Trapping-Box setup starts with the first cylindrical lens L_z which forms with L_{xz} and L_x a coupled telescope to

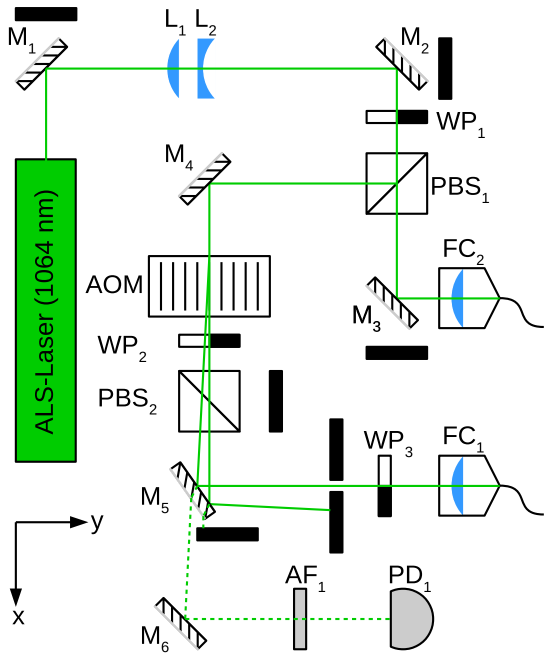

Figure 6.5: Laser setup: The beam from the laser is collimated by a telescope formed by L_1 and L_2 to optimize the coupling efficiency of the fibre coupler FC_1. PBS_1 distributes polarized light over two arms ending with FC_1 and FC_2. The relative amount of power in the two arms can be adjusted by the orientation of WP_1. The AOM is used to control the power of the beam coupled into FC_1 dynamically in time. Therefore the power output of the first diffraction order is maximized. PBS_2 cleans the polarization of the output beam from the AOM and WP_2 is used to maximize the clean polarization output. Finally, WP_3 is used to adjust the polarization axis such that it fits to the polarization-maintaining axis of the high-power fibre connected to FC_1. A small fraction of the light transmitting through M_5 is collected on a photodiode to register the amount of power which goes into the fibre.

create a large elliptical beam on the final focus lens L_{F1}. Inside the Trapping-Box a special high-power non-polarizing beam-splitter cube splits the laser beam into two equal parts which are guided in parallel onto a two-inch Gradium lens L_{F1}, after transmitting through a dichroic mirror. The final lens focusses the two identical beams, which are about 32 mm apart from each other, under a half-crossing angle of $\theta \approx 7.3°$ to the centre of the experimental chamber.

The dichroic mirror is used to integrate two additional beams with the resonance wavelength of $\lambda = 671$ nm onto the same optical axis as the 2D Trap beams: the atom absorption imaging-beam and one beam for the magneto-optical trap. Both beams are coupled out of a fibre. If one assumes a mode field diameter in the fibres of $MFD = 2W_{MF} = 4.6\ \mu$m at a wavelength of $\lambda = 671$ nm, the imaging-beam is collimated with a lens of focal length $f = 11$ mm to a beam diameter of about $2W_0 = 2.0$ mm and the MOT-beam is collim-

ated with a lens of focal length $f = 50$ mm to a beam diameter of about $2W_0 = 9.3$ mm. This corresponds roughly to the observed beam diameters. Because the imaging-beam has horizontal polarization in the lab frame and the MOT-beam vertical polarization, it is possible to combine both beams by a thin-film polarizing cube beam splitter with very clean polarization output to the same optical path. The lens L_4 with a focal length of $f_4 = 125$ mm afterwards in the optical path forms together with the final focus lens L_{F1} whose focal length is $F = 120$ mm nearly a 1:1 telescope. In this way it is guaranteed that the output beam to the experimental chamber is again collimated, which is important especially for the MOT-beam. Behind L_4 both beams are reflected at the dichroic mirror and guided on the same optical axis as the 2D Trap beams. In contrast to the 2D Trap beams, the imaging-beam and the MOT-beam travel through a small $\lambda/4$-wave-plate with a diameter of 1/2 inch, such that the 2D Trap beams can bypass unchanged. The wave-plate changes the polarization of the imaging-beam and the MOT-beam from linear to circular, which is necessary for the MOT-beam.
Apart from the described beam paths there are paths which are caused by imperfect properties of the used optical elements. Therefore, the other beam paths are mainly blocked by beam dumps if it is possible. Table 6.1 shows the relevant properties for the Trapping-Box in this context:

beam	reflection	transmission
@ 1064 nm (p-pol): 2D Trap beams	0.52%	99.48%
@ 671 nm (p-pol): imaging-beam	99.23%	0.77%
@ 671 nm (s-pol): MOT-beam	99.67%	0.38%

Table 6.1: Relevant reflection and transmission properties of the first dichroic mirror: DM_1.

6.3.1 Elliptical beam shaping

Apart from the module splitting the infrared 2D Trap beam into two identical ones and guiding them under a half-crossing angle θ to the centre of the experimental chamber, the trapping setup consists mainly of a coupled telescope which creates the right ellipticity to create circular light sheets in the interference pattern. In order to reach pure circularity the ellipticity of the beams has to be adjusted precisely. For the elliptical beam shaping two coupled cylindrical telescopes are used. In this way one can supersede one lens in comparison to two decoupled cylindrical telescopes because the spherical lens L_{xz} serves for both telescopes. As depicted in figure 6.7 for case 1, the two lenses L_z and L_{xz} expand the vertical axis of the beam profile to a nearly collimated beam, whereas L_{xz} and L_x compress the beam width in horizontal axis. The final lens L_{F1} focusses the large beam to the crossing point while inverting the beam width ratio to the desired widths of $W_{0z} \approx 17.1$ μm and $W_{0x} \approx 133.5$ μm.
The demonstrated beam profile in figure 6.7 is calculated with an on-axis Gaussian beam matrix calculation, which is conceptionally already described in [27]. The distances between the lenses can be adjusted such that the foci in both elliptical beam axes meet

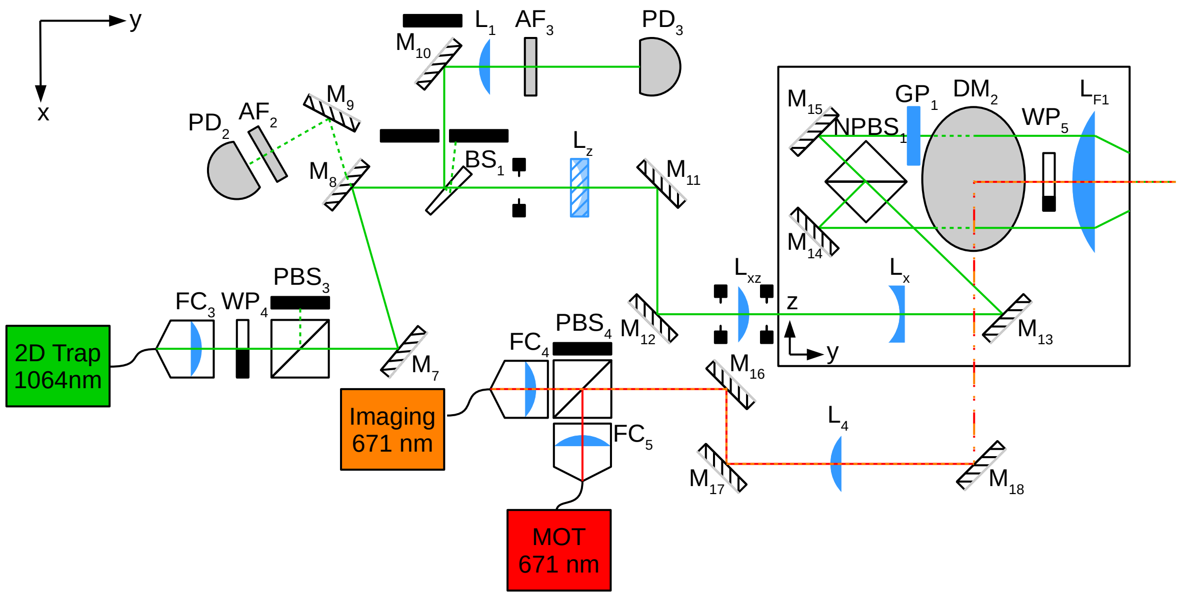

Figure 6.6: Trap setup: In the beam path of the 2D Trap (green), PBS_3 cleans the polarization of the light out of the fibre connected to FC_3, whereas WP_4 maximizes the horizontal polarization output for the 2D Trap. Subsequently, a small fraction of the light is collected on two photodiodes. PD_1 should measure the beam power out of the fibre to control the coupling efficiency into the fibre, and PD_3 is used for the power stabilization. Afterwards, the lens system consisting of L_z,L_{xz} and L_x shapes the beam elliptical. The 2D Trap beam is split into two equal parts by $NPBS_1$ and the two parallel beams behind $M_{14,15}$ are focused by L_{F1} such that they are crossing each other in the centre of the experimental chamber. In the beam path of the MOT-beam and the imaging-beam, $FC_{4,5}$ creates both collimated output beams, and PBS_4 connects both beam paths to one. L_4 forms with L_{F1} nearly a one-to-one telescope, such that the output beams after L_{F1} are again collimated beams, and the dichroic mirror reflects both beams on the same optical axis as the 2D Trap beams are on. The polarization of the MOT-beam and the imaging-beam is transformed to circular polarization by WP_5.

each other at about 126 mm away from the final focus lens L_{F1}, as portrayed in figure 6.7 for case 2. Here the single minimal beam widths in the two elliptical beam axes are comparable to case 1 with: $W_{0z} \approx 16.8$ μm and $W_{0x} \approx 131.5$ μm. However for this case, the geometrical crossing point of the two 2D trap beams after about 120 mm does not overlap any more with the two single-beam foci. In this configuration, one has to adjust the incoming parallel beams to L_{F1} such that the parallelism of the beams and orthogonality to L_{F1} are broken to overlap the single-beam foci with the crossing point. Unfortunately, this procedure can cause spherical aberrations, and the beam quality suffers.

Therefore, a better choice is the solution in figure 6.7 (case 1), where the two foci of the elliptical beam axis do not exactly match. However, the marks on the telescope board are made for the non-collimated version. The focus distance in z-direction approaches nearly the geometric limit of the focal length of L_{F1}, whereas the focus in x-direction is more far apart. This fact does not lead to a problem because the beam in x-direction is much broader than the beam in z-direction and changes its size much slower along its propagation direction. This can be seen from the Rayleigh lengths: $L_{Rz} \approx 850\ \mu$m and $L_{Rx} \approx 50$ mm. The Rayleigh length corresponds to the distance at which the beam width has increased to $\sqrt{2}W_0$. From this perspective, only the position of the z-axis focus matters, whereas the position difference of the x-axis focus to the focal length of L_{F1} is still only a small fraction of the Rayleigh length.

6.3.2 Trapping-Box

As already described before, the individually designed mounting construction for the optical components in the second setup part is used to prevent any disturbance of the interference pattern, like mechanical vibrations, moving air, as well as heating effects. All parts were designed with a CAD-software called CATIA. The project, visible in figure 6.8, consists of a telescope plate on which the first two lenses of the coupled telescope L_z and L_{xz} are mounted and a box, or container, for the part of the optical path where the infrared beam is already split up into two similar parts. Both elements are directly connected with each other. Apart from the mechanical stability, this allows also the motion of the main part of the setup as a whole.
Starting with the beam path of the infrared beam depicted in green, the first lens L_z is mounted in a cage system from Thorlabs. In this way, one can easily change the axial position of the lens along the optical path. On top of that, the lens is glued on a rotatable cage plate, such that the precise orientation of the elliptical beam axis can be adjusted by rotating the cylindrical lens around the optical axis. The height of the lens has to be adjusted once in the beginning with cylindrical plates because they are fixed from the bottom. After two mirrors mounted on adjustable and stable kinematic mirror mounts (POLARIS-K1S4), the lens L_{xz} follows in an adjustable lens tube. Also in this case, the position of the lens along the optical axis can be changed by rotating the spherical lens tube, and the height above the optical table has to be fixed once in the beginning by choosing cylindrical plates of an appropriate thickness. All other optical elements for the 2D Trap beam are mounted on a vertical board inside the Trapping-Box. This board can be moved in vertical direction by unlocking the five screws at the backside of the box and turning the micrometer screw at the top of the box. One rotation corresponds to 250 μm. The lens L_x is fixed on a very small translation stage (Thorlabs: MS1/M) with a total range of 6.4 mm. Nevertheless, one can also shift this lens position continuously along the optical axis. A mirror glued in a fixed mirror mount (Polaris-B1G) reflects the beam upwards through a non-polarizing beam-splitter cube, which was glued directly on a tower-like extension of the vertical board in the box. The two parts of the beam after the beam splitter are reflected at two small half-inch sized mirrors fixed in piezo mirror mounts (Newport: AG-M050N with controller: AG-UC8) which can be adjusted automatically by a computer program. This allows a very precise alignment of the two mirrors to guarantee two parallel output beams hitting the final focus lens L_{F1} orthonormally and to allow the final alignment of the beams on the atom cloud. Directly after the two piezo mirrors, it

is possible to mount an alignment plate with two thin holes with a diameter of 1 mm. This helps to align the beams appropriately but should only be fixed temporally for the alignment procedure. In the beam path of the top beam, a thin glass plate is inserted to be able to adjust the relative phase between the beams. Afterwards, the dichroic mirror follow under an angle of 45° through which the infrared light just transmits. Still connected to the vertical board is the mount for the final focusing lens L_{F1}. This mount also enables the motion of the lens along the optical axis to adjust the actual position of the crossing point and the single-beam foci.

In parallel, one can consider the beam path for the resonant light shown in red. Here, the starting point forms the lens L_4, mounted in an adjustable lens tube to be able to collimate the beam after L_{F1} separately from the infrared beam path. As can be seen in figure 6.8, one can connect the optical elements in the previous optical path of the resonant light with a cage-system from Thorlabs to the cage plate in which the lens tube of L_4 is mounted. The cage plate is fixed at the entrance plate outside of the Trapping-Box. The mirrors $M_{16,17}$ are mounted in right-angle cage mirror mounts. In this way, even a larger part of the trapping setup can be moved as a whole. Behind L_4 follow just a fixed mirror and the fixed dichroic mirror. Finally, the $\lambda/4$-wave-plate is inserted in a rotation mount before the focusing lens L_{F1}.

6.4 Imaging setup

In the last part of the full setup one has to follow the beam paths starting from the focusing lens L_{F2} directly before the experimental chamber. As portrayed in figure 6.9, the two diverging 2D Trap beams in green are collimated to two parallel beams by L_{F2}, which has the same focal length as L_{F1}. Subsequently, they pass a 2 inch sized $\lambda/4$-wave-plate unchanged, which causes an axis dependent shift of λ for the infrared beams. Finally, the main power of the 2D Trap beams is reflected at the dichroic mirror DM_2 to a beam dump. However, a small part of about 1.83% transmits through the dichroic mirror and also through the polarizing beam splitter PBS_5, because it is horizontally polarized. Afterwards two lenses L_6 and L_7 with focal lengths $f_6 = 150$ mm and $f_7 = -40$ mm act as a single lens with an effective focal length depending on their relative distance. This connection is described in the subsection below. In this way the lens system forms an imaging system, which creates an image of the trap behind L_7, where a camera can detect it.

Besides, the collimated imaging-beam and the MOT-beam are focused by L_{F2} and the $\lambda/4$-wave-plate acts for laser light with a wavelength of $\lambda = 671$ mm really as $\lambda/4$-wave-plate and changes the circular polarized light into linearly polarized light. The horizontally polarized imaging-beam transmits through the dichroic mirror as well as the polarizing beam splitter cube and the imaging lenses behind create a magnified absorption image of the atoms. The image of the atoms can be detected by moving the camera C_2 along the optical axis into the image plane. In contrast to that, the MOT-beam mainly transmits through the dichroic mirror and is reflected at the polarizing beam splitter into a vertical tower. Here a lens L_5 with focal length $f_5 = 100$ mm collimates the MOT-beam again and the beam is retro reflected to the experimental chamber following its path backwards.

Apart from the described beam paths, there are paths which are caused by imperfect properties of the used optical elements. Therefore the other beam paths are mainly blocked by beam dumps if it is possible. Table 6.2 and 6.3 show the relevant properties for the Imaging-Box in this context: The main imperfection is caused by the reflection

beam	reflection	transmission
@ 1064 nm (p-pol): 2D Trap beams	98.17%	1.83%
@ 671 nm (p-pol): imaging-beam	1.01%	98.99%
@ 671 nm (s-pol): MOT-beam	**4.33**%	95.67%

Table 6.2: Relevant reflection and transmission properties of the second dichroic mirror: DM_2.

beam	reflection	transmission
@ 1064 nm (p-pol): 2D Trap beams	$\approx$ 0.3%	$\approx$ 99.7%
@ 671 nm (p-pol): imaging-beam	0.7%	$\approx$ 99.3%
@ 671 nm (s-pol): MOT-beam	$\approx$ 99.3%	0.7%

Table 6.3: Relevant reflection and transmission properties of the fifth polarizing beam splitter: PBS_5.

of the MOT-beam at the dichroic mirror. Besides the internal reflections of the infrared beams in the dichroic mirror lead to higher order reflections in the trap image direction. As they have a large enough relative distance of about 4 mm, one can block them out temporally with a beam dump between PBS_5 and L_6, while observing the trap image and not the atoms.
One has to remark, that the reason to use two inch large optics in the main part of the imaging setup is caused by the two parallel 2D Trap beams with a distance of about 32 mm away from each other. In addition to that the atom absorption imaging demands to collect as much as possible light from the experimental chamber.

6.4.1 Imaging system

From fundamental geometrical optics follows ([11]):

$$\frac{1}{f_{eff}} = \frac{1}{f_1} + \frac{1}{f_2} + \frac{d_{12}}{f_1 f_2} \tag{6.1}$$

, where d_{12} is the distance between the two lenses. For example for $d_{12} = 122$ mm and $f_1 = f_6$ as well as $f_2 = f_7$ the relation leads to $f_{eff} = 500$ mm and a magnification of the lens system with L_{F2} of $M = \frac{f_{eff}}{F} = 4.17$. Figure 6.10 shows the dependence of the effective focal length from the distance between the lenses: The desired magnification was chosen such, that one can resolve the interference pattern of the 2D Trap in the image plane with camera C_2. The actual camera was exchanged during this thesis. Finally it was inserted the camera: BFLY-PGE-23S6M-C with a pixel size of 5.86×5.86 μm. As the layer distance of the interference pattern is: $d = \frac{\lambda}{2\sin(\theta \approx 7.3°)} \approx 4.19\ \mu$m, the imaging system is desired to have a magnification of 5 to 10. As demonstrated in figure 6.10, this magnification can be reached in a very small window from $d_{12} \approx 115$ mm with $f_{eff} \approx 1200$ mm to $d_{12} \approx 120$ mm with $f_{eff} \approx 600$ mm. Actually the camera was selected for the purpose to detect at the same time not only the whole trap distribution, but also the atom cloud. So the magnification has to be chosen such that both images fit on the CMOS sensor of the camera with a size of: 1920×1200 px $= 11251.2 \times 7032\ \mu$m. The maximal magnification to detect the whole atom cloud with the old camera, Stingray F-033, is $M_{max,old} \approx 4$. The sensor size of the old camera is: 656(H) $\times$ 492(V) px together with a pixel size of: 9.9 μm. The maximal magnification for the new one is therefore in the horizontal axis:

$$M_{max,new,h} = \frac{\text{new sensor size}}{\text{old sensor size}} M_{max,old} = \frac{1920 \cdot 5.86}{656 \cdot 9.9} 4 \approx 6.93 \tag{6.2}$$

and in the vertical axis:

$$M_{max,new,v} = \frac{\text{new sensor size}}{\text{old sensor size}} M_{max,old} = \frac{1200 \cdot 5.86}{492 \cdot 9.9} 4 \approx 5.77 \tag{6.3}$$

So the vertical maximum of the magnification is the limiting one. If one wants to detect the whole atom cloud with the camera, a magnification of 5.8 seems to be reasonable.
In order to avoid aberrations for the two lenses L_6 and L_7 with focal lengths $f_6 = 150$ mm and $f_7 = -40$ mm one has chosen high-quality achromatic doublets. Apart from the tunable magnification, the main reason for the choice of this lens system is the much shorter optical path as demonstrated by the comparison of the two described options in figure 6.11 from a ray trace calculation.
In the first configuration of figure 6.11, a single lens L_{6+7} with focal length of $f_{6+7} = 700$ mm is used to create the image with a magnification of $M \approx 5.83$. The total optical path length from the centre of the experimental chamber to the trap image is in this case $d_{tot,1} = 1440$ mm. In comparison, the target imaging system as described above and visible in the second configuration of figure 6.11 leads for $d_{12} \approx 118.57$ mm and $f_{eff} \approx 700$ mm to a total optical path length of only $d_{tot,2} \approx 655$ mm. One possible choice for the distances between the lenses can be seen in figure 6.12.

6.4.2 Imaging-Box

As the imaging setup has to be able to monitor the stability of the interference pattern of the 2D Trap, also the imaging setup has to be designed with a mechanically stable construction together with a sufficient covering of the optical paths to avoid air motions. Similar to the Trapping-Box, for the Imaging-Box which is shown in figure 6.13 the main optical components between L_{F2} and PBS_4 are fixed on a vertical board whose height can be adjusted with a micrometer-screw at the top of the box. The first lens L_{F2} seen from the experimental chamber can be shifted along the optical axis separately in a lens tube to be able to collimate the two 2D Trap beams. The $\lambda/4$-wave-plate for 671 nm laser light is mounted in a rotatable mount such that its orientation can be appropriately adjusted. The dichroic mirror is fixed under 45° in a mirror mount. Afterwards, the polarizing beam-splitter cube is fixed by a single screw from the top. A plastic plate between the screw tip and the cube spreads the pressure of the screw over the cube head surface. Nevertheless, the screw should not be tightened too strongly. Along the MOT-beam path follows a fixed mirror which reflects the beam to lens L_5 in an adjustable lens tube used to collimate the MOT-beam. Finally, the mirror M_{20} is mounted in an adjustable kinematic mirror mount to guide the MOT-beam directly on its path backwards. The two lenses L_6 and L_7 are mounted in a closed lens tube system together with mirror M_{21} in a right-angle cage mirror mount. This should guarantee a stable interference pattern in the image plane. Nevertheless, the positions of both lenses can be adjusted separately to optimize the beam along its optical path.

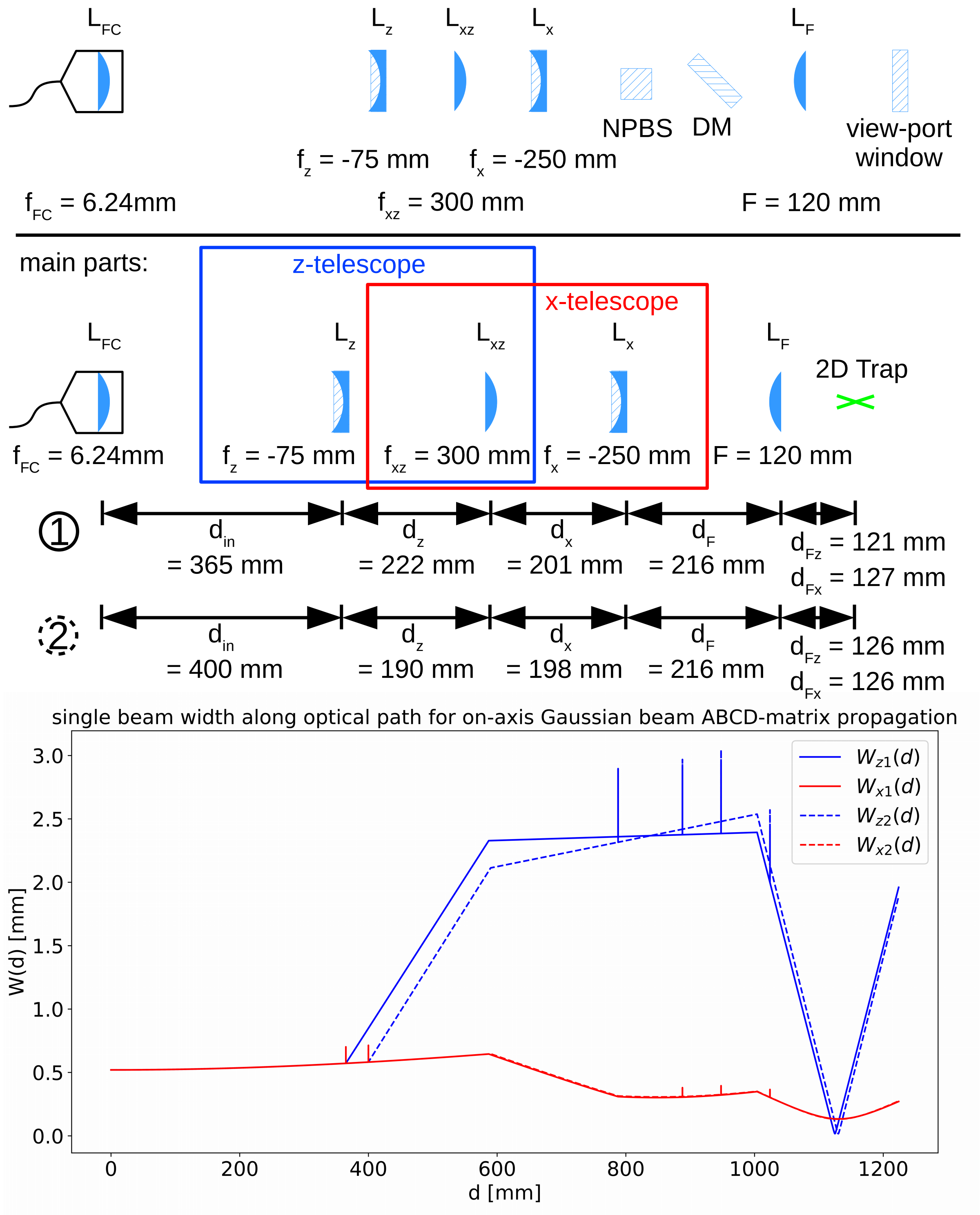

Figure 6.7: Optical path for the creation of elliptically shaped 2D Trap beams with a nearly collimated beam in the z-axis before L_{F1} for case 1 and a non-collimated beam in z-axis before L_{F1} for case 2. At the top, the sequence of considered optical elements is shown. In the centre, the main optical components for the beam shaping are depicted together with their relative distances. At the bottom, the beam width of the two elliptical beam axes are shown, calculated from an on-axis Gaussian beam ABCD-matrix propagation.

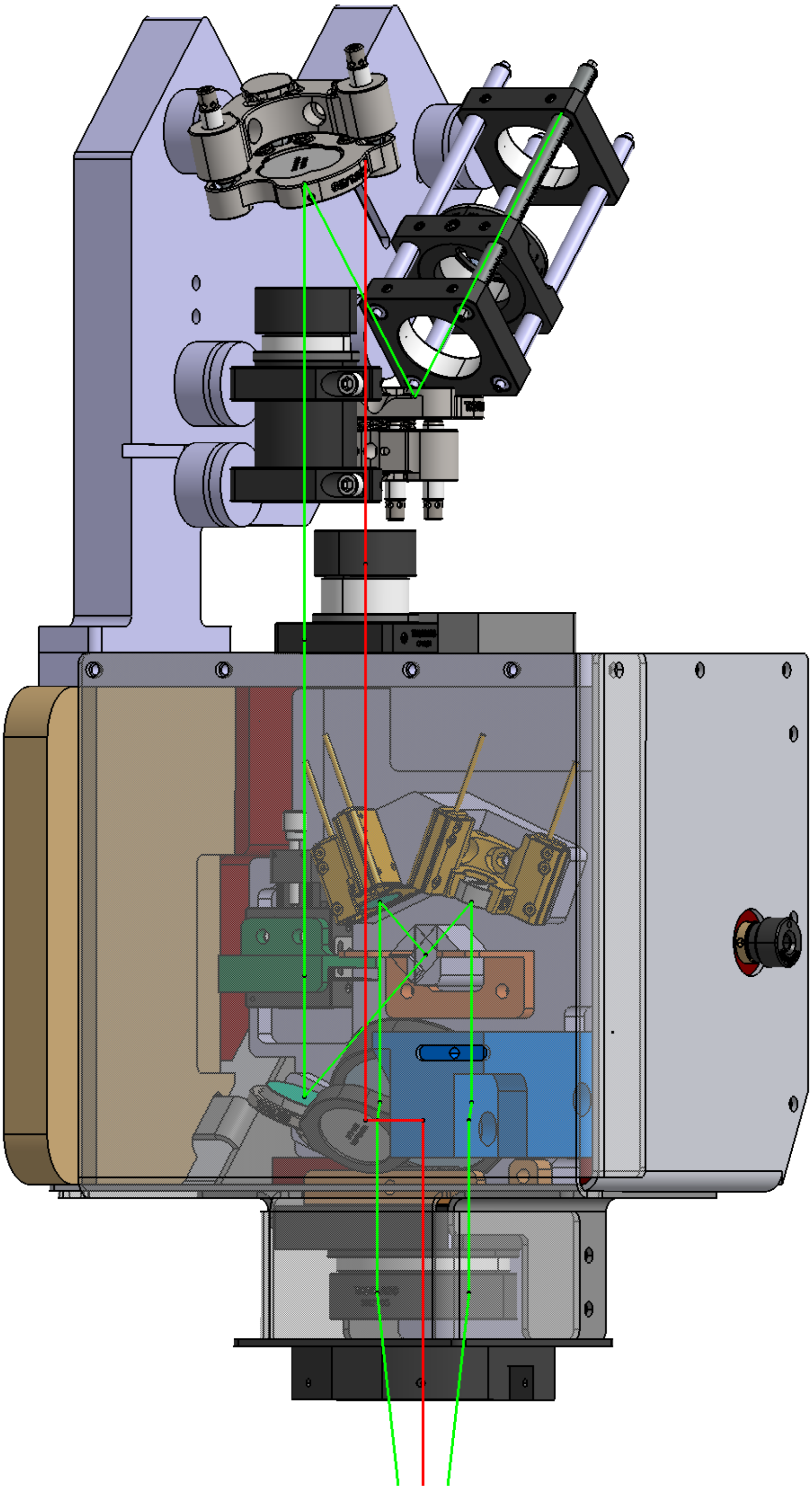

Figure 6.8: Pictures from the CAD-model designed in CATIA: Trapping-Box together with the telescope plate. The path of the 2D Trap beams is depicted as green line. The path of the MOT-beam is drawn as red line and overlaps most of the time with the path of the imaging-beam shown as yellow line.

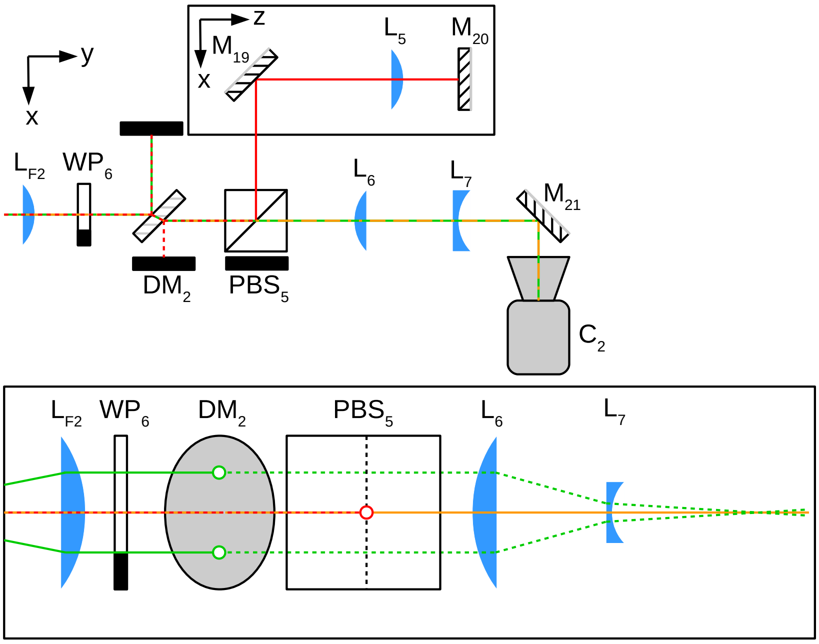

Figure 6.9: Imaging setup: Considering the 2D Trap beam path, the two 2D Trap beams depicted in green are collimated by L_{F2} to two parallel beams. Most of the beam power is reflected at DM_2 to a beam dump, and only a small fraction transmits. The horizontally polarized 2D Trap beams pass PBS_5 and are focused by $L_{6,7}$ on camera C_2 to form there an enlarged image of the 2D Trap intensity distribution. The collimated MOT-beam is focused by L_{F2}, and WP_6 changes its polarization from circular to vertically linear polarization. Subsequently, the MOT-beam is reflected by PBS_5 to a side path. Here, the MOT-beam is again collimated by L_5 and retro-reflected by mirror M_{20}. The imaging-beam is also focused by L_{F2} and passes straight the polarizing beam-splitter cube PBS_5 because of its horizontally linear polarization after WP_6. The lens system $L_{6,7}$ diverges the imaging-beam to create an enlarged absorption image of the atoms on camera C_2.

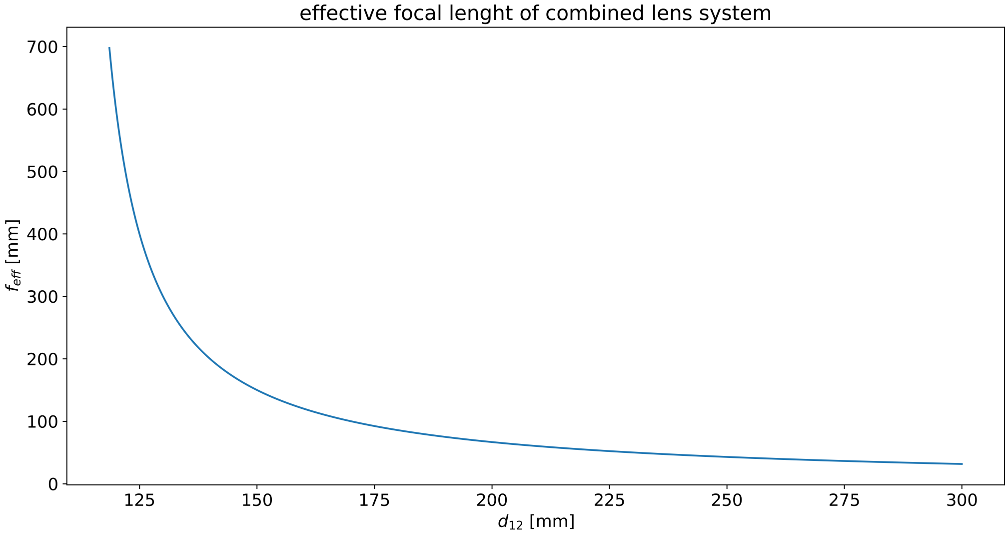

Figure 6.10: Effective focal length f_{eff} as function of distance d_{12} between the two combined lenses which form one effective lens.

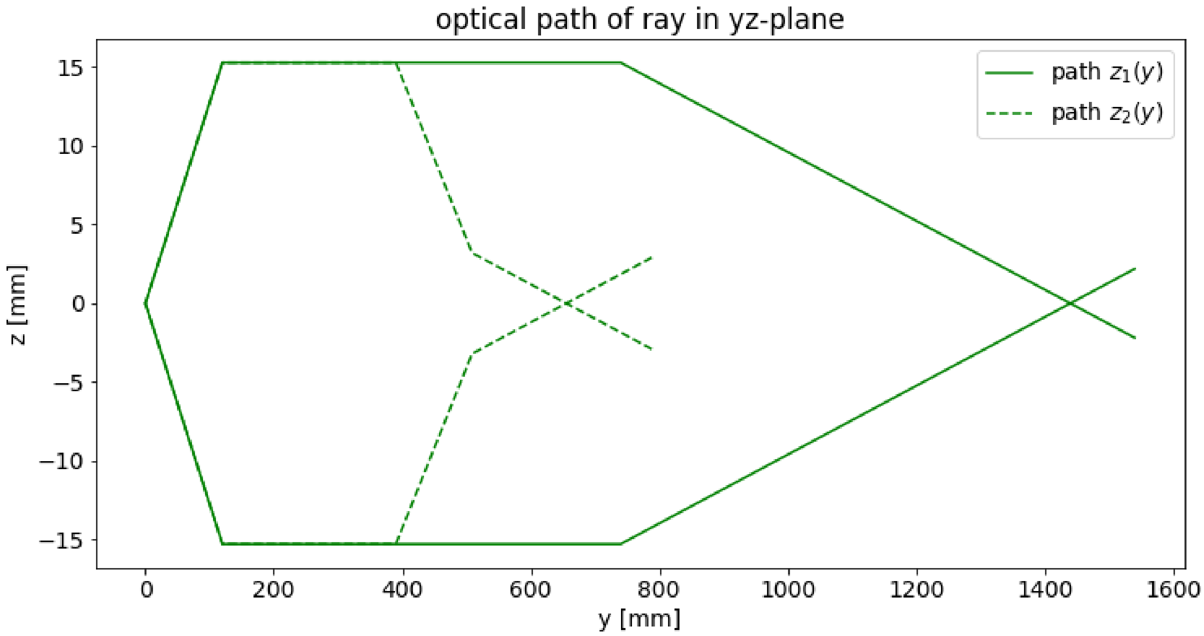

Figure 6.11: Ray trace of the two 2D Trap beams along the imaging system. The solid line shows the first configuration in which the imaging system is formed by L_{F2} and one single lens L_{6+7} with focal length $f_{6+7} = 700$ mm. The total optical path from the real trap to the trap image is for the first configuration: $d_{tot,1} = 1440$ mm. The dashed line shows the second configuration in which the imaging system is formed by L_{F2} and the two lenses $L_{6,7}$ with an effective focal length $f_{(6,7)} \approx 700$ mm. Here, the total optical path from the real trap to the trap image is: $d_{tot,2} \approx 655$ mm.

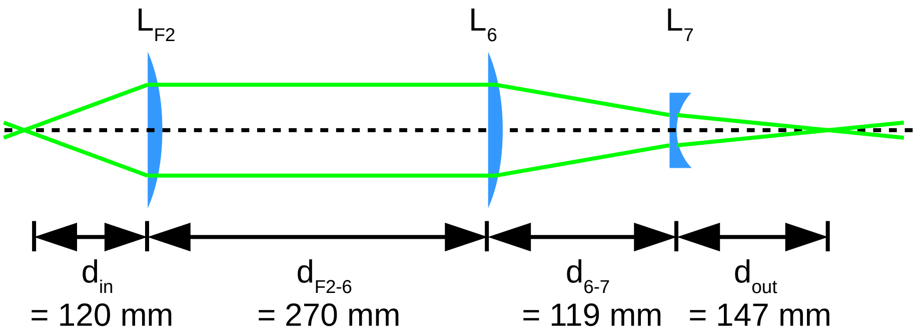

Figure 6.12: Sketch of the imaging system consisting of L_{F2}, L_6, and L_7 for the 2D Trap beam path which is depicted as green lines. Below the expected relative distances from the ray trace calculation are added.

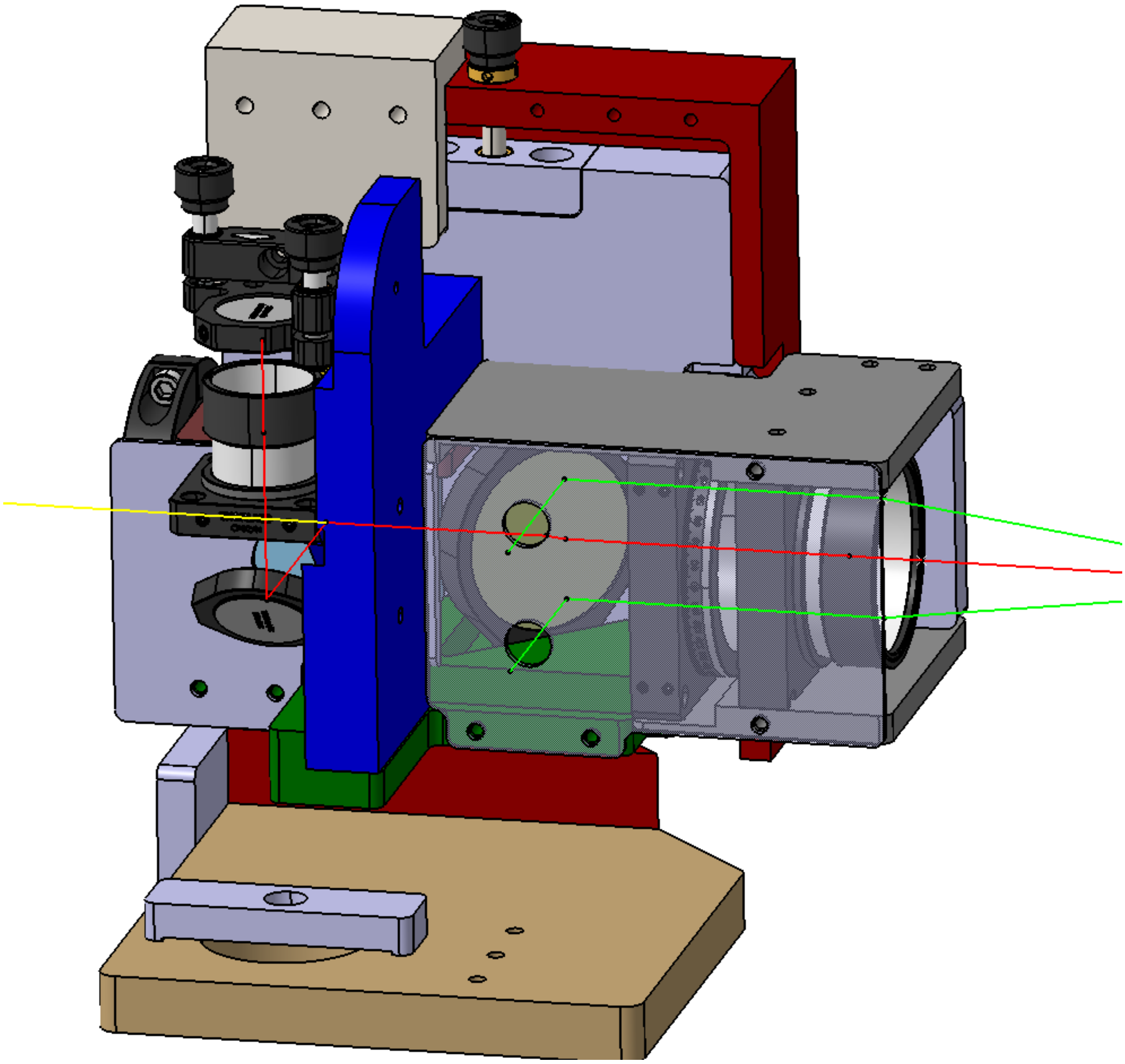

Figure 6.13: Pictures from the CAD-model designed in CATIA: three-dimensional front view on the Imaging-Box. The path of the 2D Trap beams is depicted as green line. The path of the MOT-beam is drawn as red line and overlaps most of the time with the path of the imaging-beam shown as yellow line.

7 Installation and alignment

This chapter considers the main steps to install and align the full setup described in the last chapter until it is ready to be used.

7.1 Pre-alignment setup

In order to be able to check the trap parameters directly in the trap plane where later the vacuum chamber was to be positioned, the whole setup was built up on a separate optical table. After this pre-alignment step the rough position of all lenses: L_z,L_{xz},L_x, and L_F could be fixed as they are all connected to the Trapping-Box, which later can be transported as a whole. In this step the uncollimated version was chosen where the distance of L_F to the single-beam foci should be about 126 mm. As the single-beam foci and the crossing point later have to be aligned on the atoms, the precise position especially of L_F could not be fixed. Besides, the height of the Trapping-Box and the height of the Imaging-Box were adjusted such that the central optical axis was about 10.0 cm above the optical table, which corresponds to the height of the centre of the experimental chamber and therefore to the expected height of the atoms. An important remark concerning the height adjustment: One has to unlock all five screw nuts for both boxes individually before turning the micrometer screw at the top of each box. After changing the height, the vertical boards have to be fixed by the five screw nuts again. To measure the height, it is useful to focus on the edge of the cage-mount (Thorlabs: LCP08/M) in which the lens tube for the lens L_{F1} and L_{F2} is fixed. Here one has to take care because the edges are changed by the workshop. The distance from the top edge to the centre of the mount is about: 30.0 mm.
One advantage of the pre-alignment configuration is that the parallelism of the 2D Trap beams can be adjusted while removing L_{F1} and observing the constant distance between the beams of about $31.88 \approx 32$ mm in the far field about 1 m away. In this way, also the mirrors $M_{11,12,14,15}$ were roughly pre-aligned.
In addition, $FC_{4,5}$,PBS_4 and $M_{16,17}$ are mounted on a fixed cage-system which could be connected with the Trapping-Box via the lens tube mount for L_4. All other elements were built up but could not be transported as a whole to the final experimental setup.
The trap intensity distribution could directly be observed with a small pixel-size Raspberry Pi camera (pixel size: 1.12 μm) which can be seen in figure 7.1 compared to the theoretical prediction in figure 7.2 which matches qualitatively. However, the precise trap parameters were only roughly adjusted with: $W_{0z} \approx 22$ μm and $W_{0x} \approx 151$ μm leading to an ellipticity of: $E \approx 6.9$. The beam widths can be extracted from fits to the one-dimensional intensity distributions which follow from a sum along each individual axis of the image. Therefore, the image is rotated before the summation of about $-0.6°$, such that the interference pattern is clearly visible along the vertical axis of the image. One

has to remark that, for the interpretation of the Raspberry Pi camera images, one has to convert the Bayer RGGB-pixel-pattern into the usual RGB-pixel-pattern before fitting the intensity distributions along each axis. Each RGB-element can be summarized to one intensity value.

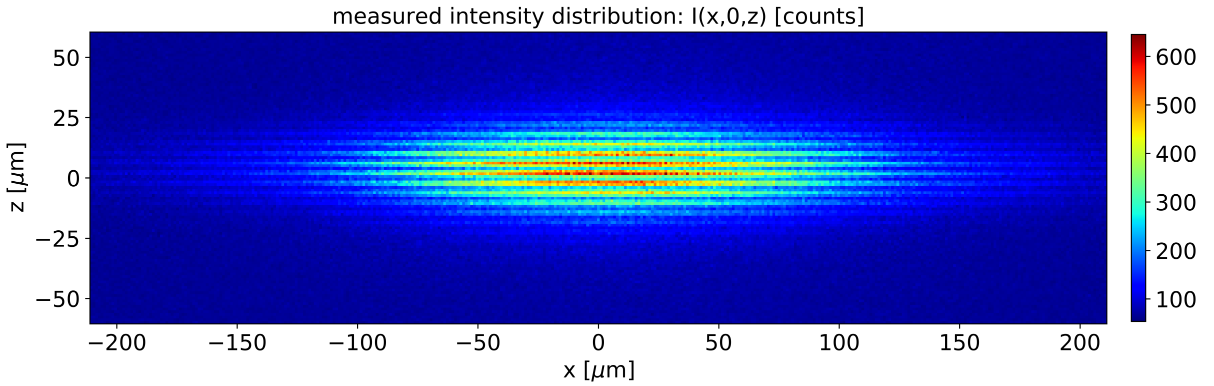

Figure 7.1: Measured intensity distribution of the 2D Trap in xz-plane in the pre-alignment setup with $W_{0z} \approx 22$ μm and $W_{0x} \approx 151$ μm.

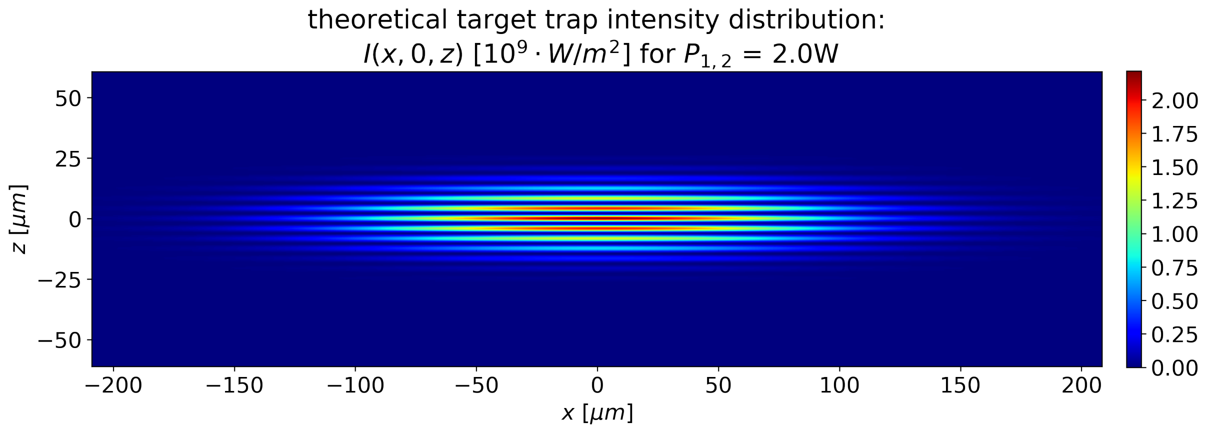

Figure 7.2: Theoretical prediction of the intensity distribution of the 2D Trap in xz-plane for $W_{0z} = 17$ μm, $W_{0z} \approx 133$ μm and $\theta = 7.3°$.

Furthermore, the MOT-beam can be collimated with a shearing plate at the fibre-coupler output and the Trapping-Box output. The polarization of the MOT-beam can be adjusted by the orientation of WP_5. As reference, one can use the original orientation of the polarization of the MOT-beam from the old fibre out-coupler in the experiment. One can connect a polarizing foil on the back side of a 1/2-inch-sized rotation mount in which a $\lambda/4$-wave-plate is fixed. The relative orientation between the two components has to be fixed such that the output power of the MOT-beam behind is minimal for the right polarization. With this tool, one can minimize the output power of the MOT-beam from the Trapping-Box visible at its output behind L_{F1} by rotating WP_5 appropriately. In the Imaging-Box WP_6 has to be rotated such that the MOT-beam is reflected at PBS_5 to the side path.

7.2 Laser setup

As the structure of the laser setup has already been described, the following description should focus on the detailed alignment steps and successes. The main duty of the laser setup is to provide a clean linearly polarized infrared laser beam with a single Gaussian mode selected by a high-power fibre, together with a large laser power range. This is a quite difficult task because the alignment has to be done such that it is stable enough over the whole, or at least a large, power range. Therefore, in a first step, the laser was characterized over nearly the whole power range with a beam profiler. During this measurement, the FC_1 was not inserted into the setup to be able to observe the laser beam in the far field up to 2.5 m away from the laser output. Also, the AOM and polarization cleaning optics were still not set up. Besides, it was necessary to insert two additional mirrors between M_1 and L_1. The first mirror reflects most of the laser power to a beam dump and the second one corrects the horizontal shift of the first one to produce an unchanged beam with a much lower power, as sketched in figure 7.3. The characterization of the output beam was executed without the telescope including the lenses $L_{1,2}$ and is shown in figure 7.4.

So, one can conclude that the infrared laser (ALS) is not collimated by itself as its focus is not directly at its output but about 1.4 m away with a relatively small minimal beam width of about 400 μm. Apart from that, one can observe that the beam profile shape corresponds not to a pure Gaussian shape over about 1.3 metres starting from the laser output. Afterwards, the beam profile shape gets better with increasing distance and the shape gets also a little bit better with increasing power. In this context, one has to remark that the input cable to the ALS-laser has to be less curved to minimize the effect of the non-Gaussian shape of the output beam.

As the beam has to be collimated for the AOM and also for the coupling into the high-power fibre, a telescope was setup to change the beam shape appropriately. To optimize the coupling into the fibre, the telescope was chosen such that the minimal waist occurs near the position of FC_1 after about 1 metre from the laser output and with a minimal waist of about 660 μm. This minimal waist corresponds to the expected output properties of the fibre coupler with a mode field diameter of about 8.2 μm and a collimating lens of focal length $f = 8$ mm. The expected output beam width was calculated with Gaussian beam matrices. Fortunately, the beam waist stability after the modification with the telescope was observed to be quite stable also for different powers. At a distance from the laser of about 2.5 m the beam width was nearly constant for different powers with around: $2W_x \sim 2050$ μm and $2W_y \sim 2200$ μm compared to an expected beam size at this distance of about $2W \sim 2700$ μm. The minimal beam width near FC_3 was observed to be $2W_0 \sim 1300$ μm at a power of $P \sim 35$ W.

Afterwards, the AOM was aligned such that the first diffraction order was optimized in power. The AOM driver board setup was adjusted such that the output amplifier for the AOM had an amplitude of about $V = 32.5$ dBm $= 1.78$ W. This can be increased to $33.5 - 34$ dBm $= 2.2 - 2.5$ W in the future where the maximum of the diffraction efficiency occurs. However, one has to take care because, for higher input amplitudes, a strong heating of the AOM was observed. The input frequency was adjusted to $\nu = 109.78$ MHz near the specified frequency of about 110 MHz. With this configuration, the

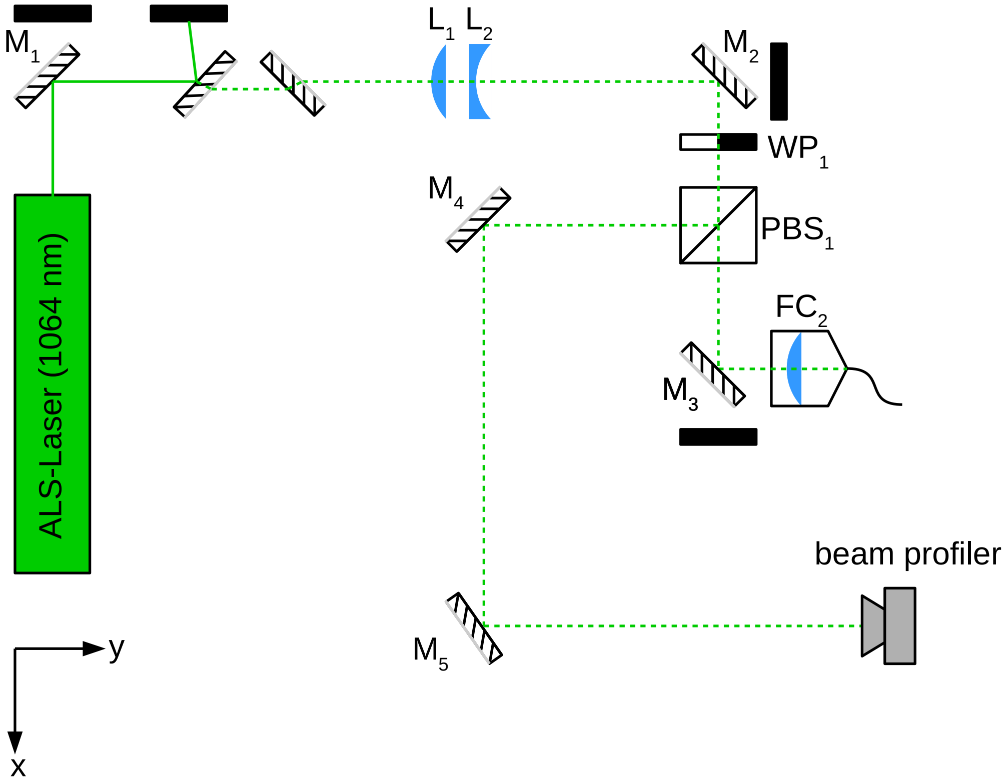

Figure 7.3: Laser alignment setup: Two additional mirrors after M_1 are inserted which distribute most of the beam power to a beam dump. The small fraction of the beam transmitting through the mirrors can be analysed with a beam profiler. The lens pair $L_{1,2}$ acts as a telescope to collimate the laser beam. PBS_1 splits the beam into two arms. The arm ending with the beam profiler is used for the 2D Trap setup.

observed diffraction efficiency (DE) was at $P = 0.12$ W $\Longrightarrow DE \sim 89\%$ and for $P = 10$ W $\Longrightarrow DE \sim 94.5\%$. Besides, one has to remark that there appear polarization drifts for the output beam from the AOM which are probably caused by heating effects after the AOM is turned on. The polarization drift slows down after the first hour when the heating equilibrates. So, this effect can cause power fluctuations after the cleaning cube PBS_2. It is recommendable to wait at least 15 min after turning on the AOM before starting with reliable and stable experiments.

Finally, one has to couple into the high-power fibre also at high powers of about $P \sim 10$ W. To do this, the $\lambda/2$-wave-plate can be orientated such that the laser power distributed to port 1 is minimized and an absorptive filter between PBS_1, and M_4 can further decrease the power. In this way, the coupling efficiency can be optimized also for different beam shapes at high beam powers, and the fibre is not damaged during the coupling schema. One possible fibre coupling procedure can be executed as follows: Initially it follows the

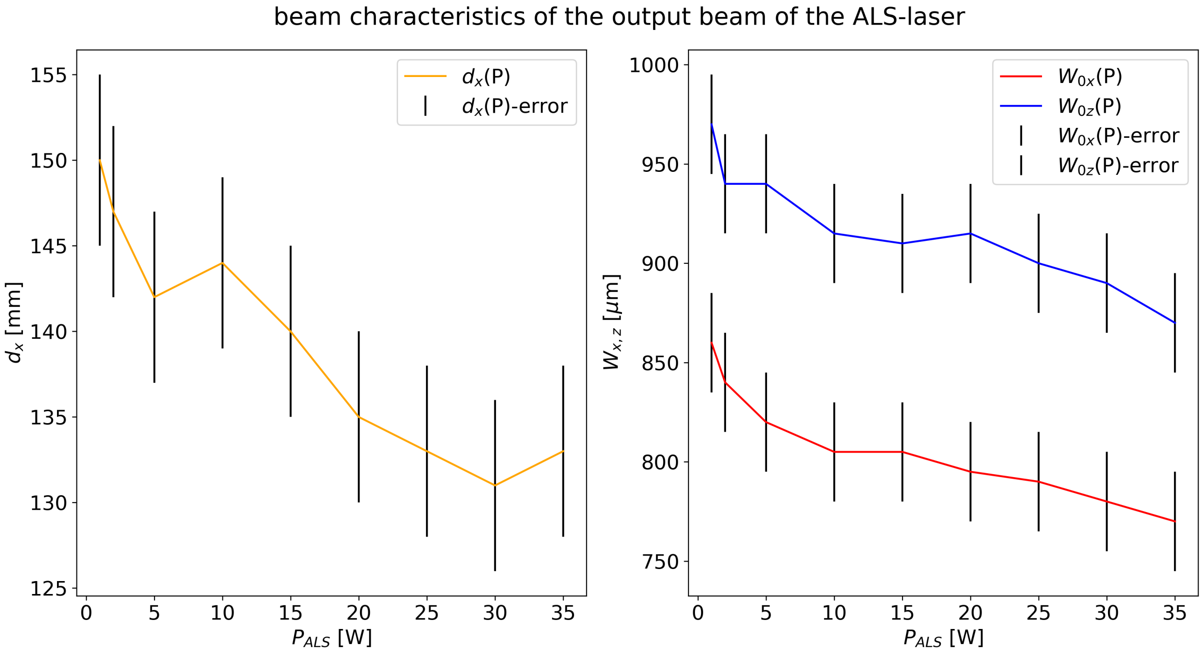

Figure 7.4: Measurement of the laser beam properties for different laser powers without the telescope consisting of $L_{1,2}$. The beam focus position $d_{focus,(x,z)}$ relative to the laser output position is visible on the left. The minimal beam widths $W_{(0x,0z)}$ at this focus position in both elliptical beam axis x and z are depicted on the right.

usual pre-collimation of the two fibre couplers $FC_{1,2}$. Afterwards one can couple a little bit of light into the second port FC_2 connected with the high-power fibre. Then one can connect the other end of the fibre with port 1 at FC_1. Here one has to take care that the beam is not guided directly back to the laser. This can be reached by rotating the polarization about 90° once in the fibre. So the fibre key is vertical at port 2 but horizontal at port 1. This configuration enables to overlap the ingoing and outgoing beam at port 1 matching with the used fibre characteristics. On top of that, also the collimation of the fibre coupling lens FC_1 can be checked and optimized with this schema. The coupling efficiency (CE) at $P \approx 10$ W was measured to be about $CE \approx 88\%$. An additional remark has to be made concerning the fibre locking polarization key because it was realized that it was not properly aligned during the fabrication. This leads to the fact that the fibre is not polarization-maintaining while heating effects occur. This can cause strong power fluctuations behind the cleaning cube PBS_3. The problem can be fixed by adjusting the $\lambda/2$-wave-plate (WP_3) properly, such that the input polarization matches the polarization-maintaining axis of the fibre when the fibre is locked in FC_1. This alignment can be executed by heating the fibre recursively with a warm human hand and minimizing the power drift observed after PBS_3.

7.3 Trapping setup

To insert the trapping setup, first the old imaging-beam and MOT-beam out-coupler were removed, and one of the posts holding the breadboard construction had to be carefully moved to create enough space for the Trapping-Box. In a first step, the vacuum view-port window was cleaned and the protection blind was fixed on the vacuum flange for the view-port window.

Everything which is directly connected to the Trapping-Box could be transported as a whole from the pre-alignment setup to the final experimental setup, meaning all components of the trapping setup beginning with L_z in the infrared beam path and starting with $FC_{4,5}$ in the resonant light path. Fortunately, the blind is constructed such that it offers a large stopper surface at which the Trapping-Box can be pushed. The rough orientation of the Trapping-Box in the xy-plane of the optical table could be found by the orientation of the MOT-beam because in the pre-alignment setup the out-coupler FC_5 was directly connected to the Trapping-Box over the cage-system. The MOT-beam could be pointed to the old MOT-out-coupler on the other side of the experimental chamber. In this way the Trapping-Box was roughly aligned on the optical axis of the according view port.

Besides, in a next step, the two resonant light out-couplers $FC_{4,5}$ were mounted on adjustable kinematic mounts separately from the cage system connected to the Trapping-Box to be able to guide both beams optimally through the optical setup.

First of all, the MOT-beam was aligned to fit through the cage system, L_4, and especially through the small half-inch large $\lambda/4$-wave-plate, using the FC_5-mount degrees of freedom and those of the mirror mounts for $M_{16,17}$. Here one has to take care that the large beam is not cut by a mirror edge in the cage-system, such that at least the main part of the beam stays untouched. One has to remark that it was not possible to guide the MOT-beam optimally through the cage-system and centrally through L_4 at the same time. Because of this reason the MOT-beam was adjusted to travel a little bit off-centred through L_4.

In a second step, the imaging-beam was overlapped with the centre of the MOT-beam only using the degrees of freedom of the adjustable mount for FC_4.

In a next step, the other optical components of the trapping setup were built up. The out-coupler FC_3 was collimated to a beam diameter of about $2W \approx 1020\ \mu$m at a distance of 5 cm and a beam diameter of $2W \approx 1660\ \mu$m at a distance of 1 m. The height of the beam from the out-coupler was adjusted to be about 57.6 mm above the optical table because this height corresponds to the height of an optimal beam entering the Trapping-Box, assuming the optical axis for the output of the Trapping-Box is adjusted to 10.0 cm above the optical table by the micrometer screw at its top. The orientations of the mirrors M_7 and M_8 were used to guide the infrared beam at the right orientation into the already fixed Trapping-Box setup starting with lens L_z. In this way, it was not necessary to change the orientation of the other mirrors, fixed in the pre-alignment setup. The positions of FC_3 and $M_{7,8}$ were chosen such that the distance between FC_3 and L_z corresponds to the target value of about 400 mm. One has to take care to hit all lenses centrally and also especially the small 1/2-inch-sized mirrors $M_{14,15}$. For a precise adjustment of the beam into the Trapping-Box, one has to use the alignment plate with the two 1 mm large holes at a distance of about 32 mm to reach a configuration of two parallel beams between the mirrors $M_{14,15}$ and the dichroic mirror. One can use the two mirrors $M_{7,8}$ to walk the input beam trough the two small holes until the output power is maximized. Finally, a first rough alignment of the Trapping-Box is achieved after checking that the two infrared trapping beams travel freely through the experimental chamber and exit on the other side without touching the view-port flanges or the blind. The polarization of the MOT-beam can be adjusted by the orientation of WP_5. This was already done in the pre-alignment setup but can be checked again with the described tool.

7.4 Imaging setup

Now, also the Imaging-Box has to be inserted into the setup. After removing also the other old MOT-out-coupler, the whole Imaging-Box was moved towards the opposite view port. Here, no protection blind was necessary. The distance of the Imaging-Box along the optical axis from the experimental chamber was adjusted such that the two infrared 2D Trap beams are collimated to two parallel beams until about 1 m away till the wall of the laboratory room. To guarantee the axial orientation of Trapping-Box in the xy-plane of the optical table, the main part of the two trapping beams has to be reflected orthogonally from the dichroic mirror, and the imaging-beam has to travel unchanged through the optical elements of the Imaging-Box. The overlap of the optical axis of the Imaging-Box with the optical axis of the view port of the experimental chamber can also be reached qualitatively by eye. One can add a mark on the bottom plate of the Imaging-Box and bring this mark on the same line starting from one edge of the octagon when watching to the view port. After the position of the Imaging-Box is fixed, the axial position of L_{F2} can still be tuned such that the two infrared axial output beams from the Imaging-Box are really parallel.

Afterwards one can adjust the position of lens L_5 in a way, that the retro-reflected MOT-beam has the same size as the outgoing beam, visible between PBS_5 and M_{19}. After this procedure the beam should be collimated at mirror M_{20}, which can be checked by shortly removing the mirror M_{20}. The $\lambda/4$-wave-plate for resonant light can be oriented such that the imaging-beam can pass straight along the view-port axis and the MOT-beam is orthogonally reflected at the polarizing beam splitter PBS_5. For the alignment of the retro-reflected MOT-beam one has to adjust M_{20} to guide the beam through the small $\lambda/4$-wave-plate mount WP_5 in the Trapping-Box on the other side. Especially between lens L_4 and mirror M_{18} one can see the overlap of the ingoing and retro-reflected MOT-beam very precisely, because there lies a tight focus between L_4 and L_{F1}. This spot can easily be exploited for the alignment procedure.

After the MOT-beam is aligned, one can start loading atoms into the magneto-optical trap to test the precision of the adjustment. The MOT-cloud has to be moved to the expected position of the crossed beam dipole trap. This can mainly be achieved by adjusting the MOT coil currents such that the trapped atom number is maximized. Subsequently, the transfer to the optical dipole trap can be optimized. Here one can carefully adjust also the ingoing and the retro-reflected MOT-beam by scanning all degrees of freedom of the MOT-out-coupler and M_{20}.

Finally, the imaging setup has to be completed by setting up $L_{6,7}$, M_{21}, and C_2. First, the imaging-beam is aligned on the Trapping-Box side using the adjusters at the out-coupler

FC_4. The imaging-beam has to go straight through the Imaging-Box at a constant height of about 10.0 cm over the optical table. One can also check if the imaging-beam lies directly in the centre between the two 2D trap beams behind the Imaging-Box as well as the MOT-beam which can be guided temporally in this direction by rotating the $\lambda/4$-wave-plate WP_6. In a further step, the two lenses L_6 and L_7 can be added one after the other at the right distances. One can check that the imaging-beam is unchanged and central on the two lenses. For this purpose, the position of the imaging-beam can be marked in the far field on the wall of the laboratory. To adjust the precise magnification of the imaging-setup formed by $L_{6,7}$, one has to change the axial position of L_7 to reach an image of the 2D Trap within a reasonable distance at the camera position a few centimetres away. The actual magnification can be measured by the comparison of the layer spacing in the trap image d_{image} with the expected layer spacing in the real trap $d_{real} \approx 4.2$ μm:

$$M = \frac{d_{image}}{d_{real}} \tag{7.1}$$

7.5 Precise alignment of the imaging-beam

The imaging-beam is diverging after L_7 to create a much enlarged absorption image of the atoms (figure 7.5). Therefore, it is challenging to align the image of the atoms on the camera chip of C_2. As a remark, one can find a quantitative estimation of the beam width of the imaging-beam along the optical path in the appendix.

7.5.1 Alignment of the imaging-beam on camera C_2

In a first step, one has to guide the imaging-beam onto the camera C_2. Therefore, one can check that the imaging-beam really travels centrally through each lens L_6 and L_7 individually at a constant height of about 10.0 cm above the optical table. The beam orientation should not be disturbed by the lens system leading to a constant position of the beam at the laboratory wall behind the Imaging-Box. One can use a round 2-inch-sized piece of paper with central hole to find the central orientation of the beam to lens L_6. Afterwards the imaging-beam has to be guided with M_{21} onto the camera by scanning both degrees of freedom of the mirror mount.

7.5.2 Alignment of the imaging-beam on the atoms

After loading atoms into the magneto-optical trap and later transferring them into the dipole trap, the orientation of the MOT-beam can also be used to align the imaging-beam on the trapped atoms. So one has to decrease the MOT-beam diameter with an iris between M_{16} and M_{17} step-wise to gain increasing precision, such that one can still observe atoms localized in the magneto-optical trap. Then, one has to align the imaging-beam co-propagating with the MOT-beam. By rotating temporally the $\lambda/4$-wave-plate for resonant light WP_6, one can observe the MOT-beam and imaging-beam simultaneously behind the Imaging-Box.

Now, one can check if the imaging-beam hits the atoms with the already aligned camera C_3 watching from the top. In the target configuration, the imaging-beam shoots out

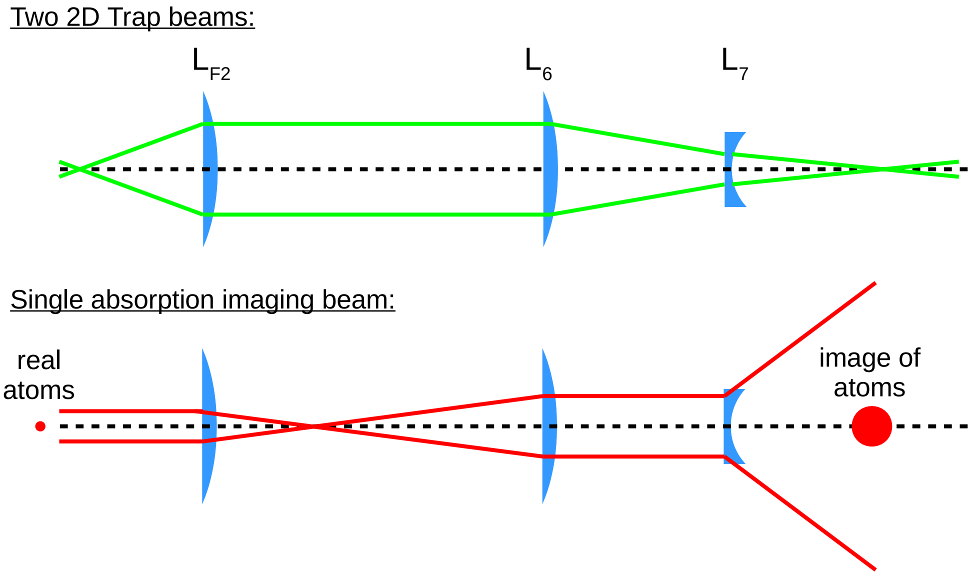

Figure 7.5: Beam paths of the 2D Trap beams in green and the imaging-beam in red through the imaging system created by L_{F2}, L_6, and L_7. The imaging system on the right side creates an enlarged image of the 2D Trap visible at the top and an enlarged absorption image of the atoms shown at the bottom.

the atoms trapped in the dipole trap after evaporation. Therefore, one has to construct a sequence in which the imaging-beam is pulsed on for variable temporal pulse length after the evaporation. To hit the atoms in this sequence with the imaging-beam, the two angular degrees of freedom and the height of the out-coupler mount for FC_4 have to be scanned. In each step, the remaining atom number has to be minimized after decreasing the illumination time further. To increase the alignment precision further, also the total intensity of the imaging-beam can be decreased. Finally, the atom number was minimized for an illumination time of about 0.002 ms.

7.5.3 Alignment of the atom image on camera C_2

After this step, one has to repeat the full alignment of the imaging-beam on the camera C_2. This means that one has to remove the two lenses L_6 and L_7, draw a new mark on the laboratory wall behind the Imaging-Box, and optimize the alignment again.
It might be helpful to use the absorption image of the atoms in the Feshbach-MOT to align the atom image on the camera. One probably needs some iterations of the alignment on the atoms and the alignment of the atom image on the camera C_2. Finally, one can use the absorption image of the atoms in the dipole trap as orientation to move camera C_2 to the right axial position in order to image the atoms in their focal plane.

7.6 Precise alignment of the 2D Trap beams

7.6.1 First alignment tests

As the camera C_2 is now aligned on the atom image, one can use it as first hint for the alignment of the 2D Trap beams on the atoms. In order to do that, one can use the two mirrors $M_{14,15}$ which are controlled via a computer software although this destroys the pre-alignment. Channel 1 controls the bottom beam and Channel 2 the top beam. Axis 1 can be used for the vertical direction and axis 2 for the horizontal direction. In this way, the 2D Trap beams can be moved on the position of the atom absorption image on the camera chip. While observing the 2D Trap beams on the camera, one should add a 40 ND absorptive filter before the camera to protect the camera chip from the focused infrared beams. Besides, one has to take care that the 2D trap beams do not hit the protection blind on the Trapping-Box side or the view-port flange on the Imaging-Box side and travel undisturbed to the camera chip. This first test allows to estimate how far the alignment in the Trapping-Box is away from the ideal configuration.

Now, one can start to align first one single beam on the atoms while the other beam is shifted to the edge of the camera chip of C_2. To find the atoms with the single 2D Trap beam, one has to scan the region of the atom absorption image of the dipole trap on camera C_2. To simplify the search, one can let the atoms in the dipole trap expand before turning on the 2D Trap beams. To find the right configuration, one has to choose a small enough step size resolution for the adjustment of the piezo mirror mounts with about ≤ 10 and amplitude 35. The success of the alignment can be observed on the two other cameras C_1 and C_3. C_1 can be exploited for the alignment of the single beam in vertical axis, and the perspective of C_3 can be used for the alignment of the single beam in the horizontal direction. To guarantee that the single-beam focus dominates over the magnetic trap, the beam power of the infrared ALS-laser should be adjusted to $P \geq 5$ W. After the alignment of the first beam is completed, this beam can be blocked in front of the experimental chamber and the second beam can be separately aligned on the atoms in the same way. Finally both beams can be observed at the same time, crossing each other at the atom position.

In addition, one can observe the position of the single-beam foci of both beams separately. If the focus is off-centred with respect to the atoms, one expects that the trapped atoms oscillate along the beam. By measuring the oscillation frequency one gets an optimization observable because the oscillation frequency has to increase if the atoms are trapped at a smaller distance from the single-beam focus. To change the position of the single-beam focus, one has to change the axial position of L_{F1}. One rotation of the adjustable lens tube corresponds to 0.625 mm. So for the scan, one should use a step size which is smaller or equal to one rotation. If necessary, one might want to add or remove one or two of the retaining rings in the lens tube which define the actual distance of the lens L_{F1} from the atoms.

7.6.2 Optimized alignment procedure of the 2D trap beams on the atoms

However, the alignment schema described above does not guarantee that the two 2D Trap beams hit the lens L_{F1} parallel and orthonormal. If this was not the case, it was for example observed that the two single-beam foci did not overlap and the foci itself were not strong enough. For the shape of the beams, the image on camera C_2 is a good observable. On top of that, as previously described, in a lens position configuration in which non-collimated beams hit the lens L_{F1}, the positions of the single-beam foci do not correspond to the position of the crossing point although the beams hit the lens L_{F1} parallel and orthonormal. So, in this scenario one is forced to guide the beams non-parallel on L_{F1} to overlap the single-beam foci with the crossing point. The non-orthonormality has to be avoided because it can produce strong aberrations even for small alignment errors. Therefore the following alignment procedure was developed to prevent these errors or at least to minimize them. It was observed that an error of the Trapping-Box height can have a huge effect on the beam quality after correcting the height error by guiding the 2D trap beams non-orthonormal on L_{F1} as sketched in figure 7.6.

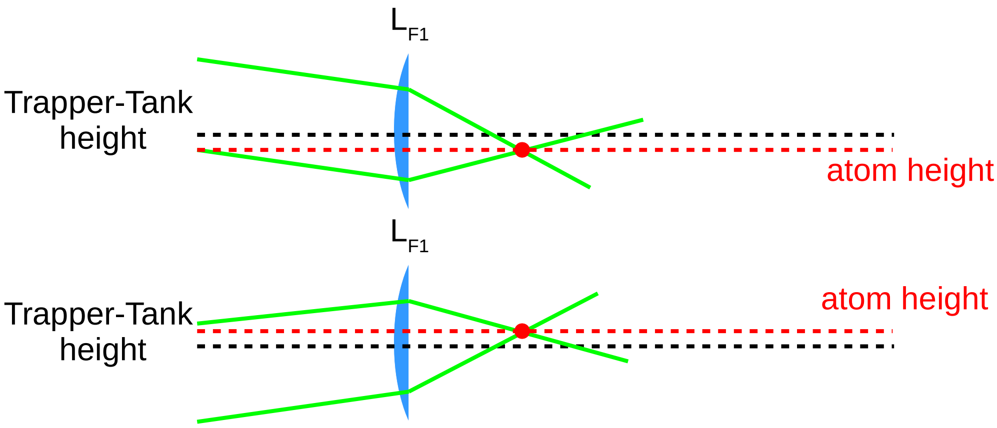

Figure 7.6: Different configurations of non-orthonormal 2D Trap beams in green at the lens L_{F1}. The atoms are depicted in red. Either the Trapping-Box with L_{F1} is higher than the atoms as in the top configuration or lower as in the bottom configuration. The non-orthonormality of the beams with respect to L_{F1} can cause serious aberrations. The two drawn configurations correspond only to estimated scenarios from reasonable expectations. The real beam configurations could not be observed directly.

After the two 2D Trap beams are aligned parallel and orthonormal to L_{F1}, one can directly see by the distance of the beams with respect to the atoms if the Trapping-Box is too high or too low as portrayed in figure 7.7.

By a recursive procedure one can approach the optimal Trapping-Box height.

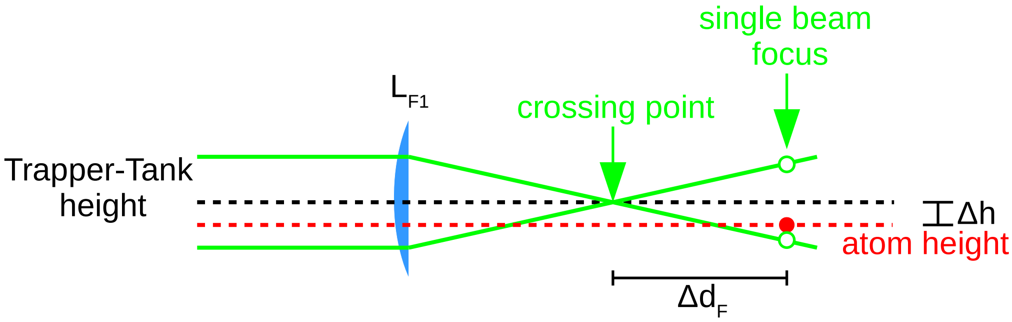

Figure 7.7: Orthonormal 2D Trap beam configuration with respect to L_{F1}: the green 2D trap beams hit the lens L_{F1} parallel and orthogonal after they are focused to the crossing point. The single-beam focus might be displaced relative to the crossing point by Δd_F and there is probably a height difference Δh between the Trapping-Box height and the height of the atom cloud.

Adjustment of the optimal Trapping-Box height and beam orientation to L_{F1}

First of all, one has to align the 2D Trap beams parallel, orthonormally, and symmetrically on the lens L_{F1}. Therefore, one has to keep the position of camera C_2 fixed in the plane of the atom absorption image which will be used as a reference. On top of that, one should remember or mark the position of the 2D Trap beams between the camera C_2 and the mirror M_{21} to simplify the alignment of the 2D trap beams on the camera C_2 later. Now, one has to walk the output beam of the infrared high-power fibre centrally through the lenses L_z, L_{xz}, and L_x as well as through the beam splitter $NPBS_1$ and on the mirrors $M_{14,15}$. To optimize the alignment further, one should use the adjustment plate with the two small 1-mm-sized holes at the expected distance of the two beams of about 32 mm behind the two mirrors $M_{14,15}$. For this purpose, the glass plate GP_1 has to be removed or just inserted after the 2D Trap beam alignment is optimized. It is sufficient to fix the adjustment plate on the vertical board in the Trapping-Box with a single screw in the top screw hole. The laser power through each pin hole has to be maximized. On top of that, one can use the two irises before and behind lens L_{xz} for the alignment. While closing the iris, the elliptical beam has to be cut symmetrically at its vertical edges. Afterwards, one has to mark or remember the axial position of L_{F1} in the lens tube. Subsequently, one can carefully exchange L_{F1} by a 2-inch-sized mirror reflecting infrared light. The mirror should be fixed in an extra tube such that one has to exchange only the lens tube with the tube of the mirror. This is recommendable, because the orientation of the lens in the lens tube can change after fixing it. Besides, one has to take care during the replacement because there is not so much space. Preferable, one should pull the lens tube downwards out after turning it out of the cage plate. After the lens is replaced by the mirror, the two beams can be walked backwards through the whole beam path till the polarizing beam-splitter cube PBS_3. To do so, the two mirrors $M_{14,15}$ have to be used. The overlap of the beams can be checked with a camera at the beam splitter PBS_3, as depicted in figure 7.8. The first overlapping steps in the Trapping-Box can be done with the alignment plate, but for the alignment outside the Trapping-Box one has to remove the alignment plate, and even for the alignment at L_x it is recommendable to remove the alignment plate. If the reflected beams are perfectly overlapping with the ingoing beams, one can replace the mirror again by the lens L_{F1}.

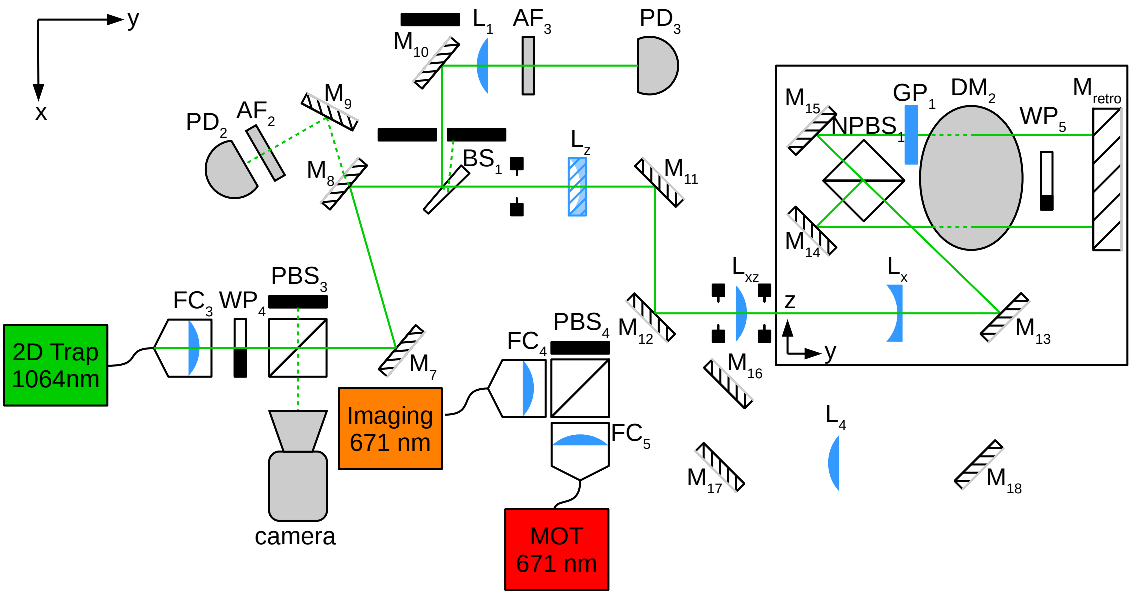

Figure 7.8: Alignment setup to guide the 2D Trap beams orthonormal on L_{F1}: The relevant beam path is the one of the 2D Trap beams drawn in green and starting at the fibre coupler FC_3. The beam is guided through PBS_3, BS_1, L_z, L_{xz}, and L_x and split up by $NPBS_1$. The glass plate GP_1 has to be removed to provide space for the adjustment plate. Finally, the two 2D Trap beams are retro-reflected at mirror M_{retro}. The system has to be aligned such that the two retro-reflected beams overlap with the incoming beams perfectly until their overlap can be checked with a camera in front of PBS_3.

After this alignment procedure, one has reached the configuration described in figure 7.7. So the two 2D Trap beams hit the lens L_{F1} parallel, orthonormal and symmetrically. However, one most probably does not hit the atoms. This can be checked by observing the distance of the 2D Trap beams on the camera C_2 from the atom image position. The horizontal distance can be corrected via the horizontal alignment of mirror M_{12} if the distance is not too large. Otherwise, one has to walk with the mirrors $M_{11,12}$. Importantly, the mirrors $M_{14,15}$ have to be untouched because their configuration was already optimized before. Besides, one most likely observes an error in the height of the beams with respect to the atom position and also in vertical direction. By comparing the distance from each beam to the atoms, one can find out if the Trapping-Box has to be lifted or lowered as it is desired that the distances of both beams to the atom image on camera C_2 are equal. In this context, one has to remember the orientation of the beams along the optical path where the beam positions in the image are inverted compared to the real trap. To check the vertical distance of the two 2D Trap beams from the atom image on C_2, one can use the mirror M_{21} to guide each beam on the camera registering the distance by the number of adjustment rotations to reach that configuration. If the distance of the upper beam to the atom cloud position on the camera C_2 is larger compared to the lower beam, the Trapping-Box height has to be increased. If the distance of the lower beam to the atom cloud position on the camera C_2 is larger compared to the upper beam, the Trapping-Box height has to be decreased. The actual height of the Trapping-Box can be measured most easily at the top edge of the cage plate in which the lens tube for L_{F1} is mounted. The distance from the cage plate edge to the optical axis is 30.0 mm. For example during the alignment procedure which was executed during this thesis, the Trapping-Box height was adjusted to 101 mm above the optical table. So, one measures 131 mm to the cage plate edge. Before turning the micrometer screw, one has to unlock the five screw nuts at the backside of the Trapping-Box.

After the height was changed, one has to repeat the described alignment schema including the exchange of the lens L_{F1} by a mirror recursively. If the height is still not optimal, one has to change it again. This cyclic procedure has to be repeated until the height of the optical axis of the Trapping-Box is sufficiently near the expected height of the atoms in the experimental chamber. For the actual alignment achieved during this thesis, it is expected that the Trapping-Box is still a little bit too high (about one rotation of the micrometer screw: $\sim 250\ \mu$m).

As depicted in figure 7.7, even if the Trapping-Box has the ideal height with respect to the atoms, this does not mean that the 2D Trap beams hit the atoms although they hit the lens L_{F1} perfectly. In this context one has two possibilities. First one can change the axial position of lens L_{F1}. In this way, one can shift the crossing point towards the atom position. A second option for a slightly asymmetric configuration is to use the mirrors $M_{14,15}$. Unfortunately, the last possibility breaks the described alignment success to the degree the mirrors are moved, but this is defensible if the changes are small enough to prevent the appearance of any strong aberrations. If the single-beam focus is not near the crossing point, one has no other possibility then changing the orientation of the mirrors $M_{14,15}$ and the position of L_{F1}, such that the beams cross near the single-beam foci and on the atom position. If the described alignment procedure of the Trapping-Box height was successful, at least the corrections of both beams with the mirrors $M_{14,15}$ are equal. So the single-beam foci appear at the same position along the beams.

7.6.3 Precise alignment of the 2D Trap beams on the atoms

Finally, one needs to align the 2D Trap beams very precisely on the atoms. So first, the position of L_{F1} can be used to move the single-beam foci as closely as possible towards the atoms. It is most convenient to do this with each single beam separately while blocking the other beam with a beam dump. In a second step one has to overlap the individual beams in horizontal and vertical direction perfectly with the position of the dipole trap and later also with the much smaller old and new Microtrap. Here again, one has to transfer atoms into each single beam while blocking the other beam and taking pictures with absorption or fluorescence imaging using the two cameras C_1 for the vertical alignment and C_3 for the horizontal alignment. In order to do that adjustment, the orientations of the mirrors $M_{14,15}$ have to be changed. This is defensible because the changes for the alignment on the atoms are very small and the piezo mirror mounts holding the two mirrors were inserted exactly for this purpose. Here, one really can exploit the fine adjustment resolution of the mirror mounts.

7.6.4 Making the 2D Trap circular

There are several possibilities to make the actual trap circular. Theoretically, this should be perfectly possible with the designed setup, but the possible aberration effects at lens L_{F1} demand also an orthonormal alignment of the 2D Trap beams to L_{F1} which leads to different positions of the crossing point and the single-beam foci. It was observed that after moving the mirrors from the orthonormal configuration to overlap the crossing point with the single-beam foci at the position of the atoms, the single-beam ellipticity decreases. This clearly can be explained with aberration effects.

So, a first procedure to reach circular layers is to optimize the Trapping-Box height as described above and stay with a lens position configuration in which the elliptical single-beam focus in z-direction is near the geometrical crossing point as described in figure 6.7. In this way, one can minimize the correction amount by the two mirrors $M_{14,15}$.

A second schema is to slightly move the two beams apart in x-direction. This increases the effective width of the interference layers in x-direction and increases therefore the effective ellipticity near the crossing point. With this procedure, one can reach a configuration in which the two radial trap frequencies are equal $f_x = f_y$, but the total trap frequencies are lowered. However, if the single-beam ellipticity is too large, meaning $f_x < f_y$, the method is not applicable. The procedure is described in the appendix in more detail.

Thirdly, if there appears a difference of the single-beam focus distance between the two beams, it is better if one aligns the two foci such that one is before the crossing point and one is behind it by moving the lens L_{F1} appropriately. Compared to the configuration in which only one single-beam focus is overlapped with the crossing point perfectly and the other one is far apart, the first configuration is better in the sense of higher intensity and therefore higher trap frequencies and probably higher ellipticity. This result can be achieved by comparing the resulting trap frequencies or just the intensity distributions as described in the appendix.

The three described techniques are illustrated in figure 7.9.

To check if the alignment procedure is successful, one first can use the trap image on cam-

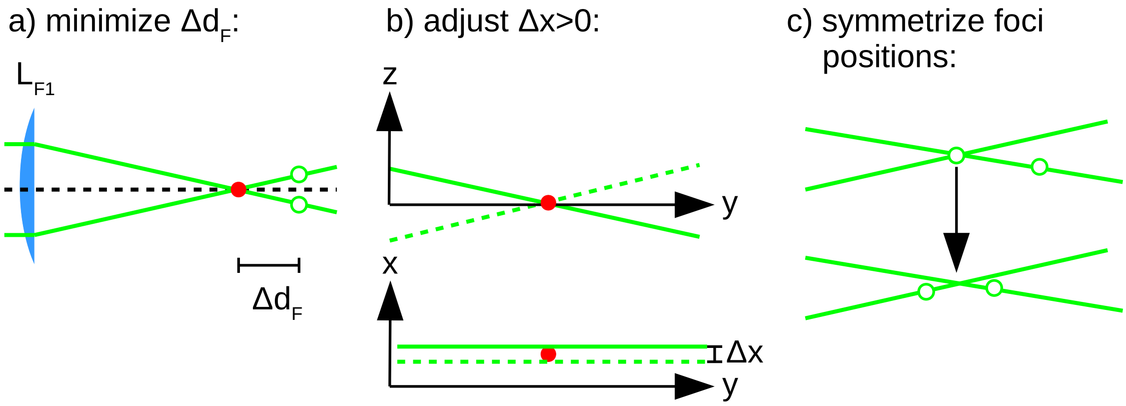

Figure 7.9: Three optimization methods of the circularity of the 2D Trap light sheets: a) minimize the distance between the single-beam foci and the crossing point. b) if the trap frequency in x-direction is too high as it is the case for too low ellipticity of the beams, one can displace the two 2D Trap beams a little bit in x-direction to decrease the trapping frequency in this direction relative to the trapping frequency in y-direction. c) If there occurs a difference in the single-beam foci positions between the two 2D Trap beams one should symmetrize their position around the crossing point to increase the intensity (and the ellipticity) in the crossing region.

era C_2 as reference, but finally one has to compare the actual measured trap frequencies of the real trap in the relevant directions.

8 Characterisation

The following chapter summarizes the most important steps of identifying the characteristic 2D Trap parameters and properties.

8.1 Trap parameters

8.1.1 Measuring the beam widths from the perspective of camera C_2

To measure the beam widths of the two 2D Trap beams, one can simply analyse the trap images on camera C_2, but one has to take care about interpretations because it is only an image of the trap. Besides, one has to block the higher internal reflection orders from the dichroic mirror DM_2 with a beam dump between PBS_5 and L_6. Unfortunately, there appeared an additional interference pattern in the top beam which probably comes from the glass plate GP_1, but the origin could not be identified exactly without intervening too strongly into the setup. However this structure has not a very large effect on the fitting procedure.
To identify the relevant parameters, there were taken three pictures: one for each single beam and one with both beams at the same time. For each image the intensity was summed along the image axis after optimizing the rotation angle for the image. The optimal rotation angle can be found by minimizing the fitted beam width for the intensity along the vertical direction as the beam width in the vertical direction is through the ellipticity smaller than in horizontal x-direction. As fit-model, the function for the full three-dimensional intensity distribution $I_{2D}(x, y, z, P_{1,2}, W_{0x}, W_{0z}, \theta, \Delta\phi)$ was used as origin.

Both beams

In the case of detecting both beams on the camera C_2, the horizontal fit-model has the form:

$$I_{tot,x} = I_{2D}(x = x - x_0, y = 0, z = 0, P_{1,2}, W_{0x}, W_{0z} = c_1, \theta = c_2, \Delta\phi = 0) \tag{8.1}$$

with $c_i > 0$ for an arbitrary positive value because the fitted beam power is not of any relevance and the vertical fit-model can be identified as:

$$I_{tot,z} = I_{2D}(x = 0, y = 0, z = z - z_0, P_{1,2}, W_{0x} = c_3, W_{0z}, \theta, \Delta\phi) \tag{8.2}$$

One can assume an additional offset in both cases, but this was not necessary for the analysed data set and the fit-model above lead to an even more reliable fit result. As

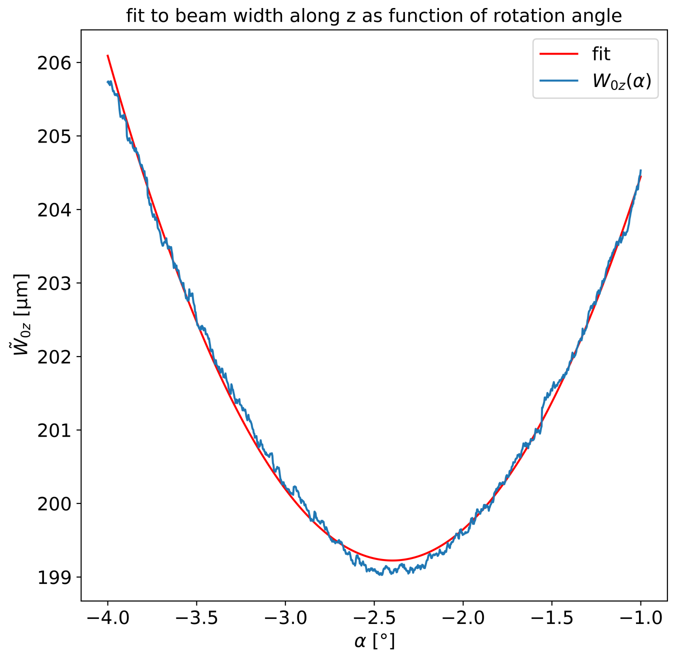

Figure 8.1: Optimization curve of the rotation angle for the measured intensity distribution of the 2D Trap image in xz-plane. The graph shows the fit-results to the beam width in z-direction as function of rotation angle. The curve is fitted by a parabola to identify the optimal rotation angle where the beam width in z-direction is minimal.

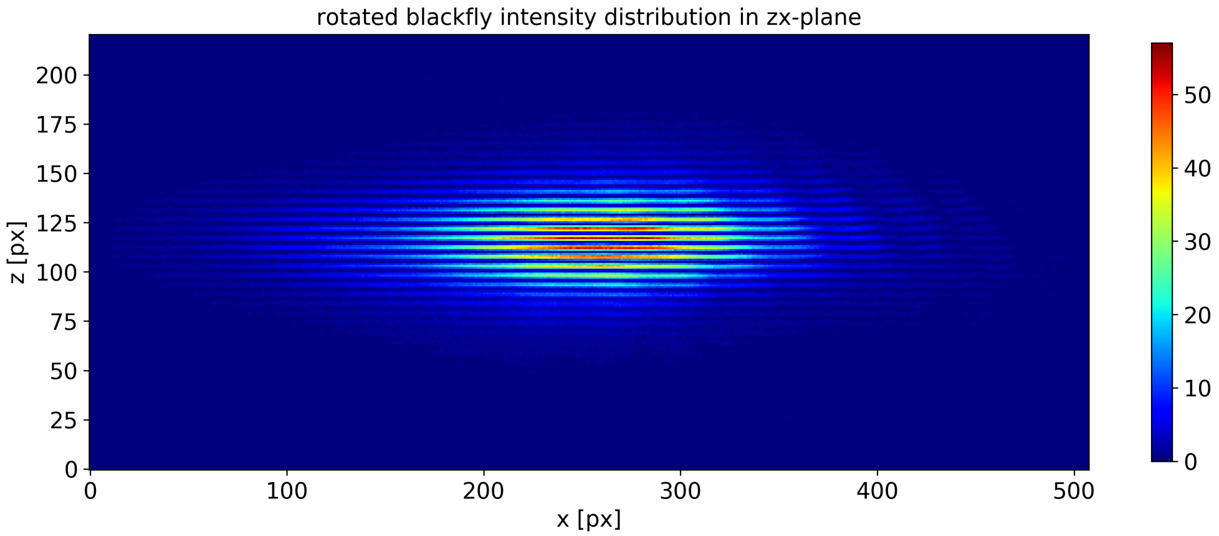

Figure 8.2: Measured intensity distribution of the 2D Trap image in xz-plane rotated by the optimal angle of about $\alpha = -2.4°$.

depicted in figure 8.1, the optimal rotation angle for the image is $\alpha = -2.4°$ leading to figure 8.2, after cutting and rotating the original image.
Afterwards one can sum the two-dimensional array of the image along the two axes individually and fit the two intensity distributions with the described fit-models to the one-dimensional data sets. On top of that, one can insert a pixel size of the camera C_2 of 5.86×5.86 μm. The resulting fits are shown in graph 8.3.

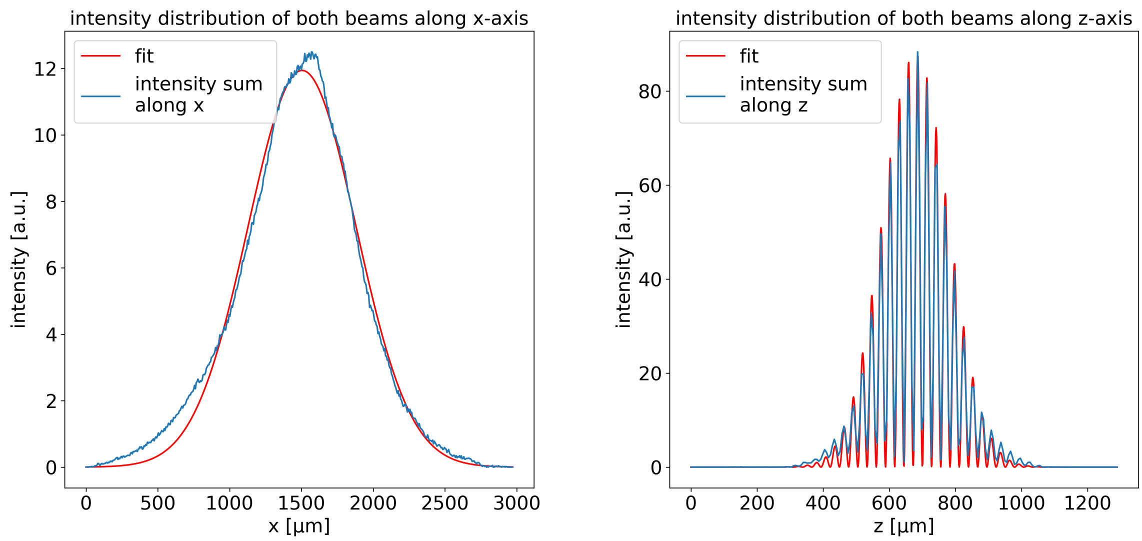

Figure 8.3: Fits to the one-dimensional intensity distributions which can be deduced from figure 8.2 by summing along the vertical and horizontal axes respectively. On the left, the intensity distribution in x-direction is fitted by a Gaussian fit-model extracted from the three-dimensional theoretical model of the intensity distribution. On the right, the intensity distribution in z-direction is fitted by a standing wave with a Gaussian envelope which is also extracted from the three-dimensional theoretical model of the intensity distribution.

From the spacing of the interference pattern in the vertical direction of the intensity distribution one can conclude the magnification M of the imaging system, assuming that the half-crossing angle of the real 2D Trap is known to be $\theta_{real} = 7.3°$:

$$M = \frac{d_{image}}{d_{real}} = \frac{\sin(\theta_{real})}{\sin(\theta_{image})} \tag{8.3}$$

with an error of

$$dM = \frac{\sin(\theta_{real})}{\sin^2(\theta_{image})} \cos(\theta_{image}) d\theta_{image} \tag{8.4}$$

As from the fit follows: $\theta_{image} = (1.0933 \pm 0.0004)°$,
the magnification is: $M = (6.659 \pm 0.003)$.
The beam widths of the image are:

$W_{0x,image} = (752 \pm 3)$ μm and
$W_{0z,image} = (199.1 \pm 1.0)$ μm.
The real trap beam widths can be concluded by considering the magnification:

$$W_{(0x,0z)} = \frac{W_{(0x,0z),image}}{M} \tag{8.5}$$

with an error:

$$dW_{(0x,0z)} = \sqrt{\left(\frac{dW_{(0x,0z),image}}{M}\right)^2 + \left(\frac{W_{(0x,0z),image} \cdot dM}{M^2}\right)^2} \tag{8.6}$$

which leads to the result of:
$W_{0x} = (113.0 \pm 0.5)$ μm and
$W_{0z} = (29.89 \pm 0.16)$ μm.

Bottom and top beam

In the case of single beams the fit-model changes to the expression in horizontal direction of:

$$I_{single,x} = I_1(x, y = 0, z = 0, P_{1,image}, W_{0x,image}, W_{0z,image} = c_1, \theta_{image} = c_2) \tag{8.7}$$

with $c_i > 0$ for an arbitrary positive value because the fitted beam power is not of any relevance, and in vertical direction:

$$I_{single,z} = I_1(x = 0, y = 0, z, P_{1,image}, W_{0x,image} = c_3, W_{0z,image}, \theta_{image} = 1.0933°) \tag{8.8}$$

Also for these two fit-models one could add an offset, but it was not necessary for the analysed data set.
Figure 8.4 and 8.5 show the top and bottom beam after the two images were cut and rotated by the optimal angle. The optimal rotation angle of the top beam is about $\alpha_{top} = -2.4°$ and the one of the bottom beam is about $\alpha_{bottom} = -1.0°$. Afterwards, the intensity can again be summed up along each axis individually to perform the one-dimensional fits.

For the top beam, one can extract the following beam widths for the real trap by normalizing the beam widths of the image beam with the magnification:
$W_{0x} = (123.8 \pm 0.6)$ μm and
$W_{0z} = (30.04 \pm 0.20)$ μm.

For the bottom beam, one can extract the beam widths for the real trap similarly by normalizing the beam widths of the image beam with the magnification:
$W_{0x} = (115.3 \pm 0.5)$ μm and
$W_{0z} = (33.48 \pm 0.20)$ μm.

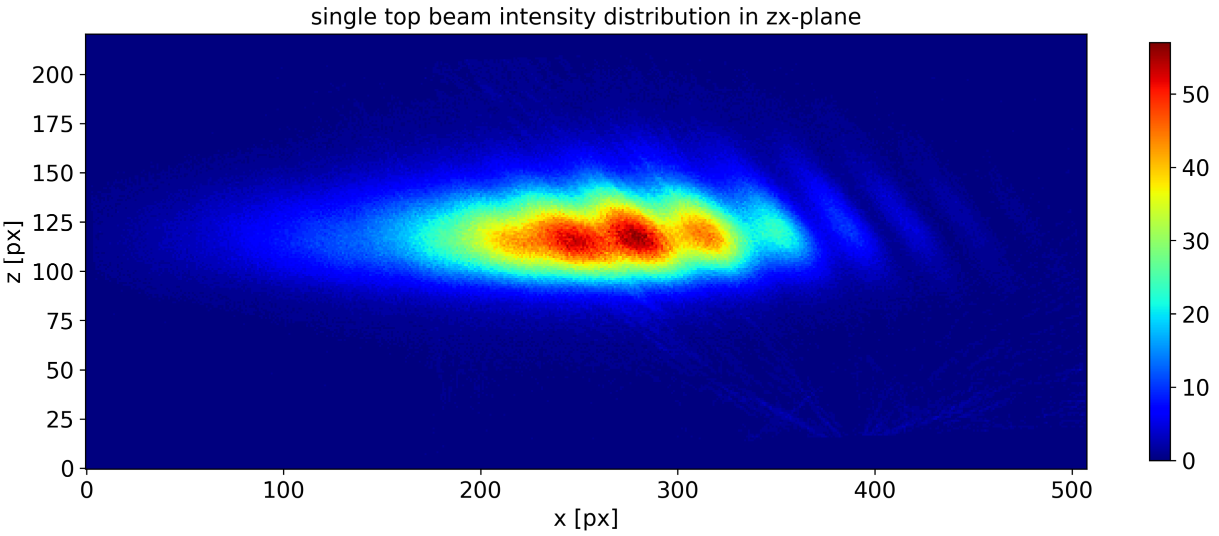

Figure 8.4: Single-beam image of the top beam intensity distribution of the 2D Trap, after rotating the image by the optimal rotation angle of $\alpha = -2.4°$ which minimizes the vertical beam width. There seems to be a small disturbing defect in the optical system which creates an unwanted interference pattern on the single-beam intensity distribution.

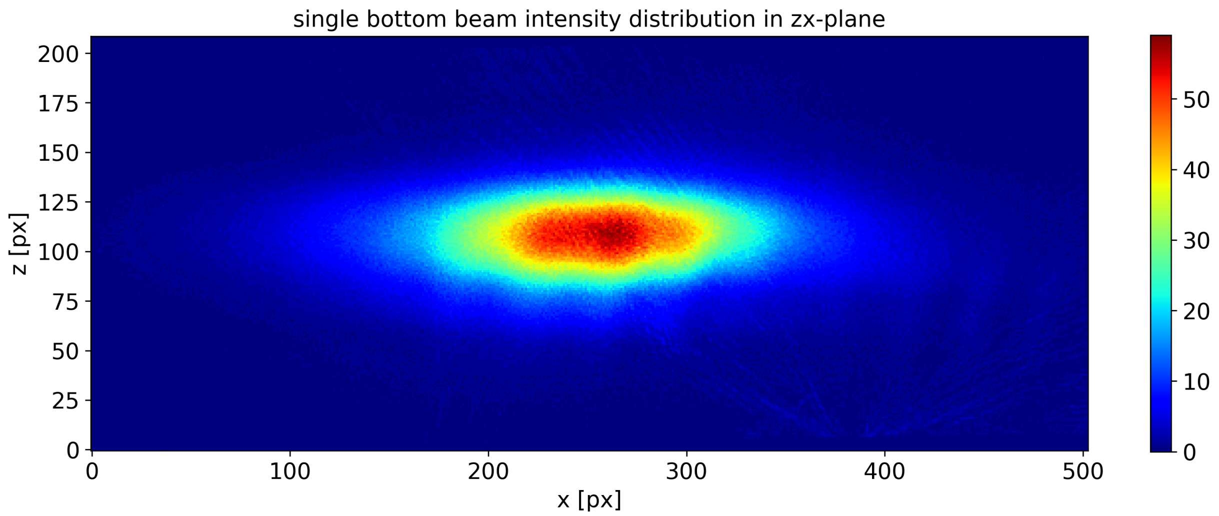

Figure 8.5: Single-beam image of the bottom beam intensity distribution of the 2D Trap, after rotating the image by the optimal rotation angle of $\alpha = -1.0°$ which minimizes the vertical beam width.

Mean values of the real beam widths determined from the trap image

The mean values over the results from all three images are for the real trap considering the magnification:
$W_{0x} = (117.4 \pm 0.3)\ \mu$m and
$W_{0z} = (31.14 \pm 0.11)\ \mu$m.

8.1.2 Estimating the crossing angle from the perspective of camera C_1

Measurement of the crossing angle

Another important trap parameter is the half-crossing angle θ. Although it is not so simple to measure the angle of the beams directly, one possible estimation is shown in the following section. After trapping atoms in one of the single 2D Trap beams, its angle can be observed on camera C_1 in an absorption image.
To analyse the image, one has to calculate the column density ([25]):

$$n_{cd} = -\ln\left(\frac{I_{abs} - I_{bg}}{I_{ref} - I_{bg}}\right) \tag{8.9}$$

with the absorption intensity I_{abs}, the background intensity I_{bg}, and the reference intensity I_{ref}. The absorption intensity includes the intensity of the imaging-beam together with the shadow from the absorbing atoms. The background intensity includes only the background signal without the imaging-beam, and the reference intensity includes only the intensity from the imaging-beam, but not the shadow from the absorbing atoms. Subsequently one needs a two-dimensional fit-model for the two beams:

$$I_{top} = I_1(x = 0, y = y - y_0, z = z - z_0, P_1, W_{0x} = c_1, W_{0z}, \tilde{\theta}_1) \tag{8.10}$$

$$I_{bottom} = I_2(x = 0, y = y - y_0, z = z - z_0, P_2, W_{0x} = c_1, W_{0z}, \tilde{\theta}_2) \tag{8.11}$$

with arbitrary positive values c_i. One could also add an offset for these two fit-models, but this was not necessary for the analysed data set. The two-dimensional fits for the top and bottom beam are portrayed in figure 8.6 and figure 8.7.

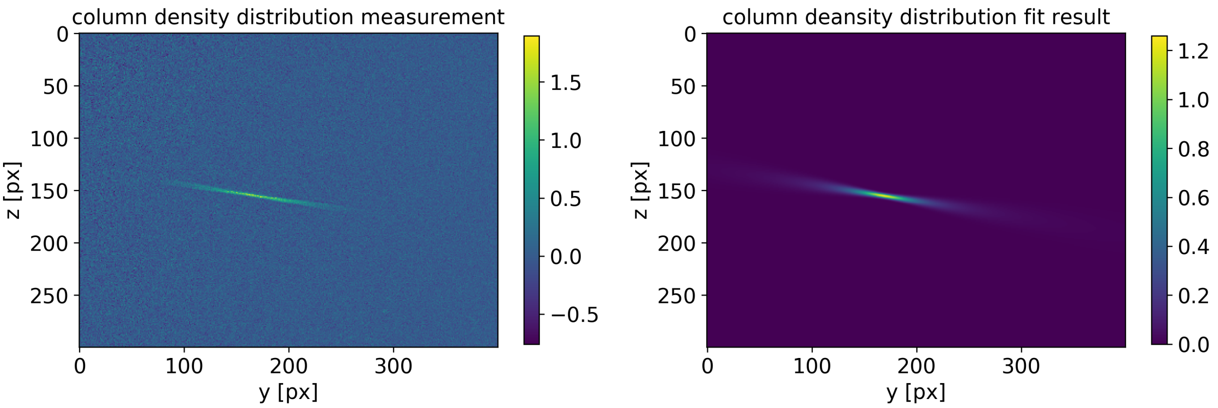

Figure 8.6: On the left, the measured column density is shown if one loads atoms only in the top beam and the bottom beam is blocked. On the right, the two-dimensional Gaussian fit to the left image is shown which is used to extract the angle of the top beam.

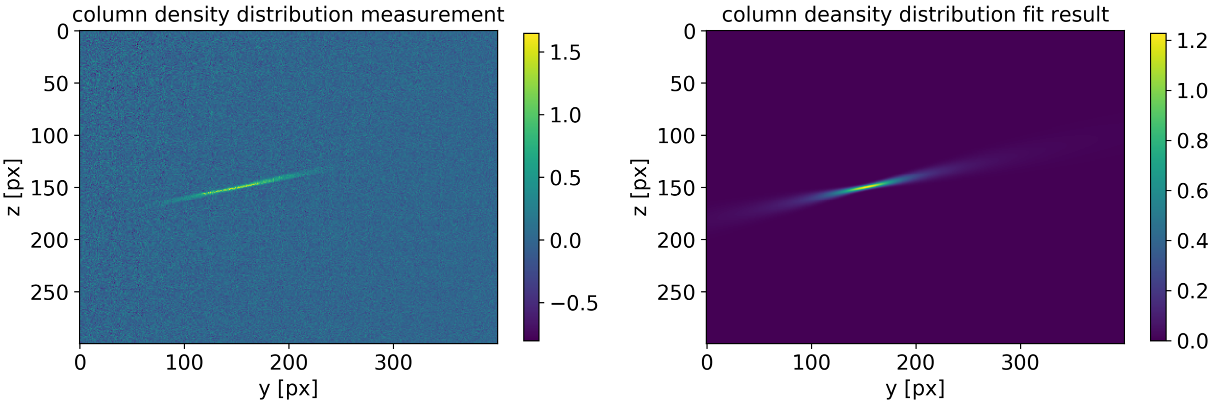

Figure 8.7: On the left, the measured column density is shown if one loads atoms only in the bottom beam and the top beam is blocked. On the right, the two-dimensional Gaussian fit to the left image is shown which is used to extract the angle of the bottom beam.

The fit-results from the two-dimensional fit-model are:
$\tilde{\theta}_1 = (8.82 \pm 0.08)^\circ$ and
$\tilde{\theta}_2 = (-11.82 \pm 0.08)^\circ$.
To confirm that the two-dimensional fit was successful, one can also perform a one-dimensional Gaussian fit with an offset after summing the two-dimensional image along the horizontal y-direction. If one plots the width of the appearing maximum in the z-direction as function of rotation angle of the image, there appears a minimum at the angle of the beam. This method of angle determination is shown in figure 8.8 for the bottom beam. The width was determined by a Gaussian fit-model and the minimum with a parabolic fit-model.
Indeed, the results from the second fit-method verifies the results from the first method with:
$\tilde{\theta}_1 = (8.745 \pm 0.004)^\circ$ and
$\tilde{\theta}_2 = (-11.754 \pm 0.003)^\circ$.

Interpretation of the measured crossing angle

However, the resulting angles seem to be far away from the expected ones. But one has to take care about their interpretations because the absolute values depend on the perspective of camera C_1 on the beams. To approach the values of the actual angles, one has to consider at least that camera C_1 sees the two beams under an angle of $\alpha = 45^\circ$. The according calculation is shown in the appendix. For rotation angles: $\alpha = 45^\circ$ around the z-axis and $\beta = -1.5^\circ$ around the y-axis follows:
$\theta_1 = (7.31 \pm 0.06)^\circ$,
$\theta_2 = (-7.38 \pm 0.06)^\circ$ and
$\chi = |\theta_1| + |\theta_2| = (14.69 \pm 0.08)^\circ$.
So it seems to be reasonable to assume the the camera C_1 is tilted about the two angles $\alpha = 45^\circ$ and $\beta = -1.5^\circ$ with respect to the two 2D Trap beams. From the total crossing

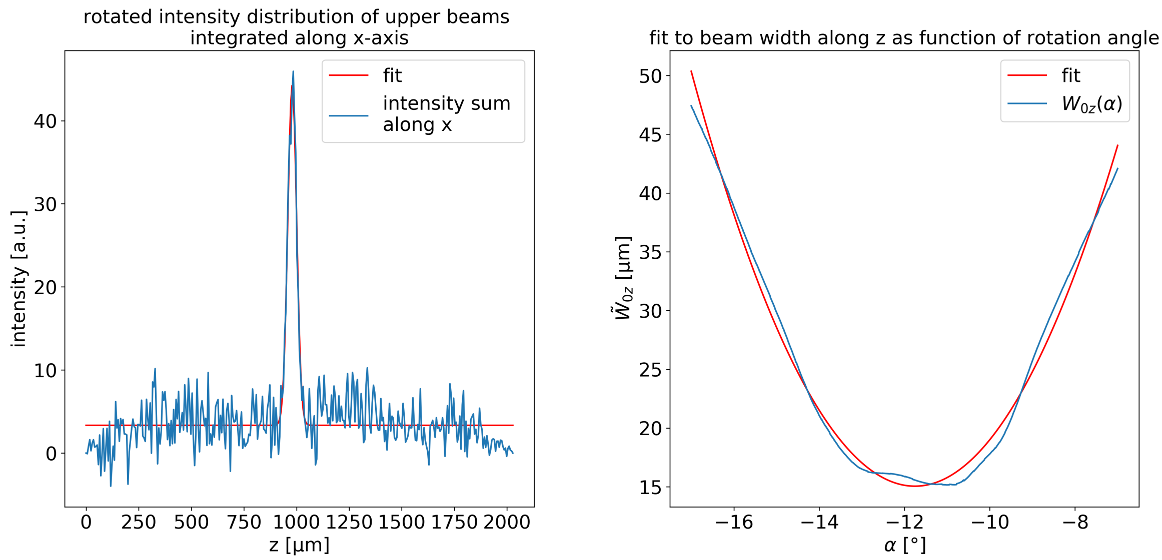

Figure 8.8: Second method to extract the angle of the single 2D Trap beams, here shown for the bottom beam. The measured column density distribution is rotated by a varying rotation angle, summed along the horizontal axis and fitted by a Gaussian to extract the width of the distribution. On the left, one of such fitted distributions is shown. On the right, one can see the beam width fit results as function of rotation angle. By fitting a parabola to the extracted beam width fit data one can identify the angle of the bottom beam. It corresponds to the angle where the fitted beam width is minimal.

angle one can deduce an expectation value of the mean half cross angle of:
$\theta = (7.35 \pm 0.04)°$.

8.2 Trap properties

8.2.1 Vertical trap frequency of the 2D Trap

The vertical trap frequency of the 2D Trap can be measured by modulating the trap curvature in vertical direction. This can be reached by periodical modulation of the laser power. If the modulation frequency reaches twice the value of the vertical trap frequency, the number of atoms which are excited to higher levels by this parametric heating process is maximal. After a spilling sequence, the number of removed atoms from the excited ones is maximal in the described case. So one can find a dip in the intensity which is proportional to the atom number in the trap while scanning the modulation frequency. The interaction of the two-component mixture is set by the magnetic field of about 800 G to weak interaction. In the left part of figure 8.9, one can see exemplarily one of such spectra in the case of a mean power corresponding to 4 V of measured photodiode voltage or 52 mW. To identify the centre frequency of each dip a Gaussian fit-model was used:

$$G(f, f_0, \sigma, A, c) = \frac{A}{\sqrt{2\pi\sigma^2}} \exp\left(-\frac{(f-f_0)^2}{2\sigma^2}\right) + c \tag{8.12}$$

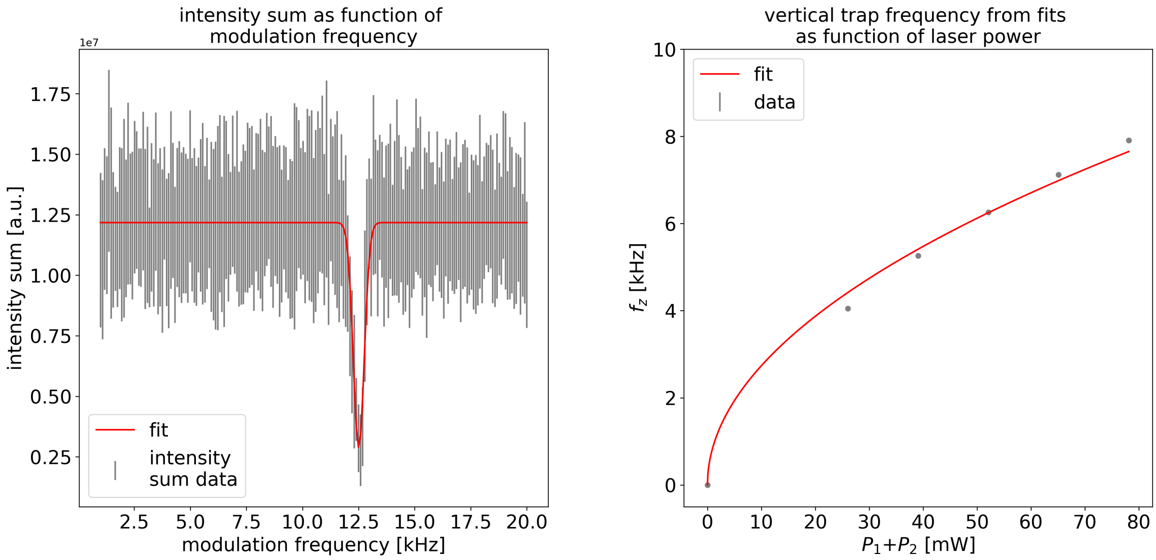

Figure 8.9: Measurement of the vertical trap frequency: On the left, the intensity sum which is proportional to the trapped atom number is plotted as function of modulation frequency. There occurs a minimum in the intensity sum if the modulation frequency corresponds to twice the vertical trap frequency. The mean power for the measurement corresponds to 4 V measured at the power-controlling photodiode. The error bars correspond to the standard deviation of each data point. On the right, a fit to the extracted trap frequency data for different mean powers is shown to identify the behaviour of the trap frequency as function of power in general.

The actual vertical trap frequency corresponds to half of the extracted centre frequency:

$$f_z(P) = \frac{f_0(P)}{2} \tag{8.13}$$

To be able to extrapolate the trap frequencies also for other power values reliably, this measurement was done for different mean power values and the vertical trap frequencies are plotted in the right part of figure 8.9. The conversion factor to translate photodiode voltage for the power measurement into Watts was measured to be: $vw \approx 13.02$ mW/V. The vertical trap frequency as function of power can be fitted with a simple square-root-fit:

$$f_z(P, A_z) = A_z \cdot \sqrt{P} \tag{8.14}$$

leading to: $A_z = (866 \pm 14)$ Hz. Here, P corresponds to the total beam power: $P = P_1 + P_2$. If one extrapolates the fit-result to a total beam power of $P = 4$ W, the vertical trap frequency is: $f_z(P = 4\text{ W}) = (54.8 \pm 0.9)$ kHz.

8.2.2 Radial trap frequencies of the 2D Trap

The radial trap frequencies can be measured by exciting the trapped atoms to oscillate in radial direction. The known lowest two possible oscillation modes are the centre-of-mass mode and the breathing mode. The centre-of-mass corresponds to a motion of the whole atom cloud in the trap, while the Gaussian centre position of the cloud oscillates exactly with the trap frequency. In the case of the breathing mode, the width of the cloud oscillates with twice the trap frequency. For the measurement a one-component atomic gas sample without interaction is prepared in the 2D Trap. For the excitation of the breathing mode which was executed here the 2D Trap power is changed step-wise. The atomic cloud was detected by camera C_3. After rotating the image appropriately, the two one-dimensional axes of the image can be extracted by summing up along the two axes individually. The one-dimensional intensity distributions can be fitted by a Gaussian fit-model to identify the centre position and the width in each axis:

$$G_x = \frac{A_x}{\sqrt{2\pi\sigma_x^2}} \exp\left(- \frac{(x-x_0)^2}{2\sigma_x^2} \right) + c_x \tag{8.15}$$

and analogue in y-direction. Subsequently, the results of all images can be plotted along time leading to an oscillating curve for the two centre positions x_0, y_0 and widths $\sigma_{x,y}$. As fit-model for each of the four quantities a single damped harmonic oscillator model can be used:

$$HO(t, \omega, \phi, \delta, A, c) = A \cdot \sin(\omega t + \phi) \cdot \exp(-\delta \cdot t) + c \tag{8.16}$$

For example in figure 8.10, the fit to a breathing mode excitation is shown at a power corresponding to 4 V of photodiode voltage or 52 mW. The resulting trap frequencies can be calculated from the fit results as:

$$f_{x,y} = \frac{1}{2} \frac{\omega_{breathing,(x,y)}}{2\pi} \tag{8.17}$$

leading to: $f_x = (73.4 \pm 1.2)$ Hz and $f_y = (69.7 \pm 1.1)$ Hz.
Figure 8.11 depicts a breathing mode excitation at a power corresponding to 2 V of photodiode voltage.
Here the results are: $f_x = (45.9 \pm 1.0)$ Hz and $f_y = (42.0 \pm 3.5)$ Hz. Again, one can investigate the power dependency also for the radial trap frequencies to be able to extrapolate the results for different laser powers with the fit-model:

$$f_{x,y}(P, A) = A_{x,y} \cdot \sqrt{P} \tag{8.18}$$

The results are plotted in figure 8.12 with the fit-parameters: $A_x = (9.68 \pm 0.41)$ Hz and $A_y = (9.59 \pm 0.21)$ Hz. So, the extrapolated trap frequencies for a total power of $P = P_1 + P_2 = 4$ W are:
$f_x(P) = (612 \pm 26)$ Hz and $f_y(P) = (607 \pm 14)$ Hz.

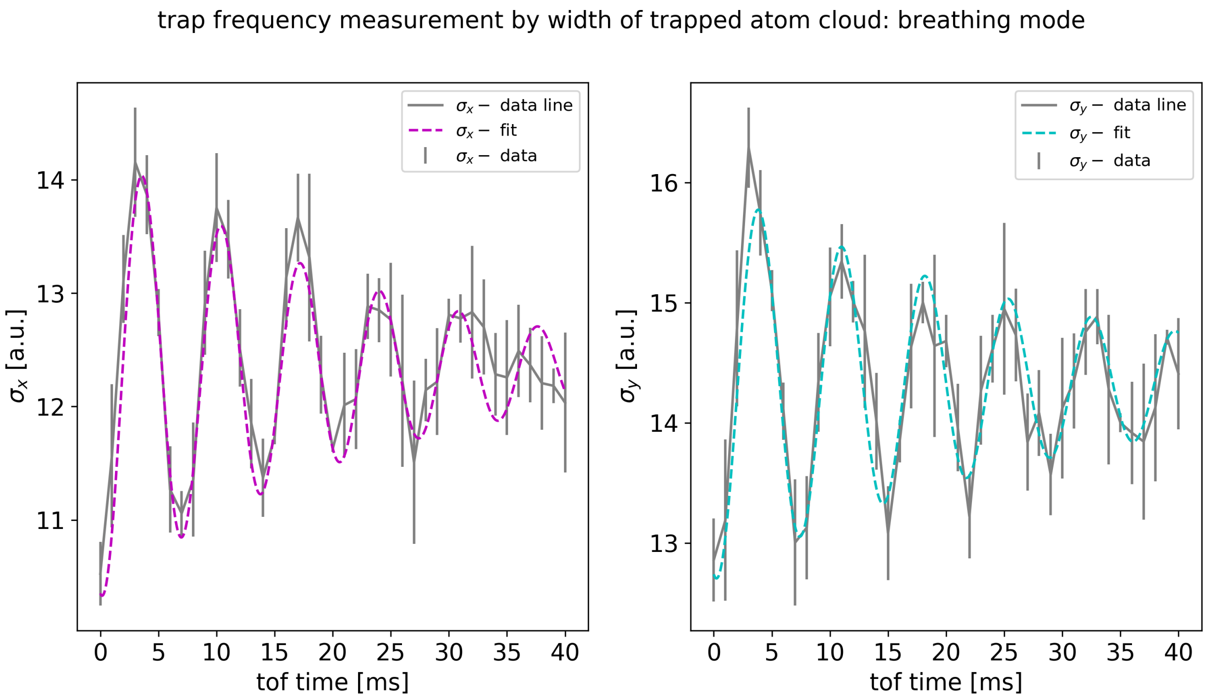

Figure 8.10: Measurement of the radial trap frequency in a breathing mode experiment: On the left, the oscillation of the width of the atom cloud in x-direction is given, whereas on the right the oscillation of the width of the atom cloud in y-direction is plotted. The error bars correspond to the standard deviation of each data point. By fitting a damped harmonic oscillation to the data, one can identify the oscillation frequencies which correspond to twice the respective trap frequencies in the two orthogonal directions. The measurement was executed with a total beam power corresponding to 4 V of photodiode voltage.

8.2.3 Radial trap frequency of the new Microtrap

To measure the radial trap frequency of the new Microtrap, the trap frequency can again be modulated by the power to reach a maximal atom loss at twice the actual trap frequency. The interaction of the two-component mixture is set by the magnetic field of about 800 G to weak interaction. In figure 8.13 one example is plotted for a mean power corresponding to 2.5 V on the photodiode monitoring the beam power. The resulting radial trap frequency in this case was determined by a Gaussian fit to be:

$$f_r = \frac{f_0}{2} = (572 \pm 4)\ \text{Hz} \tag{8.19}$$

Considering the right part of figure 8.13, the square-root fit:

$$f_r(P, A_r) = A_r \cdot \sqrt{P} \tag{8.20}$$

to the radial trap frequency as function of beam power leads to: $A_r = (174.7 \pm 1.2)$ Hz. Here, the conversion factor from photodiode voltage to actual laser power is: $vw_{MT} \approx 4.29$

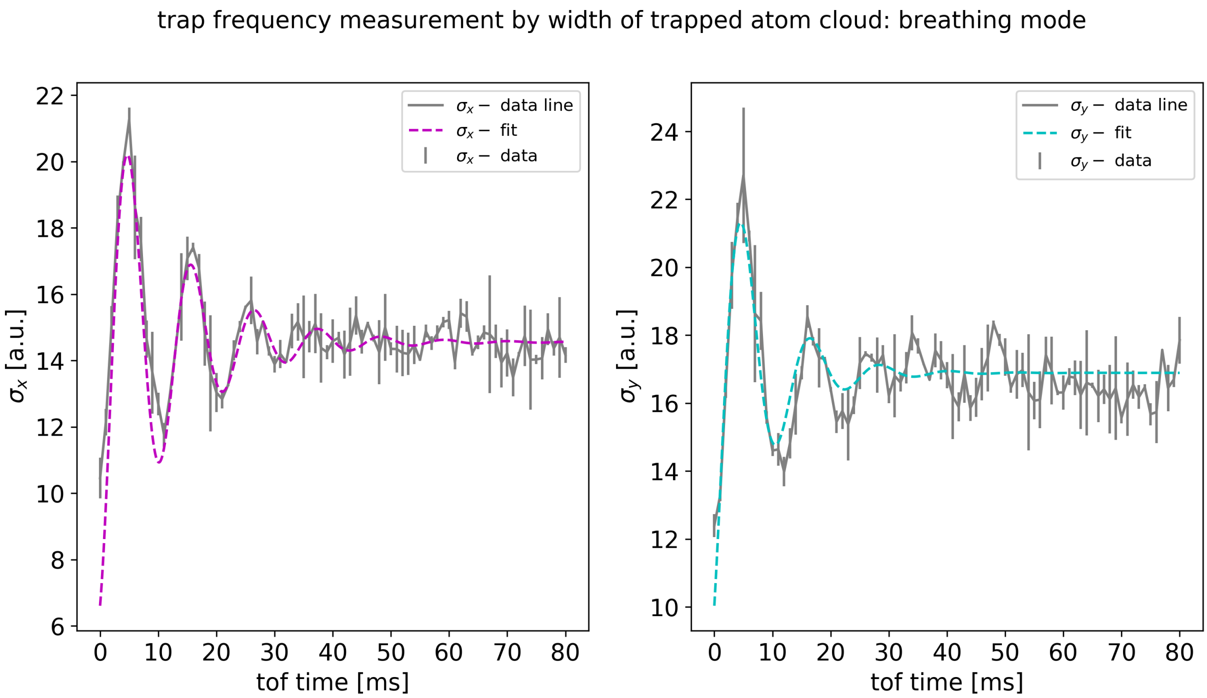

Figure 8.11: Measurement of the radial trap frequency in a breathing mode experiment: On the left, the oscillation of the width of the atom cloud in x-direction is given, whereas on the right the oscillation of the width of the atom cloud in y-direction is plotted. The error bars correspond to the standard deviation of each data point. By fitting a damped harmonic oscillation to the data, one can identify the oscillation frequencies which correspond to twice the respective trap frequencies in the two orthogonal directions. The measurement was executed with a total beam power corresponding to 2 V of photodiode voltage.

mW/V. The radial trap frequency for $P_3 = 0.2$ W can be identified as: $f_r = (2.471 \pm 0.017)$ kHz. This corresponds to a beam width of: $W_0 = (12.95 \pm 0.04)$ μm with:

$$W_0 = \left(\frac{8aP_3}{\pi m(2\pi f_r)^2}\right)^{\frac{1}{4}} \tag{8.21}$$

and

$$dW_0 = \left(\frac{8aP_3}{\pi m(2\pi)^2}\right)^{\frac{1}{4}} \frac{1}{2} \frac{df_r}{f_r^{\frac{3}{2}}} \tag{8.22}$$

8.3 Tomography

8.3.1 Conceptional working principle of tomography

The technique of tomography is based on the following mechanism as described in [24]: One can apply a magnetic field gradient along the vertical direction in which the layer

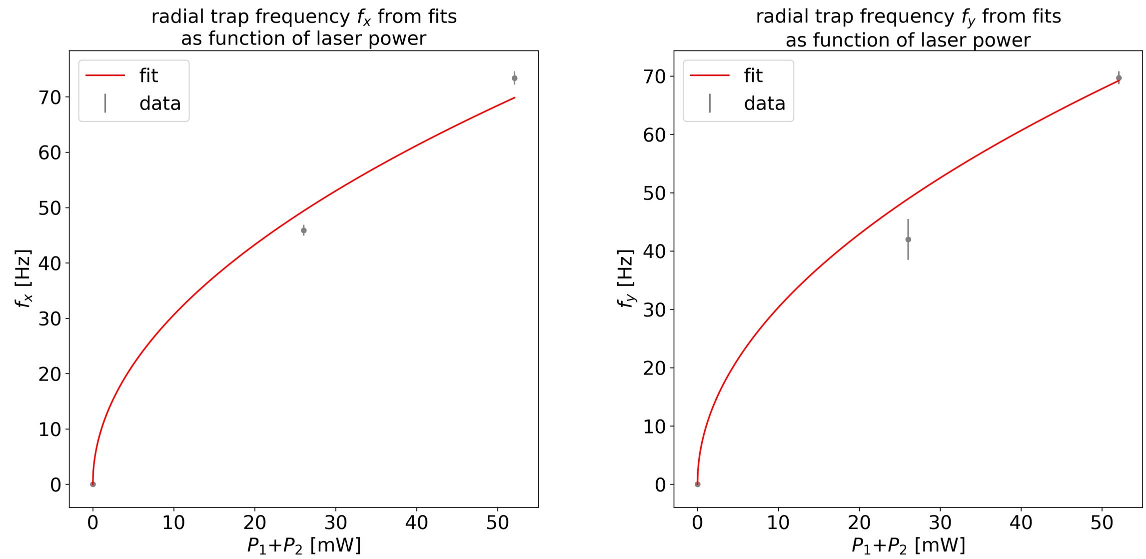

Figure 8.12: Fit of the two radial trap frequency data as function of total beam power. On the left, the fit to the data for the x-component f_x is presented and on the right the fit to the y-component f_y.

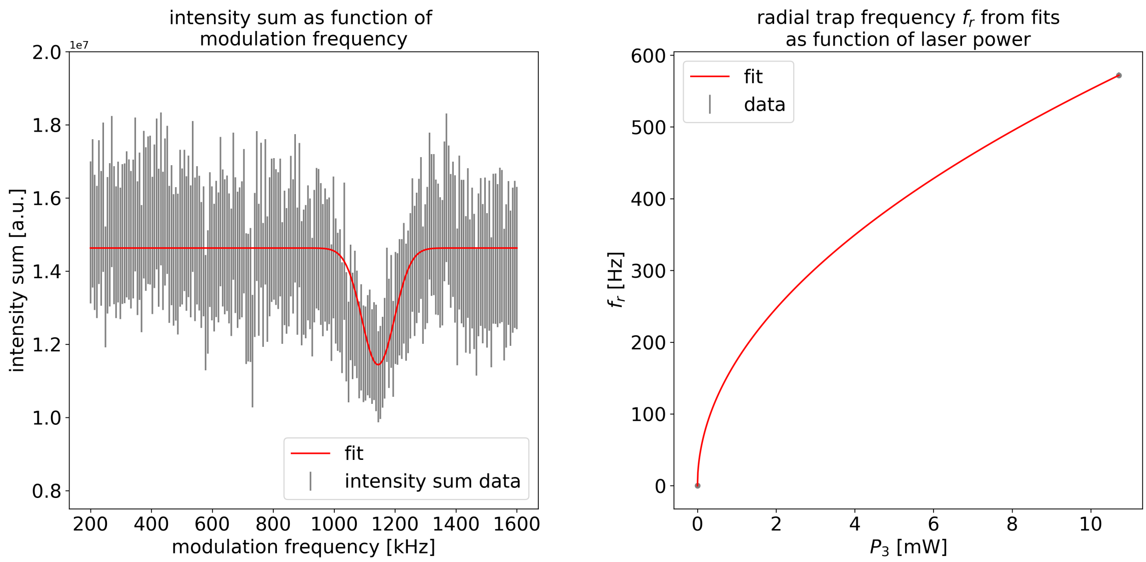

Figure 8.13: On the left: Intensity sum, which is proportional to the atom number as function of modulation frequency in radial direction. If the modulation frequency corresponds to twice the trap frequency in radial direction the trapped atom number is minimal. The error bars correspond to the standard deviation of each data point. The figure includes a Gaussian fit to the intensity sum data to identify the precise value of the radial trap frequency. On the right: Fit to data of radial trap frequency of the new Microtrap as function of power.

structure of the interference pattern from the 2D Trap appears. In this way, the hyperfine levels of the atoms are shifted depending on the position along the layer structure. By using a radio-frequency pulse, one can excite only atoms at a certain position in the interference pattern. To exploit this behaviour, one can prepare all atoms first for example in state $|2\rangle$ and subsequently excite only atoms at one position in the layer structure in state $|3\rangle$. Finally, the population in the excited state can be detected. After scanning the rf-frequency, one can get the atom number at each position in the interference pattern. If the line width of the radio-frequency pulse is smaller than the actual width of a 2D Trap layer, one can resolve the interference pattern with this technique.

8.3.2 Measurement results

In this way it is possible to resolve atoms populating the different individual layers of the 2D Trap. After averaging over several runs one gets spectra as shown in figure 8.14 where the intensity sum is proportional to the atom number. The left result corresponds to a tomography after weak spilling, such that apart from the central layer also the other layers are populated. In the right part of figure 8.14, the tomography was done after strong spilling and the population of the central layer is dominant.

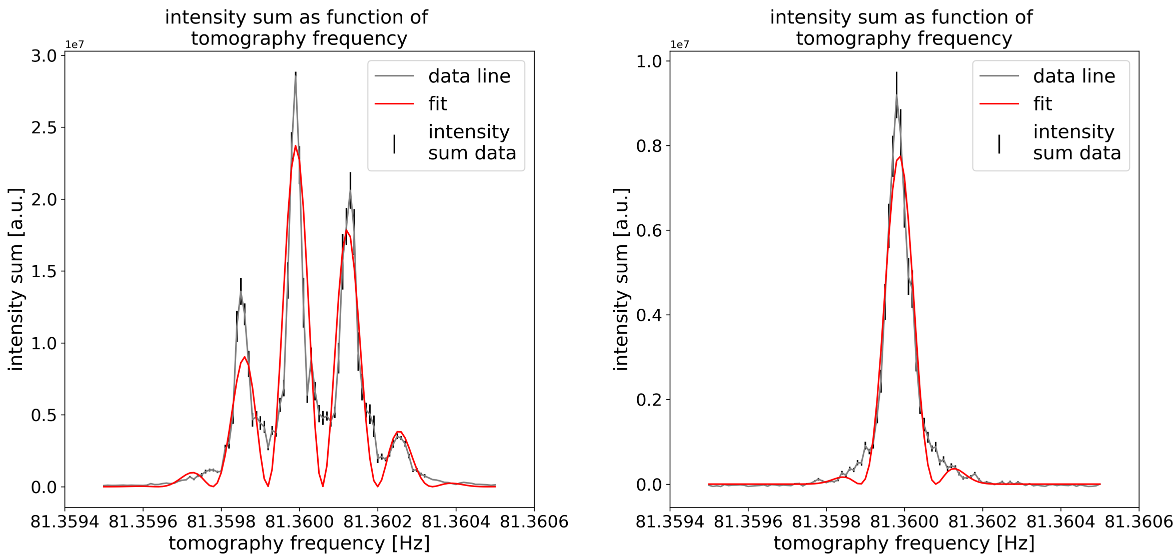

Figure 8.14: Fitted tomography data: left after weak spilling and right after strong spilling. The errors correspond to errors of the mean value.

To interpret the tomography results further, the spectrum can be fitted by a fit-model with the same shape as the vertical axis of the 2D Trap intensity distribution:

$$I(x, x_0, \sigma_x, A, B, \Delta\phi) = \frac{A}{\sqrt{2\pi\sigma_x^2}} \cdot \exp\left(-\frac{(x-x_0)^2}{2\sigma_x^2}\right)\left(1+\cos(B(x-x_0)+\Delta\phi)\right) \quad (8.23)$$

By integrating over the according regions, one can find the contribution of atoms in the central layer with respect to the total number of trapped atoms. In the case of weak

spilling this ratio is:
$N_{rel,weak} = \frac{N_{centre,weak}}{N_{tot,weak}} \approx 42.9\%$
and for the strong spilling case the ratio is:
$N_{rel,strong} = \frac{N_{centre,strong}}{N_{tot,strong}} \approx 95.0\%$

So, one can conclude that the spilling technique is very successful in leading to a major population of the central layer.
Furthermore, one can analyse the width of the tomography spectrum in the case of weak spilling in order to compare this with the expected width of trap intensity distribution. The width in units of lattice spacing δ is:

$$\frac{W_{0z,atoms}}{\delta} = \frac{B}{2\pi} 2\sigma_z \tag{8.24}$$

Assuming an ideal lattice spacing of $d = \frac{\lambda}{2\sin(7.3°)}$ the width of the atom layer distribution is: $\frac{W_{0z,atoms}}{\delta} d \approx 7.26\ \mu$m compared to the expected width of the trap of at about $W_{0z} \approx 17$ μm. So, also the weak spilling leads to an atom layer distribution which is much narrower than the trap layer distribution.
Similarly the tomography after spilling was executed for the combined trap where the 2D Trap is overlapped with the new Microtrap (figure 8.15). In the case of the left spilling

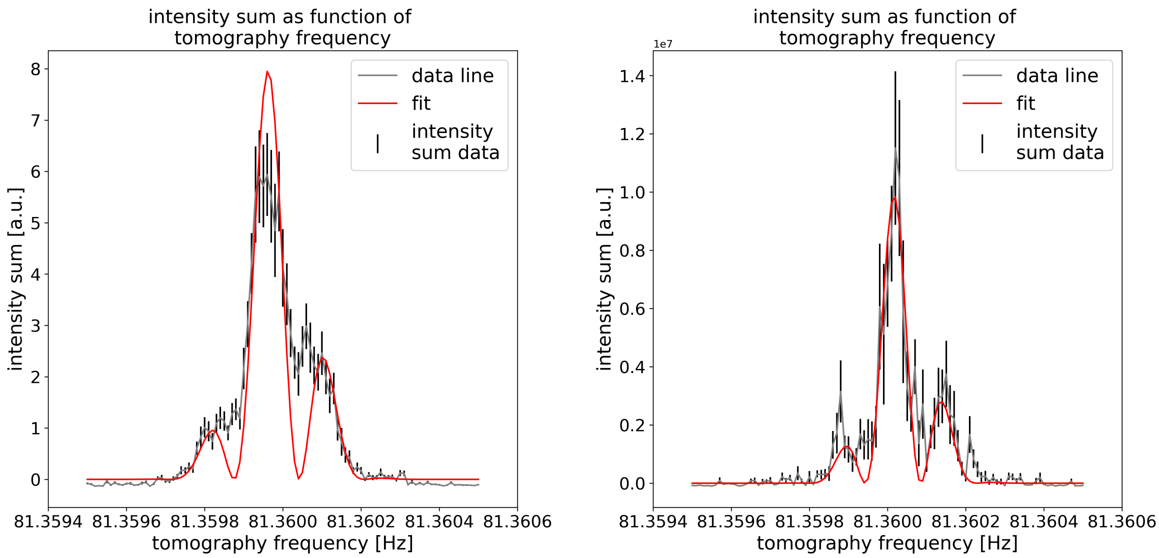

Figure 8.15: Tomography data in the combined trap, meaning the 2D Trap in overlap with the new Microtrap. Left and right graphs show results for different spilling conditions.

configuration of figure 8.15 the contribution in the central layer is:
$N_{rel,weak} = \frac{N_{centre,weak}}{N_{tot,weak}} \approx 71.8\%$
and for the right spilling configuration of figure 8.15 the central layer contribution is:
$N_{rel,strong} = \frac{N_{centre,strong}}{N_{tot,strong}} \approx 72.5\%$

8.4 Stability

In this section the stability of the 2D Trap is analysed. This contains the long term stability as well as the stability against heating disturbances.

8.4.1 Stability during tomography

Analysing the tomography data

The long term stability was investigated by analysing the tomography data by cutting the data in different tomography spectra along time and fitting them with the fit-model described above. The relevant parameters of this fit-model are the centre position of the envelope and the phase shift between the envelope and the carrier plotted in figure 8.16.

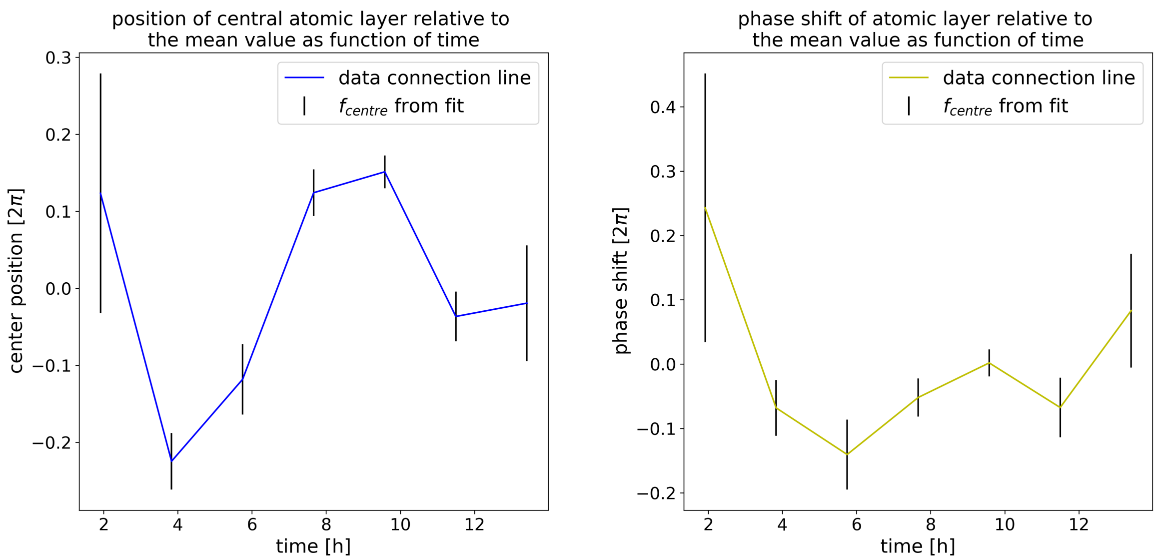

Figure 8.16: Fit results to tomography data for the 2D Trap as function of time: Each fit was executed over the statistics of 6 tomography runs. Each time value corresponds to the time of the last run. On the left, the envelope position in z-direction is shown, whereas on the right the relative phase between the carrier position and the envelope is depicted. The error bars correspond to the errors of the fit results.

One can realize that the two quantities fluctuate over 14 hours about a substantial fraction of the layer spacing (2π) but are all in all relatively stable and show no strong drifts in a specific direction.

Compare camera C_2 images

During the tomography also images with camera C_2 were taken in series. These images also can be used to detect the stability of the trap during the tomography measurement. Each image of the temporal series is rotated about an angle of $\alpha = -2.5°$ and summed along each axis individually to be able to fit the two one-dimensional distributions. As fit-model the general intensity distribution was used as starting point: The horizontal fit-model has the form:

$$I_{tot,x} = I_{2D}(x = x - x_0, y = 0, z = 0, P_{1,2}, W_{0x}, W_{0z} = c_1, \theta = c_2, \Delta\phi = 0) \tag{8.25}$$

with $c_i > 0$ for an arbitrary positive value because the fitted beam power is not of any relevance and the vertical fit-model can be identified as:

$$I_{tot,z} = I_{2D}(x = 0, y = 0, z = z - z_0, P_{1,2}, W_{0x} = c_3, W_{0z}, \theta, \Delta\phi) \tag{8.26}$$

Also for these two fit-models, one could add an offset but it was not necessary for the analysed data set. One example fit of the first image of the series is shown in figure 8.17.

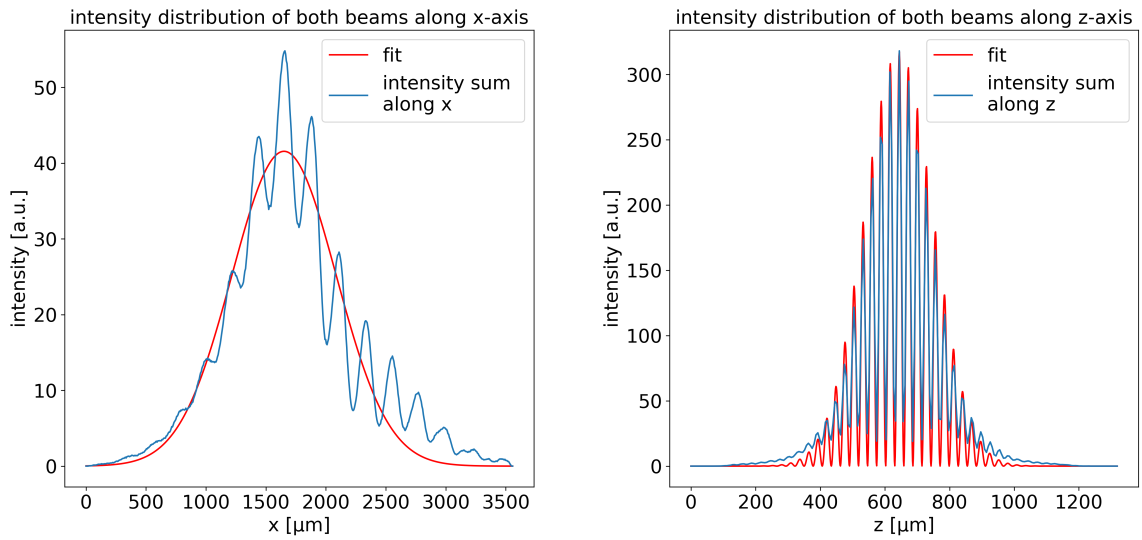

Figure 8.17: Fits to the one-dimensional intensity distributions which can be deduced from the first image of the detected sequence by summing along the vertical or horizontal axes, respectively. On the left, the intensity distribution in x-direction is fitted by a Gaussian fit-model extracted from the three-dimensional theoretical model of the intensity distribution. One has to mention that the higher reflection orders from the dichroic mirror DM_2 were not blocked out during the measurement. For this reason, an additional interference structure appears in the distribution which disturbs the fitting procedure. On the right, the intensity distribution in z-direction is fitted by a standing wave with a Gaussian envelope which is also extracted from the three-dimensional theoretical model of the intensity distribution.

One has to interpret the horizontal fit results with care as the higher reflection orders from the dichroic mirror DM_2 were not blocked out during the measurement. These reflection orders disturb the Gaussian shape of the horizontal intensity distribution by interference

effects. Nevertheless, the fluctuations of the mean position and the width can be used for the stability analysis. Figure 8.18 shows the temporal fluctuations of the resulting fit-parameters.
All quantities seem to be quite stable and remarkably, if one compares the fluctuation of the envelope position in z-direction from the camera C_2 images with the fluctuations from the tomography, they show a comparable behaviour. The same holds qualitatively for the phase fluctuations. From this fact, one can conclude that the stability of the trap can be monitored by the camera C_2. Furthermore the fluctuations can be influenced by the drift of the laboratory temperature. Similar results can be extracted from the tomography in the combined trap as portrayed in figure B.41 and B.42 in the appendix. One has to remark that the analysis of the camera C_2 images in figure B.42 can only detect the stability of the 2D Trap and not the one of the combined trap. Nevertheless, the correlation between the tomography stability results and the results from the analysis of the camera C_2 images also here hold qualitatively. However in this case, one can observe a small drift of the trap parameters although the laboratory temperature is quite stable. One reason could be a local heating effect. All in all, the quantities are still relatively constant.

8.4.2 Stability during the heat-up experiment

Finally, the effect of a strong heating was investigated. So, there were taken pictures with camera C_2 directly after covering the experimental setup and turning on all modules. Afterwards, the same analysis as previously described could be applied. In figure 8.19 the results of this analysis are shown in the form of the temporal fluctuations of the fit-parameters.
One can register a clear drift of all parameters correlated with a drift of the laboratory temperature of about $\Delta T = 0.4$ °C. One can speculate that the drift in power happens most likely because the sensitivity of the camera chip is temperature dependent. All other parameters drift presumably because of the temperature dependent alignment of the opto-mechanical components. To estimate the timescale on which an equilibration takes place, figure 8.20 shows an exponentially decaying fit to the temporal fluctuation of the envelope position in z-direction.
The fit-model has the form:

$$W = A \cdot \exp\left(-\frac{t}{\tau}\right) + c \tag{8.27}$$

The relevant time constant which characterizes the equilibration time is $\tau = (71.2 \pm 0.8)$ min. So it seems one has to wait at least τ before starting stable experiments.

8.5 Characterization results

Finally the most important results are summarized in table 8.1. Here, one can compare the target values for the 2D Trap parameters and properties with the actual measured values. There are two different comparison sets with different laser powers, one at $P_{1,2} = 0.1$

parameter/property	target value	measured values	target value	measured values
$P_{1,2}$ [W] (tunable)	0.1	0.1	2	2
λ [nm]	1064	1064	1064	1064
W_{0x} [μm]	133	117.4 ± 0.3	133	117.4 ± 0.3
W_{0z} [μm]	17	31.14 ± 0.11	17	31.14 ± 0.11
θ [°]	7.3	7.35 ± 0.04	7.3	7.35 ± 0.04
$E \equiv \frac{W_{0x}}{W_{0z}}$ [1]	7.82	3.770 ± 0.016	7.82	3.770 ± 0.016
$d \equiv \frac{\lambda}{2\sin(\theta)}$ [μm]	4.19	4.159 ± 0.023	4.19	4.159 ± 0.023
f_x [Hz]	92.7	96.8 ± 4.1	414	612 ± 26
f_y [Hz]	92.7	95.9 ± 2.1	414	607 ± 14
$f_r \equiv \frac{f_x+f_y}{2}$ [Hz]	92.7	96.4 ± 2.3	414	610 ± 15
f_z [kHz]	6.58	8.66 ± 0.14	29.4	54.8 ± 0.9
$R_{2D} \equiv \frac{f_z}{f_r}$ [1]	71	89.8 ± 2.6	71	89.8 ± 2.7
$R_{xy} \equiv \frac{f_x}{f_y}$	1	1.01 ± 0.05	1	1.01 ± 0.05
$U_0 = -aI_0$ [μK$\cdot k_B$]	-1.1	–	-22	–
$U_0 = -aI_0$ [$h \cdot f_z$]	-0.97	–	-19	–
$N_{2D} \equiv \frac{f_z^2}{4 f_x f_y}$ [1]	1260	2020 ± 116	1260	2019 ± 117

Table 8.1: 2D Trap characteristics including trap parameters and trap properties. The target values are compared with the measured values for $P_{1,2} = 0.1$ W on the first two columns and for $P_{1,2} = 2$ W in the last two columns.

W and one at $P_{1,2} = 2$ W. Unfortunately, the agreement between the measured and the target values is quite weak. The measured beam width in x-direction is smaller then the target value, and the measured beam width in z-direction is nearly twice as large as the target value. This leads to a much smaller ellipticity of the single elliptical beams. In contrast to that, the estimated half-crossing angle fits quite well to the target value which is expected as it is fixed by the opto-mechanical setup. The same holds naturally for the layer spacing which depends on the half-crossing angle.

For the trap properties, the measured trap frequencies are all much larger than the target values if one considers the set with $P_{1,2} = 2$ W. The measured radial trap frequencies are about 48% larger than the target values, and the measured vertical trap frequency is even about 86% larger than the target value. However, this partially seems to be a result of the extrapolation of the trap frequencies to values at higher beam power. For example, the agreement for the radial trap frequencies is much better for $P_{1,2} = 0.1$ W, and near this power the trap frequency measurement was executed. Remarkably, the ratio between the radial trap frequencies is nearly one, corresponding to nearly perfectly circular light sheets. This observation does not match at all with the poor measured ellipticity of the single beams. Besides, one also may not expect from the measured beam widths such high trap frequencies. However, also the flatness ratio is about 25% larger than the expected target value. The measured number of available states in the quasi-two-dimensional regime is about 60% larger than the expected target value.

So, one can conclude from table 8.1 that the measured trap parameters do not fit quite well to the target values and one may expect an unsatisfactory performance. In contrast to that, the measured 2D Trap properties outperform the target values quite remarkably in a satisfying way. This means the measured trap parameters and trap properties do not match together. The question remains if one should trust the measured trap parameters or the measured trap properties. As the beam widths were measured from the 2D Trap image and are not deduced directly from the real 2D Trap intensity distribution, it seems reasonable to assume that the 2D Trap image does not reflect perfectly the real 2D Trap parameters. Furthermore, the imaging system behind the Imaging-Box was not optimized for the detection of the 2D Trap intensity distribution with infrared laser light but for the registration of the atom absorption image with resonant laser light. This might be a reason for the inconsistency in the comparison between the measured trap parameters of the 2D Trap image and the measured 2D Trap properties. On top of that, the measured trap properties reflect the direct effect of the 2D Trap on the atoms and seem to be more reliable. So, it might be reasonable to trust the measured trap properties more than the measured trap parameters. However, the fact that all trap frequencies are much stronger than the target values with the observed amount is still unexpected. Partially, one can explain this difference with the extrapolation schema.

To investigate the difference and the reliability of the measured values, one can assume either one trusts the trap parameters and calculate from that the trap properties or one trusts the trap properties and calculates on this basis the trap parameters. The result from this analysis can be found in table B.1 and table B.2 in the appendix. It is important to remark that if one fully trusts the trap properties the resulting trap parameters are not consistent with the experimental boundary conditions. Here the resulting half-crossing angle is simply too large for the view ports. This observation appears even stronger in the extrapolated trap property set at $P_{1,2} = 2$ W. Therefore, it seems to be reasonable to execute further characterisation measurements at higher power values if one wants to know precise and reliable values for the trap frequencies. Nevertheless, one can conclude from the measured values of the trap properties, that the 2D Trap fulfills at least the target values and one can start with first experiments.

parameter/property	target value	measured values	param./prop. from prop.
P_3 [W] (tunable)	0.2	$\equiv 0.2$	$\equiv 0.2$
λ [nm]	1064	$\equiv 1064$	$\equiv 1064$
W_0 [μm]	10	–	12.95 ± 0.04
f_r [kHz]	4.1	2.471 ± 0.017	$\equiv 2.471 \pm 0.017$
f_z [Hz]	99	–	81.0 ± 0.8
$U_0 = -aI_0$ [μK$\cdot k_B$]	-12	–	-7.31 ± 0.05
$U_0 = -aI_0$ [$h \cdot f_r$]	-103	–	-61.6 ± 0.4

Table 8.2: New Microtrap characteristics including trap parameters and trap properties. The target values are compared with the measured values and trap properties and parameters are calculated from the trap properties.

The new Microtrap properties are in the right order of magnitude although the trap frequencies are a little bit weaker than the target expectations. The calculated beam width seems to be in a reasonable range, but it is 30% larger than the target value.

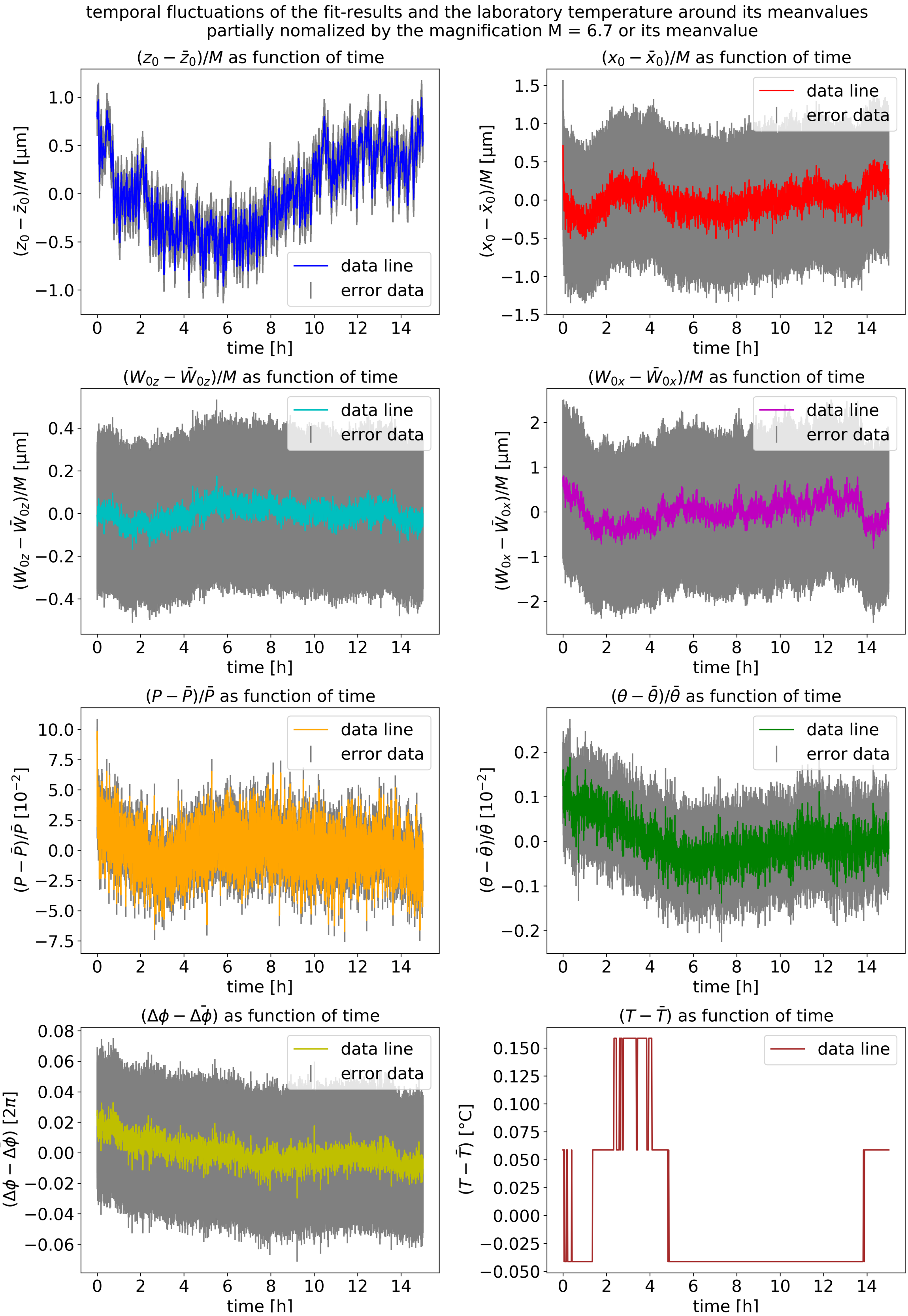

Figure 8.18: Temporal fluctuations of the fit results from the one-dimensional intensity distributions deduced from the camera C_2 images during the tomography measurement of the 2D Trap. The error bars correspond to the errors of the fit results.

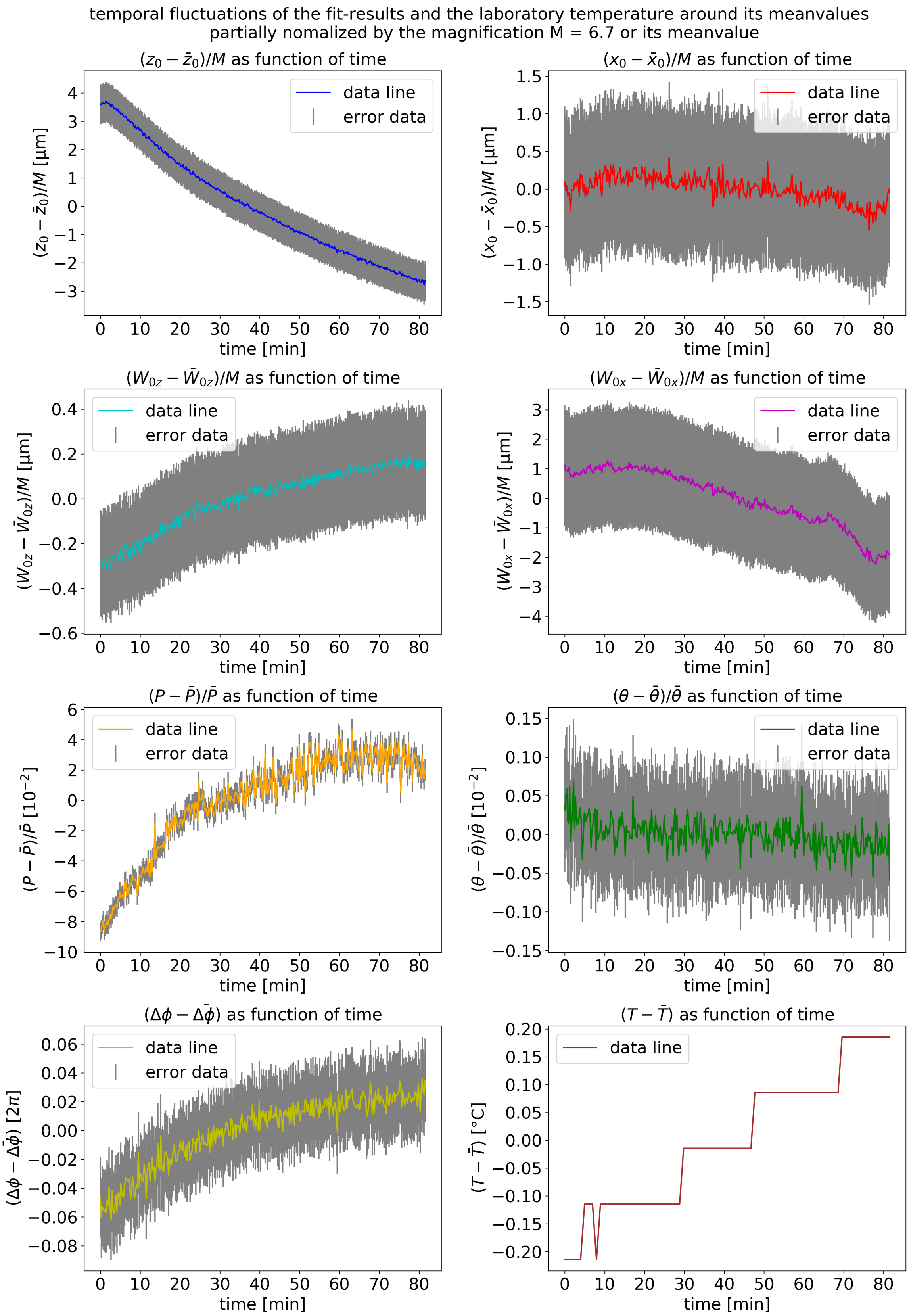

Figure 8.19: Temporal fluctuations of the fit results from the one-dimensional intensity distributions deduced from the camera C_2 images during the tomography measurement of the 2D Trap during the heat-up experiment. The error bars correspond to the errors of the fit results.

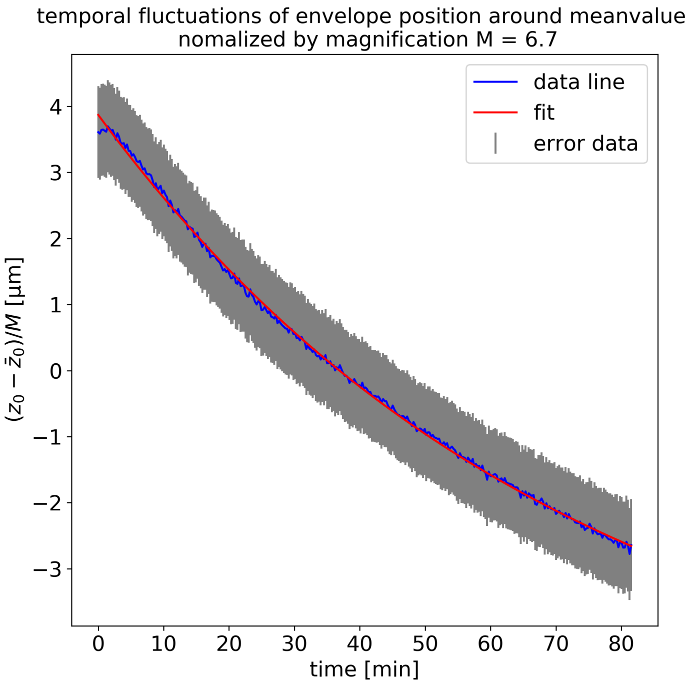

Figure 8.20: Exponential fit to the envelope position in z-direction to identify the timescale on which the equilibration happens. The error bars correspond to the errors of the fit results.

9 Conclusion and further perspectives

This master thesis ties in with the work of a bachelor thesis ([27]) which mainly has focused on the conceptional development of the quasi-two-dimensional optical dipole trap formed by two elliptical laser beams interfering in their crossing point and the main part of the opto-mechanical design as well as the definition of target properties. Apart from the two-dimensional trap, the target trap was extended in this thesis by the new Microtrap consisting of an additional single focused beam from the top which enables the control over the radial trap frequency independent from the vertical confinement controlled by the 2D Trap. Besides the identification of reasonable target values for this combined tunable 2D Trap during this thesis, the opto-mechanical design was finalized and actually installed and integrated into the few fermionic experimental system. More important, the thesis presents alignment schemas to optimize the performance of the trap and approach eventually the target trap properties. By the characterisation of the trap parameters and properties in the finally reached configuration, the success of the design and alignment could be tested. In this state, one can conclude that the 2D Trap has adequate properties in terms of trap frequencies, flatness ratio, and roundness ratio. The new Microtrap reaches also the expected properties to an acceptable degree, such that the tunable 2D Trap is ready to be used. The 2D Trap image can be exploited for stability measurements, but reflects at this time not the precise parameters of the real 2D Trap. Furthermore, it is possible to load the main part of the atoms into a single layer of the 2D Trap and the 2D Trap is stable enough at least over about half a day. However, it was observed that the setup is temperature-sensitive why it is highly recommendable to start with reliable experiments only after the setup temperature is sufficiently equilibrated.

For future experiments, it might be helpful to measure the precise values of the trap frequencies also for higher beam powers if needed to check the extrapolated values given in this theses. Besides, if the roundness of the trap turns out to be not good enough, it can be interesting to change the elliptical beam configuration before the final focus lens to a better collimated beam by changing the relative distances between the lenses. A second promising method to reach a round trap is to displace the two crossing beams in x-direction from each other. However for most of the experiments, the radial confinement is anyway dominated by the single new Microtrap beam which is perfectly round by itself.

As first demonstration of the new setup, figure 9.1 shows the binarized images from the fluorescence signal of an atomic cloud prepared in the 2D Trap which is made nearly as shallow as possible for this purpose. Besides, figure 9.2 depicts the corresponding atom number distributions and figure 9.3 shows the mean atom number distribution of the atom cloud localized in the 2D Trap.

It is expected that the analysis of these density distributions together with time-of flight images which reflect the momentum distribution can provide deeper understanding of the system of a 2D Fermi gas and its correlations. Here the few-body normal-to-superfluid transition is a subject of interest as well as pairing correlations in the quasi-two-dimensional

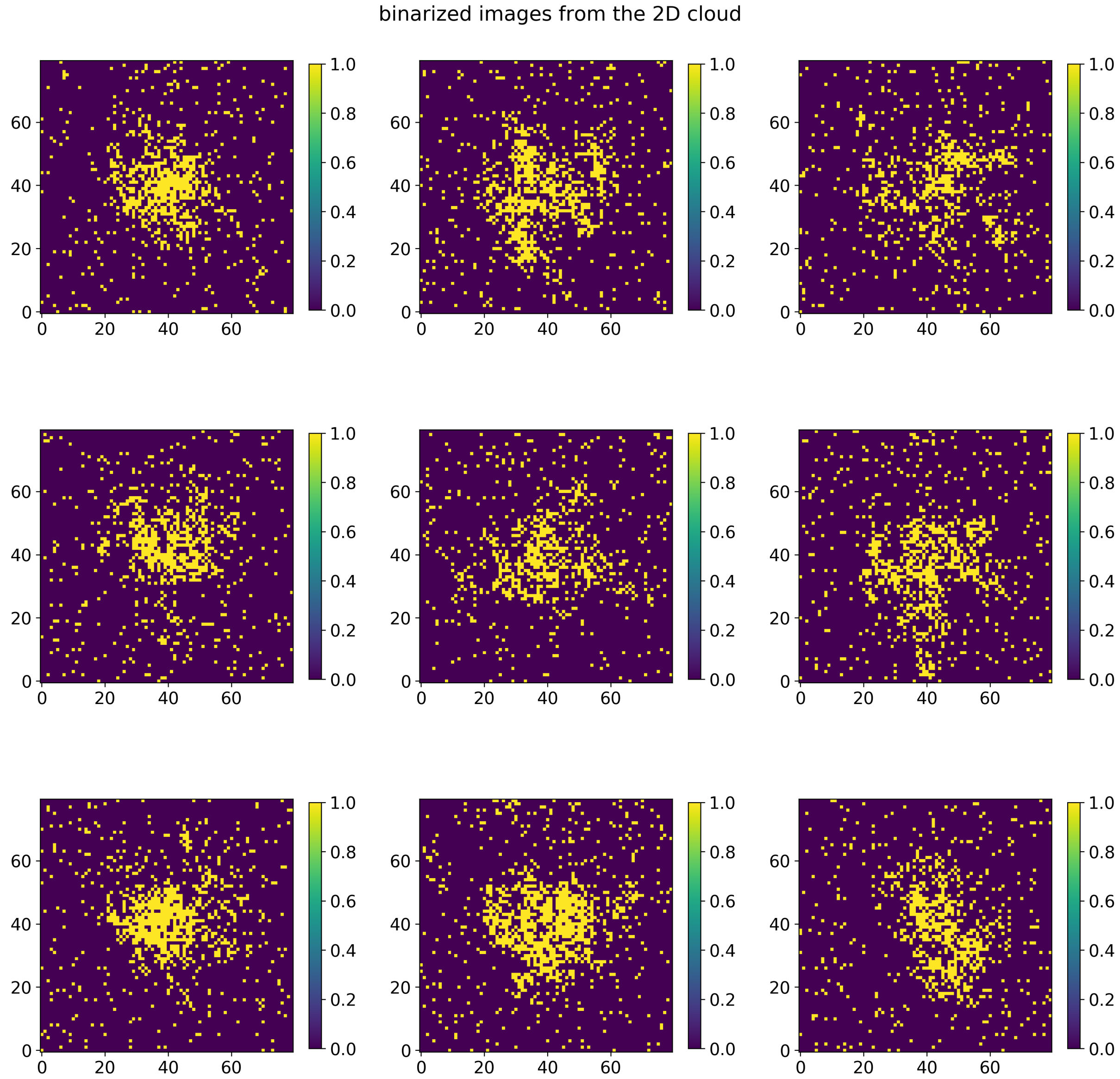

Figure 9.1: Binarized fluorescence images from an atomic cloud in the 2D Trap taken from the top by camera C_3. Bright pixel reflect the count of a photon. The identification of atoms demands the application of an additional low-pass filter. However, this method is not applicable in this case as the atoms are too close to each other.

sample ([9]), the emergence of the described Higgs mode ([3]), and quasi-two-dimensional systems with strong interactions. Furthermore, with an additional upgrade of the experimental setup by a rotating trap designed in [26], it will be possible to investigate even quantum Hall physics.

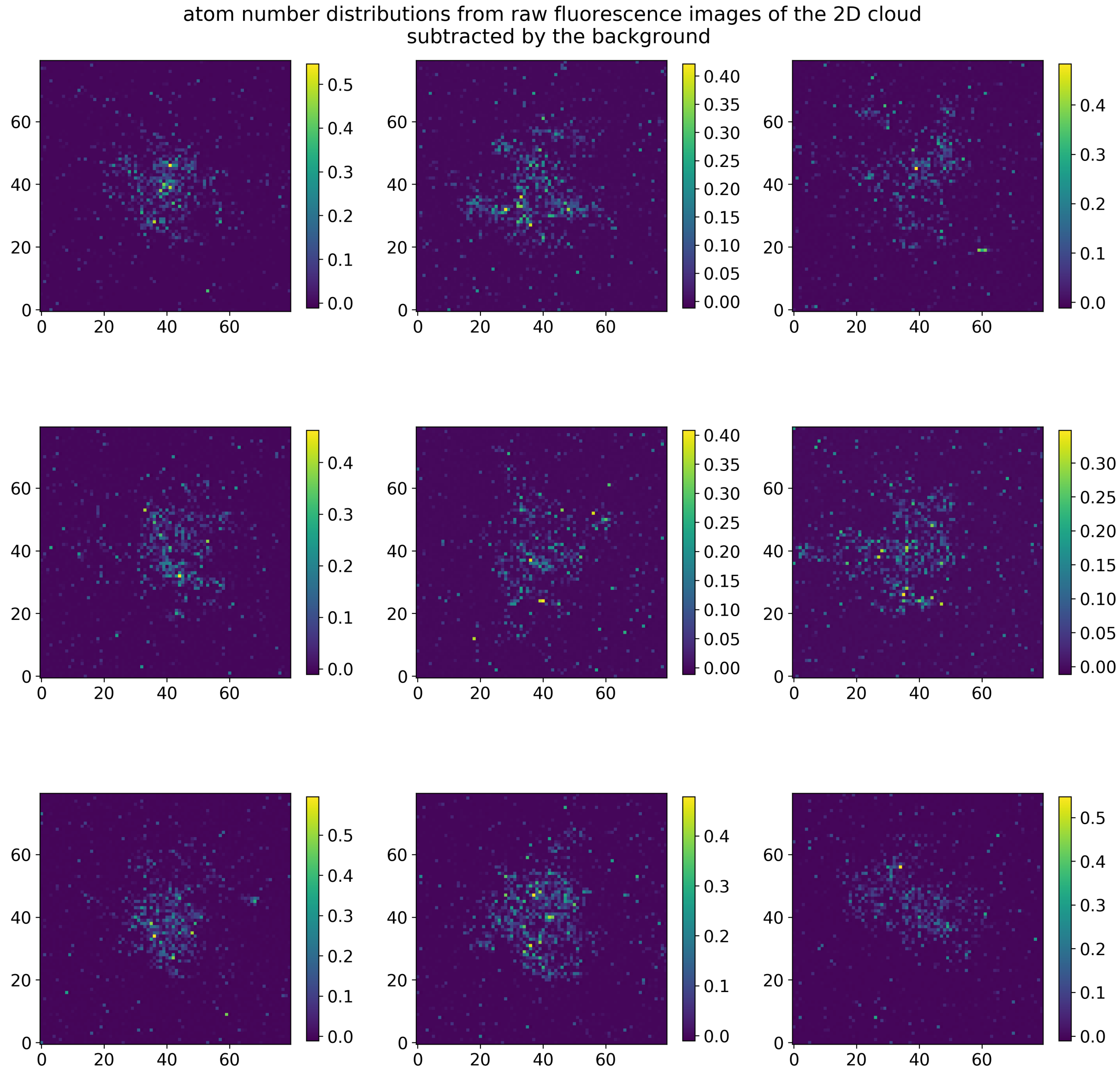

Figure 9.2: Atom number distributions in the 2D Trap corresponding to the raw fluorescence images from the atomic cloud in the 2D Trap normalized by the number of counts per photon which is assumed to be about 300 counts/photon and normalized by the number of photons per atom which is about 24.3 photons/atom. Here, an intensity of $I = 3.12 \cdot I_{sat}$ was assumed leading to a resonant scattering rate of $\Gamma_{sc} = 13.97$ photons/μs. It was also assumed that about 8.7% of the scattered photons are detected and the exposer time is about 20 μs ([2]). A formula for the resonant scattering rate can be found in the appendix.

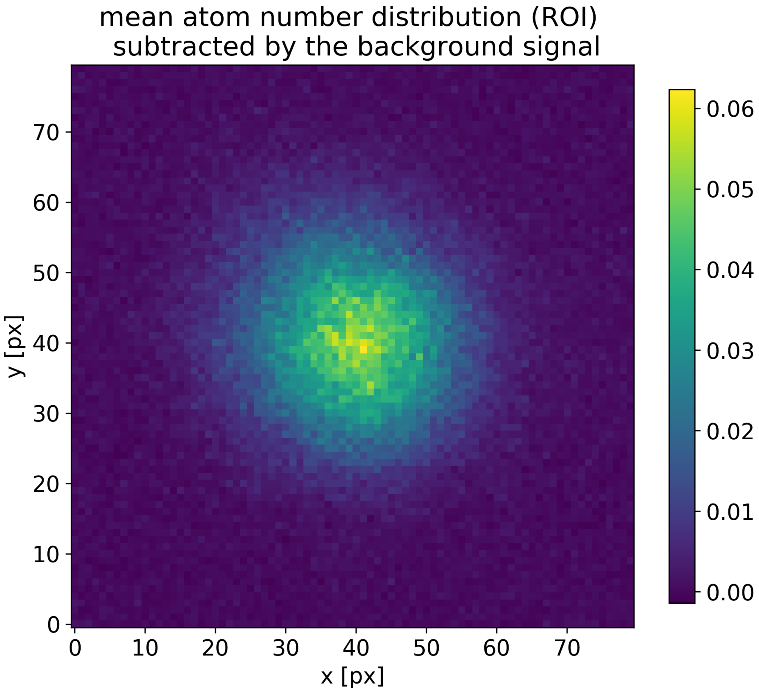

Figure 9.3: Mean atom number distribution in the 2D Trap corresponding to the averaged raw fluorescence image from the atomic cloud in the 2D Trap normalized to the number of counts per photon which is assumed to be about 300 counts/photon and normalized to the number of photons per atom which is about 24.3 photons/atom. Here an intensity of $I = 3.12 \cdot I_{sat}$ was assumed leading to a resonant scattering rate of $\Gamma_{sc} = 13.97$ photons/μs. Furthermore it was assumed that about 8.7% of the scattered photons are detected and the exposer time is about 20 μs ([2]). A formula for the resonant scattering rate can be found in the appendix. If one integrates over the region of interest image, one can count about 37 atoms which are localized on average in the 2D Trap. The standard deviation of the mean atom number from the analysis over all taken images is about 6 atoms. As only one spin state is imaged at a time, this holds for both spin states and the total atom number localized in the trap is twice as large.

Part V

Appendix

A Tunable 2D Trap

A.1 Harmonic approximation

In order to be able to calculate the trap parameters from measured trap properties, one can invert the equations in the following way. To simplify the inversion one can consider only the leading terms in the y- and z-direction which is justified as the last term in both cases scales with λ^2 and $d < W_{0z}$:

$$\omega_y \approx \sqrt{\frac{32aP_{1,2}\sin^2(\theta)}{\pi m W_{0x} W_{0z}^3}} \tag{A.1}$$

$$\omega_z \approx \sqrt{\frac{16aP_{1,2}}{\pi m W_{0x} W_{0z}} \left[\frac{2\cos^2(\theta)}{W_{0z}^2} + \left(\frac{\pi}{d}\right)^2\right]} \approx \sqrt{\frac{16aP}{\pi m W_{0x} W_{0z}} \left(\frac{\pi}{d}\right)^2} \tag{A.2}$$

The inverted equations are then:

$$\boxed{W_{0x} = \left(\frac{32aP_{1,2}}{\pi m (2\pi f_x) W_{0z}}\right)^{\frac{1}{3}} \approx \left(\frac{\sqrt{2}\cdot 8aP_{1,2} f_y}{\pi^2 m f_x^2 \lambda f_z}\right)^{\frac{1}{3}}} \tag{A.3}$$

$$\sin(\theta)^2 \approx \frac{\pi m (2\pi f_y)^2 W_{0x} W_{0z}^3}{32aP_{1,2}} = \left(\frac{m\lambda^4 f_z^4}{32\pi a P f_x f_y}\right)^{\frac{2}{3}} \tag{A.4}$$

$$\boxed{\theta \approx \arcsin\left(\left(\frac{m\lambda^4 f_z^4}{32\pi a P_{1,2} f_x f_y}\right)^{\frac{1}{3}}\right)} \tag{A.5}$$

$$\boxed{W_{0z} \approx \frac{16aP_{1,2}\pi^2 4\sin(\theta)^2}{\pi m W_{0x} (2\pi f_z)^2 \lambda^2} = \sqrt{\frac{\lambda^2 f_z^2}{2\pi^2 f_y^2}}} \tag{A.6}$$

A.2 Finding the target trap: experimental boundary conditions

In this section the central steps for the determination of the optimization curve $W_{0z,min}(\theta)$ that already have been published in [27] should be summarized.

The diameter of the blind before the view port of the experimental vacuum chamber is $D = 0.034$ m, the diameter of the experimental chamber octagon itself is: $q = 0.2027$ m, and the blind thickness is about $b = 0.002$ m. The total diameter of the octagon is therefore:

$$Q = q + 2 \cdot b \tag{A.7}$$

One can conclude that the geometrically maximal half-crossing angle is:

$$\alpha = \arctan\left(\frac{D}{Q}\right) \tag{A.8}$$

The distance from the chamber centre to the blind edge is:

$$L = \sqrt{\left(\frac{D}{2}\right)^2 + \left(\frac{Q}{2}\right)^2} \tag{A.9}$$

The correction shift at the view-port window can be expressed as:

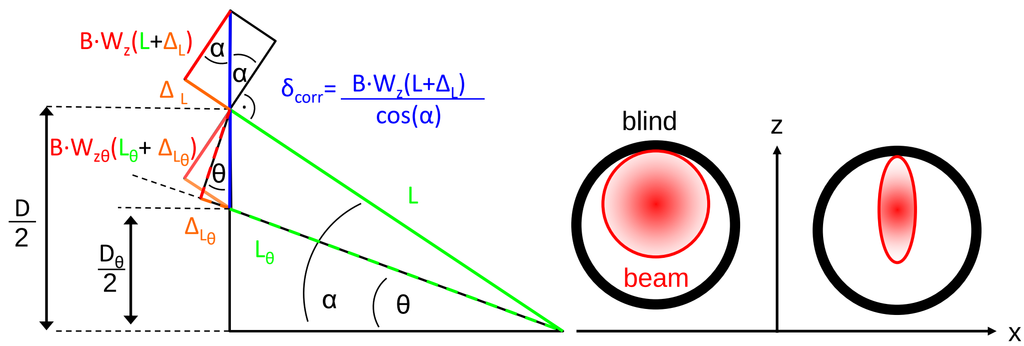

Figure A.1: Experimental boundary conditions: On the left, a schematic of the restriction to the half-crossing angle is shown. On the right, it is demonstrated that the relevant beam size is the vertical component which has to fit through the blind at a half-crossing angle θ. The figure was taken from [27].

$$\delta_{corr} = \frac{D}{2} - \frac{Q}{2}\tan(\theta) \tag{A.10}$$

where $0 \leq \theta \leq \alpha$ is scanned.
Then the maximal beam width at the vacuum window is:

$$W_{z,window} = \frac{1}{B}\delta_{corr}\cos(\theta) \tag{A.11}$$

with $B = 1.7$ including the full power beam radius. In order to find now the corresponding minimal beam waist, one needs the distance between the vacuum window and the beam focus in the centre of the experimental vacuum chamber:

$$L_{fw} = \frac{Q}{2\cos(\theta)} + \delta_{corr}\tan(\theta) \tag{A.12}$$

Then the minimized minimal waist is as function of half-crossing angle is:

$$W_{0z,min} = \sqrt{\frac{W_{z,window}^2 - \sqrt{W_{z,window}^4 - \frac{4L_{fw}^2\lambda^2}{\pi^2}}}{2}} \tag{A.13}$$

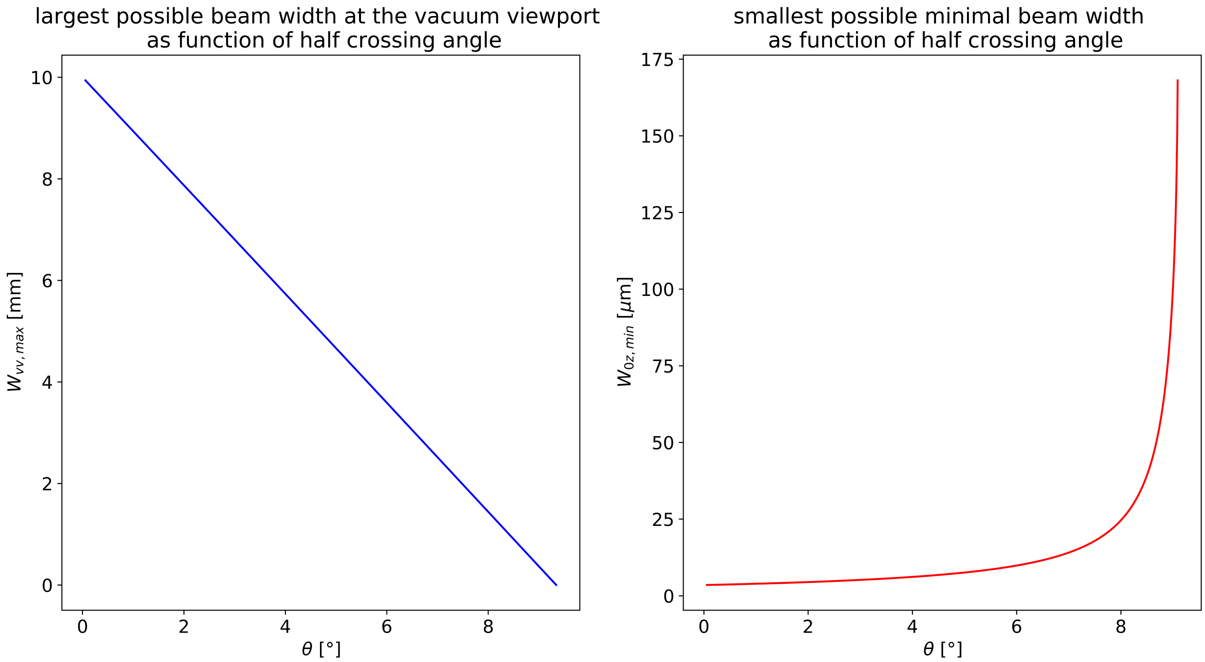

Figure A.2: On the left, the maximal beam width at the view-port blind (window) as function of half-crossing angle is plotted. On the right, the corresponding minimal beam width of the focus in z-direction as function of half-crossing angle is shown.

B Realization of the tunable 2D Trap

B.1 Opto-mechanical design

B.1.1 List of opto-mechanical components

- $M_{1,2,3,4,5,6,7,8,9,10}$: mirror/ high reflective @ 1064 nm/ 1 inch/ $0-45°$/ fused silica/ Lens Optics
- $WP_{1,2,3,4}$: $\lambda/2$-wave-plate/ @ 1064 nm/ 1/2 inch/ FOCtek
- $M_{11,12,13}$: broadband mirror/ BK7/ @ $760-1064$ nm/ 1 inch/ $0-45°$/R $\geq 99.6\%$/ 10 kW/cm^2 CW/Lens Optics: M760-1064/1"
- $M_{14,15}$: broadband mirror/ BK7/ @ $760-1064$ nm/ 0.5 inch/ $0-45°$/R $\geq 99.6\%$/ 10 kW/cm^2 CW/Lens Optics: M760-1064/0.5"
- $M_{16,17,19,20}$: mirror/ 1 inch/ high reflective @ 671 nm/ $0-45°$/ Lens Optics
- M_{18} : dichroic mirror/ 1 inch/ high reflective @ 671+1064 nm (+532 nm)/ $0-45°$/ Lens Optics
- WP_5 : $\lambda/4$-wave-plate / @ 1064 nm/ 0.5 inch/ FOCtek
- WP_6 : $\lambda/4$-wave-plate / 2 inch/ λ @ 1064 nm and $\lambda/4$ @ 671 nm/ FOCtek: WPD0169
- DM_1 : dichroic mirror (long pass)/ 2 inch/ 50% T/R @ 950 nm/ Thorlabs: DMLP950L
- DM_2 : dichroic mirror (short pass)/ 2 inch/ Thorlabs: DMSP805L
- $PBS_{1,2,3}$: polarizing beam splitter cube/ @ 1064 nm/ 0.5 inch/ high power/ Altechna: 2-HPCB-C-0125
- PBS_4 : thin film polarizing beam splitter cube/ extinction ratio = 10000:1/ 1 inch/ @ 671 nm/ LINOS: G335749000
- PBS_5 : polarizing beam splitter cube/ NIR: @ 1064 nm and not so well @ ~ 671 nm/ 50 mm/ Edmund optics
- $NPBS_1$: non-polarizing beam splitter cube/ 0.5 inch/ high power: ~ 1 MW/cm^2 CW/ Spectral Optics: RCBS-50-S-050-BK (or: -FS)
- BS_1 : beam sampler/ @ 1064 nm/ 1 inch/ Thorlabs: BSF10-B
- L_1 : spherical lens/ $f = 75$ mm/ 1 inch/ @ 671+1064 nm/ BK7/ FOCtek

- L_2 : spherical lens/ $f = -50$ mm/ 1 inch/ @ 671+1064 nm/ BK7/ FOCtek
- L_3 : spherical lens/ $f = 50$ mm/ 1 inch/ @ 671+1064 nm
- L_4 : spherical lens/ $f = 125$ mm/ 1 inch/ 0.5% @ 1064 nm and 0.25% @ 671 nm / CASIX: PCX 0305
- L_5 : spherical lens/ $f = 100$ mm/ 1 inch/ 0.5% @ 1064 nm and 0.25% @ 671 nm / CASIX
- L_6 : achromatic doublet/ spherical lens/ $f = 150$ mm/ 2 inch/ B-Coating/ Near IR/ Thorlabs: AC508-150-B
- L_7 : achromatic doublet/ spherical lens/ $f = -40$ mm/ 2 inch/ B-Coating/ Near IR/ Thorlabs: ACN254-040-B
- L_z : cylindrical lens/ $f = -75$ mm/ 1 inch/ @ 1064 nm/ BK7/ FOCtek
- L_{xz} : spherical lens/ $f = 300$ mm / 1 inch/ @ 671+1064 nm/ K9/ FOCtek
- L_x : cylindrical lens/ $f = -250$ mm/ 1 inch/ @ 1064 nm/ N-BK7/ Thorlabs: LK1030L1-C
- $LF1, F2$: spherical lens/ $F = 120$ mm/ 2 inch/ @ 1064 nm/ Gradium Lens/ Light Path: GPX50-120-1
- FC_1 : fibre coupler/ $f = 8$ mm/ @ $650 - 1100$ nm/ Thorlabs: C240TME-B
- FC_2 : fibre coupler/ $f = 8$ mm/ @ 1064 nm/ Thorlabs: C240TME-1064
- FC_3 : fibre coupler/ $f = 6.24$ mm/ @ 1064 nm/ Thorlabs: C110TME-1064
- FC_4 : fibre coupler/ $f = 11$ mm/ @ $650 - 1100$ nm/ Thorlabs: C220TMD-B
- FC_5 : fibre coupler/ spherical lens/ $f = 50$ mm/ 1 inch/ B-coating/ LiCs Fibre: high power/ @ 980 nm/ AMS Technology AG: PMJ-A3AHPCA3AHPC-980-6/125-3AS-1-1-AR2
- AOM : acousto-optical modulator/ $\nu_s = 110$ MHz/ @ 1064 nm/ Gooche and Housego: 3110-197
- AF_1 : absorptive ND filter/ 1 inch/ $ND = 1.0$/ Thorlabs: NE10A
- AF_2 : absorptive ND filter/ 1 inch/ $ND = 0.5$/ Thorlabs: NE05A
- AF_3 : absorptive ND filter/ 1 inch/ $ND = 0.6$/ Thorlabs: NE06A
- $PD_{1,2}$: home-made photodiode
- $PD_{1,2}$: logarithmic photodiode
- GP_1 : glass plate/ 1 inch/ 1 mm thick/ @ $650 - 1050$ nm/ Thorlabs: WG41010-B

B.2 Installation and alignment

B.2.1 Installation of the Trapping-Box

All aluminium components fabricated in the workshop are listed in figures B.3, B.4, B.5, B.6, B.7, B.8, B.9, B.10, B.11, B.12, and B.13. The installation of the Trapping-Box can be executed in the following way:

- Clean all mechanical parts from the workshop.
- Put the micrometer thread (Thorlabs: F6MSSA1) into the central hole of the micrometer screw plate.
- Fix the micrometer screw plate with two M6 screws in the top pocket of the central basis plate, such that the micrometer thread is sandwiched in between.
- Fix the five stud screws at the backside of the central basis plate. Ask the workshop to do it. Alternatively, one can use two screw nuts at the top of the stud screws and rotate them against each other to create a temporal screw head. In this way the stud screw can be fixed and the screw nuts can be removed afterwards. However, the last of the two possibilities presumes a careful procedure because the brass stud screws can be broken apart by the force of the steel screw nuts. Therefore the first possibility is preferable.
- Make sure that the central basis plate can freely be moved in the front pocket of the back plate (you might contact the workshop to fit both parts together).
- Fix the dichroic mirror tower with two M6-screws to the central basis plate while pushing it to the stopper surface.
- Fix the basis plate in the front pocket of the back plate with five screw nuts from behind and lay both horizontally on a table.
- Connect the lock nut (Thorlabs: LN6M25) to the top end of the micrometer screw (Thorlabs: F6MSS50). On top connect a removable adjuster knob (Thorlabs: F6MSSK1). Turn the adjuster knob against the lock nut to fix it at the screw head.
- Connect the micrometer screw to the top hole through the back plate into the central basis plate.
- Glue $NPBS_1$ in the right orientation on top of the beam splitter tower of the central basis plate while pushing it to the stopper surface.
- Fix DM_1 in a lens mount (Thorlabs: LMR2/M), such that the surface reflecting the laser with a wavelength of $\lambda = 671$ nm points to the closed surface of the lens mount.

- Connect the lens mount (Thorlabs: LMR2/M) with the dichroic mirror to the lower pocket in the dichroic mirror tower with a long enough M4-screw. The closed surface of the lens mount has to point up and one has to push the open side to the stopper surface while fixing the mount.
- Fix mirror M_{18} in a mirror mount (Thorlabs: FMP1/M), such that the reflecting side points to the open side of the mirror mount.
- Connect the mirror mount with M_{18} to the upper pocket in the dichroic mirror tower, such that the open side of the mount points downward to the surface of the central basis plate and fix it with a M4-screw while pushing the open side of the mount to the stopper surface.
- Glue mirror M_{13} in a fixed mirror mount (Thorlabs: POLARIS-B1G) with the reflecting side to the open side of the mount.
- Connect the mirror mount with M_{13} to the lower right step on the central basis plate while pushing the open side of the mount to the stopper surface.
- Connect the translation stage (Thorlabs: MS1/M) in the lower pocket of the central basis plate while pushing it to the bottom side. One might want to put a paper in between the translation stage and the bottom surface while fixing the translation stage with two M4-screws. Afterwards one can remove the paper and the translation stage can move freely but is well defined in position.
- Glue L_x in the L_x-lens mount with the flat surface pointing to the closed side. Make sure that the cylindrical lens is oriented such that the curvature appears to be along the x-direction, in the same direction as the fixing screws of the lens mount.
- Fix the lens mount with L_x on the translation stage with two M4-screws, such that the screws are to the left of the lens. One has two possible configurations which are 12.5 mm apart. It is recommended to choose the right hole pair because of the calculated lens distances.
- Put WP_5 into a rotatable mount (Thorlabs: RSP05/M).
- Connect the rotatable mount to the wave-plate holder, such that laser light can travel straight through the wave-plate and the rectangular hole in the holder. The rotation ring has to point to the same side as the top edge of the holder.
- Connect the wave-plate holder to the right side of the central basis plate with two M4-screws. The rotation ring of the wave-plate mount has to point to the dichroic mirror.
- Put $M_{14,15}$ into the two piezo mirror mounts (Newport: AG-M050N).
- Connect the two mirror mounts with the mirrors $M_{14,15}$ to the two steps on the left side of the central basis plate. Fix the mirror mounts each with a single M4-screw from the top into the surface of the central basis plate and ignore the side holes. Use

the side surface next to the mirror mount to align the orientation properly before fixing it.

- Connect the bottom plate to the central basis plate with five M6-screws while the basis plate lies on the table. Exploit the stopper surface for proper alignment.
- Thread the cable from the fixed piezo mirror mounts through the respective holes of the entrance plate such that the guiding edge of the entrance plate points towards the central basis plate. The top hole is intended for the cables of the top mirror and the two holes at the bottom are for the cables from the bottom mirror, but the central hole of the three bottom holes is for the infrared beam.
- Connect the entrance plate to the back plate and the bottom plate with five M6-screws.
- Orientate the setup, such that the bottom plate is at the bottom.
- Connect the bottom cover plate with a single M4-screw with a countersunk head to the bottom plate.
- Connect the side cover plate with eight M4-screws to the setup by pushing it carefully over the back plate.
- Connect the MOT-lens holder to the entrance plate with three M4-screws.
- Connect a cage plate (Thorlabs: CP02/M) with a single M4-screw to the MOT-lens holder roughly in the central position of the elongated hole.
- Put L_4 into an adjustable lens tube (Thorlabs: SM1V10) with the flat side to the open side of the tube.
- Connect the lens tube with L_4 to the cage plate fixed at the MOT-lens holder from the outer side, such that the open side of the tube points away from the entrance plate.
- Connect the modified cage plate (modified Thorlabs: LCP08/M) with three M4-screws to the pocket on the right side of the central basis plate while pushing it to the stopper surface. Two holes are added to the single hole at the bottom of the cage plate and the cut surfaces should be left of the open sides.
- Put L_{F1} into an adjustable lens tube (Thorlabs: SM2V05) such that the flat surface of the lens points to the open side of the tube.
- Connect the lens tube with L_{F1} to the modified cage plate, such that the open side of the tube points to the right, away from WP_5.
- Connect the top exit cover with the central basis plate on the right side above L_{F1}, such that the edge points to the side cover plate.

- Connect the bottom exit cover with the central basis plate on the right side below L_{F1}, such that the edge points to the side cover plate.
- Insert the glass plate GP_1 with an appropriate Thorlabs mount system.
- Connect the front cover plate with maximally seven M4-screws to the side of the entrance plate, the bottom plate, and the dichroic mirror tower.
- Push the front exit cover plate over the lens tube of L_{F1}.
- If one wants to open the setup, reverse the steps above.
- Connect two cage plates (Thorlabs: CP02/M) with two long M4-screws to the left part of the telescope plate. Use round spacer plates of total width of 16 mm for each cage plate to fix them, such that the optical axis is about 57.6 mm above the optical table.
- Glue L_z on a rotatable cage plate (Thorlabs: CRM1/M) with the flat lens surface on the rotation ring.
- Integrate the rotatable cage plate with L_z between the two fixed cage plates on the telescope plate with four cage rods (Thorlabs: ER4). The upper front cage rod should have adjustment marks (Thorlabs: ER4E). The curved lens surface has to point to the left. As first orientation, one can position L_z above the mark on the telescope plate (non-collimated configuration).
- Connect two lens tube holders (Thorlabs: SM1RC/M) to the left of the telescope plate with two long M4-screws. Use round spacer plates of total height of 17 mm to reach a height of the optical axis of about 57.6 mm above the optical table. The two lens tube holders should be positioned to one of the hole pairs on the right and should be as close as possible to each other.
- Put L_{xz} in an adjustable lens tube (Thorlabs: SM1V15), such that the flat surface of the lens points to the open side of the tube.
- Put the adjustable lens tube with L_{xz} in a lens tube (Thorlabs: SM1L15).
- Put the lens tube with L_{xz} into the two lens tube holders on the telescope plate, such that the closed side of the tube points to the right and the open side with L_{xz} points to the left where L_z is already fixed. As first orientation, one can position L_{xz} above the mark on the telescope plate (non-collimated configuration).
- Put the mirrors $M_{11,12}$ into two mirror mounts (Thorlabs: POLARIS-K1S4).
- Connect the two mirror mounts to the two holes in the front and back sides of the central part of the telescope plate. Use round spacer plates of a total height of 12 mm, such that the optical axis is about 57.6 mm above the optical table. The front mirror should have an angle of about 22.5° relative to the edge of the telescope plate behind him, and the back mirror should be parallel to the right edge of the telescope plate behind him.

- Connect the telescope plate with two M6-screws through the two holes on the right edge of the telescope plate to the entrance plate of the Trapping-Box.

B.2.2 Installation of the Imaging-Box

All aluminium components fabricated in the workshop are listed in figures B.17, B.18, B.19, B.20, B.21, B.22, B.23, and B.24. The installation of the Imaging-Box can be executed in the following way:

- Clean all mechanical parts from the workshop.
- Put the micrometer thread (Thorlabs: F6MSSA1) into the central hole of the micrometer screw plate.
- Fix the micrometer screw plate with two M6 screws in the top pocket of the central basis plate, such that the micrometer thread is sandwiched in between.
- Fix the five stud screws at the backside of the central basis plate. Ask the workshop to do it. Alternatively, one can use two screw nuts at the top of the stud screws and rotate them against each other to create a temporal screw head. In this way the stud screw can be fixed and the screw nuts can be removed afterwards. However, the latter of the two possibilities presumes a careful procedure because the brass stud screws can be broken apart by the force of the steel screw nuts. Therefore the first possibility is preferable.
- Make sure that the central basis plate can be moved freely in the front pocket of the back plate (you might contact the workshop to fit both parts together).
- Connect the side plate to the lower pocket of the central basis plate with four M6-screws while pushing it to the stopper surface and align the side edges on top of each other.
- Connect the MOT-path plate with one M6-screw to the central basis plate and two M6-screws to the side plate while pushing it to the stopper surface of the side plate.
- Connect the beam-splitter fixing foot to the central basis plate with a single M6-screw while pushing it to the stopper step next to it.
- Insert WP_6 into a rotatable cage plate (Thorlabs: LCRM2-M) with the edge mark aligned to the zero of the rotation ring.
- Connect the rotatable cage plate with WP_6 by using maximally three M4-screws to the left pocket of the two pockets on the right side of the central basis plate, such that the rotation ring points to the left.
- Insert DM_2 into a mirror mount (Thorlabs: FMP2/M), such that the side which reflects laser light with a wavelength of $\lambda = 1064$ nm points to the closed side of the mirror mount.

- Connect the mirror mount with DM_2 to the side plate with a single M4-screw while pushing the closed side of the mount to the stopper surface at an angle of 45°. The side which reflects infrared laser light should point now away from the central basis plate.

- Connect the bottom plate with five M6-screws to the back plate while pushing it to the stopper surface and align the side edges on top of each other.

- Fix the basis plate in the front pocket of the back plate with five screw nuts from behind. One can orientate the setup with the bottom plate on the table during this procedure.

- Connect the lock nut (Thorlabs: LN6M25) to the top end of the micrometer screw (Thorlabs: F6MSS50). On top connect a removable adjuster knob (Thorlabs: F6MSSK1). Turn the adjuster knob against the lock nut to fix it at the screw head.

- Connect the micrometer screw to the top hole through the back plate into the central basis plate.

- Connect the fixing plate to the back plate and the bottom plate with four M6-screws.

- Put PBS_5 on the left side of the side plate and push it to the stopper surface from the central basis plate. The cube should be orientated such that the vertically polarized light is reflected away from the surface of the central basis plate.

- Put the beam-splitter cube hat on the top of PBS_5 such that the central hole points upwards and the stopper surface at the bottom side of the hat pushes the cube to the surface of the central basis plate.

- Fix the beam-splitter cube hat and PBS_5 carefully with a single M4-screw through the beam-splitter fixing foot pushing with the tip into the central hole of the hat. The screw should not be fixed too strongly as PBS_5 can break.

- Connect the modified cage plate (modified Thorlabs: LCP08/M) with three M4-screws to the pocket on the right side of the central basis plate while pushing it to the stopper surface. To the single hole at the bottom of the cage plate two holes are added and the cut surfaces should be left of the open sides.

- Put L_{F1} into an adjustable lens tube (Thorlabs: SM2V05), such that the flat surface of the lens points to the open side of the tube.

- Connect the lens tube with L_{F1} to the modified cage plate, such that the open side of the tube points to the right, away from WP_6.

- Put mirror M_{19} into a mirror mount (Thorlabs: FMP1/M) with the reflecting side to the closed side of the mirror mount.

- Connect the mirror mount with M_{19} to the lower hole in the MOT-path plate while pushing the closed and reflecting side to the stopper surface. The mirror is fixed at an angle of 45°.
- Connect a cage plate (Thorlabs: CP02/M) to the central hole in the MOT-path plate while pushing it to the stopper surface.
- Put L_5 into an adjustable lens tube (Thorlabs: SM1V10), such that the curved side of the lens points to the open side of the tube.
- Connect the lens tube with L_5 to the top side of the cage plate which is fixed to the MOT-path plate, such that the open side of the tube points upwards.
- Put mirror M_{20} into a mirror mount (Thorlabs: KM100).
- Connect the mirror mount with M_{20} to the top hole of the MOT-path plate, such that the reflecting side points downwards and is parallel to the optical table.
- Connect the guiding hand plate to the upper left side of the back plate with three M4-screws.
- Connect the beam-splitter cover plate to the left side of the side plate with two M4-screws, such that the curved edge points away from the central basis plate.
- Connect a lens tube holder (Thorlabs: SM2RC/M) to the left hole in the side plate next to PBS_5 with a single M4-screw.
- Connect the bottom cover plate to the central basis plate and the cage plate of L_{F2} with five M4-screws.
- Connect the top cover plate to the central basis plate and the cage plate of L_{F2} with four M4-screws.
- connect the front cover plate to the side plate and the top and bottom cover plates with four M4-screws.

B.2.3 Precise alignment of the imaging-beam

The beam width of the imaging-beam along its optical path can be found in figure B.29.

B.2.4 Precise alignment of the 2D Trap beams

Making the 2D Trap circular

The original intensity distribution of the 2D Trap has the following form. The two individual intensity distributions can be written as ([27]):

$$I_1(x, y, z) = \frac{2P}{\pi \cdot W_x(l_2) W_z(l_2)} \cdot \exp\left(- \frac{2x^2}{W_x^2(l_2)} - \frac{2}{W_z^2(l_2)} \cdot (\sin(\theta)y + \cos(\theta)z)^2 \right) \quad \text{(B.1)}$$

$$I_2(x,y,z) = \frac{2P}{\pi \cdot W_x(l_1) W_z(l_1)} \cdot \exp\left(- \frac{2x^2}{W_x^2(l_1)} - \frac{2}{W_z^2(l_1)} \cdot (-\sin(\theta)y + \cos(\theta)z)^2 \right) \quad \text{(B.2)}$$

where $l_1 = \cos(\theta)y - \sin(\theta)z$ for the first beam and $l_2 = \cos(\theta)y + \sin(\theta)z$ for the second beam are the distances to the focal points which lie on the crossing point of both beams. The wave-vectors indicating the propagation direction of both beams are:

$$\vec{k}_1 = k \cdot (0, \cos(\theta), -\sin(\theta)) \quad \text{and} \quad \vec{k}_2 = k \cdot (0, \cos(\theta), \sin(\theta)) \quad \text{(B.3)}$$

where the wave-number $k = \frac{2\pi}{\lambda}$ can be expressed by the wavelength λ, which is in the experiment red-detuned to $\lambda = 1064$ nm. The total original intensity distribution is then:

$$I_{tot}(x,y,z) = I_1(x,y,z) + I_2(x,y,z) + 2 \cdot \sqrt{I_1(x,y,z)} \sqrt{I_2(x,y,z)} \cdot \cos((\vec{k}_1 - \vec{k}_2) \cdot \vec{x} + \Delta\phi) \quad \text{(B.4)}$$

In contrast, the real intensity distribution might be modified because of non-optimal alignment or aberrations. This can be considered by small shifts of both beams in each spatial dimension and small changes of the half-crossing angle, but with $\Delta\phi = 0$:

$$I_{mod}(x,y,z) = I_1 + I_2 + 2 \cdot \sqrt{I_1}\sqrt{I_2} \cdot \cos(\vec{k}_1 \vec{x}_1 - \vec{k}_2 \vec{x}_2) \quad \text{(B.5)}$$

with:

$$I_1 = I_1(x + dx_1, y + dy_1, z + dz_1, \theta + d\theta_1) \quad \text{(B.6)}$$

$$I_2 = I_2(x + dx_2, y + dy_2, z + dz_2, \theta + d\theta_2) \quad \text{(B.7)}$$

$$\vec{k}_1 \vec{x}_1 = k \cos(\theta + d\theta_1)(y + dy_1) - k \sin(\theta + d\theta_1)(z + dz_1) \quad \text{(B.8)}$$

$$\vec{k}_2 \vec{x}_2 = k \cos(\theta + d\theta_2)(y + dy_2) + k \sin(\theta + d\theta_2)(z + dz_2) \quad \text{(B.9)}$$

Relative shift in x-direction To decrease the trap frequency in x-direction relative to the trap frequency in y-direction, one can shift both beams apart from each other in x-direction by the shift distance Δx, such that it holds: $dx_1 = \Delta x/2$ and $dx_2 = -\Delta x/2$. The observed effect is demonstrated in the graphs B.30, B.31 and B.32 for $\Delta x = 100$ μm and the usual trap parameters: $W_{0x} \approx 133$ μm, $W_{0z} = 17$ μm and $\theta = 7.3°$.
However, this procedure can not be executed for arbitrarily large shifts in x-direction because for too large shifts there exists no unique maximum in x-direction anymore as is exemplarily shown in figure B.33. The maximal possible shift for the given trap configuration is about $\Delta x \approx 180$ μm, such that there still appears a unique intensity maximum in x-direction. To investigate the effect of the shift on the shape of the effective harmonic

trap in the centre of the intensity distribution, figure B.34 depicts the harmonic trap frequencies, the roundness ratio, and the potential depth as functions of relative beam shift. One can conclude that this method allows the manipulation of the circularity of the light sheets quite effectively. The method can be applied if the trap frequency in y-direction is smaller than in x-direction. This is the usual case for a too small ellipticity of the beams. However, one has to mention that the procedure leads to a decrease of the overall absolute values of the trap frequencies. For a small correction of the circularity in the range of a few percent, the method is nevertheless a good choice.

Symmetric focus shift During the alignment procedure, it is possible that one faces the case that the two single-beam foci appear not at the same position and both can not be overlapped with the crossing point at the same time. In this case two scenarios are possible. Either only one of the two single-beam foci can be overlapped with the crossing point, or one can place the two foci left and right from the crossing point symmetrically. It is clear that it is desirable to move the single-beam foci as close as possible to the crossing point to reach high trap frequencies and to maximize the ellipticity in the overlapping region for circular light sheets. The question remains which of the two procedures leads to a better performance of the trap. To answer this question one can introduce a shift parameter d_f to shift the single-beam foci along the beam propagation direction with following relations:

$$dy_1 = d_{f1} \cos(\theta + d\theta) \tag{B.10}$$

$$dz_1 = -d_{f1} \sin(\theta + d\theta) \tag{B.11}$$

$$dy_2 = d_{f2} \cos(\theta + d\theta) \tag{B.12}$$

$$dz_2 = d_{f2} \sin(\theta + d\theta) \tag{B.13}$$

The figures B.35, B.36, and B.37 show the effect of a symmetric shift of the single-beam foci around the crossing point with: $d_{f1} = 500\ \mu$m and $d_{f2} = -500\ \mu$m. One has to remark that the cuts through the interference pattern are made through the central layer and in the case of the symmetric shift a phase shift appears which shifts the central layer along the z-direction.
In figure B.38, the two described cases are compared with each other, and one can see that if the foci are symmetrically positioned around the crossing point the overall intensity is slightly larger.
In the symmetric case holds:
$d_{f1} = \Delta d_f/2$ and $d_{f2} = -\Delta d_f/2$
and for the asymmetric case:

$d_{f1} = \Delta d_f$ and $d_{f2} = 0$

One can conclude that it is slightly preferable to align the two single-beam foci symmetrically before and behind the crossing point, but the difference is not very large and also depends on the relative single-beam focus distance Δd_f. One has to remark that for a distance of $\Delta d_f = 2000\ \mu$m the asymmetric configuration seems to be a little bit better as portrayed in figure B.39.
So, for small relative single-beam focus distances the symmetric configuration is preferable, whereas for larger ones the asymmetric configuration is better. To check this behaviour more precisely, figure B.40 shows the identified intensity maximum along the z-direction as function of focus shift Δd_f for the two configurations.

B.3 Characterization

B.3.1 Trap parameters

Estimation of the crossing angle: interpretation of the measured crossing angle

The two half-crossing angles for the top and bottom beams could be identified from a two-dimensional fit to the atom-absorption image while the atoms are trapped in the single beams. However, the resulting angles seem to be far away from the expected ones, but one has to take care about their interpretations because the absolute values depend on the perspective of camera C_1 on the beams. To approach the values of the actual angles one has to consider at least that camera C_1 sees the two beams under an angle of $\alpha = 45°$. Conceptionally, one can rotate the two 2D Trap beams represented by two unit vectors:

$$\vec{e}_1 = (0, \cos(\theta_1), -\sin(\theta_1)) \tag{B.14}$$

and

$$\vec{e}_2 = (0, \cos(\theta_2), \sin(\theta_2)) \tag{B.15}$$

around the z-axis using a rotation matrix of the form:

$$R_z(\alpha) = \begin{pmatrix} \cos(\alpha) & -\sin(\alpha) & 0 \\ \sin(\alpha) & \cos(\alpha) & 0 \\ 0 & 0 & 1 \end{pmatrix} \tag{B.16}$$

From a rotation of $\alpha = 45°$ around the z-axis follows:

$$R_z(\alpha = 45°)\vec{e}_1 = \left(-\frac{\cos(\theta_1)}{\sqrt{2}}, \frac{\cos(\theta_1)}{\sqrt{2}}, -\sin(\theta_1) \right) \tag{B.17}$$

and

$$R_z(\alpha = 45°)\vec{e}_2 = \left(-\frac{\cos(\theta_1)}{\sqrt{2}}, \frac{\cos(\theta_1)}{\sqrt{2}}, \sin(\theta_1) \right) \tag{B.18}$$

Subsequently, one can use the yz-plane as camera perspective, and one can just use the projection of the two unit vectors on the yz-plane to determine the half-crossing angles seen by the camera:

$$\tilde{\theta}_1 = \arctan\left(\frac{|e_{1,rot,z}|}{|e_{1,rot,y}|}\right) = \arctan\left(\frac{|-\sin(\theta_1)|}{\cos(\theta_1)}\sqrt{2}\right) = \arctan\left(\tan(\theta_1)\sqrt{2}\right) \tag{B.19}$$

$$\tilde{\theta}_2 = \arctan\left(\frac{|e_{2,rot,z}|}{|e_{2,rot,y}|}\right) = \arctan\left(\frac{\sin(\theta_2)}{\cos(\theta_2)}\sqrt{2}\right) = \arctan\left(\tan(\theta_2)\sqrt{2}\right) \tag{B.20}$$

By inverting the two equations, one can calculate the real expected angles from the angles measured on the camera images:

$$\theta_{1,2} = \arctan\left(\frac{\tan(\tilde{\theta}_{1,2})}{\sqrt{2}}\right) \tag{B.21}$$

and error:

$$d\theta_{1,2} = \frac{d\tilde{\theta}_{1,2}}{\left(\frac{\tan^2(\tilde{\theta}_{1,2})}{2}+1\right)\sqrt{2}\cos^2(\tilde{\theta}_{1,2})} \tag{B.22}$$

With the results from the two-dimensional fit-model one can conclude:
$\theta_1 = (6.26 \pm 0.06)°$ and
$\theta_2 = (-8.42 \pm 0.06)°$.
Unfortunately, this result is still asymmetric in the two crossing angles although the total crossing angle of: $\chi = |\theta_1| + |\theta_2| = (14.68 \pm 0.08)°$ is quite promisingly near the expected value of: $\chi_{ideal} = 14.6°$. However, it is not very probable that the asymmetry observed on camera C_1 is real because the 2D Trap beams were properly aligned. In contrast, one can assume that the camera sees the two 2D Trap beams under an additional angle from a rotation around the y-axis. To check if this hypothesis is possible, one can use an additional rotation matrix:

$$R_y(\beta) = \begin{pmatrix} \cos(\beta) & 0 & \sin(\beta) \\ 0 & 1 & 0 \\ -\sin(\beta) & 0 & \cos(\beta) \end{pmatrix} \tag{B.23}$$

From an additional rotation of $\beta = 1.5°$ around the y-axis follows:

$$R_y(\beta = 1.5°)R_z(\alpha = 45°)\vec{e}_1 = \begin{pmatrix} -\frac{\cos(\beta)}{\sqrt{2}}\cos(\theta_1) - \sin(\beta)\sin(\theta_1) \\ \frac{\cos(\theta_1)}{\sqrt{2}} \\ \frac{\sin(\beta)}{\sqrt{2}}\cos(\theta_1) - \cos(\beta)\sin(\theta_1) \end{pmatrix} \tag{B.24}$$

and

$$R_y(\beta = 1.5°)R_z(\alpha = 45°)\vec{e}_2 = \begin{pmatrix} -\frac{\cos(\beta)}{\sqrt{2}}\cos(\theta_2) + \sin(\beta)\sin(\theta_2) \\ \frac{\cos(\theta_2)}{\sqrt{2}} \\ \frac{\sin(\beta)}{\sqrt{2}}\cos(\theta_2) + \cos(\beta)\sin(\theta_2) \end{pmatrix} \tag{B.25}$$

The angles detected on camera C_2 can again be concluded by using the projection components of the two unit vectors on the yz-plane:

$$\tilde{\theta}_1 = \arctan\left(\frac{|e_{1,rot,z}|}{|e_{1,rot,y}|}\right) = \arctan\left(\frac{\frac{\sin(\beta)}{\sqrt{2}}\cos(\theta_1) - \cos(\beta)\sin(\theta_1)}{\cos(\theta_1)}\sqrt{2}\right) \tag{B.26}$$

$$\tilde{\theta}_2 = \arctan\left(\frac{|e_{2,rot,z}|}{|e_{2,rot,y}|}\right) = \arctan\left(\frac{\frac{\sin(\beta)}{\sqrt{2}}\cos(\theta_2) + \cos(\beta)\sin(\theta_2)}{\cos(\theta_2)}\sqrt{2}\right) \tag{B.27}$$

Finally, one can invert the equations to get the real expected half-crossing angles from the angles measured on the camera images:

$$\theta_1 = \arctan\left(\frac{\sin(\beta) - \tan(\tilde{\theta}_1)}{\sqrt{2}\cos(\beta)}\right) \tag{B.28}$$

$$d\theta_1 = \frac{d\tilde{\theta}_1}{\left(\left(\frac{\sin(\beta)-\tan(\tilde{\theta}_1)}{\sqrt{2}\cos(\beta)}\right)^2 + 1\right)\sqrt{2}\cos^2(\tilde{\theta}_1)} \tag{B.29}$$

$$\theta_2 = \arctan\left(\frac{\tan(\tilde{\theta}_2) - \sin(\beta)}{\sqrt{2}\cos(\beta)}\right) \tag{B.30}$$

$$d\theta_2 = \frac{d\tilde{\theta}_2}{\left(\left(\frac{\tan(\tilde{\theta}_1)-\sin(\beta)}{\sqrt{2}\cos(\beta)}\right)^2 + 1\right)\sqrt{2}\cos^2(\tilde{\theta}_1)} \tag{B.31}$$

For rotation angles: $\alpha = 45°$ and $\beta = -1.5°$ follows:
$\theta_1 = (7.31 \pm 0.06)°$,
$\theta_2 = (-7.38 \pm 0.06)°$ and
$\chi = |\theta_1| + |\theta_2| = (14.69 \pm 0.08)°$.
So, it seems to be reasonable to assume the the camera C_1 is tilted about the two angles $\alpha = 45°$ and $\beta = -1.5°$ with respect to the two 2D Trap beams. From the total crossing angle one can deduce an expectation of the mean half cross angle of: $\theta = (7.35 \pm 0.04)°$.

B.3.2 Stability

Stability during the tomography

Figure B.41 shows the stability analysis of the combined 2D Trap, whereas the analysis of the camera C_2 images in figure B.42 can only reflect the stability of the 2D Trap.

parameter/property	prop. from param.	param. from prop.	pa. from pr. (fixed θ)
$P_{1,2}$ [W] (tunable)	–	$\equiv 0.1$	$\equiv 0.1$
λ [nm]	–	$\equiv 1064$	$\equiv 1064$
W_{0x} [μm]	–	119.2 ± 3.5	167.5 ± 7.6
W_{0z} [μm]	–	21.63 ± 0.59	7.80 ± 0.52
θ [°]	–	10.35 ± 0.28	$\equiv 7.35 \pm 0.04$
$E \equiv \frac{W_{0x}}{W_{0z}}$ [1]	–	5.51 ± 0.22	21.5 ± 1.7
$d \equiv \frac{\lambda}{2\sin(\theta)}$ [μm]	–	2.96 ± 0.08	$\equiv 4.159 \pm 0.023$
f_x [Hz]	82.6 ± 0.3	–	–
f_y [Hz]	39.9 ± 0.3	–	–
$f_r \equiv \frac{f_x+f_y}{2}$ [Hz]	61.23 ± 0.23	–	–
f_z [kHz]	5.19 ± 0.04	–	–
$R_{2D} \equiv \frac{f_z}{f_r}$ [1]	84.7 ± 0.7	–	–
$R_{xy} \equiv \frac{f_x}{f_y}$	2.070 ± 0.018	–	–
$U_0 = -aI_0$ [μK$\cdot k_B$]	-0.671 ± 0.003	–	–
$U_0 = -aI_0$ [$h \cdot f_z$]	-2.695 ± 0.024	–	–
$N_{2D} \equiv \frac{f_z^2}{4 f_x f_y}$ [1]	2042 ± 36	–	–

Table B.1: 2D Trap characteristics including trap parameters and trap properties for $P_{1,2} = 0.1$ W. Here, the trap properties are calculated from the measured trap parameters, and the trap parameters are calculated from the measured trap properties. In the last column the half-crossing angle is assumed to be known to calculate the other trap parameters from the measured trap properties.

B.3.3 Characterization results

The formulas for the calculation of the 2D Trap properties from the 2D Trap parameters are summarized below together with the expressions for the calculation of the 2D Trap parameters from the 2D Trap properties. Table B.1 shows the results for $P_{1,2} = 0.1$ W and table B.2 the results for $P_{1,2} = 2$ W. If one assumes that the measured trap parameters are true, the calculated trap frequencies are smaller than the target values and much smaller than the measured values. The calculated flatness ratio fits better to the measured value, but the roundness ratio is twice as large as the measured one. If one assumes that the trap properties are true, the beam widths are smaller than the measured ones except for W_{0x} for $P_{1,2} = 0.1$ W, and the half-crossing angle is much larger than the measured one. In the case of $P_{1,2} = 2$ W the half-crossing angle even is about twice as large as the measured one which is not possible because of the experimental boundary conditions. Therefore it seems more reasonable to also assume the half-crossing angle is known to have the measured value. In this case the calculated beam width in z-direction is much smaller than the measured value.

To calculate the 2D trap properties from the 2D trap parameters the following formulas

parameter/property	prop. from param.	param. from prop.	pa. from pr. (fixed θ)
$P_{1,2}$ [W] (tunable)	–	$\equiv 2$	$\equiv 2$
λ [nm]	–	$\equiv 1064$	$\equiv 1064$
W_{0x} [μm]	–	94.7 ± 2.8	167.5 ± 7.7
W_{0z} [μm]	–	21.61 ± 0.61	3.90 ± 0.26
θ [°]	–	13.08 ± 0.36	$\equiv 7.35 \pm 0.04$
$E \equiv \frac{W_{0x}}{W_{0z}}$ [1]	–	4.38 ± 0.18	43.0 ± 3.5
$d \equiv \frac{\lambda}{2\sin(\theta)}$ [μm]	–	2.35 ± 0.06	$\equiv 4.159 \pm 0.023$
f_x [Hz]	369.2 ± 1.6	–	–
f_y [Hz]	178.4 ± 1.4	–	–
$f_r \equiv \frac{f_x+f_y}{2}$ [Hz]	273.8 ± 1.0	–	–
f_z [kHz]	23.20 ± 0.18	–	–
$R_{2D} \equiv \frac{f_z}{f_r}$ [1]	84.7 ± 0.7	–	–
$R_{xy} \equiv \frac{f_x}{f_y}$	2.070 ± 0.018	–	–
$U_0 = -aI_0$ [μK$\cdot k_B$]	-13.42 ± 0.06	–	–
$U_0 = -aI_0$ [$h \cdot f_z$]	-12.05 ± 0.11	–	–
$N_{2D} \equiv \frac{f_z^2}{4 f_x f_y}$ [1]	2042 ± 36	–	–

Table B.2: 2D Trap characteristics including trap parameters and trap properties for $P_{1,2} = 2$ W. Here, the trap properties are calculated from the measured trap parameters, and the trap parameters are calculated from the measured trap properties. In the last column the half-crossing angle is assumed to be known to calculate the other trap parameters from the measured trap properties.

were used: The trap frequency in x-direction is:

$$f_x = \frac{1}{2\pi}\sqrt{\frac{32aP_{1,2}}{\pi m W_{0x}^3 W_{0z}}} \tag{B.32}$$

with the error:

$$df_x = \sqrt{\left(\frac{3f_x dW_{0x}}{2W_{0x}}\right)^2 + \left(\frac{f_x dW_{0z}}{2W_{0z}}\right)^2} \tag{B.33}$$

The trap frequency in y-direction can be calculated from:

$$f_y = \frac{1}{2\pi}\sqrt{\frac{16aP_{1,2}}{\pi m W_{0x} W_{0z}}\left[\frac{2\sin^2(\theta)}{W_{0z}^2} + \left(\frac{\lambda\cos(\theta)}{\pi}\right)^2\left(\frac{1}{W_{0x}^4} + \frac{1}{W_{0z}^4}\right)\right]} \tag{B.34}$$

and the error from the leading terms can be approximated as:

$$df_y \approx \sqrt{\left(\frac{f_y dW_{0x}}{2W_{0x}}\right)^2 + \left(\frac{3f_y dW_{0z}}{2W_{0z}}\right)^2 + \left(\frac{f_y \cos(\theta) d\theta}{\sin(\theta)}\right)^2} \tag{B.35}$$

The trap frequency in vertical direction can be calculated from:

$$f_z = \frac{1}{2\pi}\sqrt{\frac{16aP_{1,2}}{\pi m W_{0x} W_{0z}}\left[\frac{2\cos^2(\theta)}{W_{0z}^2} + \left(\frac{\lambda\sin(\theta)}{\pi}\right)^2\left(\frac{1}{W_{0x}^4} + \frac{1}{W_{0z}^4}\right) + \left(\frac{\pi}{d}\right)^2\right]} \tag{B.36}$$

and the error from the leading terms can be approximated as:

$$df_z \approx \sqrt{\left(\frac{f_z dW_{0x}}{2W_{0x}}\right)^2 + \left(\frac{3f_z dW_{0z}}{2W_{0z}}\right)^2 + \left(\frac{f_z\cos(\theta)d\theta}{\sin(\theta)}\right)^2} \tag{B.37}$$

To calculate the 2D trap parameters from the 2D trap properties, one can exploit the following relations. The minimal beam width in x-direction is:

$$W_{0x} = \left(\frac{32aP_{1,2}}{\pi m(2\pi f_x)W_{0z}}\right)^{\frac{1}{3}} \approx \left(\frac{\sqrt{2}\cdot 8aP_{1,2}f_y}{\pi^2 m f_x^2 \lambda f_z}\right)^{\frac{1}{3}} \tag{B.38}$$

with the error:

$$dW_{0x} = \sqrt{\left(\frac{2W_{0x}df_x}{3f_x}\right)^2 + \left(\frac{W_{0x}df_y}{3f_y}\right)^2 + \left(\frac{W_{0x}df_z}{3f_z}\right)^2} \tag{B.39}$$

The minimal beam width in z-direction is:

$$W_{0z} \approx \frac{16aP_{1,2}\pi^2 4\sin(\theta)^2}{\pi m W_{0x}(2\pi f_z)^2\lambda^2} = \sqrt{\frac{\lambda^2 f_z^2}{2\pi^2 f_y^2}} \tag{B.40}$$

with the error:

$$dW_{0z} = \sqrt{\left(\frac{W_{0z}df_y}{f_y}\right)^2 + \left(\frac{W_{0z}df_z}{f_z}\right)^2} \tag{B.41}$$

The half-crossing angle can be calculated from:

$$\theta \approx \arcsin\left(\left(\frac{m\lambda^4 f_z^4}{32\pi aP_{1,2}f_x f_y}\right)^{\frac{1}{3}}\right) \tag{B.42}$$

with the error:

$$d\theta = \frac{1}{\sqrt{1-x^2}}\frac{1}{3x^2}\sqrt{\left(\frac{x^3 df_x}{f_x}\right)^2 + \left(\frac{x^3 df_y}{f_y}\right)^2 + \left(\frac{4x^3 df_z}{f_z}\right)^2} \tag{B.43}$$

including the definition:

$$x \equiv \left(\frac{m\lambda^4 f_z^4}{32\pi aP_{1,2}f_x f_y}\right)^{\frac{1}{3}} \tag{B.44}$$

If one assumes the half-crossing angle to be known, one can calculate the two left trap parameters from the trap properties in the following way: The minimal beam width in x-direction is:

$$W_{0x} = \left(\frac{32aP_{1,2}}{\pi m(2\pi f_x)^2 W_{0z}}\right)^{\frac{1}{3}} = \left(\frac{1}{8}\right)^{\frac{1}{6}} \frac{\lambda f_z}{\pi \sin(\theta) f_x} \tag{B.45}$$

with the error:

$$dW_{0x} = \sqrt{\left(\frac{W_{0x} df_x}{f_x}\right)^2 + \left(\frac{W_{0x} df_z}{f_z}\right)^2 + \left(\frac{W_{0x}\cos(\theta) d\theta}{\sin(\theta)}\right)^2} \tag{B.46}$$

The minimal beam width in z-direction can be expressed as:

$$W_{0z} = \frac{16aP_{1,2}\pi^2 4\sin^2(\theta)}{\pi m W_{0x}\lambda^2(2\pi f_z)^2} = \frac{16\sqrt{2}aP_{1,2}\sin^3(\theta) f_x}{m\lambda^3 f_z^3} \tag{B.47}$$

with the error:

$$dW_{0z} = \sqrt{\left(\frac{W_{0z} df_x}{f_x}\right)^2 + \left(\frac{3W_{0z} df_z}{f_z}\right)^2 + \left(\frac{3W_{0z}\cos(\theta) d\theta}{\sin(\theta)}\right)^2} \tag{B.48}$$

B.4 Conclusion

Here the formula for the calculation of the scattering rate should be given with the form ([37]):

$$\Gamma_{sc} = \frac{\left(\frac{\gamma s_0}{2}\right)}{1 + s_0 + \left(\frac{2\Delta}{\gamma}\right)^2} \tag{B.49}$$

with the detuning $\Delta = \omega_L - \omega_0$ depending on the laser frequency ω_L and the resonance frequency ω_0. In addition, the damping factor $\gamma = 2\pi\Gamma$ depends on the natural line width which is for the D_2-line of ^{6}Li: $\Gamma = 5.8724$ MHz ([8]). The on-resonance saturation parameter ([37]):

$$s_0 = \frac{I}{I_{sat}} \tag{B.50}$$

depends just on the intensity of the laser light I and the saturation intensity which is for ^{6}Li: $I_{sat} = 2.54$ mW/cm^2 ([2]). For resonant light the equation for the scattering rate simplifies to:

$$\Gamma_{sc,resonant} = \frac{\left(\frac{\gamma s_0}{2}\right)}{1 + s_0} \tag{B.51}$$

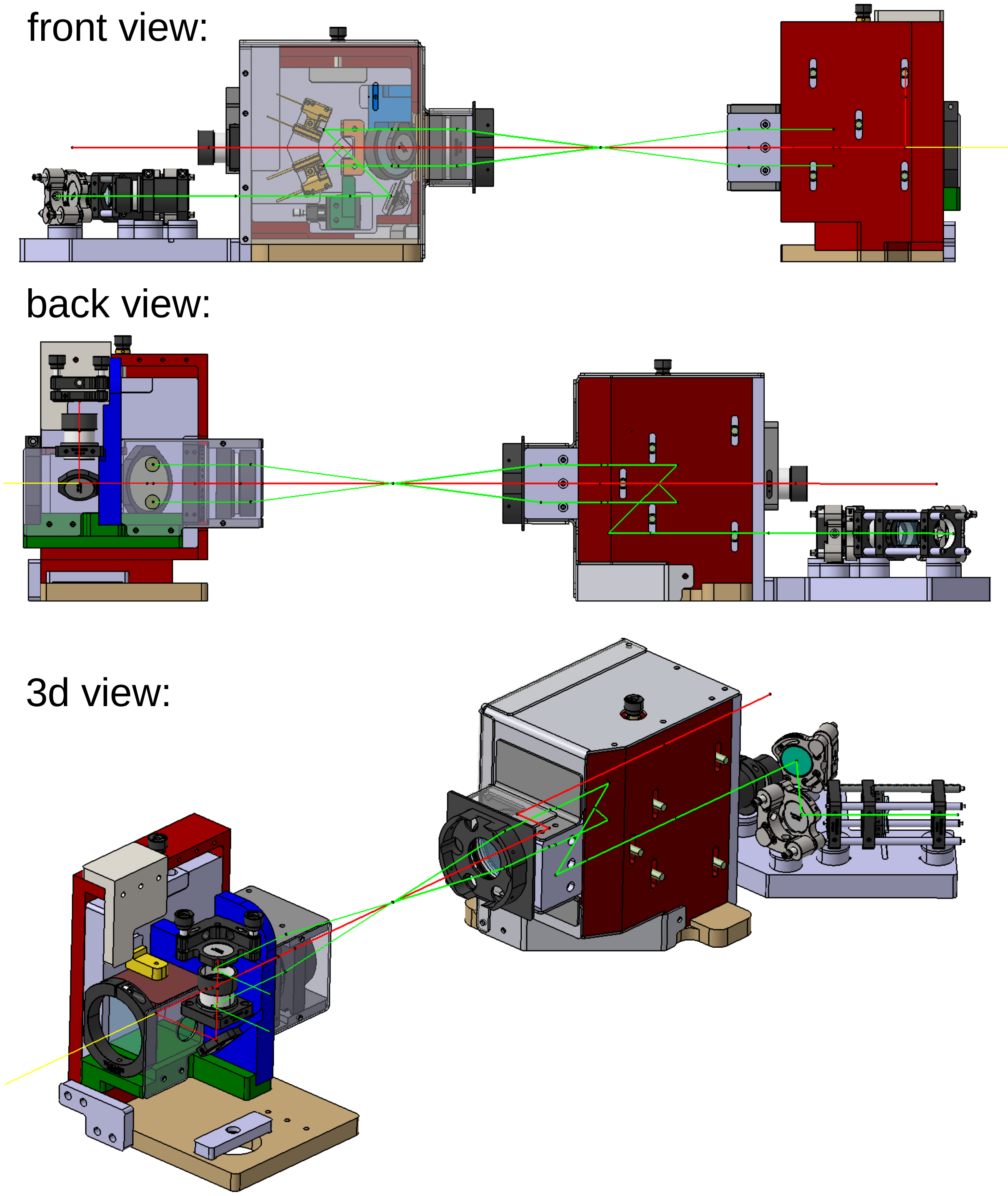

Figure B.1: Pictures from the CAD-model designed in CATIA: different view on the Trapping-Box with telescope plate together with the Imaging-Box. The path of the 2D Trap beams is depicted as green line. The path of the MOT-beam is drawn as red line and overlaps most of the time with the path of the imaging-beam shown as yellow line.

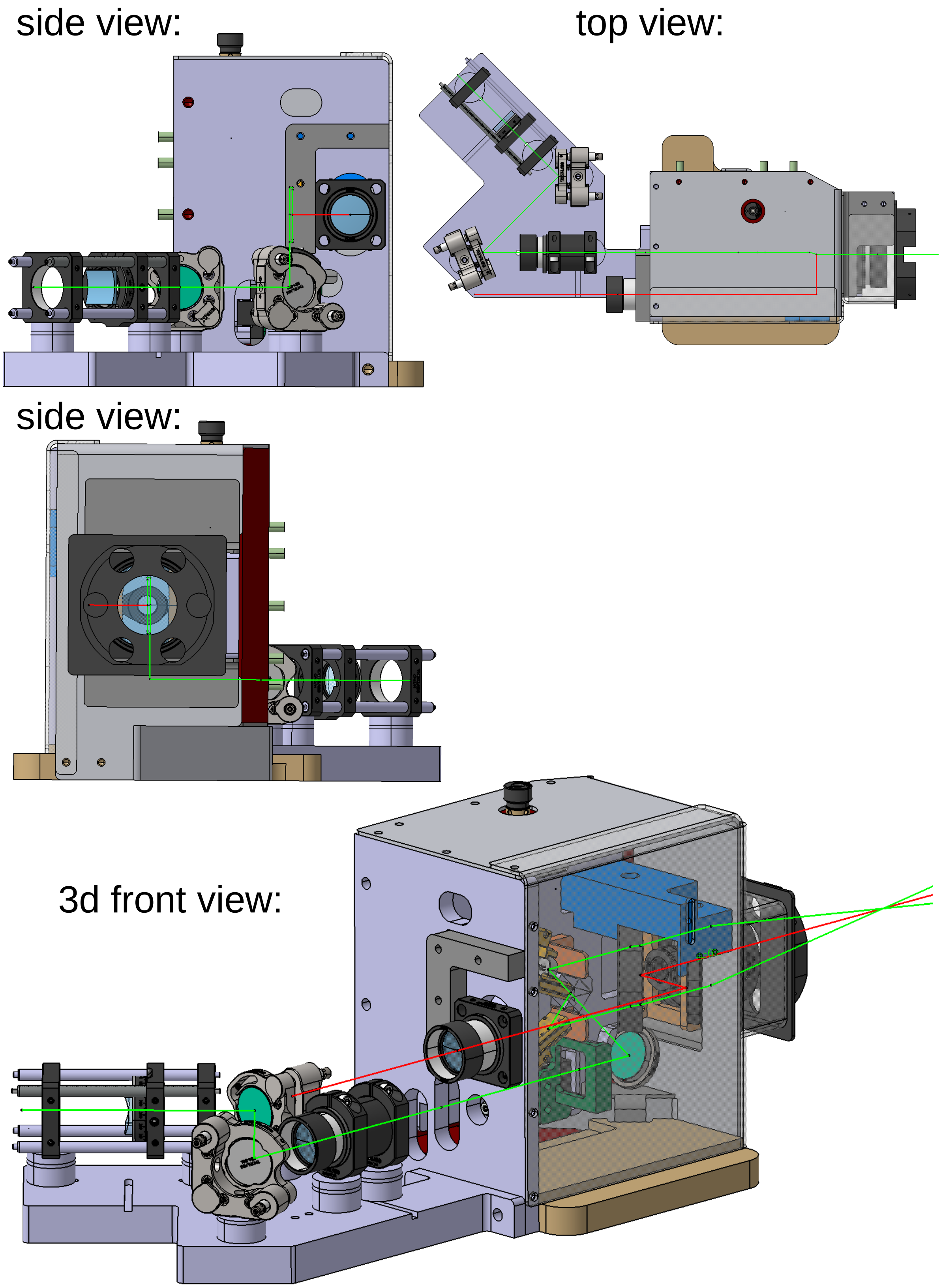

Figure B.2: Pictures from the CAD-model designed in CATIA: different views to the Trapping-Box together with the telescope plate. The path of the 2D Trap beams is depicted as green line. The path of the MOT-beam is drawn as red line and overlaps most of the time with the path of the imaging-beam shown as yellow line.

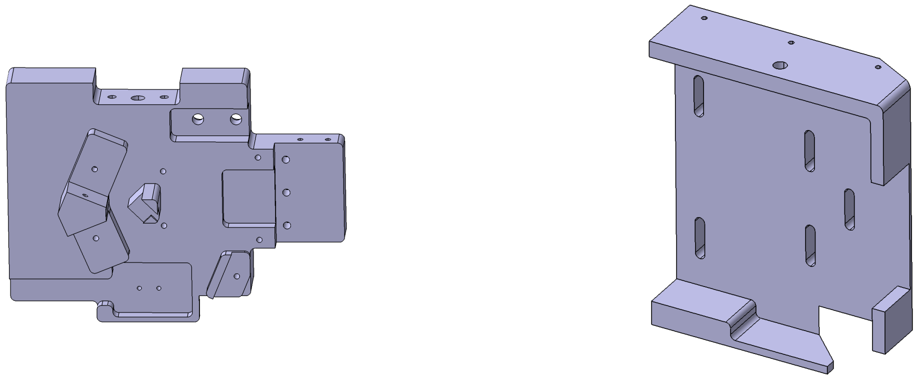

Figure B.3: On the left: central basis plate of the Trapping-Box. On the right: back plate of the Trapping-Box. The two objects have not the same length scale.

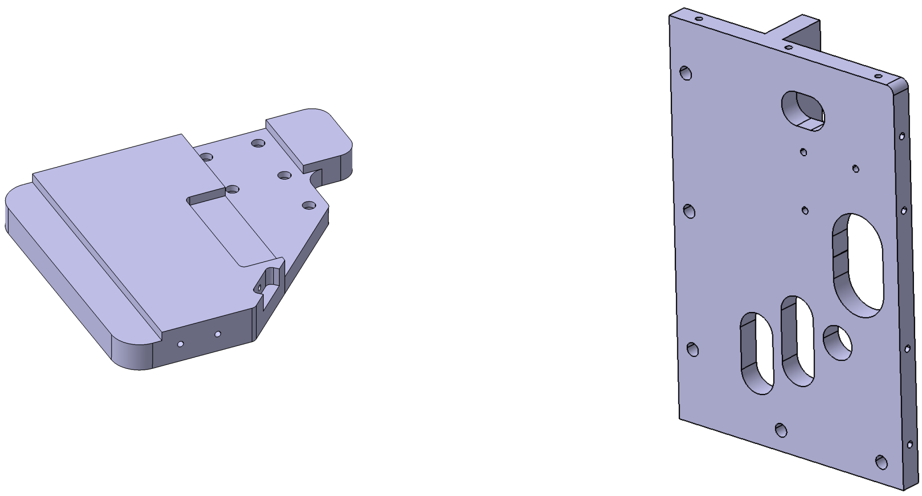

Figure B.4: On the left: bottom plate of the Trapping-Box. On the right: entrance plate of the Trapping-Box. The two objects have not the same length scale.

Figure B.5: On the left: top exit cover plate of the Trapping-Box. On the right: bottom exit cover plate of the Trapping-Box. The two objects have not the same length scale.

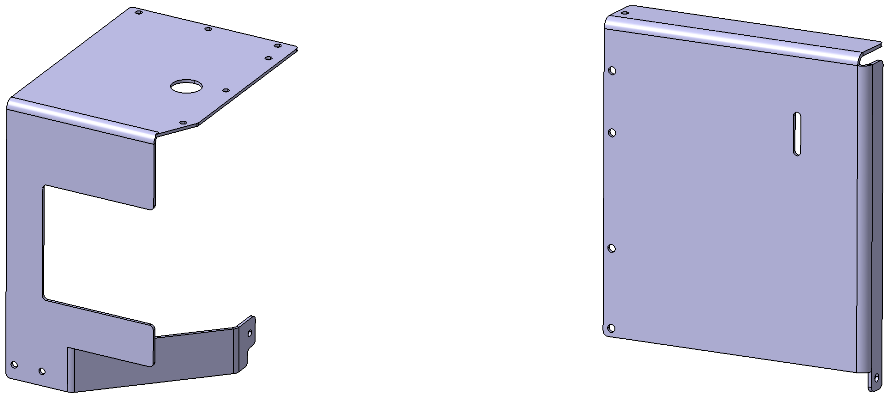

Figure B.6: On the left: side cover plate of the Trapping-Box. On the right: front cover plate of the Trapping-Box. The two objects have not the same length scale.

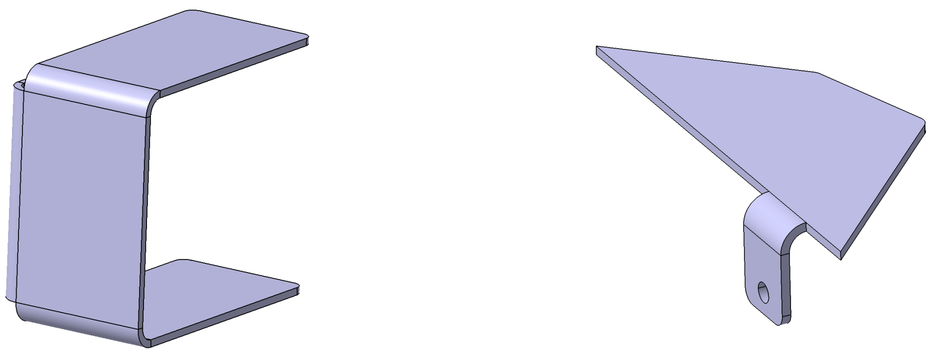

Figure B.7: On the left: front exit cover plate of the Trapping-Box. On the right: bottom cover plate of the Trapping-Box. The two objects have not the same length scale.

Figure B.8: On the left: micrometer screw plate of the Trapping-Box. On the right: stud screw of the Trapping-Box. The two objects have not the same length scale.

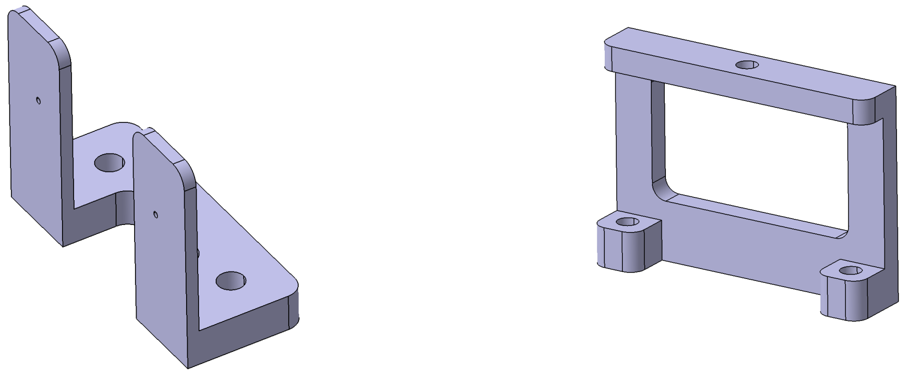

Figure B.9: On the left: alignment plate of the Trapping-Box. On the right: wave-plate holder of the Trapping-Box. The two objects have not the same length scale.

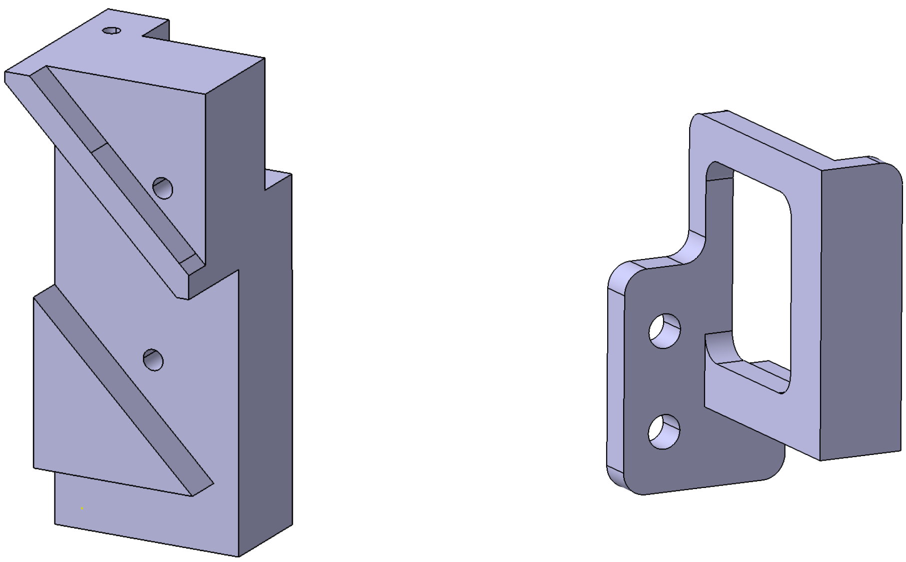

Figure B.10: On the left: dichroic mirror tower of the Trapping-Box. On the right: L_x-lens mount of the Trapping-Box. The two objects have not the same length scale.

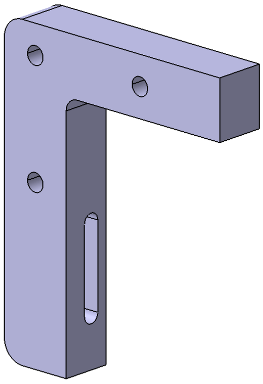 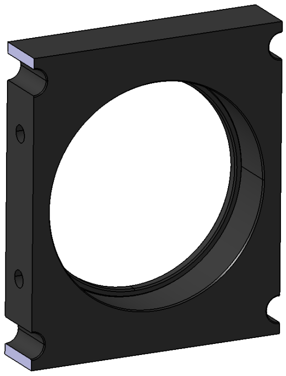

Figure B.11: On the left: MOT-lens holder of the Trapping-Box. On the right: lens cage plate of the Trapping-Box (modified Thorlabs piece: LCP08/M). The two objects have not the same length scale.

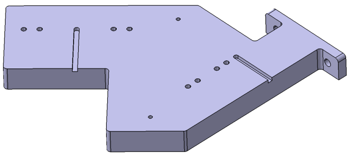 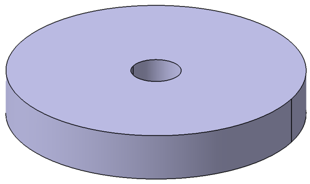

Figure B.12: On the left: telescope plate of the Trapping-Box. On the right: spacer plate of the Trapping-Box. The two objects have not the same length scale.

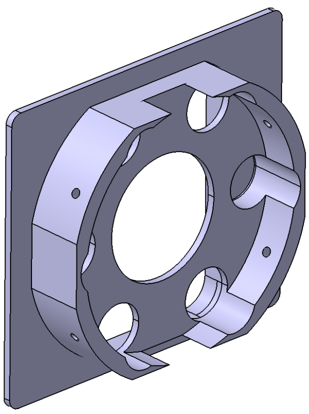

Figure B.13: View-port blind of the Trapping-Box.

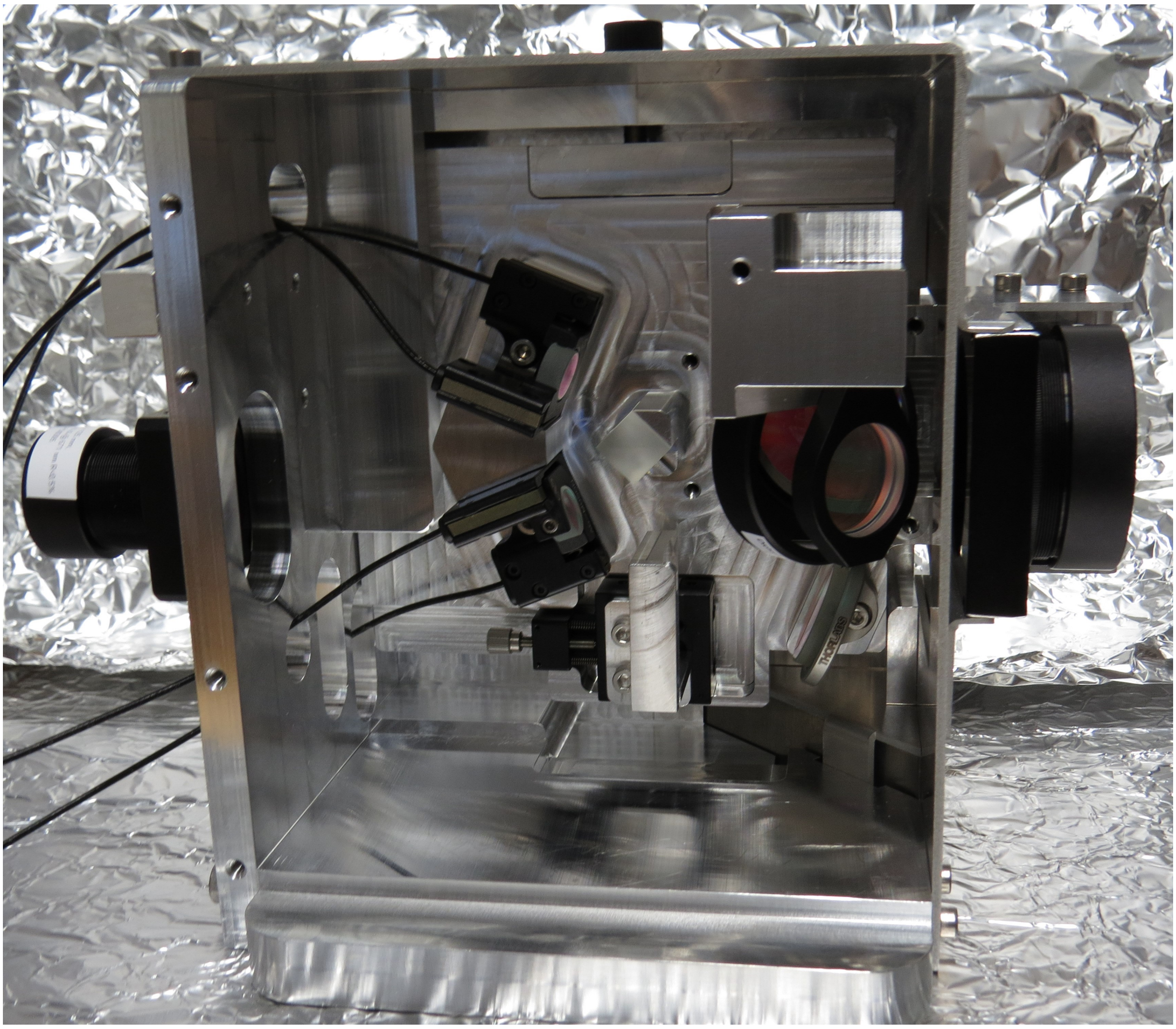

Figure B.14: Front view to the real Trapping-Box.

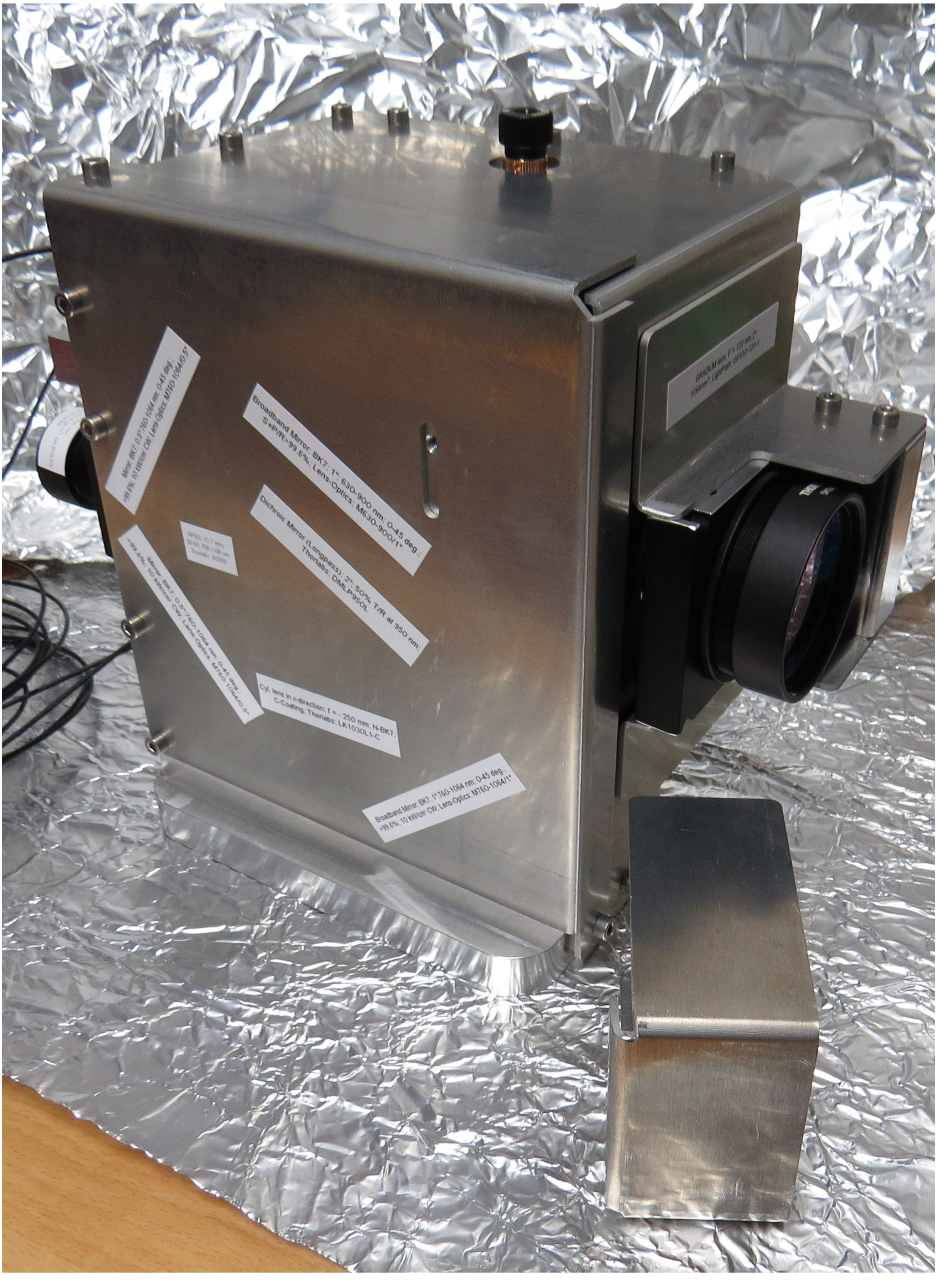

Figure B.15: Front view to Trapping-Box with complete cover.

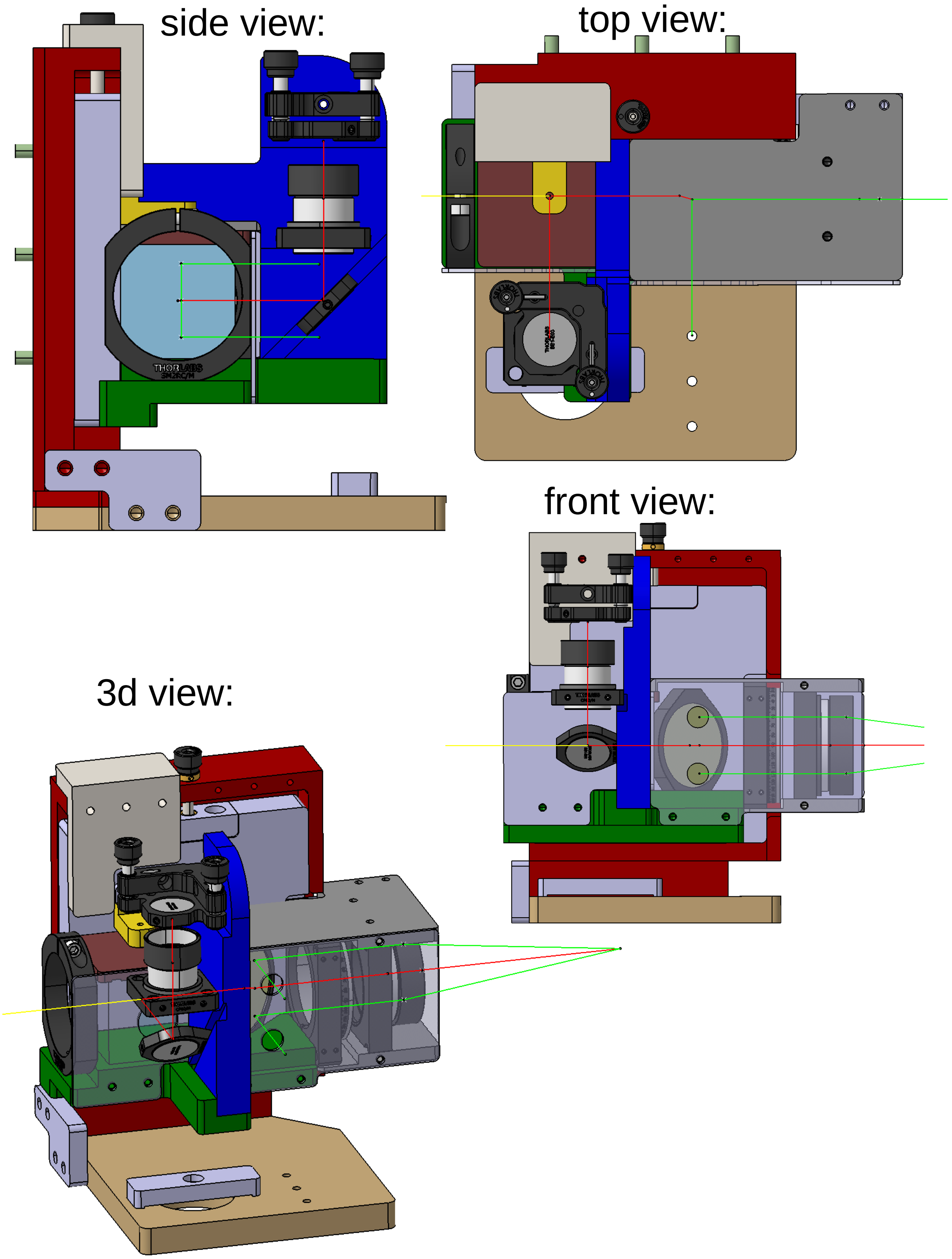

Figure B.16: Pictures from the CAD-model designed in CATIA: different views on the Imaging-Box. The path of the 2D Trap beams is depicted as green line. The path of the MOT-beam is drawn as red line and overlaps most of the time with the path of the imaging-beam shown as yellow line.

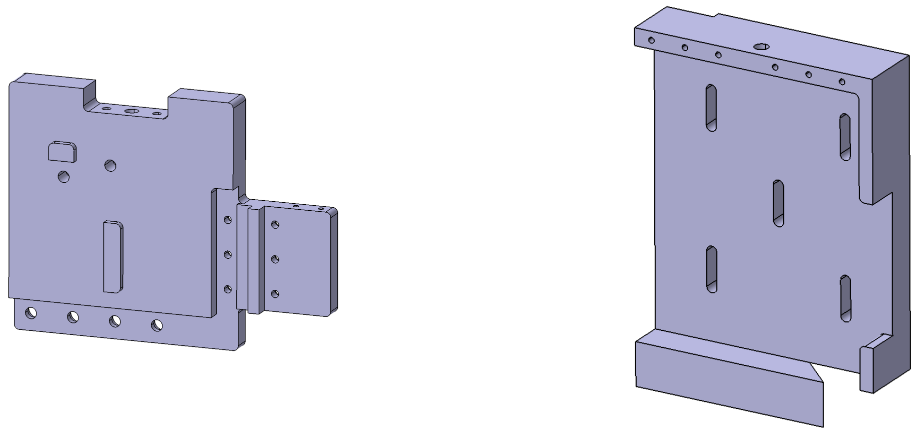

Figure B.17: On the left: central basis plate of the Imaging-Box. On the right: back plate of the Imaging-Box. The two objects have not the same length scale.

Figure B.18: On the left: bottom plate of the Imaging-Box. On the right: fixing plate of the Imaging-Box. The two objects have not the same length scale.

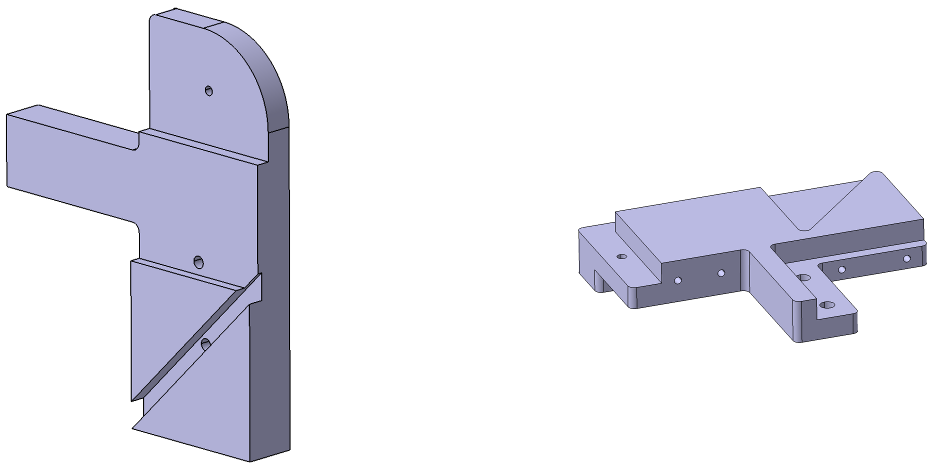

Figure B.19: On the left: MOT-path plate of the Imaging-Box. On the right: side plate of the Imaging-Box. The two objects have not the same length scale.

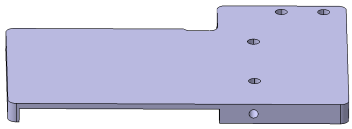 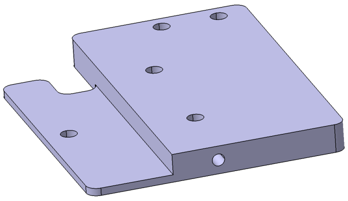

Figure B.20: On the left: top cover plate of the Imaging-Box. On the right: bottom cover plate of the Imaging-Box. The two objects have not the same length scale.

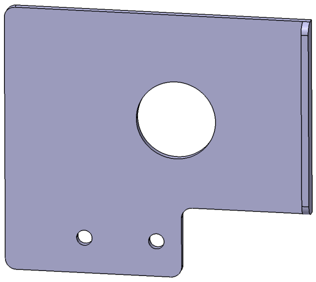 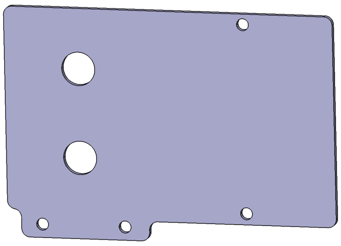

Figure B.21: On the left: beam splitter front cover plate of the Imaging-Box. On the right: front cover plate of the Imaging-Box. The two objects have not the same length scale.

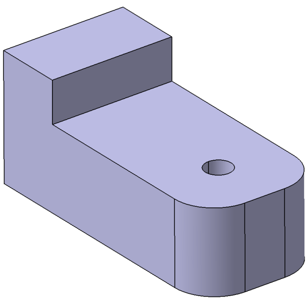 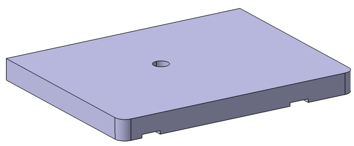

Figure B.22: On the left: beam splitter fixing foot of the Imaging-Box. On the right: beam splitter cube hat of the Imaging-Box (plastic). The two objects have not the same length scale.

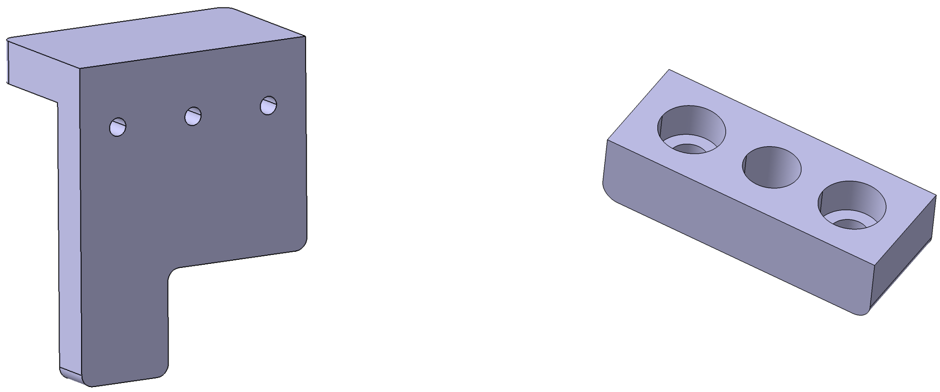

Figure B.23: On the left: guiding hand plate of the Imaging-Box. On the right: micrometer screw plate of the Imaging-Box. The two objects have not the same length scale.

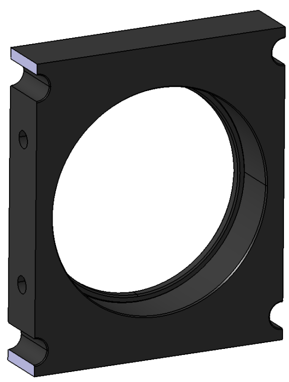

Figure B.24: Lens cage plate of the Imaging-Box (modified Thorlabs piece: LCP08/M).

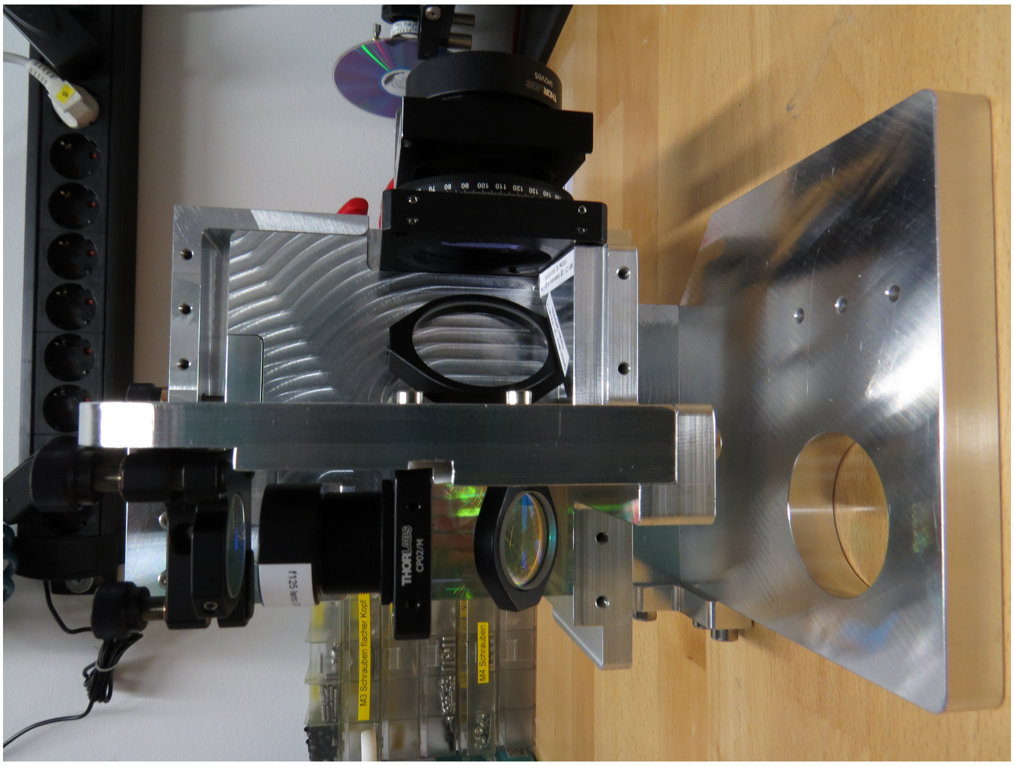

Figure B.25: Front view to the real Imaging-Box.

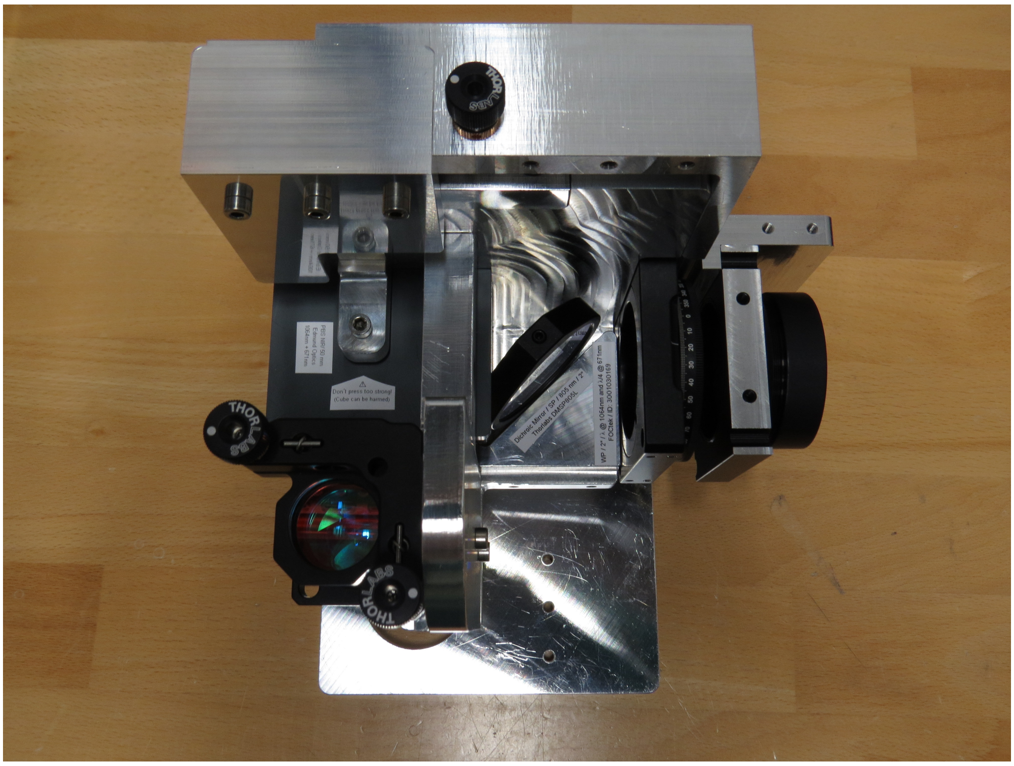

Figure B.26: Top view to the real Imaging-Box.

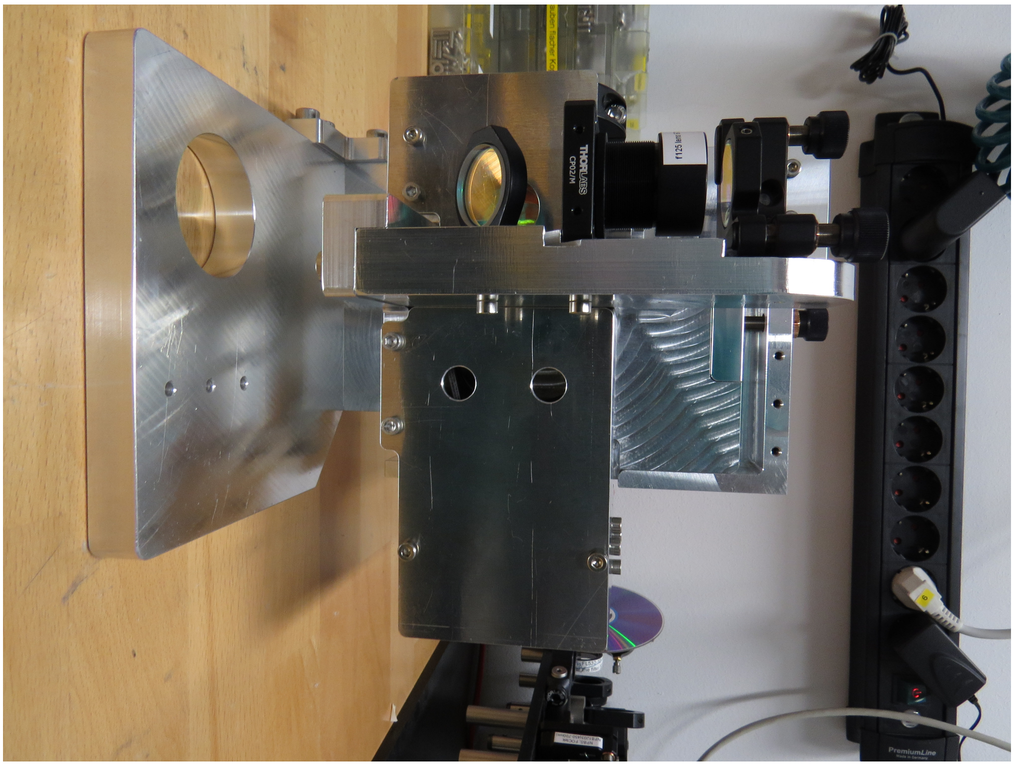

Figure B.27: Front view to the real Imaging-Box with full cover.

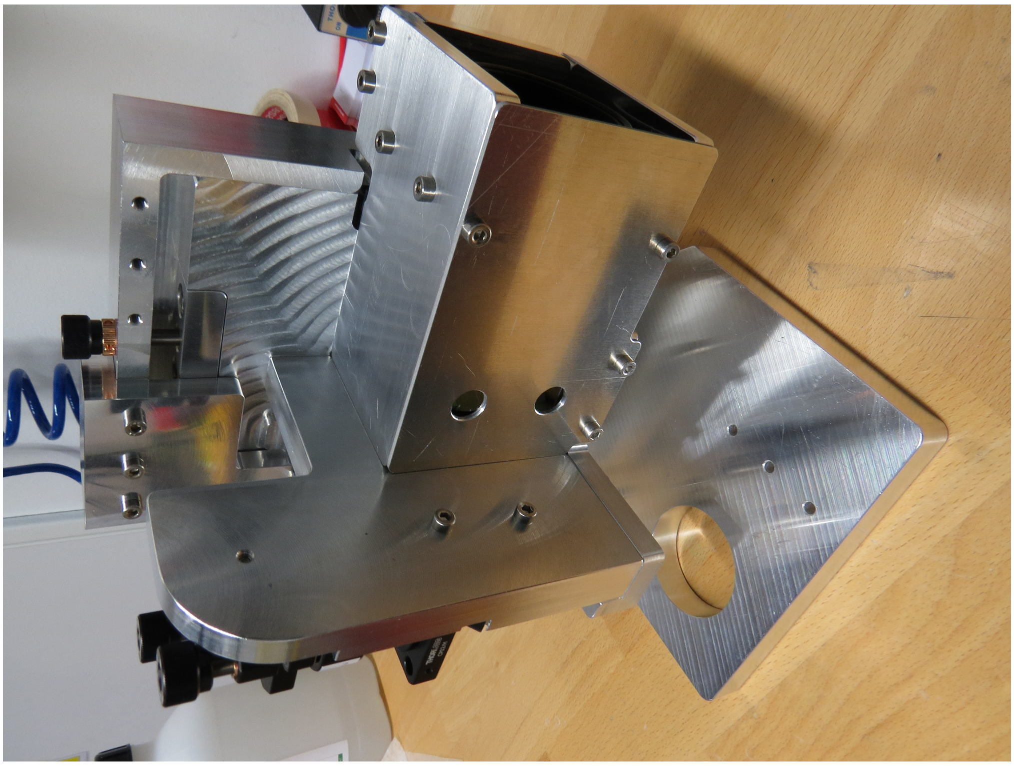

Figure B.28: Front view to the real Imaging-Box with full cover.

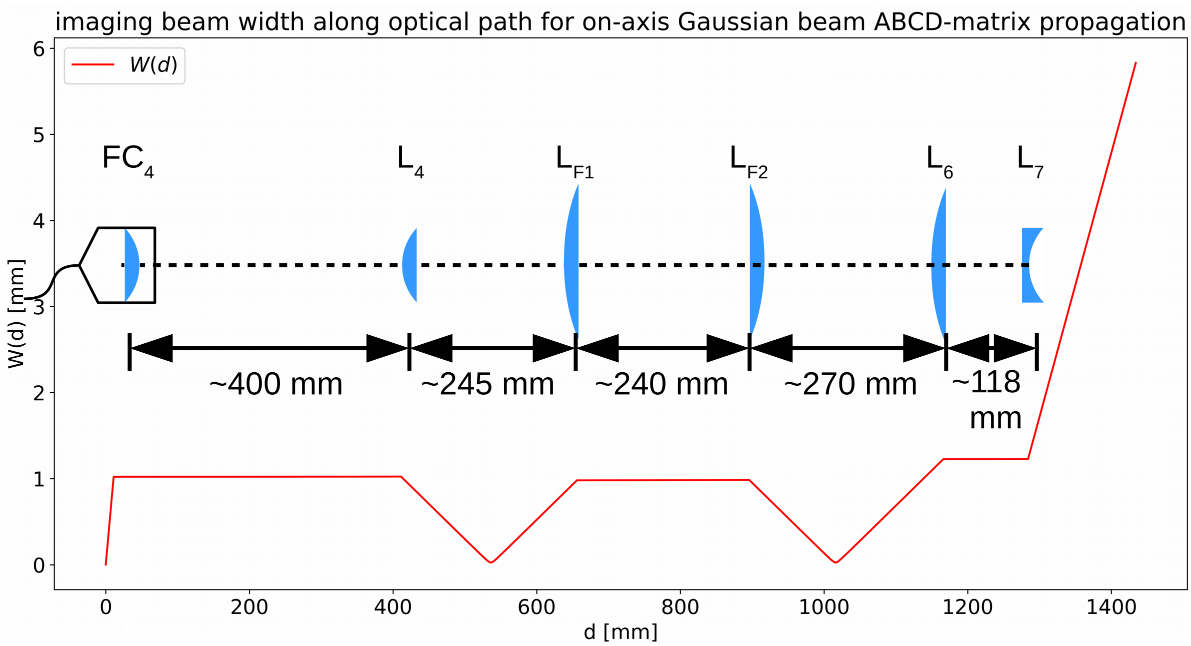

Figure B.29: Beam width of the imaging-beam along its optical path through the whole setup from an on-axis Gaussian beam ABCD-matrix calculation. Here, not all relative distances between the lenses correspond exactly to the real values but were roughly estimated.

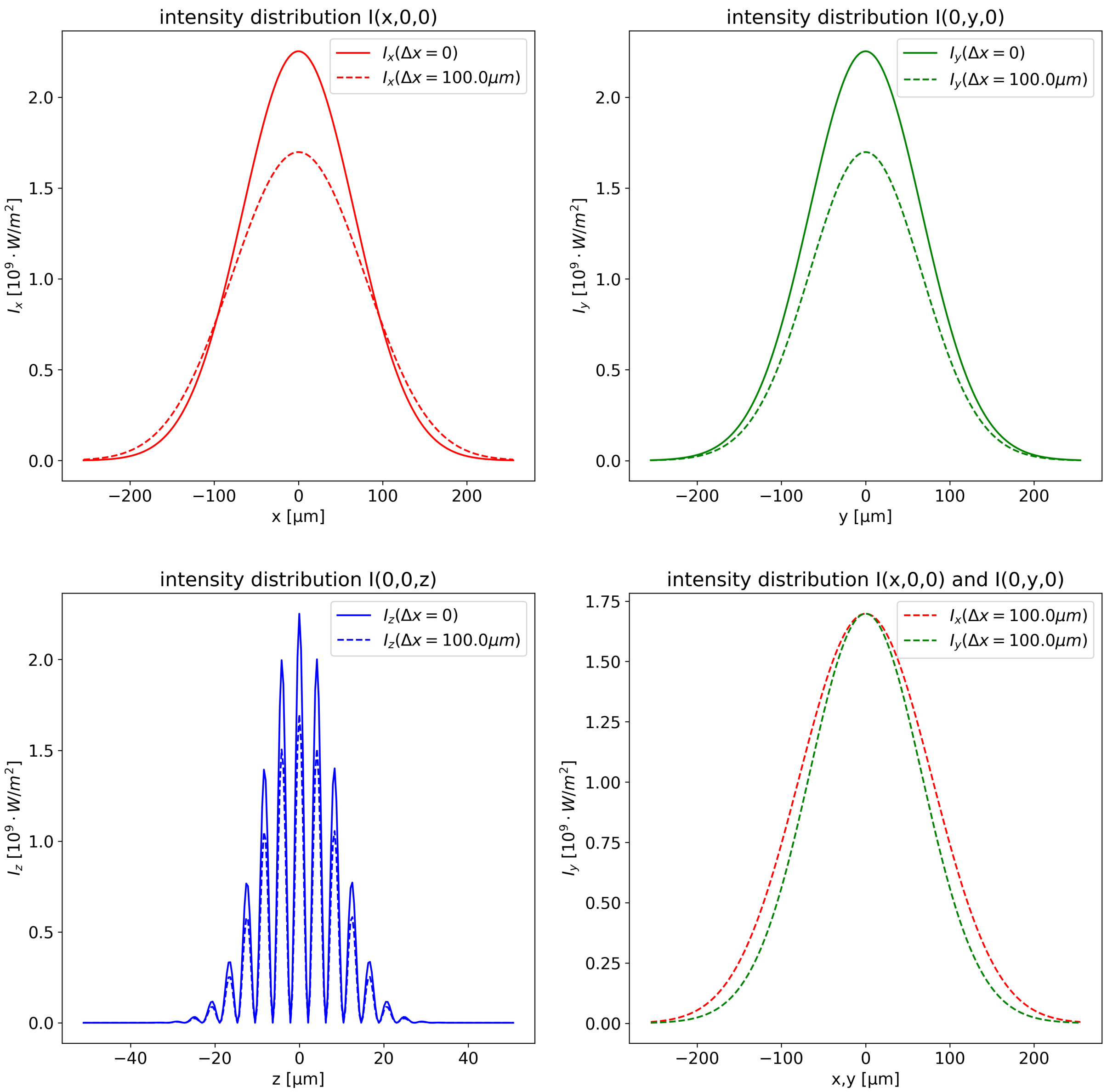

Figure B.30: One-dimensional intensity distribution in all spatial dimensions. The original distributions are plotted as solid lines, and the modified distributions with a relative shift between the beams in x-direction are plotted with dashed lines. The relative shift is: $\Delta x = 100\ \mu$m.

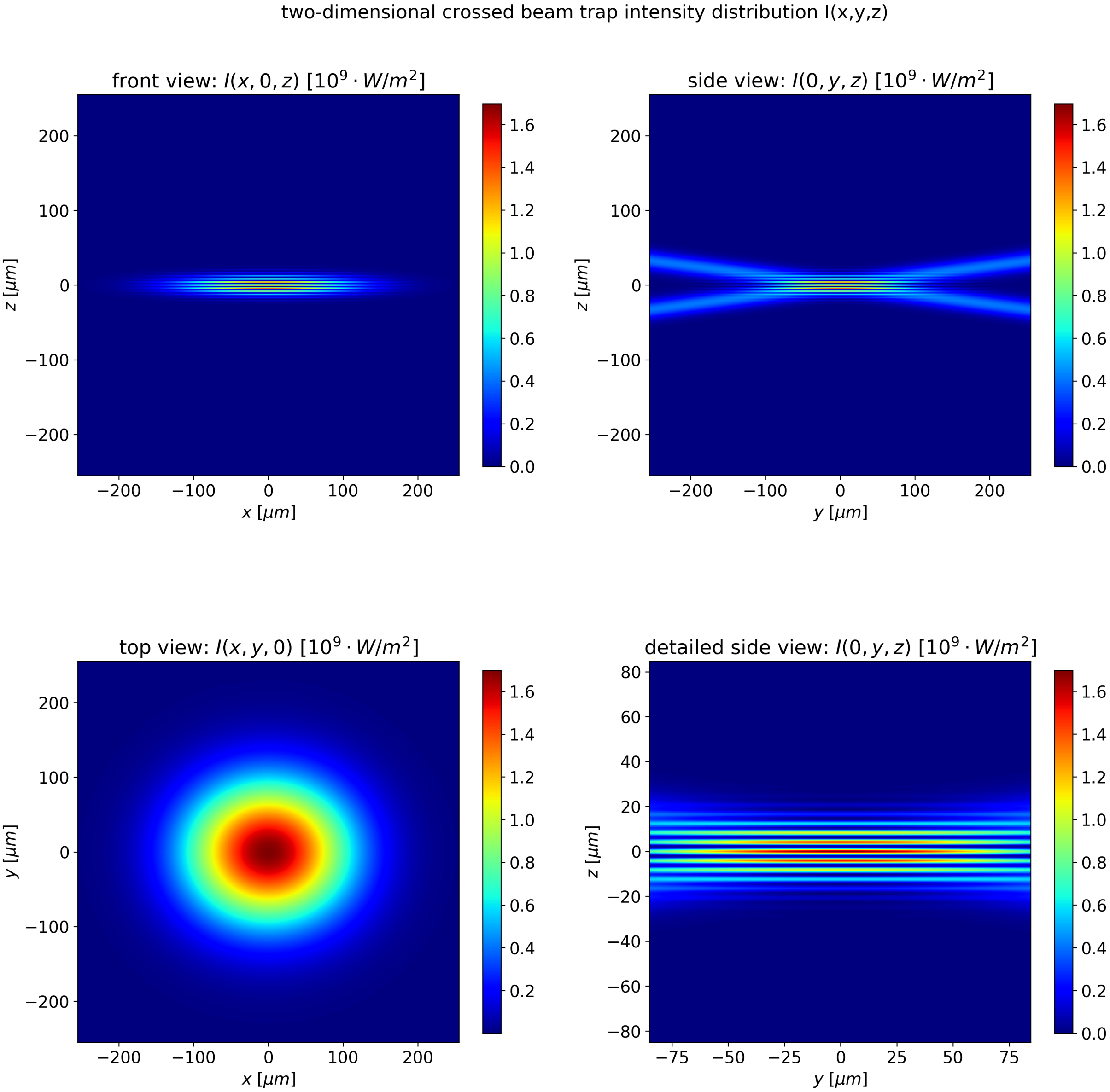

Figure B.31: Two-dimensional intensity distributions in the three spatial planes of the laboratory coordinate system. The distributions are given for a relative shift between the beams in x-direction of: $\Delta x = 100$ μm.

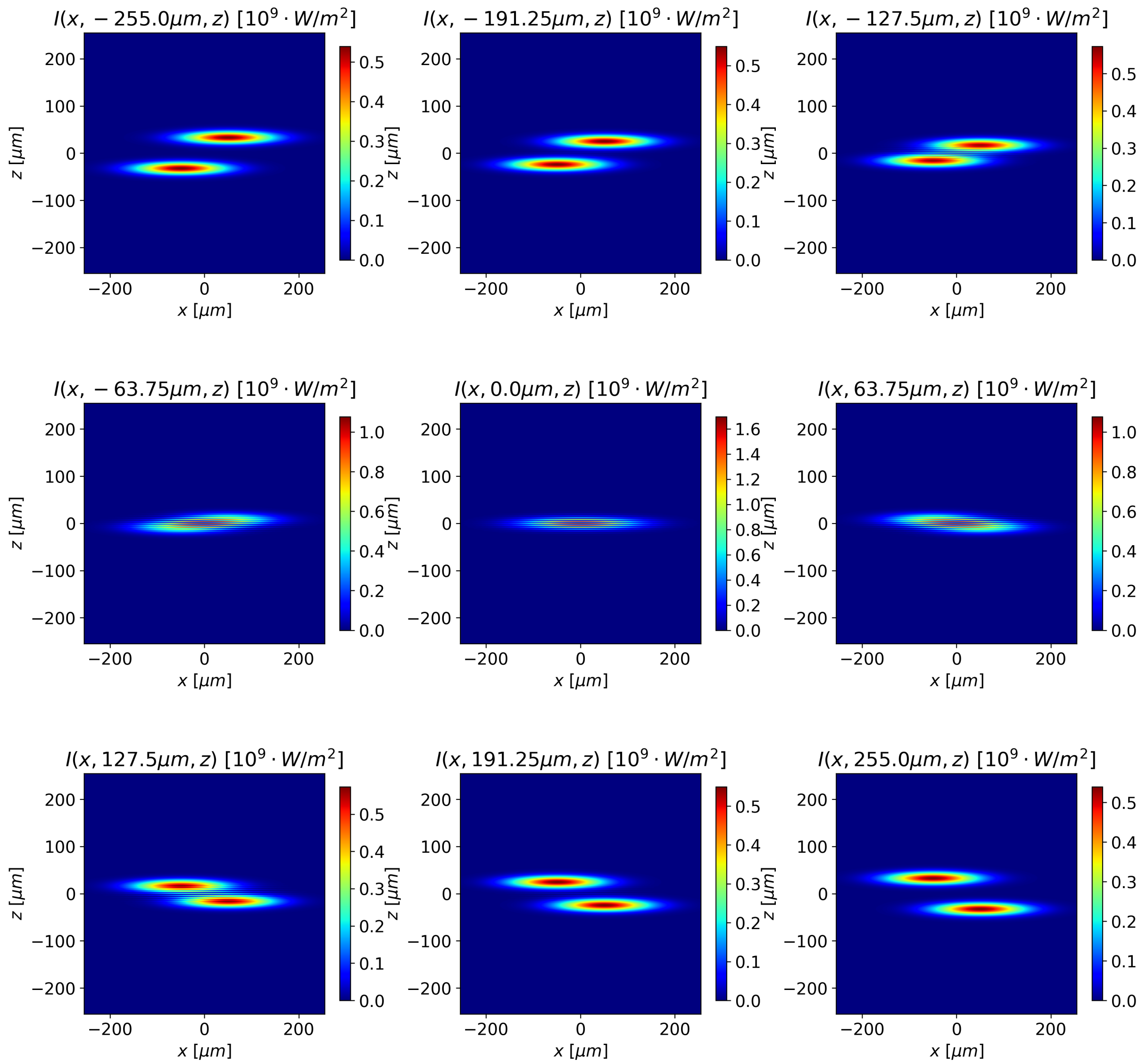

Figure B.32: Two-dimensional intensity distributions in the xz-plane, scanned along the y-direction. The distributions are given for a relative shift between the beams in x-direction of: $\Delta x = 100\ \mu$m.

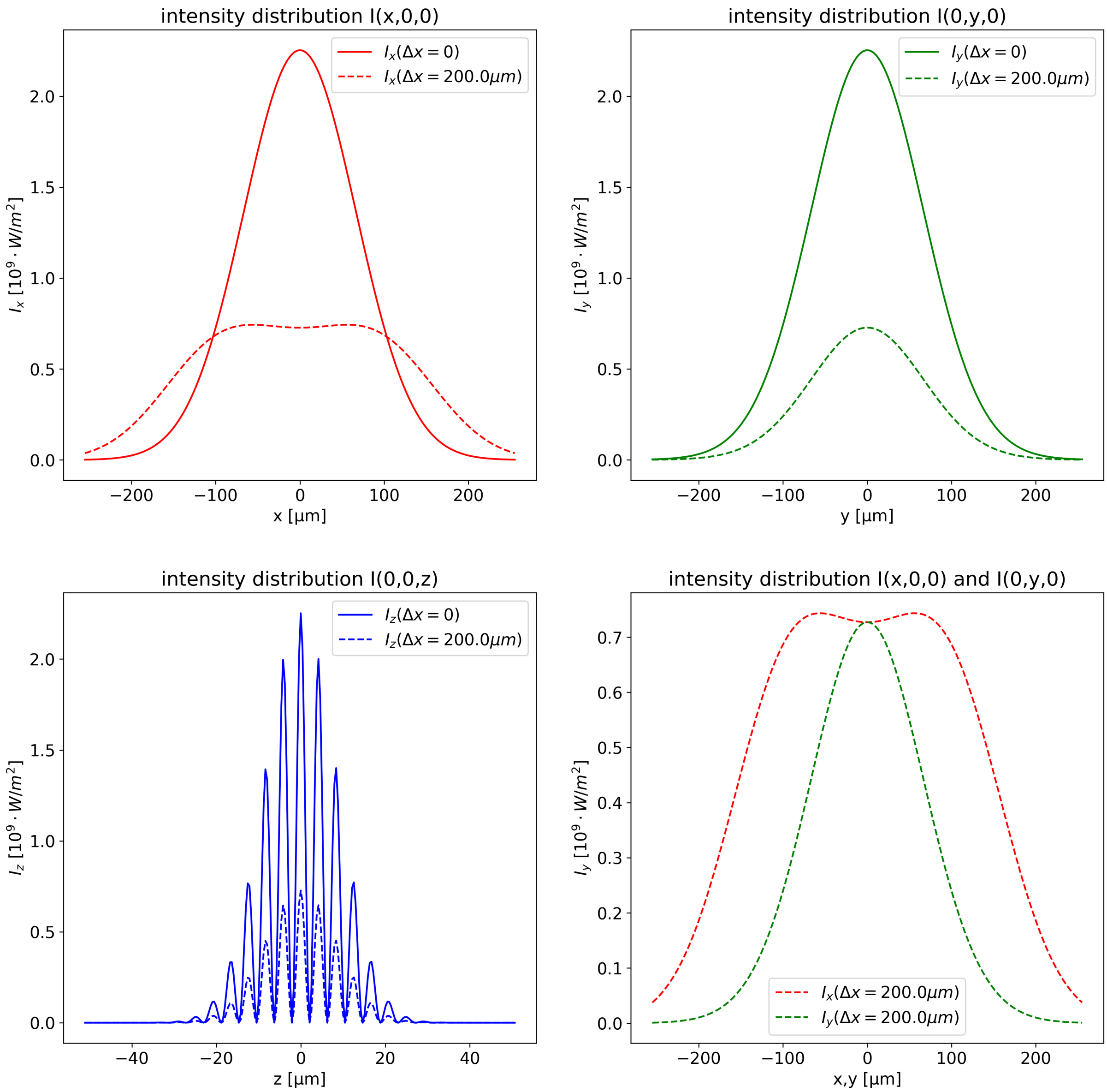

Figure B.33: One-dimensional intensity distribution in all spatial dimensions. The original distributions are plotted as solid lines, and the modified distributions with a relative shift between the beams in x-direction are plotted with dashed lines. The relative shift is: $\Delta x = 200\ \mu$m.

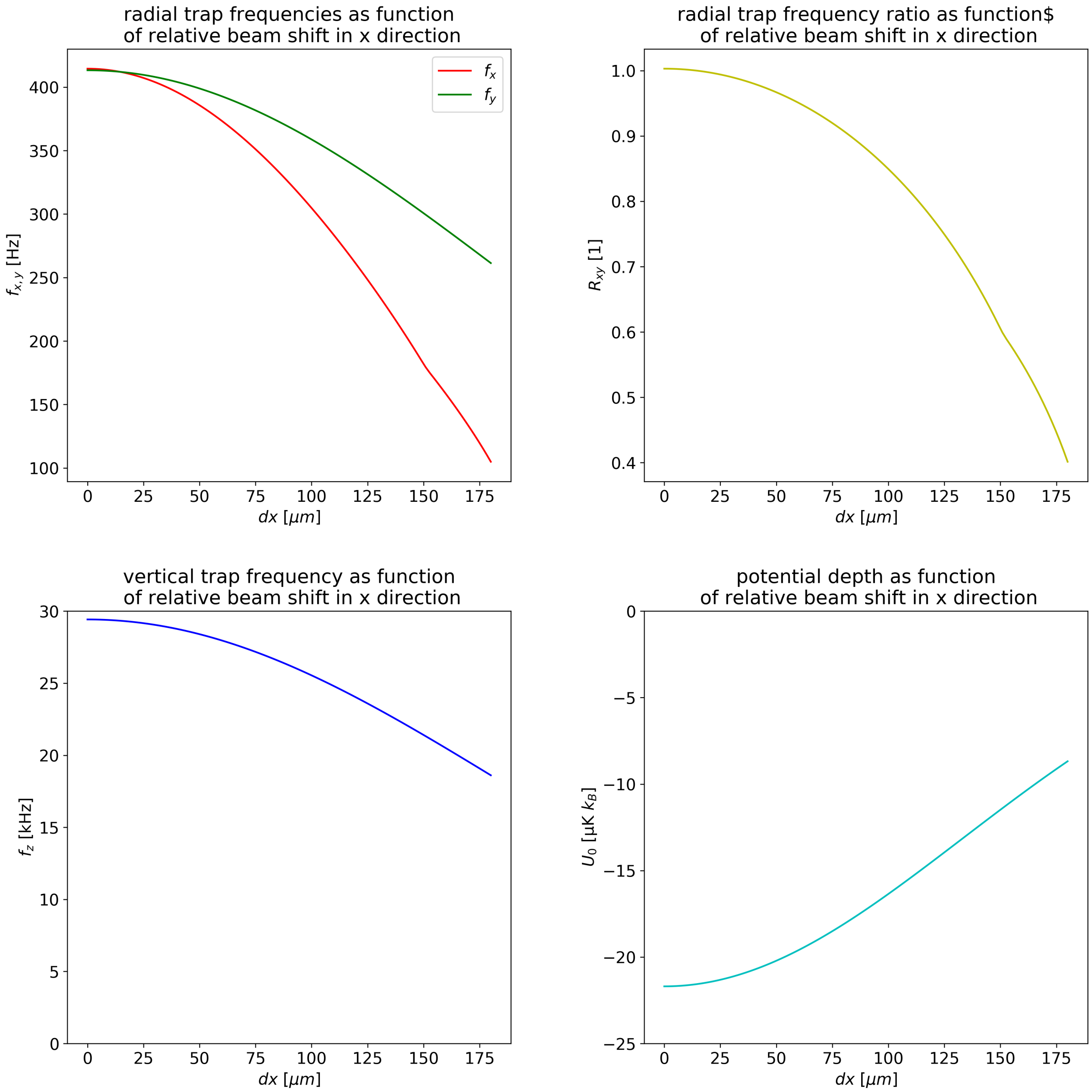

Figure B.34: Three harmonic trap frequencies, the roundness ratio, and the potential depth as functions of relative beam shift in x-direction.

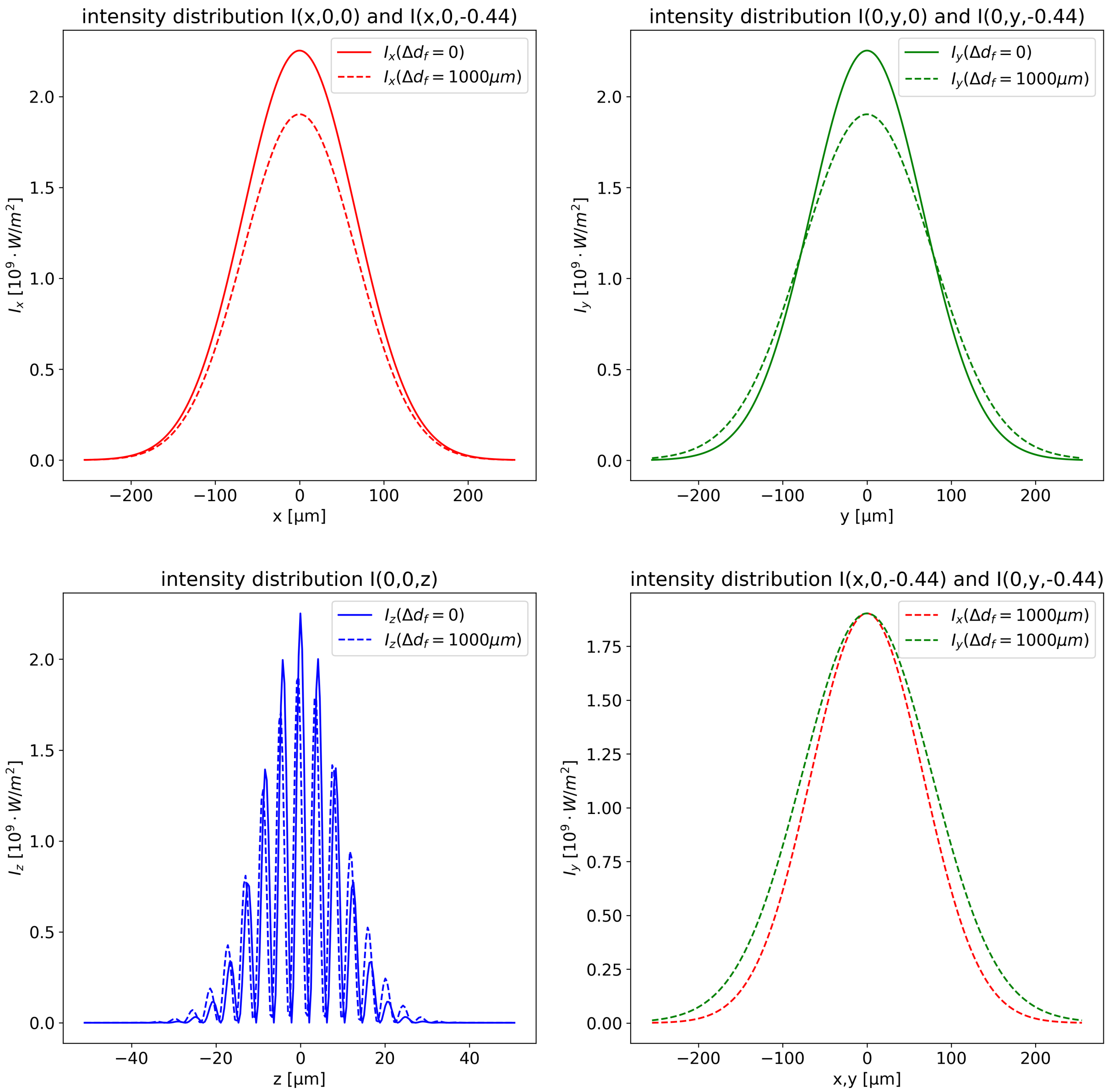

Figure B.35: One-dimensional intensity distribution in all spatial dimensions. The original distributions are plotted as solid lines, and the modified distributions with a symmetric shift of the single-beam foci around the crossing point are plotted with dashed lines. The cut line in the two horizontal directions for the dashed line is shifted along the z-direction to the layer with maximal intensity. The relative distance between the foci along the beams is: $\Delta d_f = 1000$ μm.

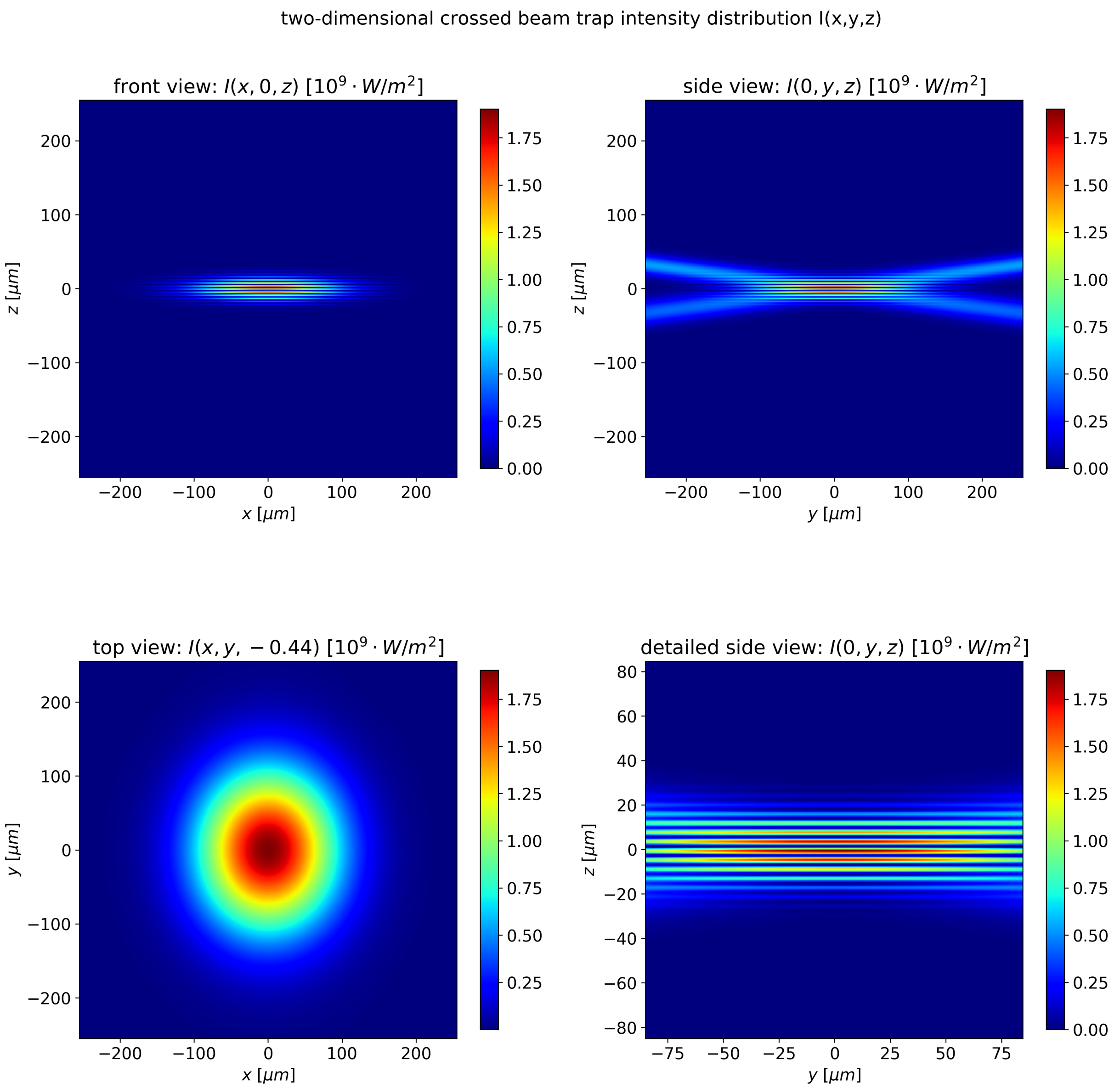

Figure B.36: Two-dimensional intensity distributions in the three spatial planes of the laboratory coordinate system. The cut plane in horizontal direction is shifted along the z-direction to the layer with maximal intensity. The distributions are given for a relative distance between the foci along the beams of: $\Delta d_f = 1000\ \mu m$.

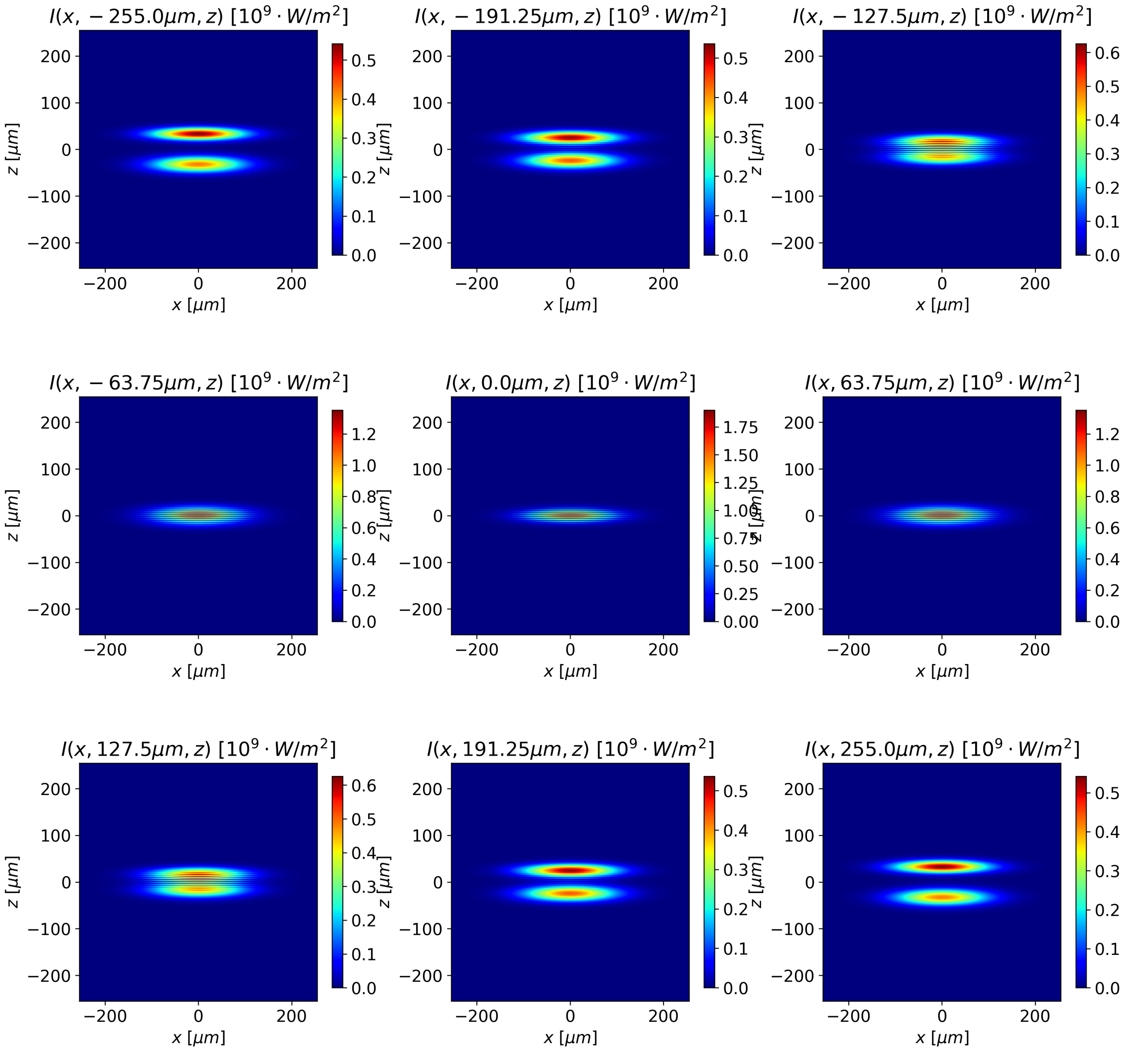

Figure B.37: Two-dimensional intensity distributions in the xz-plane, scanned along the y-direction. The distributions are given for a relative distance between the foci along the beams of: $\Delta d_f = 1000\ \mu$m.

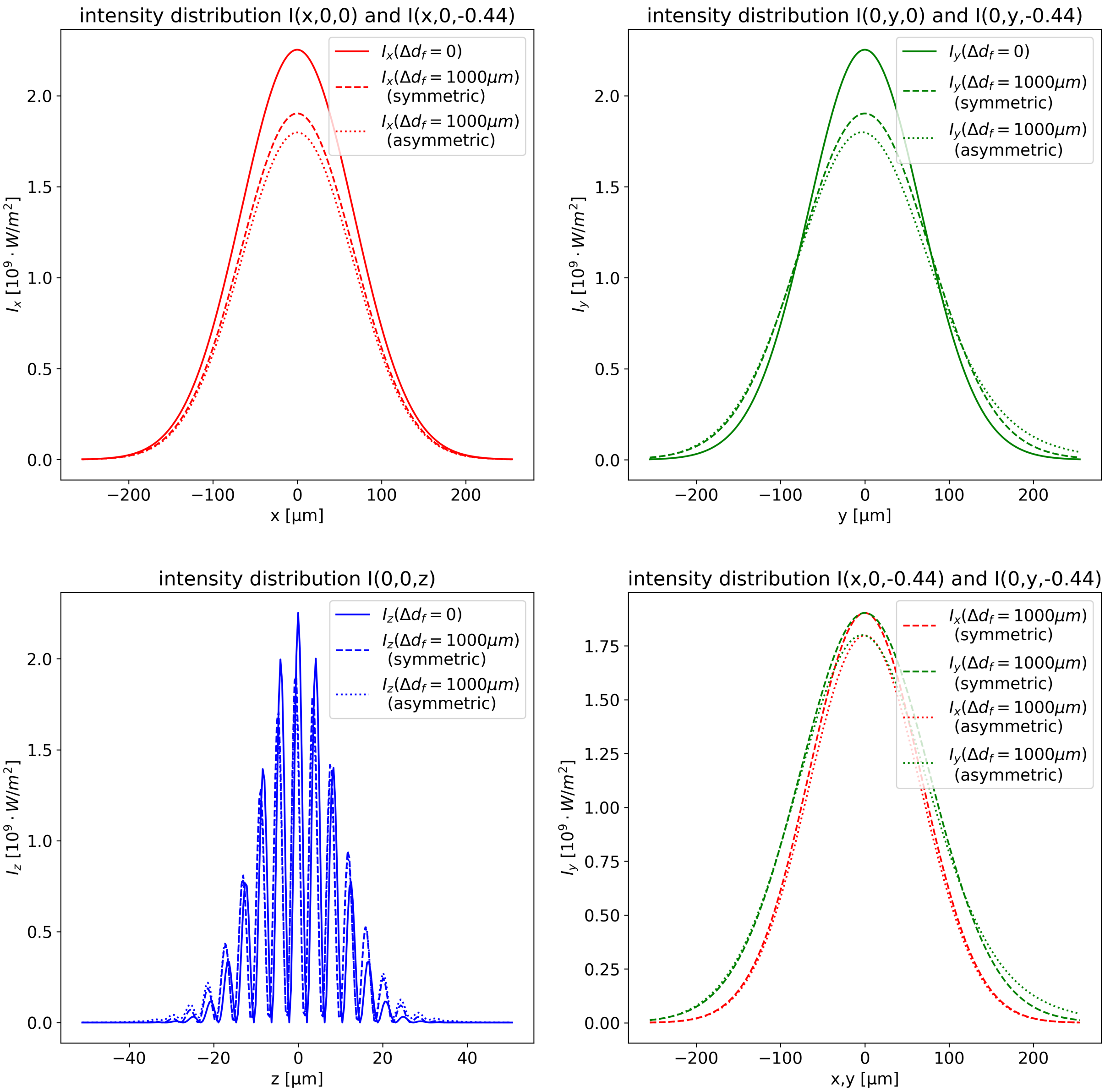

Figure B.38: One-dimensional intensity distribution in all spatial dimensions. The original distributions are plotted as solid lines, the modified distributions with a symmetric shift of the single-beam foci around the crossing point are plotted with dashed lines, and the modified distributions with an asymmetric shift of the single-beam foci around the crossing point are plotted with dotted lines. The cut line in the two horizontal directions for the dashed and dotted lines is shifted along the z-direction to the layer with maximal intensity. The relative distance between the foci along the beams is: $\Delta d_f = 1000\ \mu\text{m}$.

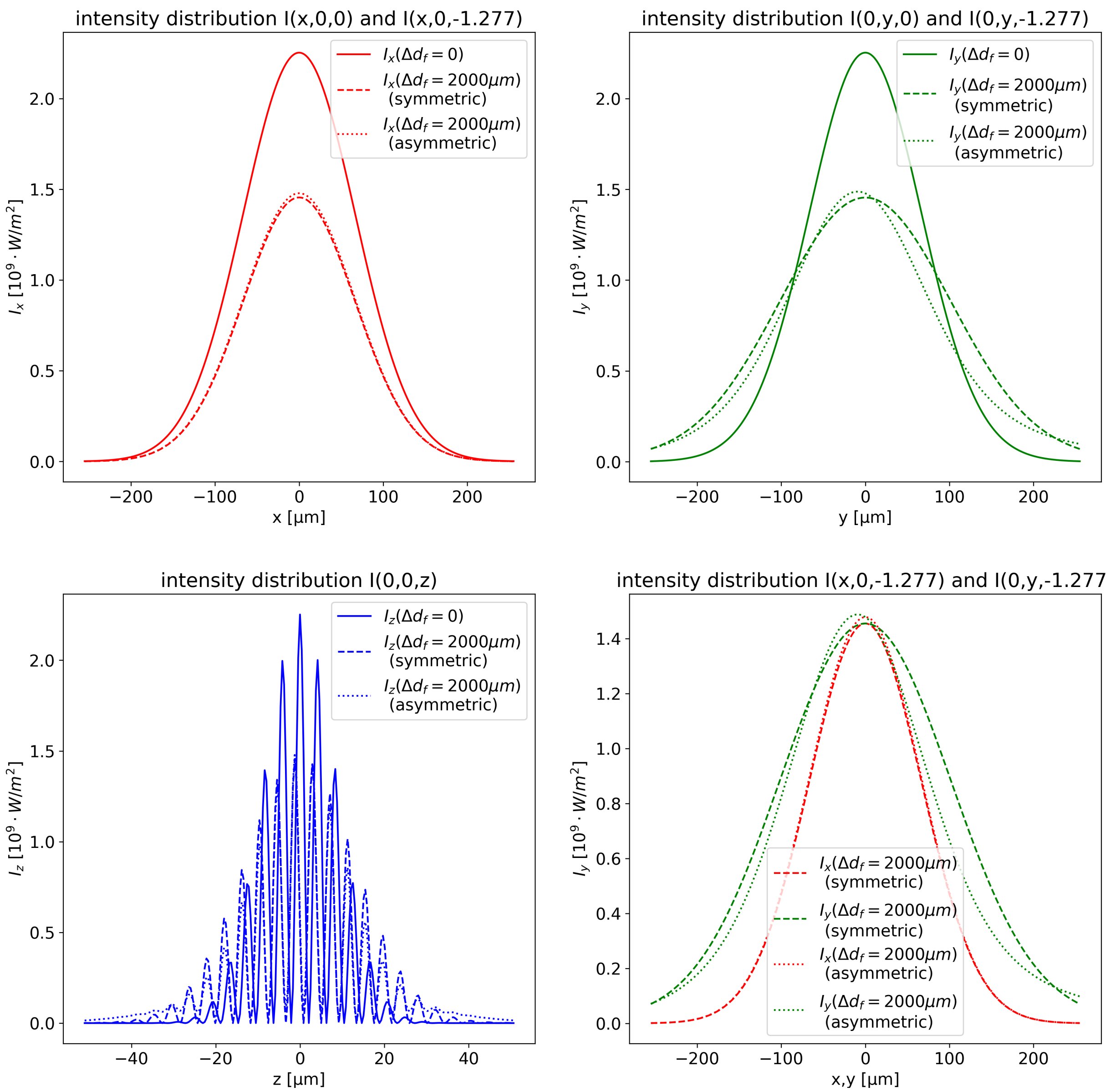

Figure B.39: One-dimensional intensity distribution in all spatial dimensions. The original distributions are plotted as solid lines, the modified distributions with a symmetric shift of the single-beam foci around the crossing point are plotted with dashed lines, and the modified distributions with an asymmetric shift of the single-beam foci around the crossing point are plotted with dotted lines. The cut line in the two horizontal directions for the dashed and dotted lines is shifted along the z-direction to the layer with maximal intensity. The relative distance between the foci along the beams is: $\Delta d_f = 2000\ \mu$m.

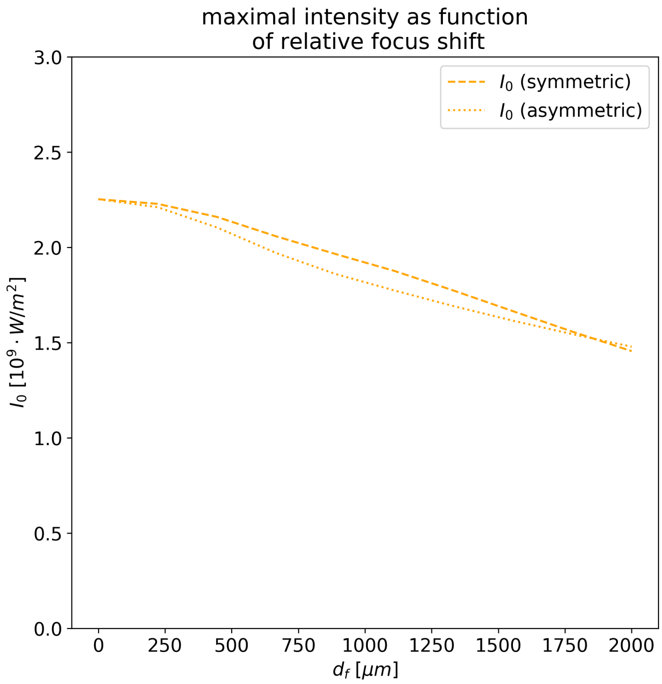

Figure B.40: Maximal intensity along z-direction as function of distance between the two single-beam foci and the corresponding potential depth.

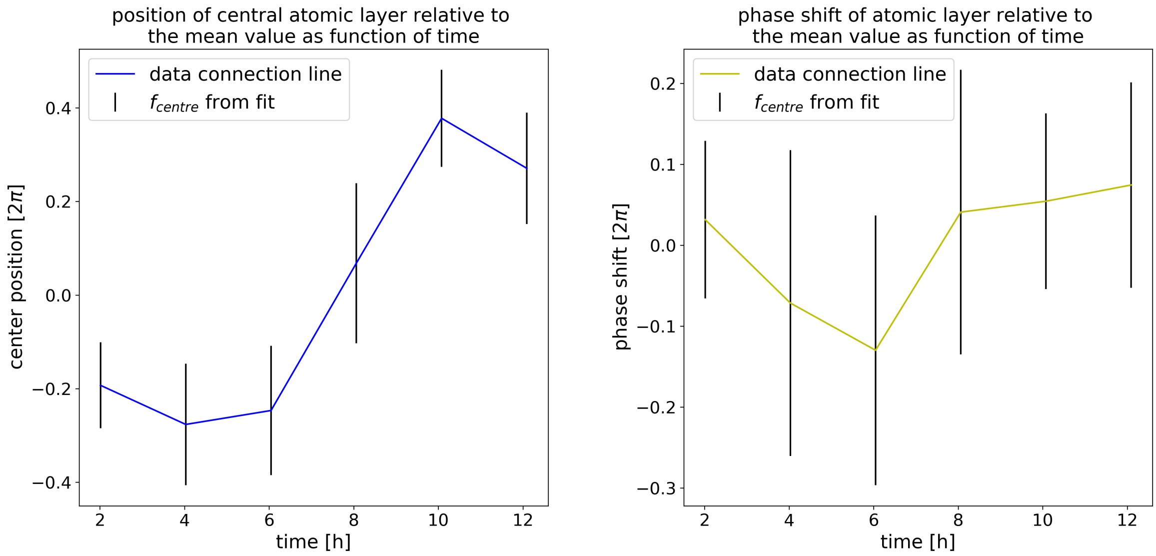

Figure B.41: Fit results to tomography data for the combined trap as function of time: Each fit was executed over the statistics of 6 tomography runs. Each time value corresponds to the time of the last run. On the left, the envelope position in z-direction is shown, whereas on the right the relative phase between the carrier position and the envelope is depicted. The error bars correspond to the errors of the fit results.

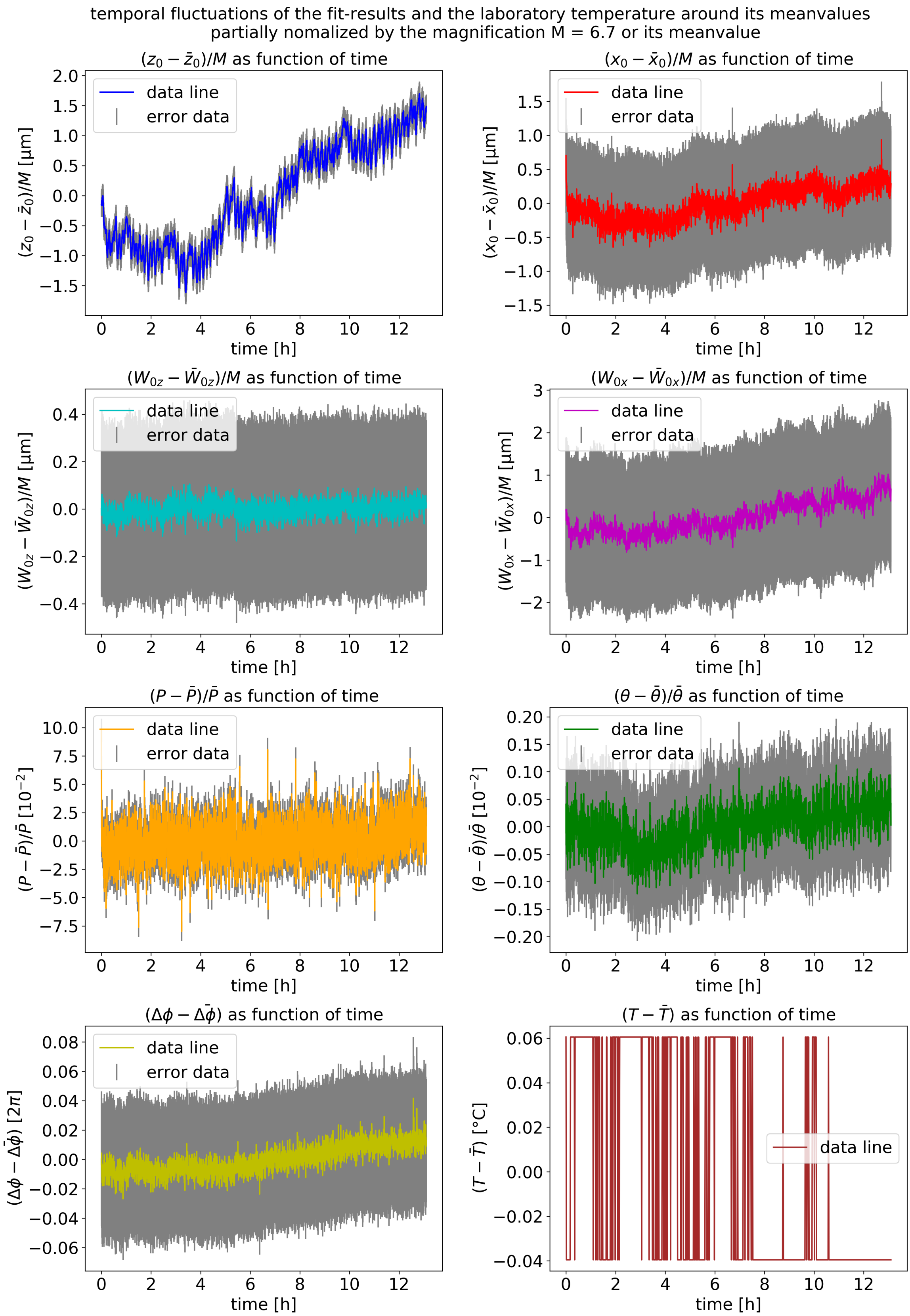

Figure B.42: Temporal fluctuations of the fit results from the one-dimensional intensity distributions deduced from the camera C_2 images during the tomography measurement of the combined trap. The error bars correspond to the errors of the fit results.

C A new laser shutter design

During this thesis the laser shutter design described in [39] was slightly modified for larger laser beam sizes and developed for high quantities. Conceptionally, a laser shutter is just used to close or open a laser beam path as depicted in figure C.1. As described in [39],

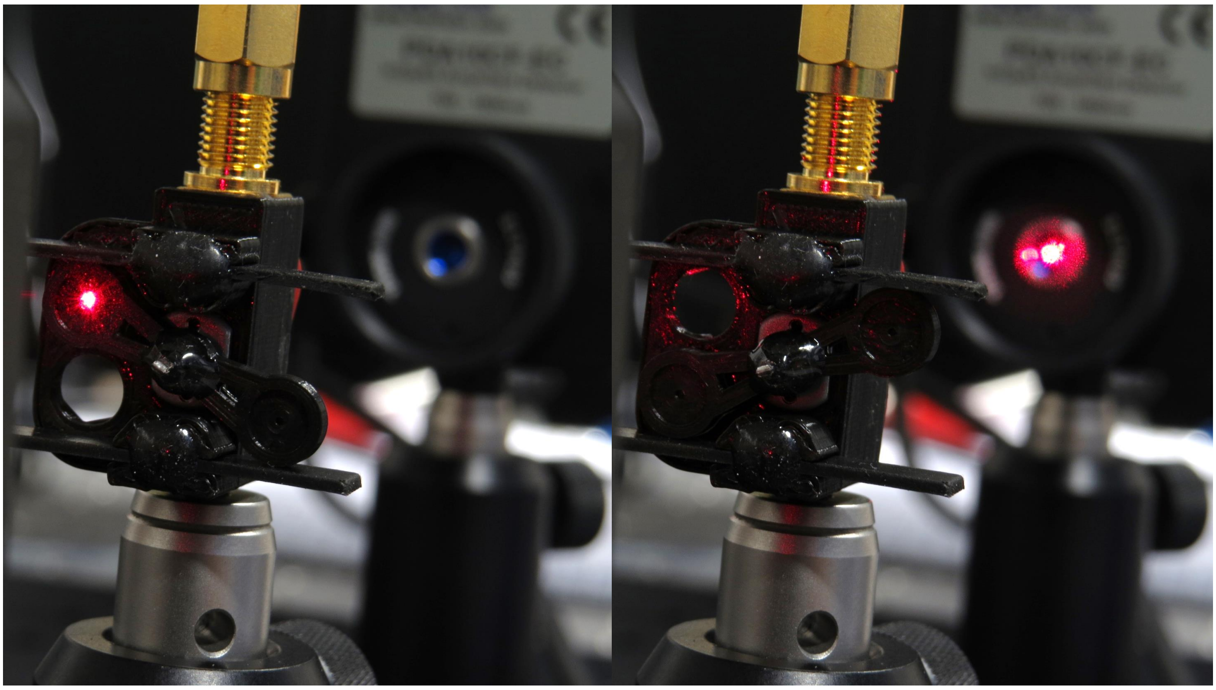

Figure C.1: On the left, a closed laser shutter in front of a photodiode and on the right an open one. For the final design the SMA-connector is exchanged by a cheaper BNC-connector.

there exists a huge list of desirable requirements for a laser shutter. The main properties are the activation delay and the switching time which is demonstrated in figure C.2. If the activation time is known and stable, it is mainly the switching time which has to be minimized. Besides a short activation delay and switching time, further requirements are a high timing precision of the opening and closing events, a large repetition rate, a low vibration and heat dissipation for minimal disturbance of the experimental setup, an aperture size which can block all relevant beam sizes, a high extinction ratio, high enough laser power handling, long operation lifetime, small size, simple usage including alignment and control, low cost, and finally the construction should have small performance inconsistencies from one laser shutter to the other ([39]). Apart from acousto-optical modulators, electro-optical modulators, or polarization-based shutters, one possible realization are mechanical laser shutters which have the advantage that they can block the beam completely. In [39] a fast and compact laser shutter design with a DC-motor and a

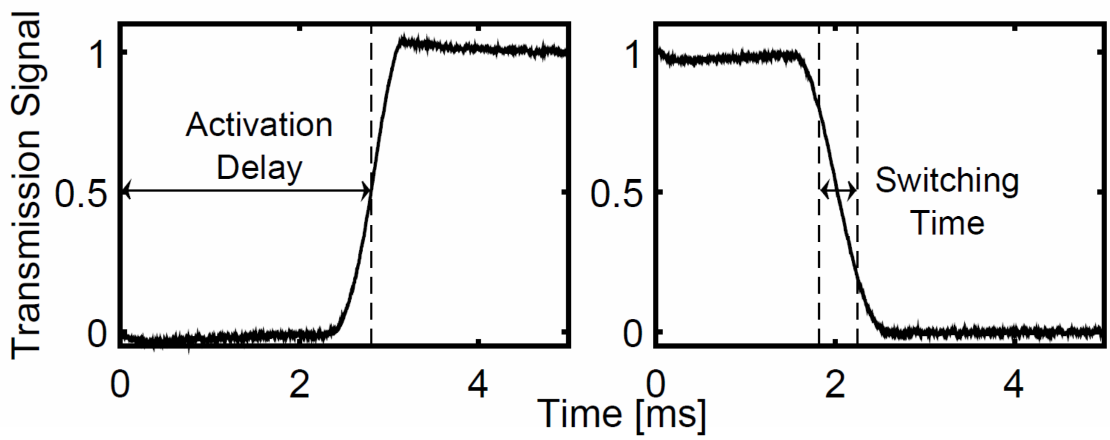

Figure C.2: Characteristic time scales of a laser shutter. The figure was taken from [39].

3D-printed body is presented which reaches 'a switching speed of (1.22 ± 0.02) m/s with 1 ms activation delay, 10 μs jitter in its timing performance' and lifetime of 10^8 cycles. The original design published in [39] is given in figure C.3, consisting of a DC-motor fixed in a mount and a blade on the DC-motor rod which can be rotated back and forth, stopped by two rubber flaps. The rubber flaps have to stop the blade such that it nearly does not oscillate at the stopping edge to guarantee a clean closing and opening edge of the rectangular beam pulse shape in time.

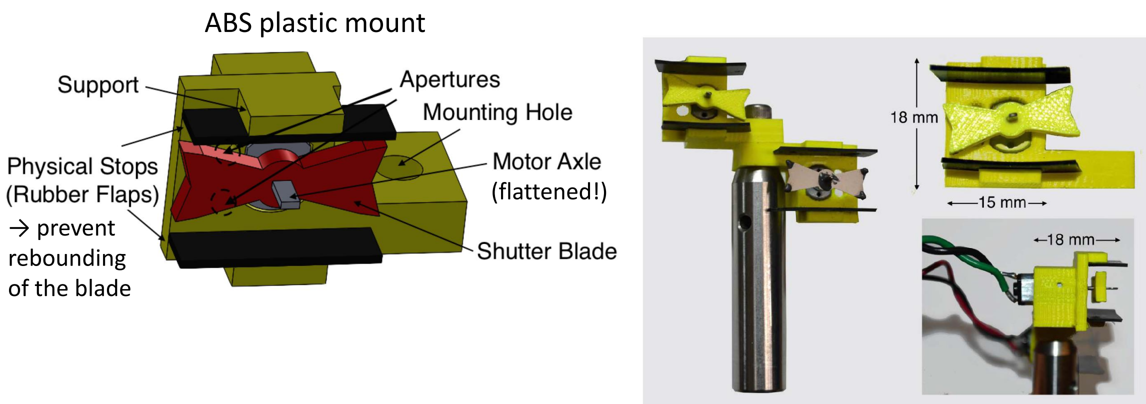

Figure C.3: Original laser shutter described in [39].

The described laser shutter is simple, reproducible, and cheap in production. The performance according to the activation delay and switching time was measured for different voltages for the DC-motor as shown in figure C.4 where one can see that both quantities decrease with increasing supply voltage. Besides the jitter is identified to be about 10 μs for the switching time and 20 μs for the activation delay. The maximum short-term repetition-rate is approximately 110 Hz, and the maximum long-term repetition-rate is about 20 Hz. The repetition rate is mainly limited by the heat-dissipation of the DC-motor to the plastic mount. To enable even larger beam sizes for our setups, the original

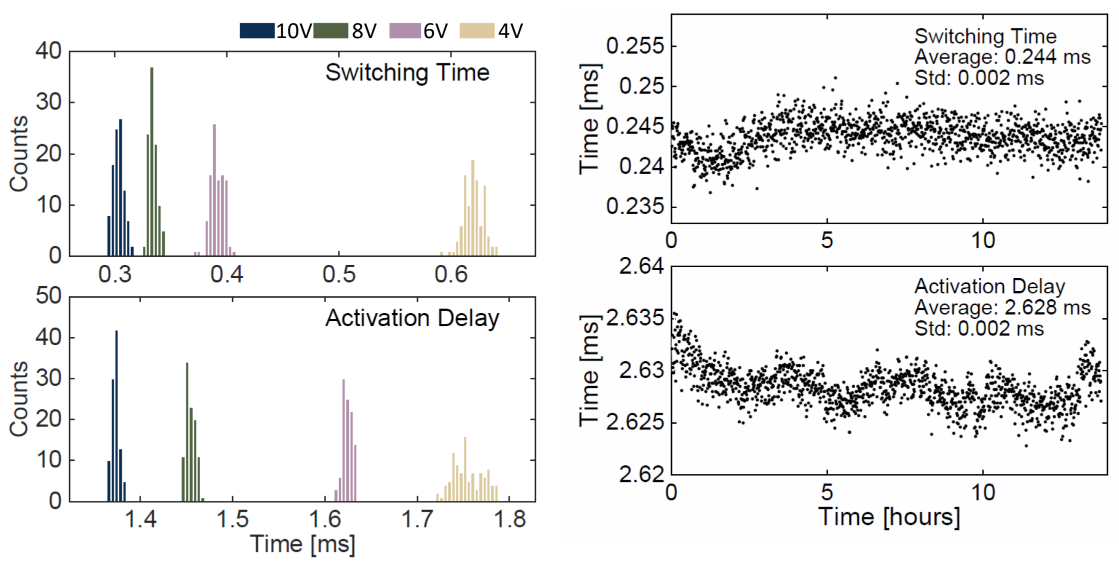

FIG. 5. Distribution of 100 measurements for the switching times (top) and delay times (bottom) at different operating voltages V_{CC}.

FIG. 6. Jitter range and distribution of delay times (top) and switching times (bottom) over 14 hours with operating voltage $V_{CC} = 9$ V.

,

Figure C.4: Original laser shutter performance described in [39].

laser shutter design was slightly modified. However, if one changes the design it is important to recover essentially the performance properties. Figure C.5 shows the main degrees of freedom which have to be taken into account during the design process. The activation time is given by the time the blade needs to move from one neoprene rubber flap to the other. So, the distance between the rubber flaps and the blade edge on the opposite side has to be minimized. At the same time, it is desirable to minimize the size and weight as well as optimize the shape to reach a small switching time. In contrast to that, for a large beam size one has to increase the blade size and the distance between the rubber flaps. So obviously, one has to make a compromise in this context. Finally, the rubber flaps have to be fixed such that they stop the blade optimally.
The modified version of the laser shutter was designed in the CAD-software CATIA, and the resulting product is shown in figures C.6 and C.7. The new laser shutter allows a maximal beam diameter of 6 mm. Besides, a BNC-connector is fixed on top of the laser shutter to simplify the electronic connection. The final laser shutter can be equipped with a black plastic blade for visible laser light or an aluminium blade for infrared laser light which reflects most of the power to protect the laser shutter from heating damages. The final version of the laser shutter, mounted on a vibrational isolator, is presented in figure

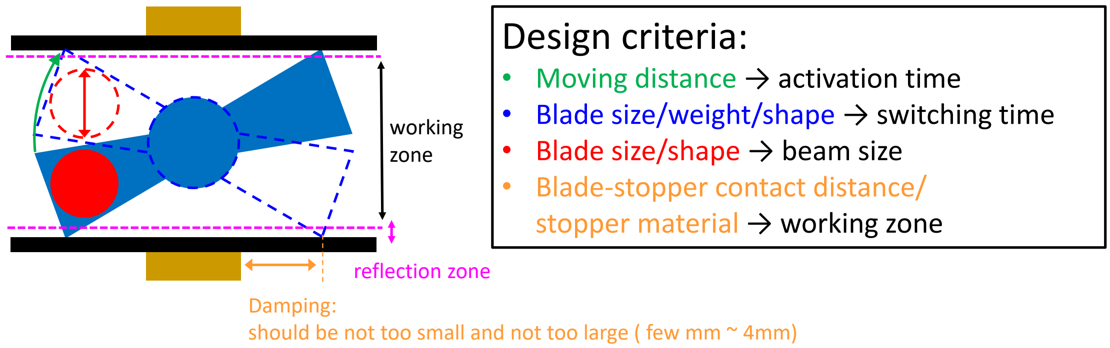

Figure C.5: Design criteria demonstrated at the schematic shape of the laser shutter. Apart from the motor itself, the activation time is limited by the time the blade needs to move from the open to the closed configurations, and the switching time is limited by the blade size, weight, and shape. At the same time, the blade shape determines the size of the beam which can be blocked. The damping of the blade stopping oscillations is mainly given by the distance between the mount edge and the contact point of the blade to the rubber flaps. Besides, the damping depends on the characteristics of stopper material itself.

C.8. As the vibrations from the laser shutter are weak, the large vibrational isolator is possibly not necessary.
Apart from the laser shutter itself [39] describes a driving circuit which is depicted in figure C.9. Here, a rectangular positive voltage signal (TTL) is converted by an inverter and an H-bridge to a rectangular signal also with negative voltage values. In this way the current flows back and forth through an RC-element and the DC-motor which rotates in one or the other direction. The resistor leads to a small holding current which fixes the position of the blade after its rotation from the opposite configuration. The capacitor collects in each step a charge which is released by a strong exponentially decaying current which accelerates the blades motion.
To simplify the circuit construction and minimize the cost, the inverter with necessary resistors and the H-bridge are replaced by a dual motor driver carrier from Pololu in our realization. The element, shown in figure C.10, can be used for two motors at the same time and requires a logic supply voltage of $2-7$ V. The motor can be driven with a voltage of up to 11 V. For this reason, it was decided to use a 9 V voltage supply and a linear voltage regulator to provide 5 V of logic voltage. The manufacturing process was optimized by the design of the circuit in Altium Designer, shown in figure C.11. The final printed circuit board (PCB) is able to drive four laser shutters at the same time and fits in a compact box. So, the box including the PCB has four BNC-connectors for the TTL-input signals and four BNC-connectors for the motor driver signals. It is important to note that one has to use isolated BNC-cables for the output signals to the laser shutters to prevent any short-circuit faults through the metallic optical table between

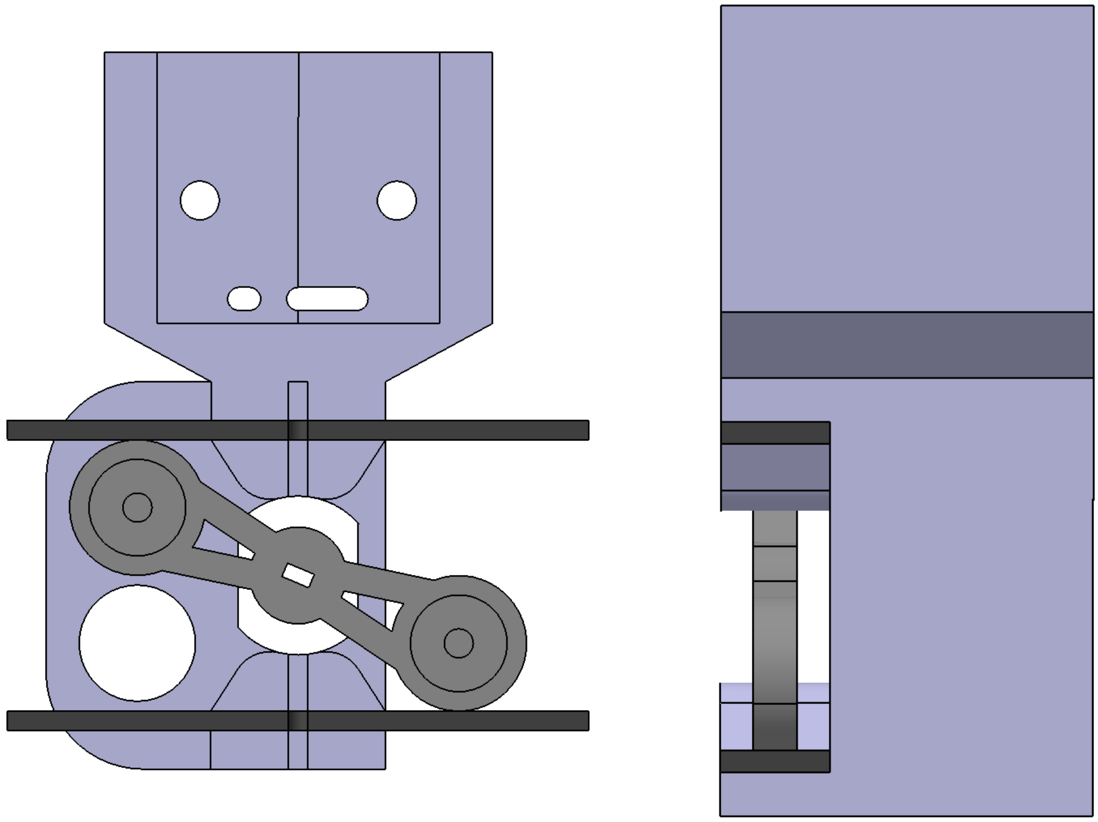

Figure C.6: Pictures from the CAD-model of the laser shutter designed in CATIA. On the left: front view to the laser shutter. On the right: side view to the laser shutter.

the shutter circuits which can lead to damages. The PCB was ordered from a company and equipped manually by the workshop. The final driver board is shown in figure C.12 and C.13. In order to check if the modified design still fulfills the necessary requirements the activation delay and the switching time were measured with a red laser beam with a beam width of about 300 μm and a photodiode behind the laser shutter. The results are given in table C.1. From the measured data, one can conclude that the characteristic performance quantities of the slightly modified design still are in the right range and lead to a satisfying result. As expected, the activation time and the switching time are for the heavier aluminium blade a little bit larger but still acceptable. The plastic blade velocity was measured to be about: $v_s = (1.41 \pm 0.06)$ m/s. If one compares two different shutters, the performance is still quite consistent as demonstrated in table C.2.
An additional question is how stable the characteristic quantities are for different repetition rates. In figures C.14 and C.15 the measured performance as function of repetition rate is shown.
One can observe, that the activation delay and the switching time stay quite stable for different repetition rates, but the time it stays stable decreases with increasing repetition rates because of heat-dissipation by the DC-motor to the plastic mount. For a repetition rate of 90 Hz, the shutter leaves a stable operation state after about less than one second,

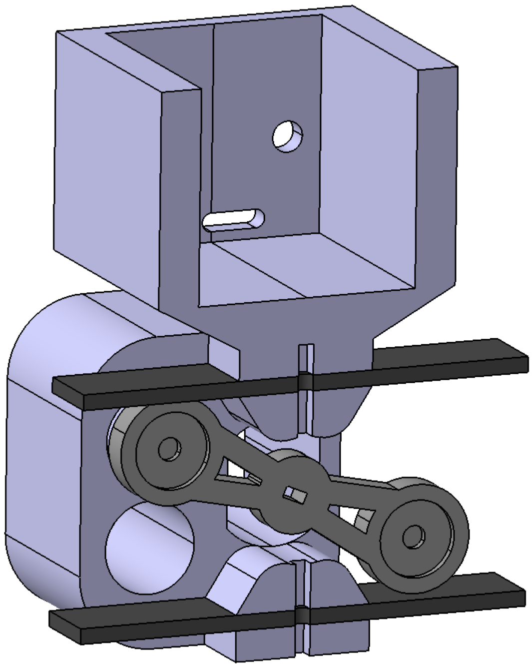

Figure C.7: Pictures from the CAD-model of the laser shutter designed in CATIA: Front view to the new laser shutter design.

design	plastic blade	aluminium blade
t_{act}(opening) [ms]	3.85 ± 0.07	6.20 ± 0.01
t_{act}(closing) [ms]	3.94 ± 0.03	5.27 ± 0.02
t_{act}(mean) [ms]	3.89 ± 0.07	5.7 ± 0.5
t_{switch} (opening) [μs]	277 ± 10	428 ± 4
t_{switch} (closing) [μs]	232 ± 2	359 ± 5
t_{switch} (mean) [μs]	254 ± 24	393 ± 35

Table C.1: New laser shutter characteristics including the activation delay and the switching time. The switching time corresponds to the time the signal amplitude changes between 10% and 90%. The repetition rate corresponds to 1 Hz. The measurement was executed for a single shutter. The performance variations between different shutters can be much larger than the jitter of the temporal quantities for a single shutter itself. The given errors are probably more limited by the measurement uncertainty of only at least three measurements per value and represent not a valid jitter measurement.

whereas for moderate repletion rates of about 20 Hz, the shutter operates stably over the whole observation time. This is consistent to the observations described in [39].

Figure C.8: Front view to the new laser shutter design.

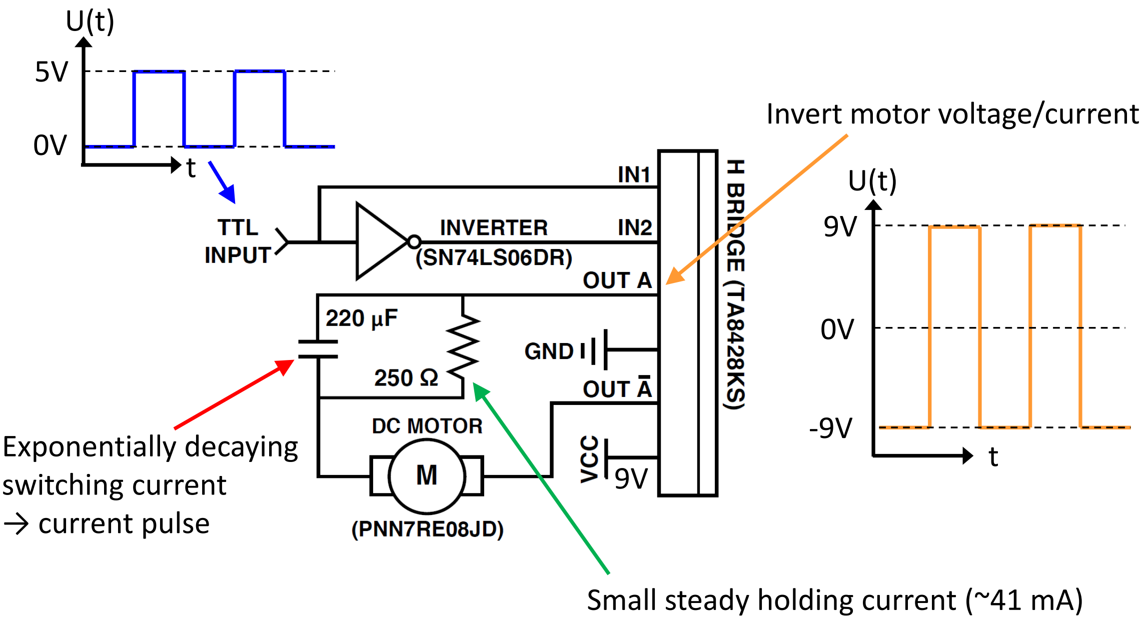

Figure C.9: Driver circuit for a single laser shutter. The figure is based on [39].

Dual Motor Driver Carrier: replaces H-bridge, Inverter (and Resistor)

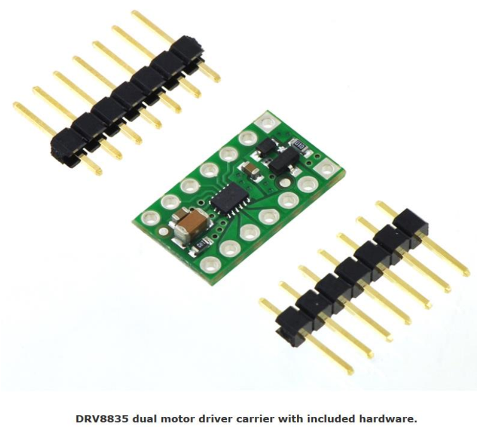

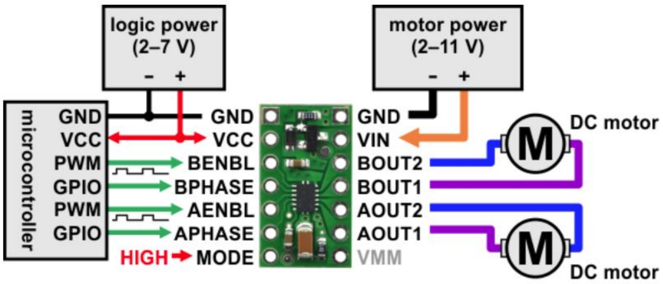

Simplified drive/brake operation with MODE=1 (PHASE/ENABLE)				
xPHASE	xENABLE	xOUT1	xOUT2	operating mode
0	PWM	PWM	L	forward/brake at speed *PWM %*
1	PWM	L	PWM	reverse/brake at speed *PWM %*
X	0	L	L	brake low (outputs shorted to ground)

Figure C.10: Dual motor driver carrier specifications from POLOLU (https://www.pololu.com/product/2135). The PWM values can be replaced by HIGH values to reach maximal speed.

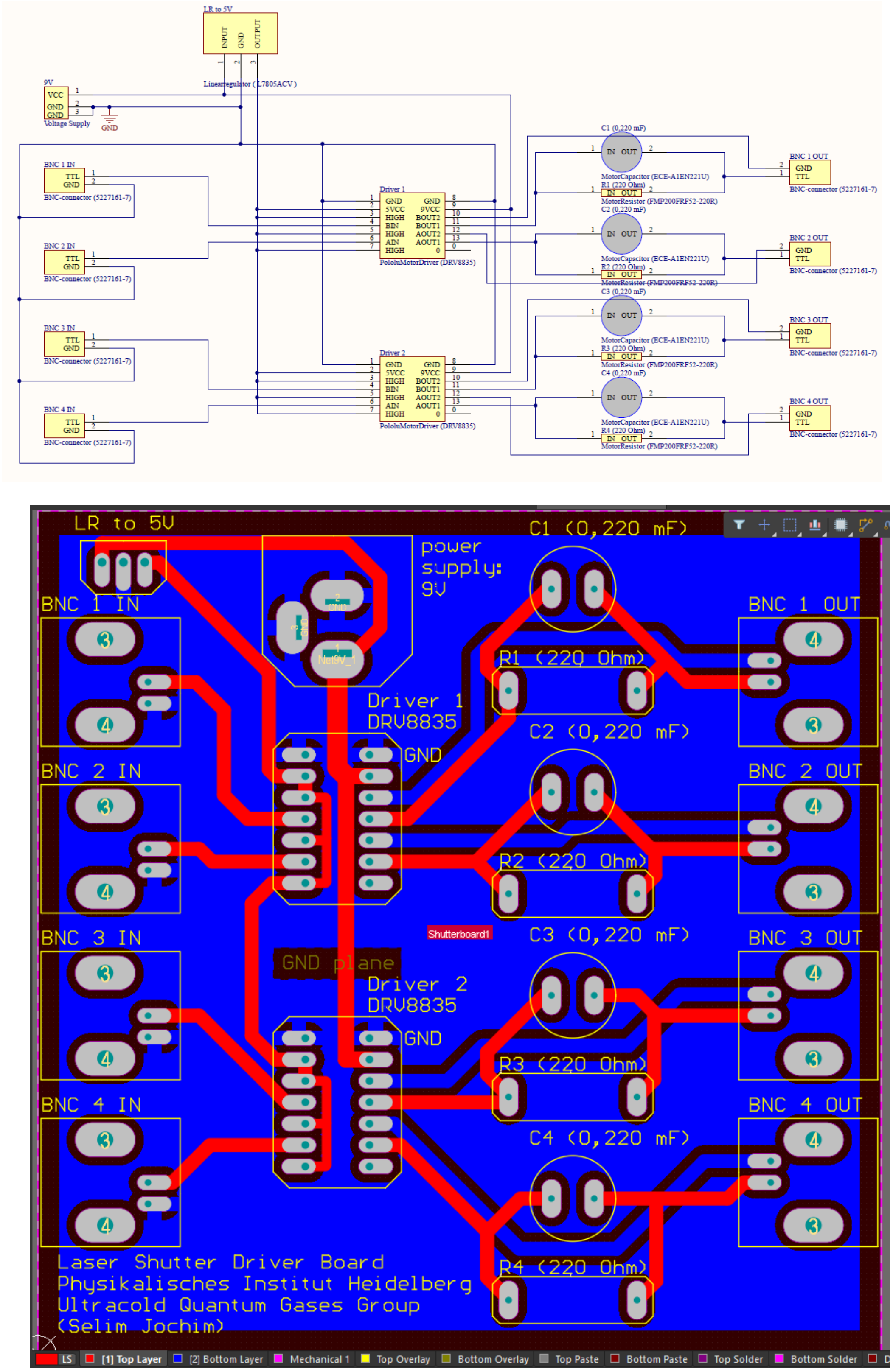

Figure C.11: Full circuit of the laser shutter driver board. The top part shows the schematic, and the bottom part provides a view on the PCB design.

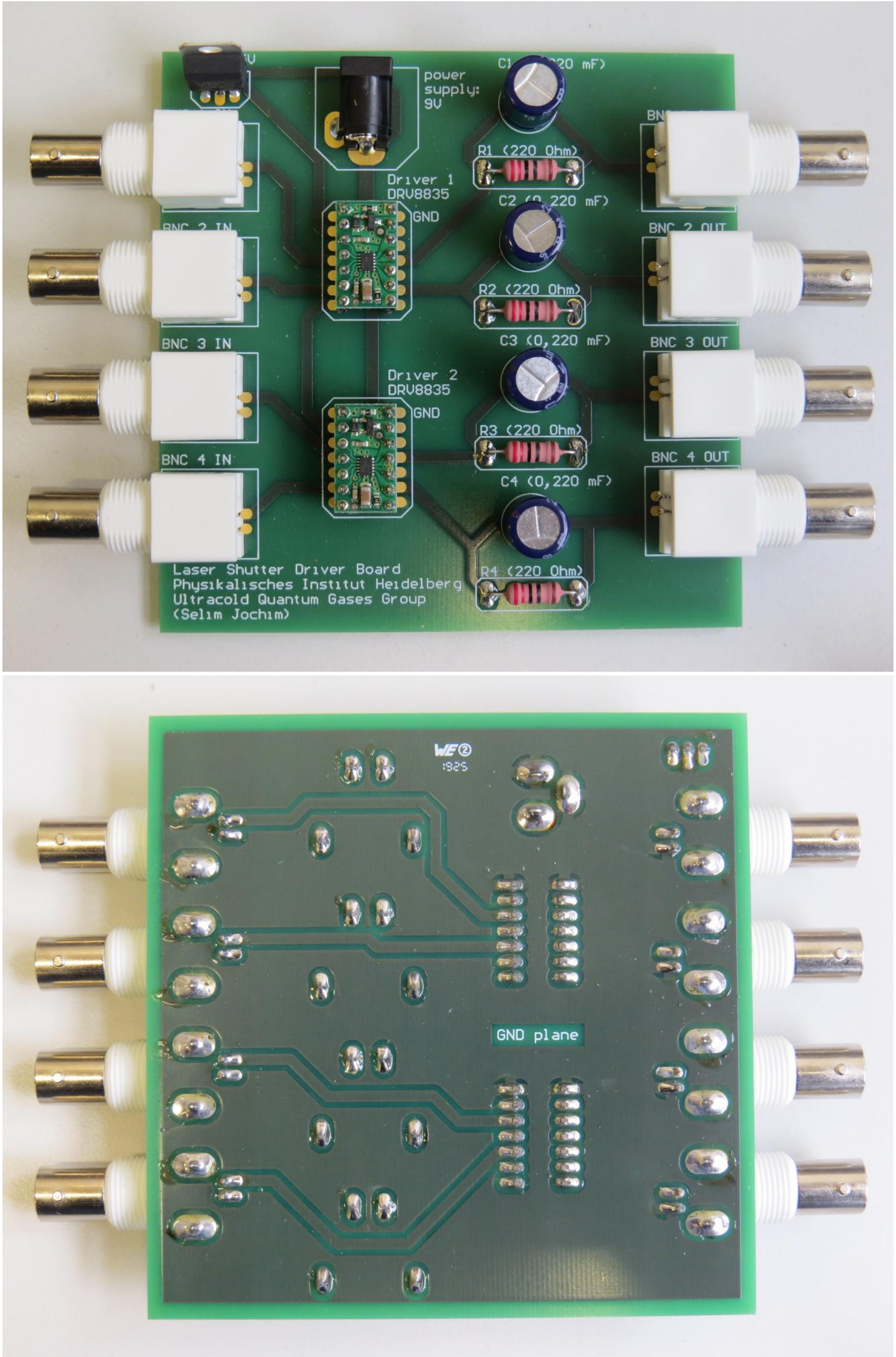

Figure C.12: Top and bottom view to the designed driver board for the laser shutter which is able to control four laser shutters at the same time.

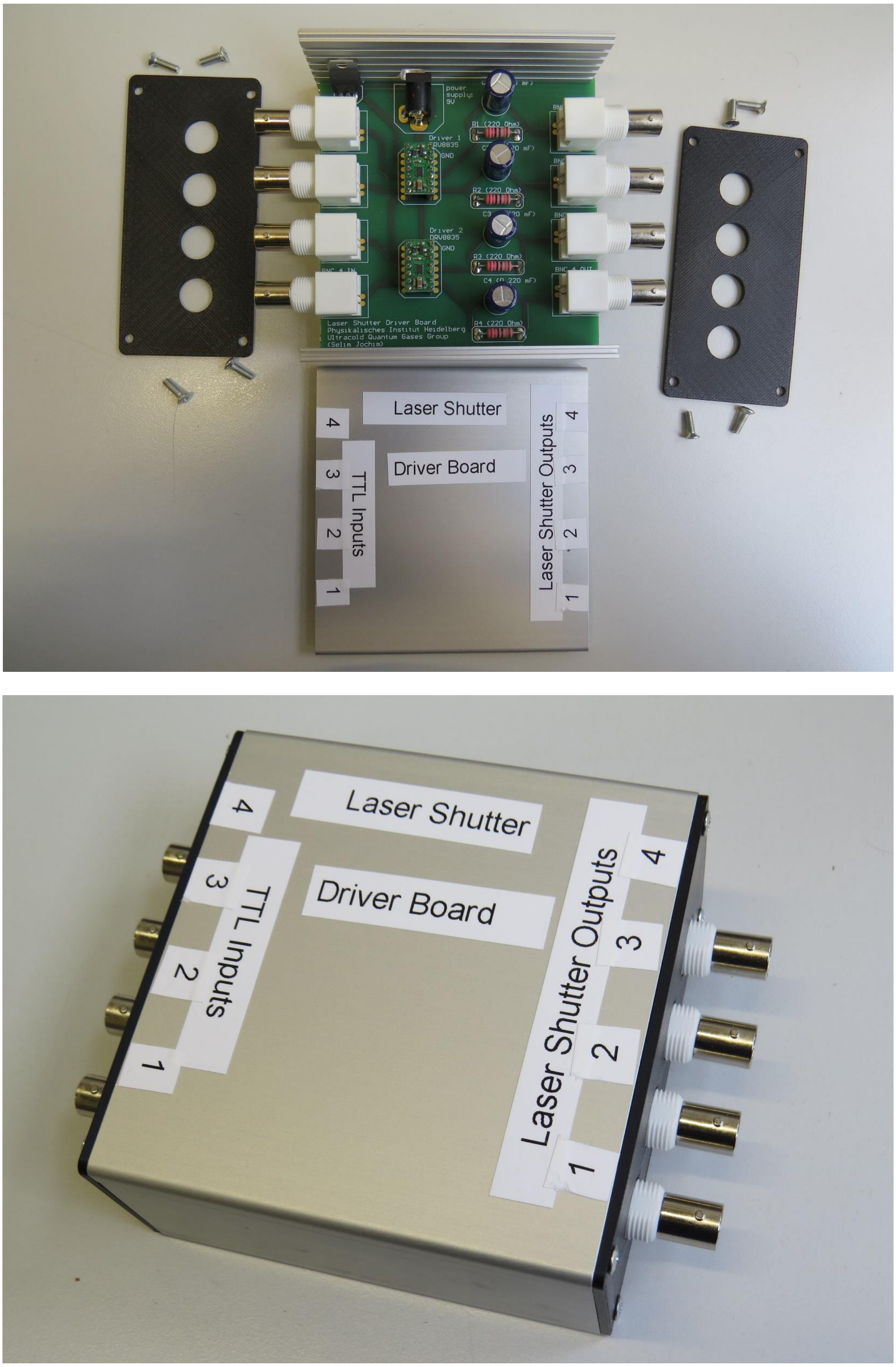

Figure C.13: The top figure shows a view to the opened driver board box and the bottom figure a view to the closed ones. This leads to a compact and robust design.

design	plastic blade
t_{act}(opening) [ms]	3.67 ± 0.18
t_{act}(closing) [ms]	4.09 ± 0.16
t_{act}(mean) [ms]	3.88 ± 0.27
t_{switch} (opening) [μs]	270 ± 10
t_{switch} (closing) [μs]	232 ± 4
t_{switch} (mean) [μs]	251 ± 21

Table C.2: New laser shutter characteristics including the activation delay and the switching time. The switching time corresponds to the time the signal amplitude changes between 10% and 90%. The repetition rate corresponds to 1 Hz. The measurement was executed for two different shutters. Three measurements per shutter and quantity were taken.

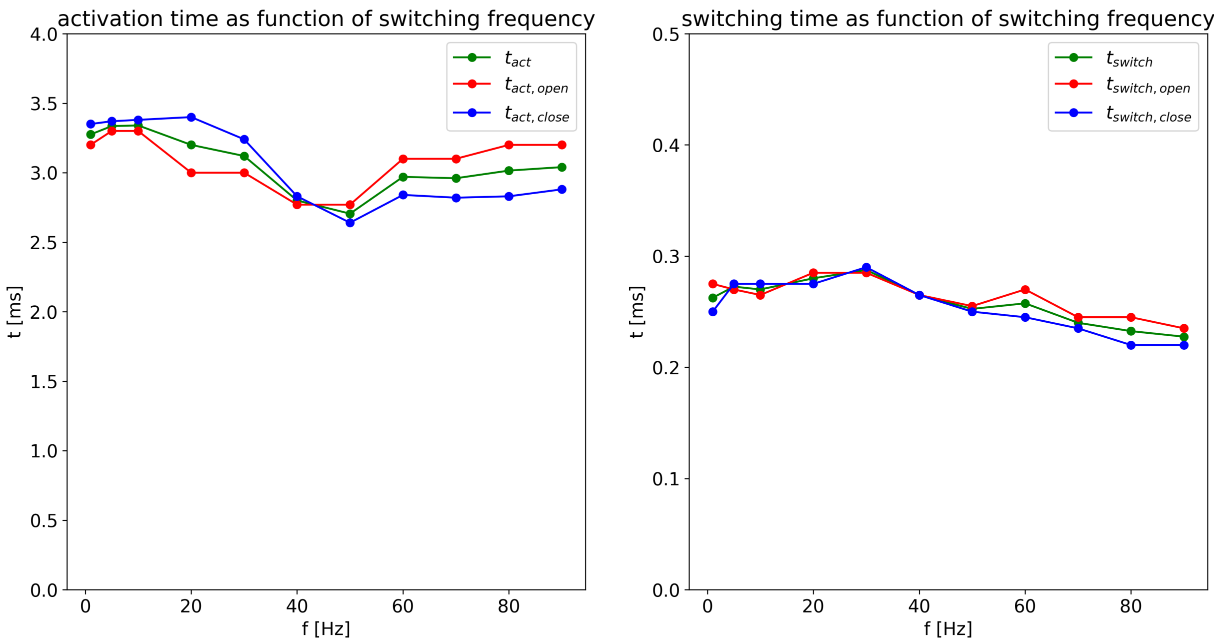

Figure C.14: Activation delay and switching time as functions of repetition rate (switching frequency). There were taken three measurements per data point.

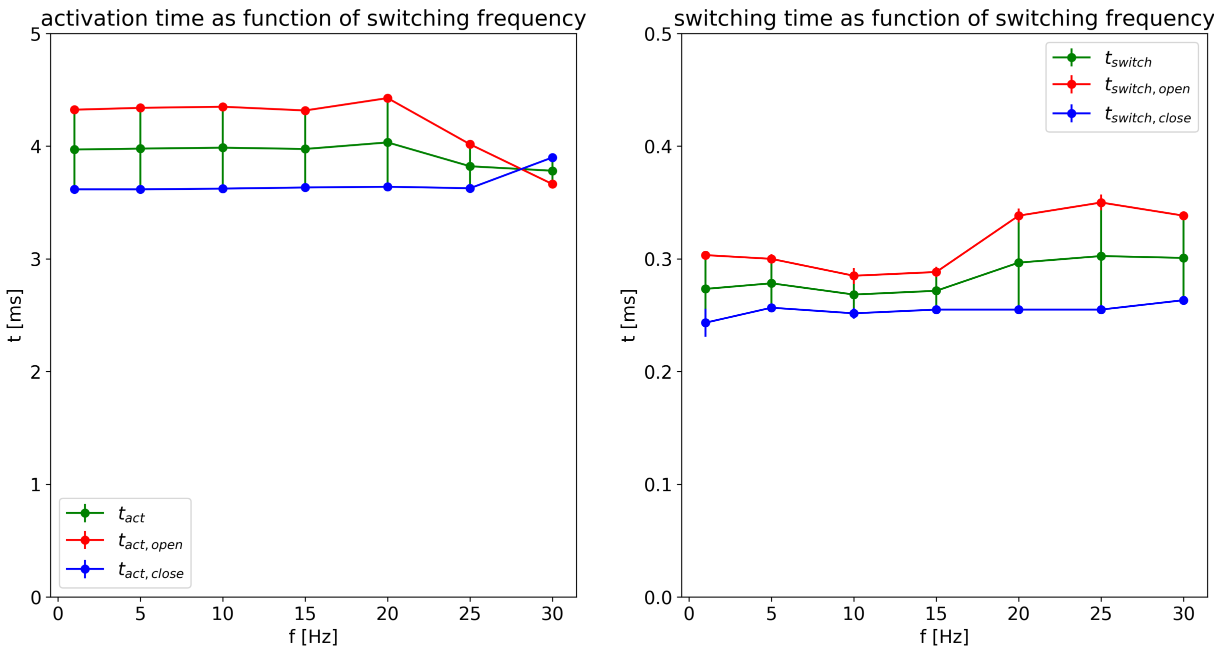

Figure C.15: Activation delay and switching time as functions of repetition rate (switching frequency). There was taken one measurement per data point.

Bibliography

[1] Bergschneider, Andrea: *Strong correlations in few-fermion systems.* Version: 2017. http://ultracold.physi.uni-heidelberg.de/files/PhD_2017_Andrea_final.pdf. – PhD thesis, Ruprecht-Karls-Universität Heidelberg

[2] Bergschneider, Andrea ; Klinkhamer, Vincent M. ; Becher, Jan H. ; Klemt, Ralf ; Zürn, Gerhard ; Preiss, Philipp M. ; Jochim, Selim: Spin-resolved single-atom imaging of ^{6}Li in free space. In: *Physical Review A* 97 (2018), Nr. 063613. https://journals.aps.org/pra/abstract/10.1103/PhysRevA.97.063613

[3] Bjerlin, J. ; Reimann, S.M. ; Bruun, G.M.: Few-Body Precursor of the Higgs Mode in a Fermi Gas. In: *Physical Review Letters* 116 (2016), Nr. 155302. https://journals.aps.org/prl/abstract/10.1103/PhysRevLett.116.155302

[4] Bohn, Johanna E.: *Towards an ultracold three-component Fermi Gas in two dimensional optical lattice.* Version: 2012. http://ultracold.physi.uni-heidelberg.de/files/diplomarbeit_johanna.pdf. – diploma thesis, Ruprecht-Karls-Universität Heidelberg

[5] Chin, Cheng ; Grimm, Rudolf ; Julienne, Paul ; Tiesinga, Eite: Feshbach Resonances in Ultracold Gases. In: *Review of Modern Physics* (2010). https://journals.aps.org/rmp/abstract/10.1103/RevModPhys.82.1225

[6] Demtröder, Wolfgang: *Experimentalphysik 3. Atome, Moleküle und Festkörper. (German).* Berlin, Heidelberg : Springer, 2010

[7] Fliessbach, Torsten: *Statistische Physik : Lehrbuch zur Theoretischen Physik IV (German).* Berlin, Heidelberg : Springer Spektrum, 2018

[8] Gehm, Michael E.: *PREPARATION OF AN OPTICALLY-TRAPPED DEGENERATE FERMI GAS OF ^{6}LI: FINDING THE ROUTE TO DEGENERACY*, Duke University, PhD thesis, 2003. https://www.physics.ncsu.edu/jet/theses/pdf/Gehm.pdf. – Appendix A: Properties of ^{6}Li , PhD thesis, Duke University

[9] Greiner, M. ; Regal, C. A. ; Stewart, J. T. ; Jin, D. S.: Probing Pair-Correlated Fermionic Atoms through Correlations in Atom Shot Noise. In: *Physical Review Letters* 94 (2005), Nr. 110401. https://journals.aps.org/prl/abstract/10.1103/PhysRevLett.94.110401

[10] Grimm, Rudolf ; Weidemüller, Matthias ; Ovchinnikov, Yurii B.: Optical dipole traps for neutral atoms. In: *Advances in Atomic, Molecular and Optical Physics* 42 (2000), 95–170. https://arxiv.org/abs/physics/9902072

[11] Griot, CVI M.: *Fundamental Optics*. http://experimentationlab.berkeley.edu/sites/default/files/ATM/fundamental-Optics.pdf

[12] Gross, Christian ; Bloch, Immanuel: Quantum simulations with ultracold atoms in optical lattices. In: *Science* 357 (2017), Nr. 6355, 995-1001. https://science.sciencemag.org/content/357/6355/995/tab-pdf

[13] Gubbels, K.B. ; Stoof, H.T.C.: Imbalanced Fermi gases at unitarity. In: *Physics Reports* 525 (2012), 255-313. https://arxiv.org/pdf/1205.0568.pdf

[14] Harshman, D. R. ; Mills, Jr. A. P.: Concerning the nature of high-T_c superconductivity: Survey of experimental properties and implications for interlayer coupling. In: *Physical Review B* 45 (18) (1992), 10684–10712. https://journals.aps.org/prb/abstract/10.1103/PhysRevB.45.10684

[15] Hartmann, Michael J.: Quantum Simulation with Interacting Photons. In: *J. Opt.* 18 (2016), Nr. 104005. https://arxiv.org/abs/1605.00383

[16] Haynes, W. M.: *CRC Handbook of Chemistry and Physics. 91st Edition 2010-2011*. Boca Raton, London, New York : Taylor and Francis Group (CRC Press), 2010

[17] Hueck, Klaus ; Luick, Niclas ; Sobirey, Lennart ; Siegl, Jonas ; Lompe, Thomas ; Moritz, Henning: Two-Dimensional Homogeneous Fermi Gases. In: *Physical Review Letters* 120 (2018), Nr. 060402. https://journals.aps.org/prl/abstract/10.1103/PhysRevLett.120.060402

[18] Ketterle, Wolfgang ; Zwierlein, Martin W.: Making, probing and understanding ultracold Fermi gases. In: *arxive* (2008). https://arxiv.org/abs/0801.2500

[19] Klemt, Ralf A.: *Many-body correlations in a quasi-two-dimensional, ultracold atomic Fermi gas*. 2016. – Master thesis, Ruprecht-Karls-Universität Heidelberg

[20] Klinkhamer, Vincent M.: *An apparatus for few-fermion systemsin multiple well potentials*. Version: 2012. http://ultracold.physi.uni-heidelberg.de/files/Masterarbeit_Vincent.pdf. – Master thesis, Ruprecht-Karls-Universität Heidelberg

[21] Luick, Niclas ; Sobirey, Lennart ; Bohlen, Markus ; Singh, Vijay P. ; Mathey, Ludwig ; Lompe, Thomas ; Moritz, Henning: An ideal Josephson junction in an ultracold two-dimensional Fermi gas. In: *arXive* (2019), Nr. 1908.09776. https://arxiv.org/abs/1908.09776

[22] Mermin, N. D. ; Wagner, H.: Absence of Ferromagnetism or Antiferromagnetism in One- or Two-Dimensional Isotropic Heisenberg Models. In: *Physical Review Letters* 17 (22) (1966), 1133–1136. https://journals.aps.org/prl/abstract/10.1103/PhysRevLett.17.1133

[23] Murthy, P.A. ; Boettcher, I. ; Bayha, L. ; Holzmann, M. ; Kedar, D. ; Neidig, M. ; Ries, M.G. ; Wenz, A.N. ; Zürn, G. ; Jochim, S.: Observation of the Berezinskii-Kosterlitz-Thouless Phase Transition in an Ultracold Fermi Gas. In: *Physical Review Letters* 115 (2015), Nr. 010401. https://journals.aps.org/prl/abstract/10.1103/PhysRevLett.115.010401

[24] Neidig, Mathias: *A realization of a two-dimensional Fermi gas in a standing wave trap*. Version: 2013. http://ultracold.physi.uni-heidelberg.de/files/Masterarbeit_2013_Mathias.pdf. – Master thesis, Ruprecht-Karls-Universität Heidelberg

[25] Neidig, Mathias: *Many-Body Pairing in aTwo-Dimensional Fermi Gas*. Version: 2017. http://ultracold.physi.uni-heidelberg.de/files/PhD_2017_Mathias.pdf. – PhD thesis, Ruprecht-Karls-Universität Heidelberg

[26] Palm, Lukas: *Exploring fractional quantum hall physics using ultracold fermions in rotating traps*. 2018. – Master thesis, Ruprecht-Karls-Universität Heidelberg

[27] Petzold, Ram-Janik: *A two-dimensional optical dipole trap for a system of few ultracold fermions*. 2016. – Bachelor thesis, Ruprecht-Karls-Universität Heidelberg

[28] Ries, Martin G.: *A Two-Dimensional Fermi Gas in the BEC-BCS Crossover*, Ruprecht-Karls-Universität Heidelberg, PhD thesis, 2015. http://ultracold.physi.uni-heidelberg.de/files/PhD_2015_Martin.pdf. – PhD thesis, Ruprecht-Karls-Universität Heidelberg

[29] Ries, M.G. ; Wenz, A.N. ; Zürn, G. ; Bayha, L. ; Boettcher, I. ; Kedar, D. ; Murthy, P.A. ; Neidig, M. ; Lompe, T. ; Jochim, S.: Observation of Pair Condensation in the Quasi-2D BEC-BCS Crossover. In: *Physical Review Letters* 114 (2015), Nr. 230401. https://journals.aps.org/prl/abstract/10.1103/PhysRevLett.114.230401

[30] Rontani, M. ; Armstrong, J. R. ; Yu, Y. ; Åberg, S. ; ; Reimann, S. M.: Cold Fermionic Atoms in Two-Dimensional Traps: Pairing versus Hund's Rule. In: *Physical Review Letters* 102 (2009), Nr. 060401. https://journals.aps.org/prl/abstract/10.1103/PhysRevLett.102.060401

[31] Saint-Jalm, R. ; Castilho, P.C.M. ; Cerf, É. L. ; Bakkali-Hassani, B. ; Ville, J.-L. ; Nascimbene, S. ; Beugnon, J. ; Dalibard, J.: Dynamical Symmetry and Breathers in a Two-Dimensional Bose Gas. In: *Physical Review X* 9 (2019), Nr. 021035. https://journals.aps.org/prx/abstract/10.1103/PhysRevX.9.021035

[32] Saleh, B.E.A. ; Teich, M.C.: *Fundamentals of Photonics*. Hoboken, New Jersey : Wiley, 2007

[33] Schwabl, Franz: *Quantenmechanik (QM1). Eine Einführung. (German)*. Berlin, Heidelberg : Springer, 2007

[34] Serwane, F. ; Zürn, G. ; Lompe, T. ; Ottenstein, T. B. ; Wenz, A. N. ; Jochim, S.: Deterministic Preparation of a Tunable Few-Fermion System. In: *Science* 332 (2011), Nr. 6027, 336-338. https://science.sciencemag.org/content/332/6027/336/tab-pdf

[35] Serwane, Friedhelm: *The setup of a Magneto Optical Trap for the preparation of a mesoscopic degenerate Fermi gas.* Version: 2007. http://ultracold.physi.uni-heidelberg.de/files/diplomarbeit-friedhelm.pdf. – Diploma thesis, Ruprecht-Karls-Universität Heidelberg

[36] Serwane, Friedhelm: *Deterministic preparation of a tunablefew-fermion system.* Version: 2011. http://ultracold.physi.uni-heidelberg.de/files/thesisfriedhelmserwane.pdf. – PhD thesis, Ruprecht-Karls-Universität Heidelberg

[37] Steinmann, Jochen: *Multiphoton Ionization of Laser Cooled Lithium.* Version: 2007. http://archiv.ub.uni-heidelberg.de/volltextserver/7585/1/Dissertation_Steinmann.pdf. – PhD thesis, Ruprecht-Karls-Universität Heidelberg

[38] Wenz, Andre N.: *From Few to Many: Ultracold Atoms in Reduced Dimensions*, Ruprecht-Karls-Universität Heidelberg, PhD thesis, 2013. http://ultracold.physi.uni-heidelberg.de/files/PhD_Andre.pdf. – PhD thesis, Ruprecht-Karls-Universität Heidelberg

[39] Zhang, Grace H. ; Braverman, Boris ; Kawasaki, Akio ; Vuletić, Vladan: Fast Compact Laser Shutter Using a Direct Current Motor and 3D Printing. In: *Review of Scientific Instruments* 86 (2015), Nr. 126105. https://arxiv.org/abs/1509.01566v2

[40] Zhang, J. ; Pagano, G. ; Hess, P. W. ; Kyprianidis, A. ; Becker, P. ; Kaplan, H. ; Gorshkov, A. V. ; Gong, Z.-X. ; Monroe, C.: Observation of a many-body dynamical phase transition with a 53-qubit quantum simulator. In: *Nature* 551 (2018), 601-604. https://www.nature.com/articles/nature24654

[41] Zürn, G. ; Lompe, T. ; Wenz, A. N. ; Jochim, S. ; Julienne, P. S. ; Hutson, J. M.: Precise Characterization of ^{6}Li Feshbach Resonances Using Trap-Sideband-Resolved RF Spectroscopy of Weakly Bound Molecules. In: *Physical Review Letters* 110 (2013), Nr. 135301. https://journals.aps.org/prl/abstract/10.1103/PhysRevLett.110.135301

[42] Zwierlein, M. W. ; Abo-Shaeer, J. R. ; Schirotzek, A. ; Schunck, C. H. ; Ketterle, W.: Vortices and superfluidity in a strongly interacting Fermi gas. In: *Nature* 435 (2005), 1047–1051. https://www.nature.com/articles/nature03858.pdf

Danksagung

Schließlich möchte ich an dieser Stelle allen herzlich danken, ohne die diese Arbeit nie denkbar gewesen wäre.

Zunächst danke ich Professor Selim Jochim für seine gute Betreuung der Arbeit, hilfreiche Ratschläge und anregende Diskussionen.

Vor allem möchte ich auch Ralf Klemt, Jan-Hendrik Becher und Philipp Preiss für ihre Hilfe im Labor beim Aufbau und der Justage der 2D-Falle danken. Besonders Ralf hat durch die Messungen für die Charakterisierung der 2D-Falle zum Gelingen dieser Masterarbeit beigetragen. Daneben will ich mich aber natürlich nicht zuletzt auch bei der gesamten Forschungsgruppe der ultrakalten Quantengase für eine gute und anregende Arbeitsatmosphäre zusammen mit Tischkicker-Runden und abendlichem Grillen bedanken.

Professor Matthias Weidemüller danke ich für die Übernahme der Zweitkorrektur.

Außerdem möchte ich mich bei allen bedanken, die in der Werkstatt des physikalischen Instituts an der Konstruktion der Einzelteile des Aufbaus für die 2D-Falle beteiligt waren, nicht zuletzt Ralf Ziegler. Besonders danke ich Stefan Hummel für die Einführung in CATIA, Diskussionen über das Design und seinen Einsatz bei der Fertigstellung und Optimierung der technischen Zeichnungen. Vielen Dank auch an die ganze CAD-Gruppe für den 3D-Druck der Laser-Shutter.

Schließlich möchte ich auch meinen Eltern für Ihr Vertrauen und Ihre bedingungslose Unterstützung all meiner Ziele und Träume danken.

Erklärung:

Ich versichere, dass ich diese Arbeit selbstständig verfasst habe und keine anderen als die angegebenen Quellen und Hilfsmittel benutzt habe.

Heidelberg, den 11. Februar 2020 ....